Experimental and numerical investigations of ionic liquid-aqueous microchannel extractions

By

QI LI

Department of Chemical Engineering

University College London

Torrington Place, London, WC1E 7JE, UK

September-5th, 2017

A thesis submitted for the degree of

Doctor of Philosophy

Declaration

I, **Qi Li**, declare that the thesis and the work presented in it are my own and have been generated by me as the result of my own original research. Where information has been derived from other sources, I can confirm that this has been clearly indicated in the thesis.

.....

Acknowledgement

I would like to express my special gratitude and thanks to my advisor Professor Panagiota Angeli for the continuous tremendous academic support of my Ph.D. study, for her motivation, patience and immense knowledge. Her advice on both research as well as on my career have been priceless. I could not have imagined having a better advisor and mentor for my Ph.D. study. I would also like to express my appreciation to Dr. Luca Mazzei, especially for sharing his taxonomic expertise so willingly, and for being so dedicated to his role as my co-supervisor.

I greatly appreciate the UCL Engineering Faculty and China Scholarship Council (CSC) for their financial support of my Ph.D. study. I am deeply obliged to all my colleagues and friends, Dr Wehliye Wehliye Hashi, Dr Valentina Dore, Dr Dimitrios Tsaoulidis, Dr Maxime Chinaud, Miss Evangelia Roumpea, Mr Kyeong Park, Dr Di Zhang, Dr Han Wu and all the PhD students in our group as they supported me in experiments, writing up and incanted me to strive towards my goal.

Last but not least, words cannot express how appreciative I am to my mother and father for their sacrifices made for me. Their supports to me have sustained me thus far. I would like express my sincere appreciation to my beloved husband Dr. Chuan Li, who has spent numerous sleepless nights with me and providing support at the moments when no one answers my queries. At the end I would like to thank my little angel, Bolun Li, to come to my life and bring endless happiness to my family.

Abstract

The thesis presents investigations on the process intensification behaviour in small scale separators operating in plug (segmented) flow. The continuous extraction behaviour, as well as the hydrodynamic characteristics of the liquid-liquid flow in microchannels is numerically and experimentally studied. The interphase mass transfer process using the extractant species Europium (III) as tracer was observed and quantified.

The Eu(III) microfluidic extraction from nitric acid solutions was carried out in 0.2 mm and 0.5 mm channels using an ionic liquid solution (0.2M n-octyl(phenyl)-N,N-diisobutylcarbamoylmethyphosphine oxide (CMPO) -1.2M Tributylphosphate) (TBP)/1-butyl-3-methylimidazolium bis[(trifluoromethyl)sulfonyl]amide; ($[C_4min][NTf_2]$) as the extraction phase. Distribution and mass transfer coefficients were found to have maximum values at nitric acid concentration of 1M. Mass transfer coefficients were higher in the small channel, where recirculation within the plugs and interfacial area are large, compared to the large channel for the same mixture velocities and phase flow rates. Within the same channel, mass transfer coefficients decreased with increasing residence time indicating that significant mass transfer takes place at the channel inlet where the two phases come into contact. The experimental results were compared with previous correlations on mass transfer coefficients in plug flows.

To better characterize the microfluidic flow, bright field Micro-Particle Image Velocimetry and high speed imaging were employed to measure velocity profiles and to obtain the geometric characterstics of the plug flow for the 1M HNO_3 solution that was used in the extraction experiments. Correlations regarding film thickness, plug velocity and plug length are developed based dimensionless parameters. It was found that the liquid film surrounding the plug is largely affected by the changes in the front cap for the range of Capillary numbers studied ($0.0224 < Ca < 0.299$), while the droplet volume is highly dependent on the channel diameter as well as the mixture velocity. The volume-of-fluid (VOF) method is then used to model the velocities and pressure distribution in the plug flow in the channel and shows good agreement with experimental results and previous models. These features will help in optimizing the microfluidic plug flow for mixing, as well as mass and heat mass transfer enhancement.

The mass transfer profiles of the extractant species Eu(III) are also studied using Laser Induced Fluorescence. Recirculation patterns appear in the dispersed aqueous phase from the plug formation stage, and 30-50 % of the mass transfer occurs during plug formation, where new interfaces are formed and mixing is enhanced from the recirculation pattern, especially at high U_{mix}. After experiencing convection and normal diffusion extraction equilibrium achieved, the fluorescent signal in the ionic liquid phase is very strong as Eu(III) transfers into it. The correlations proposed on the hydrodynamics and observations of the mass transfer characteristics during plug flow will contribute to the development of microfluidic devices.

Contents

List of Figures

List of Tables

Nomenclature

Latin Symbols

Ca	Capillary number, $Ca=\frac{\mu_{IL}U_p}{\sigma}$, dimensionless
$C_{aq,ini}$	initial concentration of Eu(III) in aqueous phase, $mol \cdot L^{-1}$
$C_{aq,fin}$	final concentration of Eu(III) in aqueous phase, $mol \cdot L^{-1}$
C_{aq}^{e}	Eu(III) concentration in aqueous phase at equilibrium, $mol \cdot L^{-1}$
$C(HNO_3)$	nitric acid concentration, M
CL	channel length, cm
dp	particle diameter, um
D	Eu(III) diffusion coefficient, $m^{2} \cdot s^{-1}$
D_{Eu}	Eu(III) distribution coefficient
E_{eff}	extraction efficiency, %
f	friction factor, dimensionless
K_L	overall mass transfer coefficient, $m \cdot s^{-1}$
K_La	overall volumetric mass transfer coefficient, s^{-1}
$K_{L,cap}$	mass transfer via cap, s^{-1}
$K_{L,film}$	mass transfer via film, s^{-1}
L	length, m
L*	dimensionless length, dimensionless
L_{film}	film length, m
L_p	plug length, m
L_s	slug length, m
L_{UC}	length of unit cell, m
n	refractive index, dimenionless
N	mass transfer flux, $mol\ m^{-2} \cdot s^{-1}$
NA	numerical aperture of objective lens, dimensionless
Q	total volumetric flow rate, $ml \cdot h^{-1}$
Q_{aq}	volumetric flow rate of aqueous phase, $ml \cdot h^{-1}$
Q_{IL}	volumetric flow rate of ionic liquid phase, $ml \cdot h^{-1}$
ID	channel internal diameter, mm
r	radius distance, m
r^0	location of recirculation centre, m

R	channel internal radius, mm
Re	Reynolds number, $Re=\frac{\rho U_{mix} ID}{\mu}$, dimensionless
R_p	plug width, m
t_{film}	Contact time of liquid film, s
T	Plug generation time, s
U_f	film velocity, $m \cdot s^{-1}$
U_{mix}	mixture velocity, $m \cdot s^{-1}$
U_p	plug velocity, $m \cdot s^{-1}$
$U_{x,p}$	horizontal velocity profile in aqueous plug, $m \cdot s^{-1}$
$U_{x,f}$	horizontal velocity profile in continuous film, $m \cdot s^{-1}$
V	flow volume, m^3
W	channel width, m
We	Weber number, $We=\frac{\rho U_{mix}^2 ID}{\sigma}$, dimensionless
ΔP	Pressure drop, Pa
Δ_{LMC}	log mean concentration difference, M

Greek Symbols

α	fitting parameter, dimensionless
β	fitting parameter, dimensionless
σ	interfacial tension, $N \cdot m^{-1}$
δ	film thickness, m
ε	dispersed phase fraction, dimensionless
θ	contact angle, °
λ	viscosity ratio, dimensionless
μ	dynamic viscosity, cp
τ	recirculation time, s
ρ	density, $kg \cdot m^{-3}$
φ	droplet effect parameter, $\varphi = \frac{\Delta P_p D}{\mu U_{mix}}$, dimensionless

Subscripts

aq	aqueous phase
c	continuous phase

d	dispersed phase
IL	ionic liquid phase
max	maximum value
mix	mixture phase
p	plug
s	slug

Chapter 1. Introduction

1.1 Background

Nuclear fuel reprocessing technology, which can be used both to recover fissionable actinides and to stabilize radioactive fission products into durable waste forms, is beneficial to reduce the volume of high-level waste and toxicity for safer storage or disposal. Various chemical separation methods, based on different water and organic solutions, have been proposed for this purpose. A general summarize of these methods can be found in **Figure 1.1**. The most well-known process is PUREX (**P**lutonium **U**ranium **R**edox **EX**traction) process, which has been adopted worldwide for the recovery of uranium and plutonium from spent nuclear fuel. It basically consists of a solvent extraction process using tri-n-butylphosphate (TBP) as extractant present in n-dodecane (n-DD) as diluent.

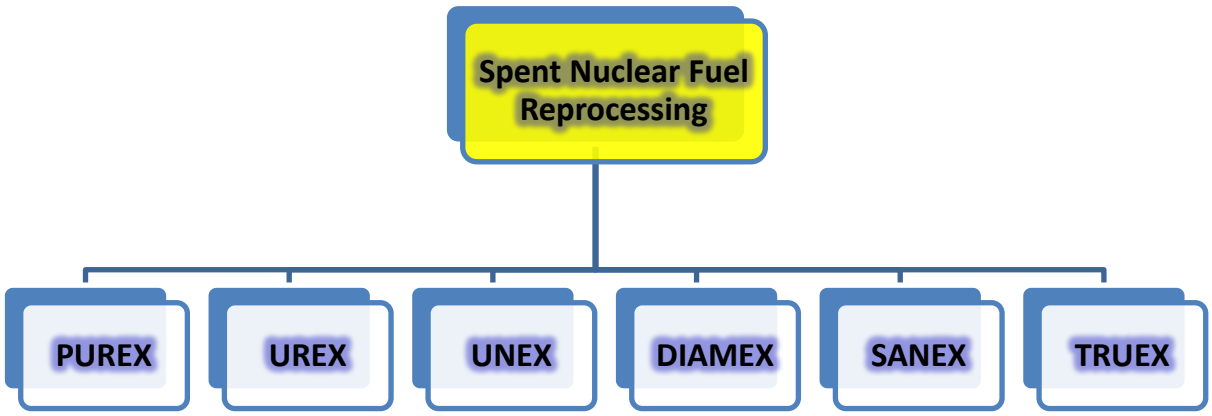

Figure 1.1: Spent nuclear fuel reprocessing methods

Lanthanides with their strong photoluminescence and magnetic properties are important to many industrial applications. Europium and yttrium oxides can be used as fluorescing agents for anodic rays in television and monitor screens (Lee and Yang 1995, Schaeffer et al. 2017). Lanthanide oxides are used to colour ceramics and glasses (Goonan 2011). Some compounds of lanthanides find applications as catalysts; for example oxides of thorium and cerium are used in the conversion of crude oil into common consumer products (Lew 2010). Lanthanides have also been used to regulate nuclear reactors as control rods because they absorb neutrons (Kučera et al. 2007) and to make strong permanent magnets (Wang et al. 2011). Scarcity on

natural resources means that the large quantities of lanthanides present in electronic waste such as spent fluorescent lamps (Rabah 2008), computer monitor scraps (Resende and Morais 2010) and colour TV tubes (De Morais 2000), need to be recycled. In the field of spent nuclear fuel reprocessing, recovery of the trivalent actinides and lanthanides is a key step in high-level waste management. Since trivalent lanthanides cannot be extracted by TBP, they are rejected to high-level liquid waste in the PUREX process (Rout et al. 2011). They can, however, be extracted by the TRUEX (TRansUranicEXtraction) solvent, which is a mixture of 0.2M n-octyl (phenyl)-N, N-diisobutylcarbamoylmethyphosphine oxide (CMPO)- 1.2 M TBP in n-dodecane (Horwitz et al. 1982, Schulz and Horwitz 1986).

Further intensification of the extraction process can be achieved by using **R**oom **T**emperature **I**onic **L**iquids (RTILs or ILs), which have emerged as alternatives to organic solvents for catalytic reactions and separations. Ionic liquids are salts with very low vapour pressure that can dissolve a wide range of organic and inorganic compounds. It has been found that when ILs are used in extractions as diluents in conjunction with appropriate extractants, the partition coefficients for lanthanides are increased compared to conventional solvents (Chun et al. 2001, Okamura et al. 2012, Rout et al. 2012). The distribution ratio of Eu(III) in CMPO-TBP/$[C_4min][NTf_2]$ can be 10 times larger than when n-dodecane (n-DD) is used (Rout et al. 2011). Nakashima et al. (2003) studied the extraction behaviour of trivalent lanthanides in the presence of CMPO/C_4mimPF_6, and found that use of ILs as the diluent of the extracting phase can reduce extractant consumption compared to a conventional solvent (n-DD). However, the industrial use of ionic liquids is still limited because of their high production costs. This barrier can be overcome with the use of the small scale separators which intensify mass transfer and can lead to the reduction of the amount of solvent required.

Technical and environmental reasons are driving the continuous development of small scale and miniaturised equipment within the frame of process intensification. The small scales reduce the molecular diffusion distances and increase the importance of surface/interfacial forces which bring new research challenges in the study of the hydrodynamic features and transport phenomena, particularly for multiphase systems (Assmann et al. 2013, Xu et al. 2013, Yang et al. 2013). Moreover, the characteristics of narrow residence time distribution and easy scale up with inherent reactor safe warrant the study of microreactors and their use for production of chemicals. Compared with macro-systems, there are three major differences in flows in microchannels (Shao et al. 2009). Firstly, the relative importance of surface over volume forces

increases. Secondly, Reynolds number is usually small and laminar flow is established, where viscous forces dominate over inertial ones. Thirdly, effects of wall roughness, wettability and flow confinement become important.

1.2 Aims and Objectives

The aim of this study is to study the Eu(III) intensified recovery behaviour in small scale reactors using ionic liquid for spent nuclear fuel recovery. The extraction mechanism, as well as the hydrodynamic characteristic of the microfluidic liquid-liquid flow is systematically investigated, and the numerical methodologies are developed to assist the optimization of the ionic liquid-aqueous processes.

1.3 Layout of the Thesis

This thesis consists of 7 chapters. Chapter 2 provides an overall reviews on the literatures related to multiphase flow regime in microchannel, Eu(III) extraction and microfluidic mass transfer behaviour. In chapter 3, a detail description of chemical materials and experimental setup/ procedures is given. Chapter 4 presents the results of continuous extraction of Eu(III) from nitric acid solutions in two microchannels using an ionic liquid solution. The mass transfer coefficients are compared against the literature correlations and values from conventional large scale systems. In Chapter 5, a detail discussion regarding the hydrodynamics of the plug flow regime for the liquid-liquid system using bright field micro-Particle Image Velocimetry is discussed, including the film thickness, plug length, plug velocity, pressure drop etc,. Results from CFD simulation show good agreement with the experimental observations. Chapter 6 investigates the mass transfer performance of the same system using the micro-LIF (laser-induced fluorescence) technique by quantifying the fluorescence images. Finally, in chapter 7, conclusions from this study, as well as future recommendations for future work are given.

Chapter 2. Literature review

Within the frame of process intensification, the miniaturization of chemical processes opens up new avenues for functions ranging from chemical production to extraction, absorption and separation. Micro-Structured Reactors (MSR) are systems with a well-defined structure of channels with an internal diameter in the range of 10-500 μm (Lowe and W.Ehrfeld 1999). Due to the large surface-to-volume ratio within small spaces, high heat transfer and mass transfer performance can be achieved. Moreover, the characteristics of narrow residence time distribution and easy scale up with inherent reactor safe (Kiwi-Minsker and Renken 2005) warrant the intensive study of micro-reactors. Driven by their unique characteristics, MRS has been the subject of many studies in two phase reactions, like gas-liquid and liquid-liquid mass transfer and heat operations. Among these applications, liquid-liquid extraction has attracted most interest as the short molecular diffusion distances and large specific interfacial area in microchannels are advantages for enhanced liquid-liquid contacting (Assmann et al. 2013). As extraction efficiencies depend on concentration gradients, interfacial area and residence times (Okubo et al. 2008), the exact flow pattern within the separation unit becomes important. Taylor (plug / segmented) flow in gas-liquid and liquid-liquid systems, where a continuous liquid phase separates elongated bubbles or drops (plugs) is a preferred pattern because the plug sizes are regular and can be controlled via the choice of inlet geometry. In addition, recirculation patterns establish in the liquid phases while the thin films that separate the bubbles/plugs from the channel wall enhance interphase mass transfer (Burns and Ramshaw 2001, Kashid et al. 2005, Okubo et al. 2008, Jovanović et al. 2012). Liquid-liquid microfluidics finds applications in solvent extraction(Kralj et al. 2007, Li and Angeli 2016, Breisig et al. 2017), dispersion(Lan et al. 2017), chemical synthesis/catalysis and biomedical analysis which often involve organic solvents with high hazard ratings. Compared to gas-liquid Taylor flow, the liquid-liquid plug flow provides better mass and heat transfer enhancement as the contribution of the dispersed phase is not negligible (Gupta et al. 2013).

2.1 Flow pattern in microstructured reactors

In multiphase flow systems, flow pattern are widely used to characterize the performance of micro-reactors, as it influence the heat/mass transfer and pressure drop. The maps are usually

plotted against the superficial velocities or the volumetric flow rates of each phase with distinct markers. They were developed based on dimensionless numbers (Reynolds, Capillary, and Weber numbers) representing the relative ratios of forces (Foroughi and Kawaji 2011):

$$Re_i = \frac{\rho_i U_i D}{\mu_i} \quad (2.1.1)$$

$$Ca_i = \frac{\mu_i U}{\sigma} \quad (2.1.2)$$

$$We_i = \frac{\rho_i U_i^2 D}{\sigma} \quad (2.1.3)$$

$$U_i = \frac{Q_i}{\frac{1}{4}\pi D^2} \quad (2.1.4)$$

Where ρ is the density, μ is the viscosity, σ is the oil-water interfacial tension, and U_i is the superficial velocity of phase i. Q is the volumetric flow rate and D is the microchannel diameter. The Reynolds number represents the ratio of inertia to viscous forces, the Capillary number the ratio of viscous to interfacial forces, and Weber number the ratio of inertia to interfacial forces. The Bond number, Bo, is usually very small therefore the gravitational effects on the flow pattern can be ignored for microfluidic flow.

$$Bo = \frac{\Delta p g D^2}{\sigma} \quad (2.1.5)$$

Where Δp is the difference between the densities of the two phases, and g is the gravitational acceleration.

The occurrence of different flow patterns in small channels is attributed to the competition between these forces. For example, the interfacial force tends to minimize the interfacial area while the inertia force tends to extend the interface in the flow direction and keep the fluid continuous (Joanicot and Ajdari 2005). The viscous forces dissipate the energy of perturbations at the interface and smooth the flow interface (Foroughi and Kawaji 2011, Kashid et al. 2011). It was found that inlet configurations, either T or Y-junction, have little effect on the flow pattern (Tsaoulidis et al. 2013). A typical flow pattern observed in two-phase microchannels is given in **Figure 2.1**.

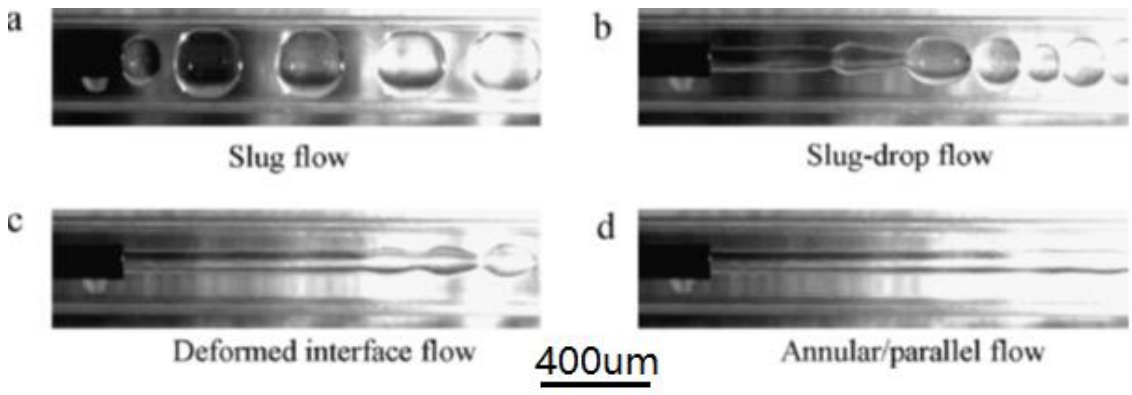

Figure 2.1: Flow patterns observed in two-phase microchannels. The above snapshots of flow pattern were presented for equal flow rates of both phases(Kashid and Kiwi-Minsker 2011).

a) Droplets, plugs and slugs

At the low Capillary and Weber numbers the interfacial forces dominated in this zone. The water plugs has a bullet shaped nose and surrounded by the continuous oil film. The viscous force deformed the water droplets and prevents them from touching the channel wall.

b) Slug and annular flow

The inertia force tends to make the water-oil interface wavy due to shear instability, while the viscous effect smooth the flow interface. Viscous forces also fights with the interfacial tension to keep the water core stable and continuous.

c) Deformed interface flow

The oil-water interface was smooth but shows sausage-shaped distortions due to interfacial tension effects. The viscous forces still dominates the interface smoothness and the inertia force was not strong enough to make any waives.

d) Annular/parallel flow

The inertia force in water phase is dominant and the velocity between the water core and oil film was sufficiently high.

Kashid and Agar (2007) investigated the effect of different capillary dimensions on flow regime for different capillaries with constant Y-junction dimensions. The transition boundary,

either from drop flow to slug flow or slug flow to deformed interface flow, broadens with increase in the capillary internal diameter as shown in **Figure 2.2**.

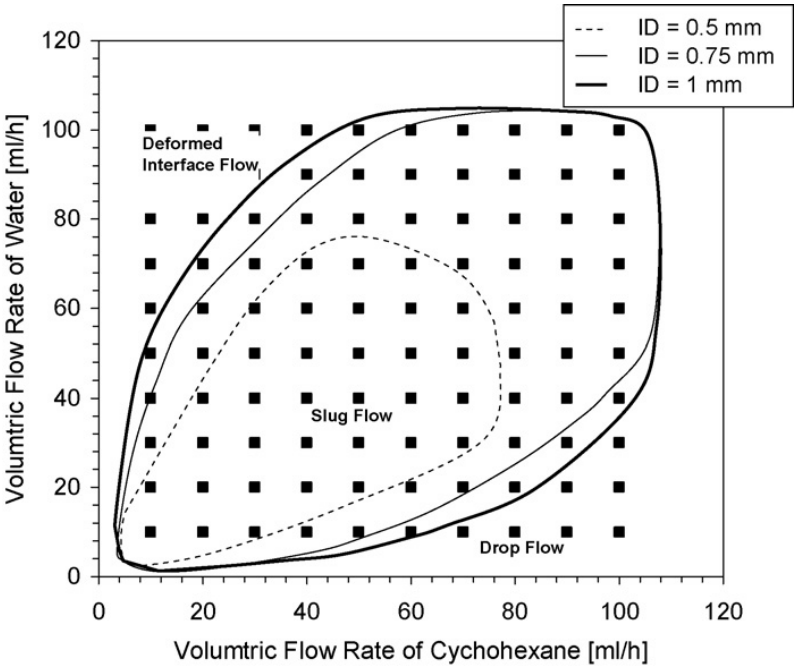

Figure 2.2: Observed flow regimes for equal capillaries and Y-junction diameter (ID=0.5, 0.75 and 1 mm)(Kashid and Agar 2007)

2.2 Taylor flow

Taylor (plug / segmented) flow in gas-liquid and liquid-liquid systems, where a continuous liquid phase separates elongated bubbles or drops (plugs) is a preferred pattern because the plug sizes are regular and can be controlled via the choice of inlet geometry. In addition, recirculation patterns established in the liquid phases while the thin films that separate the bubbles/plugs from the channel wall enhance interphase mass transfer (Burns and Ramshaw 2001, Kashid et al. 2005, Okubo et al. 2008, Jovanović et al. 2012).For the design of microfluidic devices operating in liquid-liquid plug flow knowledge of hydrodynamic parameters such as film thickness, plug length/velocity and pressure drop is particularly important (Gupta et al., 2013).

2.2.1 Film thickness

The significance of the film, which is formed due to viscous effects between the liquid plug and the wall is that the whole enclosed plug surface can participate in mass transfer. The film is formed due to viscous effects at the solid-liquid interface. The magnitude, however, depends on a number of parameters, including interfacial tension, the viscosity ratio between the two phases and phase flow rates. Because the enclosed plug exerts considerable shear stress on the wall film, it moves at a very low velocity.

One problem in determining the film thickness is no agreed standard about measurement location since it varies along the length of the slug. Some authors (Han and Shikazono 2009, Jovanović et al. 2011) report film measurements based on the thickness at the flat section midway between the front and rear caps; while others (Taylor.G 1960, S.Irandoust and B.Andersson 1989, M.N.Kashid et al. 2005, Grimes et al. 2007) have overcame the variation in film thickness by giving an average along the length of the slug. The film thickness, as captured in **Figure 2.3**, is characterized against dimensionless lengthL_D^* (L_D^*= L/D, D is the capillary diameter). For $L_D^* \leq 1.25$ (dimensionless length, L_D^*= L/D, D is the capillary diameter), the film thickness varied along the entire length of the slug. For $1.25 \leq L_D^* \leq 1.86$, a distinct transition region emerged between the front and rear slug caps. When it comes to $L_D^* \geq 1.86$, a uniform film was found to be present along the aqueous slug over a specific length.

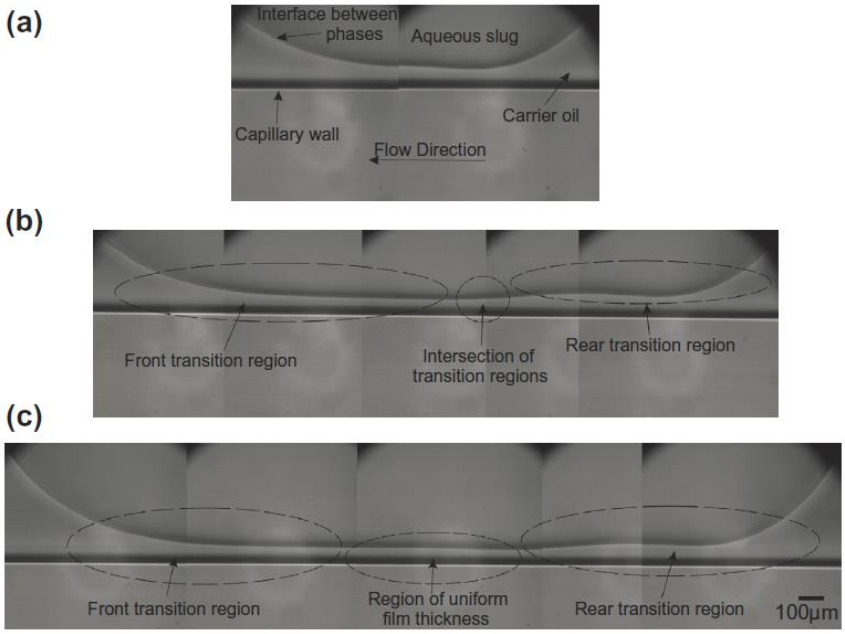

Figure 2.3: Experimental images of FC40/water flow, flowing at Ca=0.0072, highlighting the variation in slug profile with length at L* of (a) 1.15, (b) 1.81 and (c) 2.76(Mac Giolla Eain et al. 2013).

Due to the mismatch of refractive index between the channel wall and continuous phase in plug flow, an optical correction should be taken into consideration as visible film might not be identical to actual film. Mac Giolla Eain et al. (2013) proposed a correction method to minimize the light distortion for circular channel in a transparent water bath. A schematic illustration of the correction method is given in **Figure 2.4**. By measuring the plug radius (r_A), the incidence angle θ_1 and refracted angle θ_2, as well as the refractive index of the tubing the continuous liquid n_1 and n_2, respectively, the actual aqueous plug radius can be determined:

$$r_{Act} = r_A - (\sqrt{R^2 - r_A^2}) \tan(\theta_1 - \theta_2) \quad (2.2.1)$$

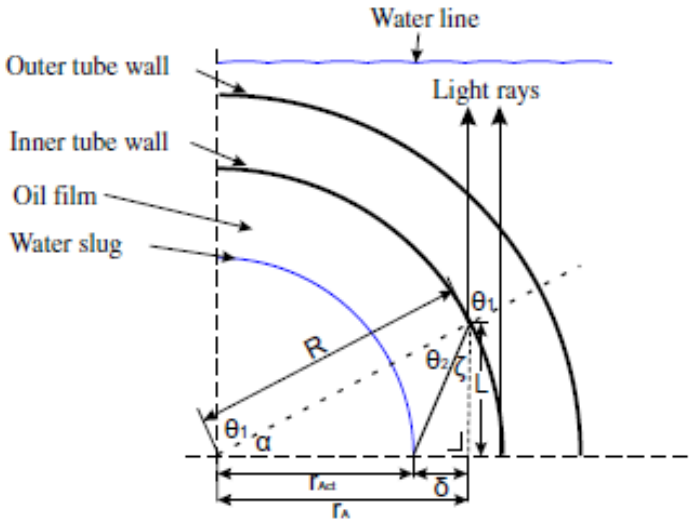

Figure 2.4: Schematic illustration of technique used to correct for refractive index mismatches (Mac Giolla Eain et al. 2013).

A similar method was proposed by Han and Shikazono (2009) to overcome the focus scatter problem caused by laser beam distortion due to the curvatures between axial and azimuthal directions, for circular channel in a glycerol (n=1.47) environment to match with the glass (n=1.474) channel. The effect of inner wall curvature is corrected based on the laser path and refraction as shown in **Figure 2.5**. The final liquid film thickness can be obtained as follows:

$$\delta = \frac{1}{2} y_m \left(\frac{\tan \theta_w}{\tan \theta_f} + 1 \right) + \frac{1}{4} D \sin(\theta_w - \theta'_w) \cdot \left(\frac{x_0}{\tan(\theta_w - \theta'_w - \theta'_f)} - \frac{1}{\tan \theta_w} \right) \quad (2.2.2)$$

where n_f and n_w are the refractive indexes of working fluid and the tube wall, y_m is the difference of the distance from the cover glass to the dry inner wall and the thickness with liquid film, θ'_w and θ'_f are the angle of incidence and the angle of refraction in X axis. The curvature effect on the film thickness is very small (less than 4%) and therefore can be ignored.

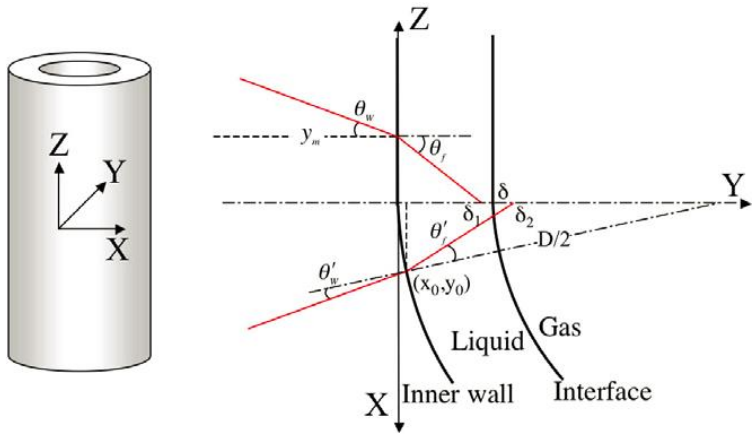

Figure 2.5: Correction for the inner wall curvature(Han and Shikazono 2009).

In a pioneering research work done by Bretherton (1961), the film thickness of gas-liquid Taylor flow was measured using conductimetry with lubrication theory for very small capillary number (Ca<0.003). Their work indicated that the film thickness was proportional to $Ca^{1/2}$. Further experiment work at a larger capillary number range was carried out using various optical diagnose method, including light absorption (Irandoust and Andersson 1989), video recording (Aussillous and Quéré 2000) and laser focus displacement (Han and Shikazono 2009) for gas-liquid Taylor flow. Aussillous and Quéré (2000) revealed the presence of two distinct flow regimes: a visco-capillary regime and a visco-inertial regime. For visco-capillary regime ($Re \gg 1$, $Ca \ll 1$ and $We \ll 1$), the normalized film thickness is only dependent on Capillary number. For visco-inertial regime, where Re>15 and Ca<0.01, a more accurate prediction model based is developed by Mac Giolla Eain et al. (2013). Unlike conventional definition of the Capillary number using the mean two phase velocity, the plug velocities calculated using captured images for refined Capillary number, which provides a truer representation of the forces influencing the magnitude of the film thickness. At $Ca<10^{-3}$ inertial effects is stronger and the film thicken, the Weber and Reynolds number is introduced to accurately describe the film thickness. A summarization of the correlations of normalized film thickness for two-phase Taylor flow is given in **Table 2.1**. The neglect of viscosity for dispersed phase and shear forces at the interface for gas-liquid flow may lead to large errors when applying these models in liquid-liquid flow.

Table 2.1: Correlations of normalized film thickness (δ/R) for two-phase Taylor flow

Correlation	Parameters	Measuring technique	Reference
$\frac{\delta}{R} = 0.5Ca^{1/2}$	Ca < 0.003, gas – liquid Taylor flow	Conductimetry	Bretherton (1961)
$\frac{\delta}{R} = 0.33[1 - \exp(-3.08Ca^{0.79})]$	9.5×10^{-4} < Ca < 1.9, gas – liquid Taylor flow	Light absorption	Irandoust and Andersson (1989)
$\frac{\delta}{R} = \frac{1.15\ Ca^{\frac{2}{3}}}{1 + 1.34\left(2.5Ca^{\frac{2}{3}}\right)}$	10^{-3} < Ca < 1.4, gas – liquid Taylor flow	Video recording	Aussillous and Quéré (2000)
$\frac{\delta}{R} = \frac{1.34Ca^{\frac{2}{3}}}{1+3.13Ca^{\frac{2}{3}}+0.504Ca^{0.672}Re^{0.589}-0.352w_e{}^{0}}$	Re < 2000, 0.002 < Ca < 0.16 gas – liquid Taylor flow	Laser focus displacement	Han and Shikazono (2009)
$\frac{\delta}{R} = 0.3\left(1 - e^{-6.9Ca^{0.54}}\right)$	0.007 < Ca < 0.159, liquid-liquid Taylor flow	Micro-PIV	Dore et al. (2012)
$\frac{\delta}{R} = 0.35Ca^{0.354}We^{0.097}$	0.002 < Ca < 0.119, liquid-liquid Taylor flow	High speed image capture	Mac Giolla Eain et al. (2013)
$\frac{\delta}{R} = \frac{1.34Ca^{\frac{2}{3}}}{1+[1+\emptyset(Re)]2.93\times Ca^{0.764}}$ $\emptyset(Re) = \left[\frac{33.1}{Re^{0.539}} + 0.000472Re^{1.909}\right]^{-1}$	0.005 < Ca < 2, 0 < Re < 900, gas-liquid Taylor flow	Open source CFD code (Gerris)	Langewisch and Buongiorno (2015)
$\frac{\delta}{R} = 0.658Ca^{0.6409}Re^{0.1067}$	0.03 < Ca < 0.18, liquid-liquid Taylor flow	High speed image capture	Tsaoulidis and Angeli (2016)

2.2.2 Plug length

Transport phenomena in two-phase Taylor flow, such as heat and mass transfer, are significantly affected by the plug / slug size (Angeli and Gavriilidis 2008, Okubo et al. 2008). Within the squeezing regime of gas-liquid and liquid-liquid flow, Garstecki et al. (2006) found droplet size increases linearly with the flow rate ratio and independent of fluid viscosities or interfacial tension. However, recent work shows the plug length has complicated relationship to system parameters, such as fluid properties, superficial velocities or even the configuration of the nozzle setup. In these works, the continuous capillary number Ca_c was used to represent the balance of cross flow shear force and Laplace pressure caused by the interfacial tension, which should be modified based on the geometry of the channel. Recent work has also shown that the inlet configuration has a significant effect on the plug or slug size and attempts have been made to predict it by studying the plug formation mechanisms. In the squeezing regime ($10^{-4} < Ca < 0.002$, $L_p/D > 2.5$), when the interfacial forces dominate over the shear forces, the plug break-up process is mainly controlled by the pressure drop across the plug, and the plug size is determined solely by the volumetric flow ratio of two immiscible fluids (Garstecki et al. 2006). In the dripping regime ($0.01 < Ca < 0.3$, $L_p/D < 1$), the formation process is dominated by both the shear and interfacial forces, and the size depends on the Capillary number only (Van der Graaf et al. 2006, Xu et al. 2008). In the transition regime ($0.002 < Ca < 0.01$, $1 < L_p/D < 2.5$), the plug size depends on all these forces (Fu et al. 2010).

Laborie et al. (1999) studied the gas-liquid Taylor flow in 1-4 mm circular channel for low capillary number ($1.5 \times 10^{-3} < Ca < 0.1$), by injecting the air via a porous membrane. An increment in liquid viscosity, superficial velocity and capillary size will lead to a decrease of the bubble length. Qian and Lawal (2006) proposed an empirical correlation of bubble length through 2D simulation of the gas-liquid flow in T-junction for $2.78 \times 10^{-3} < Ca < 0.01$, and they proposed a correlation based on capillary number and Reynolds number. Similar correlation was suggested by Tsaoulidis and Angeli (2016) by experimentally studying the liquid-liquid Taylor flow in 0.5 to 2 mm microchannels. Considering the high viscosity ratio between ionic liquid and dispersed aqueous nitric acid, μ_c/μ_d was not included in the correlation as it doesn't affect the plug size for $Ca<0.1$. These empirical correlations are summarized in **Table 2.2**, together with models based on plug formation mechanisms as given before.

Table 2.2: Correlations of normalized plug length (L_p/D) for two-phase Taylor flow

Correlation	Taylor flow type	Parameter	Reference
$\frac{L_p}{D} = 0.0878\frac{Re_p^{0.63}}{Eo^{1.26}}$ $Re_V = \frac{\rho U_p D}{\mu}$ $E_o = \frac{\rho D^2 g}{\sigma}$	gas – liquid flow in 1-4mm circular channel	$1.5 \times 10^{-3} < Ca < 0.1$	Laborie et al. (1999)
$\frac{L_p}{D} = 1.637\varepsilon^{0.107}(1-\varepsilon)^{-1.05}Re^{-0.075}Ca^{-0.0687}$	gas – liquid flow T-junction, 2D simulation	$0.09 < \varepsilon < 0.91$ $15 < Re < 1500$ $2.78 \times 10^{-4} < Ca < 0.01$	Qian and Lawal (2006)
$\frac{L_p}{D} = 1 + \alpha\frac{Q_{in}}{Q_{out}}$	Liquid/gas-liquid flow, rectangular channel, T-junction	$Ca < 10^{-2}$	Garstecki et al. (2006)
$\frac{L_p}{D} - \varepsilon = k(Q_d/Q_c)^{\alpha}Ca^{\beta}$	Liquid-liquid flow Rectangular channel, T-junction	$10^{-4} < Ca < 0.3$	Xu et al. (2008)
$\frac{L_p}{D} = 1.3\varepsilon^{0.07}(1-\varepsilon)^{-1.01}We^{-0.1}$	gas – liquid flow square/circular/rectangular channel, Y-junction	$0.1 < We < 26$ $0.02 < U_p < 1.2$ m/s $0.06 < \varepsilon < 0.85$	Sobieszuk et al. (2010)
$\frac{L_p}{D} = 0.72(Q_d/Q_c)^{0.14}Ca^{-0.19}$ $(L_p/D < 2.35)$ $\frac{L_p}{D} = 0.30(Q_d/Q_c)^{0.23}Ca^{-0.42}$ $(L_p/D > 2.35)$	Liquid-liquid flow Rectangular channel, co-flow	$0.001 < Ca < 0.01$	Fu et al. (2012)

$\frac{L_p}{D} = 2.282 \cdot Ca^{0.2728} \cdot Re^{0.4617} \cdot Re_c^{-0.9634}$	Liquid-liquid flow Rectangular channel, T-junction	$0.03 < Ca < 0.18$	Tsaoulidis and Angeli (2016)
$\frac{L_p}{D} = \theta_0 + \theta_1 \frac{Q_d}{\mu Q_c}$	Liquid-liquid flow Circular channel, T-junction	$0.001 < Ca < 0.01$	Prileszky et al. (2016)

2.2.3 Droplet volume

The versatility of microfluidic system also lies essentially in the ability to reliably transport and precisely control of the fluid volumes of each individual droplet. In small scale channels, average volume of individual bubble/droplet can be obtained by determining the input flow rate and bubble/droplet frequency. This approach, however, not only suffers from the inaccuracy description of flow rate, but also cannot be used when isolated bubbles and droplets are the topic of the investigation (Khodaparast et al. 2014). In addition, the local dispersed phase hold-up is not always identical to its transport fraction in microfluidic system, as the droplet moves slightly faster due to the existence of a nearly stagnant film surrounding in some cases. Therefore, in this work, local droplet volume is measured by rotation of the detected interface around the centerline of the capillary from the high resolution images.

Lac and Sherwood (2009) used boundary integral methods to analyze the effect of droplet size, capillary number (Ca) and viscosity ratio (λ) on the droplet shape, droplet speed and the pressure drop for the flow of a viscous droplet in a circular tube filled with an immiscible viscous liquid. They concluded that the shape of the droplets was not affected by the presence of the wall (i.e, it remained circular) unless the ratio of the diameter of a spherical droplet having the same volume as the Taylor droplet to the channel diameter, d*, was 0.7 or more. When the ratio became 1.1, the droplet shape and velocity were found to be independent of the droplet volume and a further increase in the droplet volume resulted in an increase of the droplet length without any change in the shape of leading and trailing menisci.

2.2.4 Plug velocity

Due to the presence of non-stagnant film surrounding the enclosed plug, the dispersed phase moves with a velocity is slightly higher than the mixture velocity, and the difference between the plug velocity and mixture velocity increases with increasing mixture velocity. These velocities are key characteristics that determine the performance of the chemical reactors involving mass transfer.

The plug velocity can be calculated via empirical method, or by assuming a fully developed laminar velocity profile distribution. In the study of gas-liquid Taylor flow, a relative excess velocity is proposed for bubble with uniform film, $m = (U_P - U_{mix})/U_p$. Previous work (Bretherton 1961, Liu and Zhang 2009) found the plug velocity was only influenced by the liquid properties and mixture velocity for low capillary number in gas-liquid Taylor flow. These correlations may fail to accurate in predicting the plug velocity for liquid-liquid Taylor flow because the film thickness estimation associated only with Bretherton (Bretherton 1961) equation. For a large droplet with sufficient long uniform thickness film region, the velocity profiles in the center region that far away from the plug end influence can be given by an ideal annular flow velocity:

$$U_{x,p} = 2U_{mix}\frac{\left[\left(1-\frac{R_p^2}{R^2}\right)+\frac{1}{\lambda}\left(\frac{R_p^2}{R^2}-\frac{r^2}{R^2}\right)\right]}{\left(1+\frac{R_p^4}{R^4}\right)\left(\frac{1}{\lambda}-1\right)} \tag{2.2.3}$$

where Rp and R is the radius of plug and channel, respectively. Kashid et al. (2005) estimated the plug velocity by neglecting the flow in continuous film surrounding the dispersed phase, which is accurate for gas-liquid flow but not for liquid-liquid flow. Gupta et al. (2013) proposed a similar correlation by considering the viscosity ratio in liquid-liquid Taylor flow, and it shows excellent agreement with experimental results for low Capillary number ($0.0045 < Ca < 0.0089$). A summarization of the plug velocity correlations for two-phase Taylor flow is given in **Table 2.3.**

Table 2.3: Correlations of plug velocity for two-phase Taylor and plug flows

Correlation	Parameters	Reference
$\frac{U_p - U_s}{U_p} = 1.29(Ca)^{2/3}$	Ca < 0.003, gas – liquid Taylor flow	Bretherton (1961)
$\frac{U_p}{U_{mix}} = \frac{1}{1 - 0.61Ca^{0.33}}$	$2 \times 10^{-4} < Ca < 0.39$ gas – liquid Taylor flow	Liu et al. (2005)
$\frac{U_p}{U_{mix}} = \frac{2}{1 + (R_p/R)^2}$	$0 < U_{mix} < 0.2$ m/s, liquid - liquid Taylor flow	Kashid et al. (2005)
$\frac{U_p}{U_{mix}} = \frac{\left[2 + \left(\frac{R_p}{R}\right)^2\right]\left(\frac{1}{\lambda} - 2\right)}{\left[1 + \left(\frac{R_p}{R}\right)^4\right]\left(\frac{1}{\lambda} - 1\right)}$	$0.076 < U_{mix} < 0.151$ m/s, $0.0045 < Ca < 0.0089$ liquid - liquid Taylor flow	Gupta et al. (2013)
$\frac{U_p}{U_{mix}} = \left(1 - 2\frac{\delta}{D}\right)^{-2}$	$0.005 < Ca < 2$, $0 < Re < 900$ gas – liquid Taylor flow	Langewisch and Buongiorno (2015)

2.2.5 Pressure drop

The pressure drop is an important parameter in the reactor design as it provides crucial information regarding the energy consumption, required pump capacity as well as the materials needed for the reactor construction. Compared to the large number of gas-liquid investigation, little attention was paid on the liquid-liquid slug flow pressure drop. Furthermore, few correlations have been proposed so far which include both the influence of the surface tension and the slug lengths. Finally, the influence of the liquid film should be included in predictive models. A common way to calculate the total pressure drop is to sum the Laplace pressure drop, caused by the presence of the immiscible interface, to the frictional pressure drop of dispersed plugs and continuous slugs (Jovanović et al. 2011, Gupta et al. 2013, Tsaoulidis and Angeli 2016). In these models it is assumed that the film is uniform along the plug. Another path is to characterize the two-phase friction factor by adding the Laplace component to the single-phase Hagen-Poiseuille flow (Kreutzer et al. 2005, Walsh et al. 2009, Walker 2016).

A large distinction of research in liquid-liquid slug flow pressure drop prediction from gas-liquid flow is the interfacial effects are either neglected or included in the form of We and Bo

numbers (Chen et al. 2002), therefore not accounting for the influence of the slug length on the overall pressure drop. Kashid and Agar (2005) proposed pressure drop model which can be interpreted in terms of two contributions: the frictional pressure drop of the individual phase (ΔP_{Fr}) and the pressure drop due to the interfacial effects (ΔP_I). For the purpose of the pressure drop modelling the slug unit length (l_U), dispersed phase length fraction (α), and the contact angle were used as input parameters. The overall pressure drop was written as:

$$\Delta P_{slugflow} = \Delta P_{Frictional} + \Delta P_{Interfacial} = \Delta P_{Fr,c} + \Delta P_{Fr,d} + \Delta P_I \quad (2.2.4)$$

The frictional pressure drop, $\Delta P_{Fr,}$ was calculated from Hagen-Poiseuille equation for a cylindrical tube and was expressed as a function of the slug unit length ($l_U=l_d+l_c$) and the dispersed phase length fraction ($\alpha=l_d/l_U$), and the interface pressure ΔP_I was obtained from the Young-Laplace equation:

$$\Delta P_{Fr,d} = \frac{8\mu_d v \alpha l_U}{R^2} \quad (2.2.5)$$

$$\Delta P_{Fr,c} = \frac{8\mu_d v(1-\alpha) l_U}{R^2} \quad (2.2.6)$$

$$\Delta P_I = \frac{2\gamma}{R}\cos\theta \quad (2.2.7)$$

where θ is the contact angle of continuous and dispersed phase on channel wall. Combining the above equations yielded the model for the pressure drop across the length of the capillary:

$$\Delta P_{slugflow} = \frac{L}{l_U}\left(\Delta P_{Fr,c} + \Delta P_{Fr,d}\right) + \frac{2L-l_U}{l_U}\Delta P_I \quad (2.2.8)$$

Kashid et al.Kashid et al. (2008) analyse the influence of the film velocity on the slug flow pressure drop and two models were developed and evaluated: the stagnant film model and the moving film model. The only difference between the stagnant (SF) and moving film (MF) pressure drop models is in the terms of describing the frictional losses of the dispersed phase:

$$\Delta P_{MF} = \frac{4v_{slug}L\alpha}{\frac{R^2-(R-h)^2}{\mu_C}+\frac{0.5(R-h)^2}{\mu_d}} + \frac{8\mu_c v(1-\alpha)l_U}{R^2} + \frac{l}{l_U}7.16(3Ca)^{2/3}\frac{\gamma}{d} \quad (2.2.9)$$

Gupta et al. (2013) developed a model to predict the overall pressure drop in a unit cell, consisting a Taylor droplet surrounded by the two halves of continuous phase slugs is also presented by summing up the pressure drop distributions from the continuous phase liquid slugs, uniform thickness film region and interfacial pressure drops at the droplet front and rear:

$$\left(\frac{\Delta P}{L}\right)_{UC} = \frac{8\mu_C U_{TP} L_{Slug}}{L_{UC}} + \frac{8\mu_C U_{TP}}{R^2\left[\left(1+\left(R_i^4\right)/R^4\right)(1/(\lambda-1))\right]}\frac{L_{Film}}{L_{UC}} + \frac{4.52}{L_{UC}}\frac{\sigma}{R}(3Ca)^{2/3} \quad (2.2.10)$$

For a microchannel initially filled with continuous solution, the Lockhart-Martinelli correlation can be employed to predict the pressure drop (Kawahara et al. 2005). The pressure drop containing separate terms for individual pressure drops in each phase, and two-phase friction multipliers as well as the Lockhart-Marinelli parameter are defined as:

$$\left(\frac{\triangle P}{L}\right)_{TP} = \left(\frac{\triangle P}{L}\right)_{w} + \eta\xi_0\left(\frac{\triangle P}{L}\right)_{0} \quad (2.2.11)$$

$$\varphi_W = \sqrt{\frac{\left(\Delta P/L\right)_{TP}}{\left(\Delta P/L\right)_W}}\varphi_O = \sqrt{\frac{\left(\Delta P/L\right)_{TP}}{\left(\Delta P/L\right)_O}} \quad (2.2.12)$$

$$\chi = \frac{\varphi_W}{\varphi_o} = \sqrt{\frac{\left(\Delta P/L\right)_o}{\left(\Delta P/L\right)_W}} \quad (2.2.13)$$

where ξ_0 is the ratio of the volumetric oil flow rate over the total flow rate, η is a constant depending on the microchannel property, φ_w and φ_o is the water and oil phase friction multiplier respectively, and χ is the Lockhart-Martinelli parameter. For plug and annular flows, Kawahara et al.Kawahara et al. (2005) proposed the friction multiplier can be written as $\varphi_w^2 = 1 + \alpha\chi + \beta\chi^2$, where α and β are constants. Foroughi and Kawaji (2011) experimentally confirms the above equation can accurately predict the pressure drop of oil-water in a 250 μm diameter microchannel, like slug , annular and annular-droplet flow, as given in **Figure 2.6.**

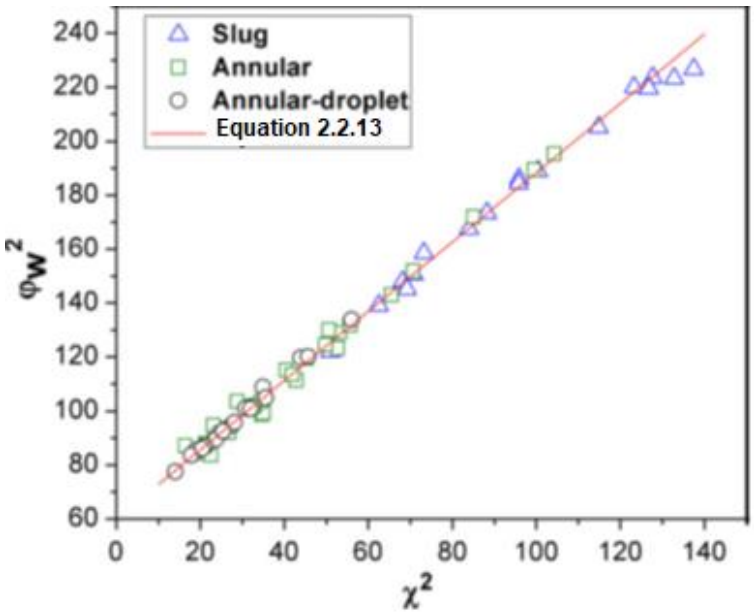

Figure 2.6: Linear variation of the water two-phase friction multiplier with Lock-Martinelli parameter (Foroughi and Kawaji 2011).

2.2.6 Numerical microfluidic

An insight representation of the liquid-liquid mixing phenomenon and hydrodynamic characteristic in small scale channels are crucial for numbering-up. To date most numerical studies on two-phase flows in microchannels are conducted for gas/liquid flows in circular microtubes. Some pioneer research in liquid-liquid microfluidic simulation, done by Kashid (Kashid et al. 2007, Kashid et al. 2010, Kashid et al. 2012), predicted the flow pattern and slug inner circulation.

Two major methods has been applied to capture the interface of two phases: the Volume of Fluid (VOF) method and the Level Set method (LS) (Talimi et al. 2012). The VOF method is developed based on a fraction function number 'C' that varies between 0 and 1. C is 0 and 1 when the cell is filled with main phase and secondary phase, respectively, and the value between them indicates the existence of interface in the cell. For the LS method, the interface is developed based on a function that represents the distance to the interface. The value of 0 means the interface, while positive and negative values indicate either side of the interface.

For VOF method, the hydrodynamics were calculated by the finite-volume method, developed by Hirt and NicholaHirt and Nicholes (1981) and implemented in the flow solver FLUENT. The fluids were described using the incompressible Navier-Stokes equations. The governing equations of the VOF formation for the liquid-liquid flow are as follows (Qian and Lawal 2006):

Equation of continuity:

$$\frac{\partial \rho}{\partial t} + \nabla \cdot \left(\rho \underset{v}{\rightarrow}\right) = 0 \tag{2.2.14}$$

where ∇ is the nabla operator representing the the curl of a vector field.

Equation of motion:

$$\frac{\delta\left(\rho \underset{v}{\rightarrow}\right)}{\delta t} + \nabla \cdot \left(\rho \underset{v}{\rightarrow} \underset{v}{\rightarrow}\right) = -\nabla p + \nabla\left[\mu\left(\nabla \underset{v}{\rightarrow} + \nabla \underset{v}{\rightarrow}^{T}\right)\right] + \rho \underset{g}{\rightarrow} + \underset{F}{\rightarrow} \tag{2.2.15}$$

Volume fraction

$$\frac{\delta \alpha_{aq}}{\delta t} + \underset{v}{\rightarrow} \cdot \nabla \delta \alpha_{aq} = 0 \tag{2.2.16}$$

$$\rho = \alpha_{org}\rho_{org} + \alpha_{aq}\rho_{aq} \tag{2.2.17}$$

$$\mu = \alpha_{org}\mu_{org} + \alpha_{aq}\mu_{aq} \tag{2.2.18}$$

To simulate the curvature of the slugs, a dynamic contact angle equation was implemented as follows:

$$\theta_{dyn} = \theta_{const} + (\theta_A - \theta_R) \cdot \tanh\left(\frac{\bar{n}_{wall}}{\bar{n}_{theta}}\right) \tag{2.2.19}$$

where θ_A is the contact angle at the front of the curved slug and θ_R at the rear of the slug.

A common model for microfluidic investigation is a fixed frame computational domain, as given in **Figure 2.7**, which consists of a junction and two microchannels downstream. In order to allow the multiphase flow system fully developed, the minimum ratio of length to diameter (L/D) was studied and should be no less than 40 (Lakehal et al. 2007, Talimi et al. 2012). It, however, indicates long computing resources especially when heat or mass transfer are involved.

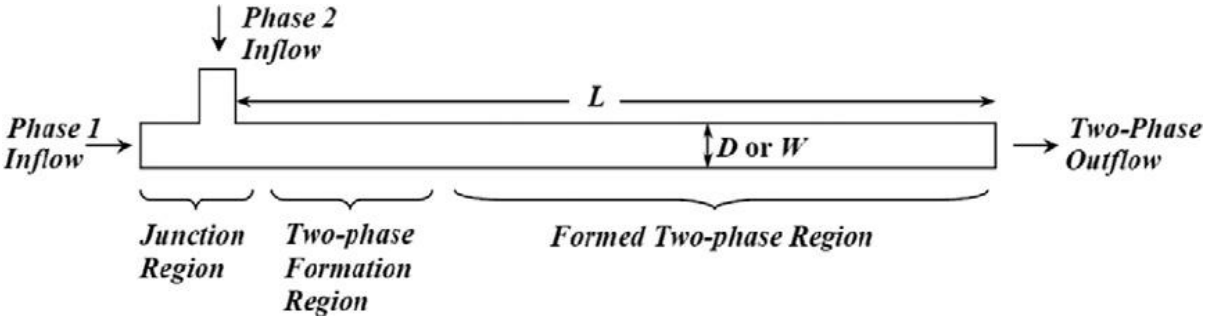

Figure 2.7: A typical computational domain frequently used in fixed frame simulations (Lakehal et al. 2007).

Simulation based on 2D or 3D computational domain is still a conversational issue. 2D computation domain means less calculations time, but it only applicable for rectangular microchannel with a very large aspect ratio. It has been proven that for a circular microchannel, the 2D computational domain gives different bubble generation compared to a 3D simulation (Goel and Buwa 2008), although in some cases they gives comparable results in predicting the plug length (Cherlo et al. 2009). Generally for the case of circular microtube, 3D computational domain should be chosen for accurate prediction.

The boundary conditions of microtube inlets, walls and exit play an important role in two-phase flow. The mostly used boundary condition at the inlet is specified velocity (Kashid et al. 2007, Lakehal et al. 2007). A specified pressure, normally the standard atmospheric pressure, was used for outlet numerical simulations. Some authors also reported reliable prediction using outflow boundary condition (Goel and Buwa 2008, Cherlo et al. 2009), but outflow boundary condition is not recommended to use with junction of VOF model. The no-slip boundary condition can be applied in most of the situations specially when there is a pre-occupied liquid flow. Deciding on slip or no-slip boundary condition depends on a dimensionless group which is called Knudsen number (Talimi et al. 2012), Kn, and defined as follows:

$$\mathrm{Kn} = \frac{\lambda}{\mathrm{L}} \tag{2.2.20}$$

Where λ is the mean free path of the gas molecules and L is a characteristic length e.g. hydrodynamic diameter. More fundamental details can be found in Renardy et al. (2001) and Spelt (2005).

As for grid resolution, a very fine mesh near the walls in computational domain is essential to capture the thin film. Gupta et al. (2009) proposed a criterion for mesh refinement near the wall based on film thickness which is a function of Capillary number. In their study, the hydrodynamics of air and water in a circular channel of diameter 0.5 mm and length of 10D is carried out. In order to successfully predicting the thin film between gas and liquid phases, a grid having uniform square elements of size 5μm in the core and rectangular elements (2.4μm × 5μm) in the 12 μm thick film region was used for the simulation. Mehdizadeh et al. (2011) uses dynamic grid to optimize the simulation cost. Only refined grid was used near the interface region, for example the plug ends and film region, and coarsened grid where only one phase is calculation.

The VOF algorithm will add considerable computational cost, especially in the case of interface reconstruction, which requires a very small time step (normally between 1E-7s to 1E -4s) compared to required simulation time (usually several seconds or more). To increase the simulation speed in terms of solver setup, using automatic time stepping, non-iterative time steps or parallel process is necessary (Glatzel et al. 2008). To optimize the time step, the Courant number is defined as a comparison between the particle moving distance during the assumed time step and control volume dimension:

$$\mathrm{Co} = \frac{\Delta t}{\Delta x / V} \tag{2.2.21}$$

Where Δx is the grid size and V is the fluid velocity. Mehdizadeh et al. (2011) adopt a maximum Courant number of 0.25. Considering the very fine grid near close to interface region, the time steps are usually in the range of 10^{-7}s. It may go even smaller during the plug break up process.

The hydrodynamics of liquid-liquid plug flow in microchannels have been studied numerically with computational fluid dynamics simulations, which considered the plug formation at the inlet (Liu and Zhang 2009, Li et al. 2012), film thickness (Gupta et al. 2013), velocity profiles and circulation inside the plugs (Silva et al. 2008, Afkhami et al. 2011) and pressure drop (Jovanović et al. 2011, Yan et al. 2012). These studies have used either a fixed reference frame when plug formation is considered or a moving one and periodic conditions when an isolated plug is investigated (Talimi et al. 2012). Kurup and Basu (2011) compared the results from CFD simulations and experimental velocity profiles obtained with micro Particle Image Velocimetry (μPIV) and found the circulation patterns largely depend on the Capillary number.

The simulations on recirculation time, defined as the average time to displace material from one to the other end of the plug/slug, indicate that the flow pattern is influenced by a combination factors such as flow velocity, plug length, channel size and viscosity ratio between the two phases (Kashid et al., 2008; Lececi et al., 2009; Abadie et al., 2012; Meyer et al., 2014).

While these numerical methods have been successful to a great extent, reliable experimental measurements, which can assist in validating the simulation results, is still needed at the same pace. Non-intrusive optical velocitmetry technique, like Micro-Particle Image Velocimetry (μPIV), is designed to extract multipoint information of velocity field with high accuracy and spatio-temporal resolutions. With this method, detail mixing characteristics during plug formation and inside the microdroplet can be captured by tracking fluorescence signals in either dispersed or both phases. However, this effective technique is still limited by several facts: simultaneous particle tracking and interface detection; high intensity reflections at mismatched interface and side intrusive effects (Khodaparast et al. 2014). Therefore bright field Micro-Particle Image is developed to realize simultaneous interface detection and velocity measurement in the fast moving dispersed plug with relatively simple optical setup. Compared to the laser illuminated μPIV, where the fluorescence measurement is highly dependent on the nature and size of the particle, the bright field technique is affected by many factors, such as light position, channel material and microscope magnification etc. (Hagsäter et al. 2007). These factors would lead to high measurement uncertainty. Besides, the filter in front of camera in fluorescence PIV excludes unwanted light, which can ensure high signal-to-noise ratio. On the other hand, without introducing laser in the apparatus, the bright field has more widely used.

2.3 Europium extraction based on ionic liquid

Ionic liquid, also refers to ‘room temperature ionic liquids’ (RTILs) or ‘liquid organic salts’, emerged as an alternative solvent for catalytic, biocatalytic and organic reactions. It is defined as the organic salts molten at temperatures lower than 373K (Huddleston et al. 1998, T.Welton 1999, J.F.Brennecke and E.J.Maginn 2001). Because of their properties such as insignificant vapor pressure, amazing ability to dissolve organic and inorganic compounds and tenability to get task-specific form (Rout et al. 2011), the application of RTILs as new separation media in nuclear fuel cycle has investigated recently (S.Dai et al. 1999, S.Chun et al. 2001, Rout et al. 2012). These studies showed that extractant in conjunction with RTILs diluents have provided

an improved extraction of target metals from aqueous solution under the condition that gave negligible or meagre extraction with customary diluents. This was attributed to the extraordinary solvating ability of RTILs in the extracted phase (Rout et al. 2012). It is widely accepted S.Dai et al. (1999) were the first to suggest that a unique salvation environment offered by ionic liquids (ILs) could make them especially efficient as solvents for the extraction of cationic metal complexes from aqueous solutions.

In the case of lanthanides recovery using ionic liquid, three types of ionic liquid system were proposed by previous researchers. The first one was developed as an improvement of TUREX solvent, using ionic liquid to replace the conventional organic solution. The second system employs acidic chelating extractants such as Htta (2-thenoyltrifluoroacetone (1-(2-thienyl)-4,4,4-trifluoro-1,3-butanedione) because they are more favourable in the IL extraction system. Instead of being diluent in the previous two sytems, ionic liquid can also act as extractant.

2.3.1 Improved TUREX system

Rout et al. (Rout et al. 2011) studied the extraction behaviour of Eu(III) from nitric acid medium by a solution of CMPO-TBP/$[C_4min][NTf_2]$. Remarkable enhancement in distribution ratio was achieved with the addition of CMPO, and the application of $[C_4min][NTf_2]$ (nearly 50 times higher than conventional solution such as n-DD, as shown in **Figure 2.8**). During the solvent extraction, neutral extractant such as CMPO are crucial to avoid the formation of third phase, which is the splitting of organic phase into two phase with the heavier one, rich in metal-solvate and the lighter phase rich in diluent (Vasudeva Rao and Kolarik 1996). The distribution ratio of Eu(III) increases with increasing nitric acid concentration and reaches a maximum value around 1 M then followed by decrease. Although the addition of TBP may slight reduce the Eu(III) distribution ratio, it however, is crucial in reducing the formation of 'crud-type' precipitate at high Eu(III) loading, and reducing the viscosity of the ionic liquid phase (viscosity of 0.2 M CMPO- 0.2 M TBP/$[C_4min][NTf_2]$ system is higher than that of 0.2 M CMPO- 1.2 M TBP/ $[C_4min][NTf_2]$).

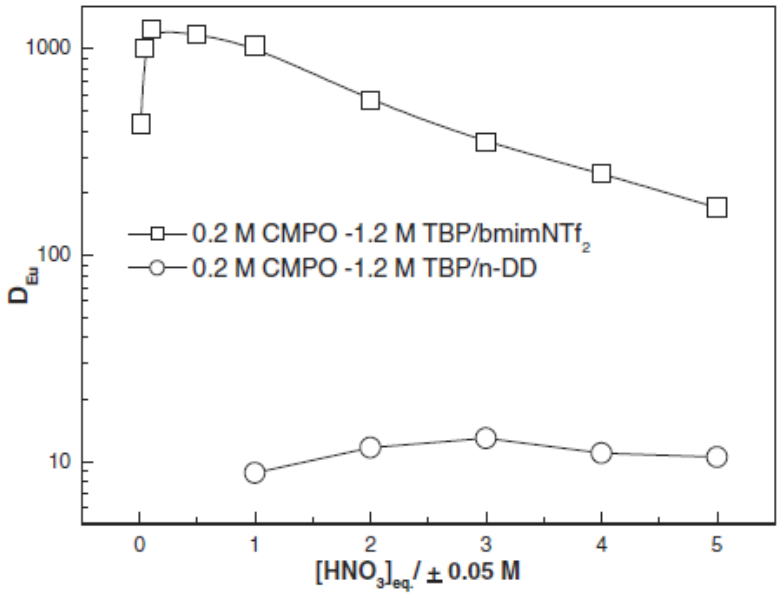

Figure 2.8: Variation in the distribution ratio of Eu(III) with concentration of nitric acid at 303K. Organic phase= 0.2 M CMPO-1.2 M TBP/[C_4min][NTf_2] (or n-DD), aqueous phase=0.01-5 M HNO_3 spiked with Eu(III) tracer (Rout et al. 2011).

Nakashima et al. (Nakashima et al. 2003) studied the extraction behaviour of trivalent lanthanides in the present of CMPO/bminPF_6, and found high efficient extraction of lanthanides can be achieved without an anionic species in the ILs-based extraction system. In a further study, Rout et al. (Rout et al. 2011) found the distribution ratio decreases with increase in the chain length of alkyl group attached to the cation part of the ionic liquid(as shown in **Figure 2.9**), which is probably attributed to the decrease in the ability of ionic liquids to undergo ion exchange with increase of hydrophobicity. Similar conclusion was also drawn by Jensen et al. (2003), showing [C_4min][NTf_2] is a preference in lanthanides recovery.

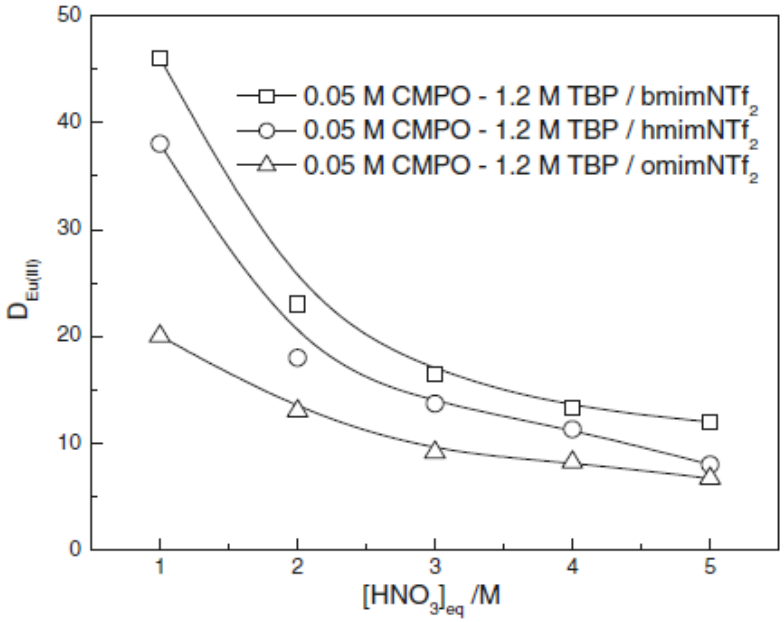

Figure 2.9: Distribution ratio of in 0.05M CMPO-1.2 M TBP/[C_4min][NTf_2] (or hminNTf2 or ominNTf2). O:A=1:1, T=303K(Rout et al. 2011)

2.3.2 Htta

The above extraction mechanisms which are specific in the IL extraction system, however, make difficulty in recovery of the extracted metal ions from the IL phase because the hydrophobic ionic species extracted becomes part of the IL and cannot be isolated by the evaporation after the forward extraction. Furthermore, the relatively low solubility of the common extractants in the IL compared with that in conventional organic solvents, and the leakage of the IL into the aqueous phase accompanied with the ion-exchange extraction are serious disadvantages. To solve these problems, the use of acidic chelating extractants, such as Htta, is more favourable in the IL extraction system, because the extracting ligand tends to combine with a proton rather than the metal ion under acidic conditions. Okamura et al. (Okamura et al. 2012) uses an ionic liquid solution of [C_4min][NTf_2] and Htta to extract Eu(III) from lithium chloride and acetate butter environment. The result indicates that Eu(III) was extracted into [C_4min][NTf_2] as the neutral $Eu(tta)_3$ at the lower concentration and the anionic $Eu(tta)_4^-$ at the higher concentration. Moreover, despite the significant water content of the equilibrated [C_4min][NTf_2] phase (1.05 M) and in contrast to the recent reports of the formation of hydrated complexes through cation exchange reactions in RTILs, all the water is expelled from the inner coordination sphere of the metal ion of this complex (Jensen et al. 2003).

2.3.3 Diglycolamide (DGA)

Compared to conventional organ phosphorus extractant (such as CMPO), Diglycolamide (DGA) extractant have been found to be significantly more effective for minor actinide partitioning. TODGA (N,N,N',N'-tetra-n-octyldiglycolamide), as one of the most widely investigated DGA, has been found more promising and hence been evaluated by many research groups for 'actinide partitioning' test (Modolo et al. 2007, Modolo et al. 2007, Magnusson et al. 2009, Panja et al. 2013).

Panja et al. (2013) studied the Eu(III) extraction behavior with PTFE membranes from nitric acid feed conditions using several substituted diglycolamide (DGA) extractants such as N,N,N',N'-tetra-n-octyldiglycolamide (TODGA), N,N,N',N'-tetra(2-ethylhexyl) diglycolamide (T2EHDGA), N,N,N',N'-tetra-n-pentyldiglycolamide (TPDGA) and N,N,N',N'-tetra-n-decyldiglycolamide (TDDGA). In view of the third phase formation with the DGAs, 30% iso-decanol was used as the phase modifier. Transport studies using 0.1 M DGA as the extractant suggested the trend as TDDGA > TODGA > T2EHDGA ~THDGA which significantly changed to TPDGA > TODGA > TDDGA > T2EHDGA in the presence of 30% iso-decanol as the phase modifier (**Figure 2.10** and **Figure 2.11**).

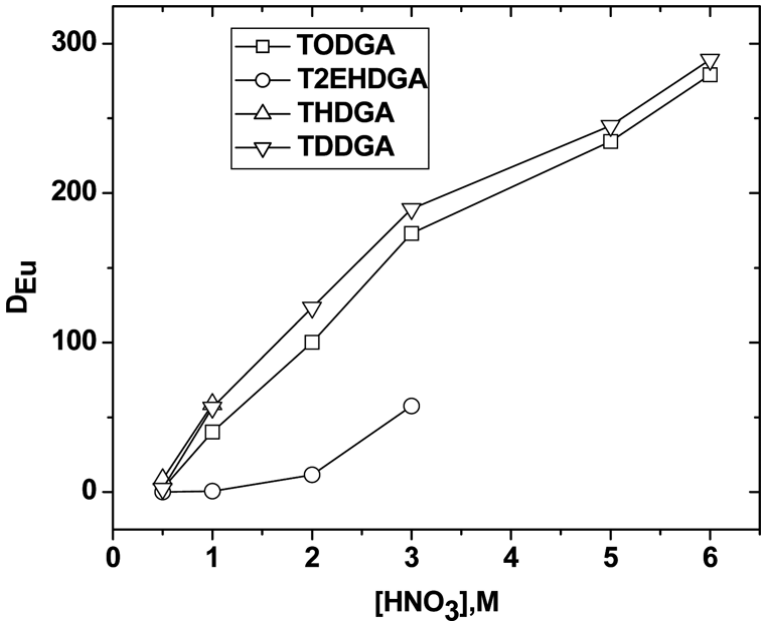

Figure 2.10: Effect of feed nitric acid concentration on the extraction of Eu(III)by 0.1M DGA's (Panja et al. 2013)

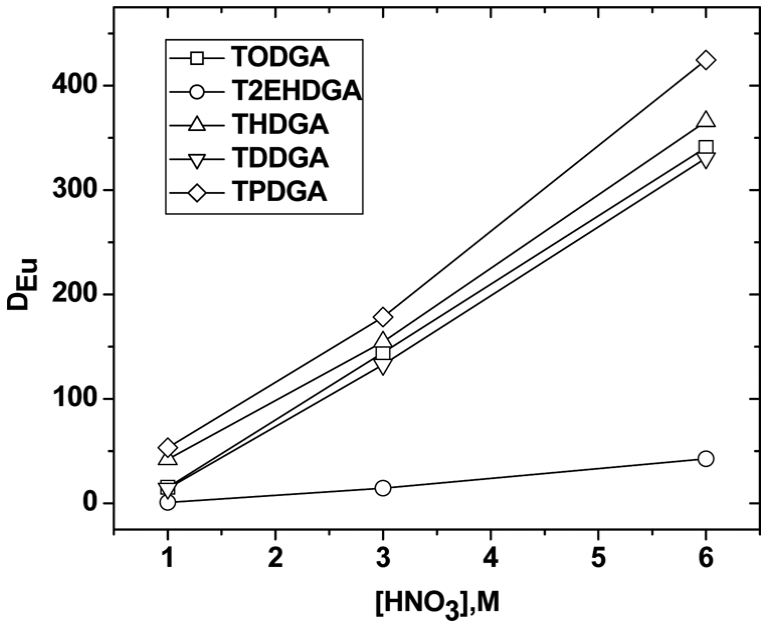

Figure 2.11: Effect of feed nitric acid concentration on the extraction of Eu(III) by 0.1M DGA's in presence of 30% iso-decanol (Panja et al. 2013).

Therefore, the extraction of Eu^{3+} from nitric acid medium by diglycolamide extractants (L) can be presented by the following equation (Panja et al. 2013).

$$Eu^{3+} + mL_{(o)} + 3NO_3^- \leftrightarrow Eu(NO_3)_3 \cdot mL_{(o)} \quad (2.3.1)$$

The extraction of Eu (III) is expected to increase with an increase in nitrate ion concentration which in turn is dependent on the feed nitric acid concentration. However, with increasing nitric acid concentrations, the availability of free DGA also decreases due to the formation of DGA·HNO_3 adduct. Thus at higher nitric acid concentration a decrease in the D_{Eu} value is also expected in a manner similar to that observed with other neutral extractants such as CMPO (Rout et al. 2011).

Rout et al. (2011) investigated the extraction behaviour of Eu(III) from the nitric acid medium by a solution of D2EHPA or HDEHDGA present in omimNTf_2. The effect of concentration of HNO_3, DTPA on the extraction behaviour of $^{(152+154)}$Eu(III) was studied. The choice of HDEHDGA is due to the fact that DGA are emerging as superior candidates for the separation of trivalent from high-level liquid waste. The desired concentration of HDEHDGA or (D2EHPA) varied from 0.02M to 0.2M in omimNTf_2 were prepared.

According to the distribution ratio of $^{(152+154)}$Eu(III) in a solution of 0.05M D2EHPA in omimNTf$_2$ as a function of aqueous phase pH , the ratio increases with increase of pH and could almost reach 600 for pH$_{eq}$ is 3.7. Moreover, the presence of DTPA in aqueous phase decreases the distribution ration of $^{(152+154)}$Eu(III). However, since the DTPA forms a stable complex with Am(III) than Eu(III), the separation of Eu(III) from Am(III) could be achieved with the use of DTPA. Among the extractants studied HDEHDGA was found to be superior to D2EHPA for europium, as depicted in **Figure 2.12.**

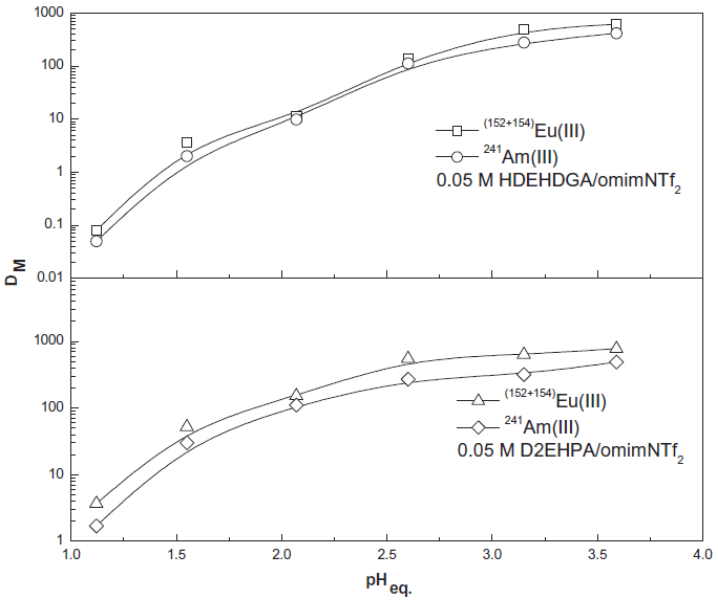

Figure 2.12: Distribution ratio of Eu (III) and Am in a solution of 0.05M D2EHPA (or HDEHDGA) in omimNTf$_2$ as a function of pH, T=298K. O/A=1,[M]=20mg/L(Rout et al. 2011).

In addition, the extraction bahavior of europium in the solution of ionic liquids, $[A336]^+$ based liquid with $[DEHP]^-$and $[NO_3]^-$ anions, present in different molecular diluents was studied by Rout et al. (Rout et al. 2012) as a function of various parameters such as pH, nature of diluent, concentration of precursors of ionic liquid. The acid of the corresponding anion, DEHPA and HDGA, were regarded as potential candidates for lanthanide-actinide separation. According to the distribution ratio of Eu(III) in a solution of $[A336]^+[DEHP]^-$ in different paraffin diluents as a function of pH, the ratio increases with increase of pH and decreases with increase in the chain length of the paraffin diluent in the order of $C_{12}>C_{14}>C_{16}$. Therefore, authors use n-DD as diluent to extract Eu(III) in 0.04M $[A336]^+[DEHP]^-$. The distribution ratio of Eu increased

with increase of pH; at pH>2, the distribution ratios obtained in ionic liquids were much higher than their precursors, as depicted in **Figure 2.13**.

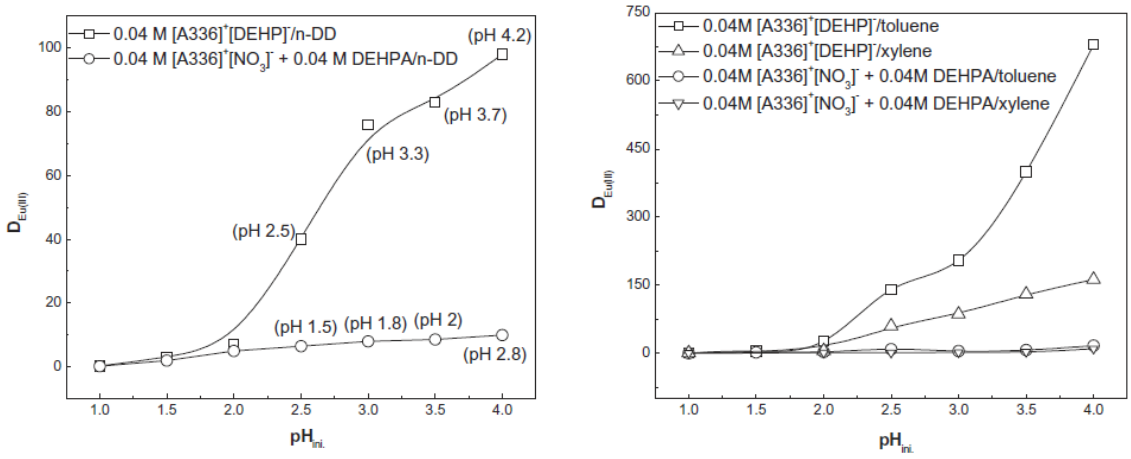

Figure 2.13: Variation in the distribution ratio of Eu as a function of pH of the aqueous phase. Aqueous phase: HNO_3. Equilobirum time=1 h. T=298K. O/A=1(Rout et al. 2012).

Based on the analysis of europium extraction present in the three types ionic liquids, remarkable extraction of europium can be achieved with the use of TUREX solvent of D_{Eu} around 1040. For organic phase, bminNTf$_2$ should be chosen to increase the likelihood of cation exchange into the aqueous phase by employing a cation containing a shorter alkyl chain, 0.2M CMPO-1.2M TBP is the optimal extractant considering viscosity, “crud-type” precipitate and metal- solvate stoichiometry. For aqueous phase, 20-50 mg/L Eu(III) in 1 M nitric acid can be chosen because of the highest D_{Eu}. The Htta/bminNTf$_2$ system, however, are difficult in application because different metal complexes are formed under various Eu(III) concentrations. The Eu(III) distribution ratio obtained from DGA group can only reaches 600, which is far lower than that from TUREX solvent (~1040). Therefore the 0.2M CMPO -1.2M TBP/ bminNTf$_2$ is a favourable system for Eu(III) recovery. **Table 2.4** gives a review of literatures on europium extraction using ionic liquids.

Table 2.4: Literatures of europium extraction using ionic liquid

Experiment	Aqueous solution	Aqueous Solution Conc.	Extractant	Extractant Conc.	Diluents (Ionic liquid)	Results	Analytical Measurement of Extraction
1.Okamura et al, 2012(Okamura et al. 2012)	Eu(III) solution containing lithium chloride acetate butter	(1) aqueous Eu(III) solution ($1.0*10^{-4}$ mol dm^{-3}) (2) $1.0*10^{-1}$mol dm^{-3} lithium chloride and $1.0*10^{-2}$mol dm^{-3} acetate butter pH=3.5-5.4	Htta	$1.0*10^{-3}$ ~ $1.6*10^{-2}$mol dm^{-3}	$[C_4min][Tf_2N]$ Benzene 1,2-dichloroethane	***1***.The solubility of $Eu(tta)_3$ in $[C_4min][Tf_2N]$is higher than that in benzene or 1,2-dichloroethane by a factor of more than 100; ***2***. The neutral Eu(III) chelate has almost no coordinated water molecules in $[C_4min][Tf_2N]$	ICP-MS, Hewlett Packard HP 4500
2. Sharova et al, 2012	Eu(III) in HNO_3 solutions	HNO_3 solutions---3M The volumes of both organics and aqueous phase were equal to 2ml	Tris-CMPO	0.025M	[Bmin] $[Tf_2N]$	Studied extraction behavior of different lanthanides element, not special for Eu	Inductively Coupled Plasma Mass-Spectrometry (ICP-MS) on a PlasmaQuad mass spectrometer with quadrupole

							mass analyzer (VG Element)
3. Jensen et al, 2003(Jensen et al. 2003)	(Na,H)ClO_4, containing Eu^{3+}	1.0 M (Na,H)ClO_4, containing Eu^{3+} ($<10^{-8}$ ~ 0.06 M Ln^{3+})	Htta	0.05~0.5M	$[C_4mim][Tf_2N]$	***1.*** The lanthanide ions are extracted as anionic tetrakis complexes of the type $[Ln(tta)_4]^-$, rather than as hydrated nertral complexes of the type $[Ln(tta)_3(H_2O)_n]$(*n*=2 or 3) ***2.*** The extraction equilibrium can be written as: $Ln^{3+}_{aq} + 4Htta_{org} + [C_4mim][Tf_2N]_{org} \leftrightarrow [C_4mim][Ln(tta)_4]_{org} + 4H^+_{aq} + [Tf_2N]^-_{aq}$	Time-resolved laser-induced fluorescence measurement of Eu containing orgainic phases were made after contact with aquesous phase containing H_2O or 99.9% D_2O
4. Nakashima (Nakashima et al. 2003), 2003	Eu(III) in denionized water AND dodeane system 1M HNO_3	Eu(III)---0.1mM Equal volume of the aqueous and ILs solution	CMPO (carbamoyl methylphosphine oxides)	0-60mM	$[Bmin][PF_6]$	***1.***The lanthanide cations can be quantitatively extracted from denionized water into ILs phase without adding acids but this makes difficulty in the recovery of the extracted metal ions from the IL phase.	The concentration of lanthanide ions (including Eu(III))in the aqueous phase were measured by an ICP-AES

						2.Anion plays a key role in the electrically neutralization of the Ln^{3+}3CMPO complex.	
5. Rout et al, 2012(Rout et al. 2012)	$^{(152+154)}$Eu(III) in DEPA and nitric acid	DTPA---10^{-5}~10^{-3} M $^{(152+154)}$Eu(Ⅲ)---20mg/L, pH_{ini}=1-4 V_{aq}: V_{org}= 1:1	DEHPA in $[A336]^+[DEHP]^-$or $[A336]^+[NO_3]^-$	0.04M	n-dodecane (n-DD), test on toluene and xylene	***1.*** The distribution ratio of Eu(III) is very small when $pH_{aq}$is less than 2, and increases with the increase of pH thereafter. ***2.*** The distribution ratio of Eu(III) decreases with increase in the chain length of the paraffin dilyent in the order of C_{12}>C_{14}>C_{16}.	well-type NaI (TI) scintillation detector
6.Rout et al, 2011(Rout et al. 2011)	$^{(152+154)}$Eu(III) in DEPA and nitric acid	HNO_3, DTPA---10^{-5} M to 0.5M $^{(152+154)}$Eu(Ⅲ)---20mg/L, pH_{ini} =1-3.5	D2EHPA or HDEHDGA	0.02M to 0.2M	omimNTf_2	***1.***The distribution ratio of $^{(152+154)}$Eu(III) increases with increase of pH and could almost reach 600 for pH_{eq} is 3.7 ***2.***The presence of DTPA in aqueous phase decreases the distribution ration of $^{(152+154)}$Eu(III) ***3.***HDEHDGA was found to be superior to D2EHPA in extraction.	The radioactivity of $^{(152+154)}$Eu(III) is measured by well-type NaI (TI) scintillation detector

7 Rout et al, 2011(Rout et al. 2011)	Eu(III) in nitric acid	Eu(III)---**20**-100mg/mL Nitric acid solution---1~5M	TBP-CMOP	0.2M CMOP-1.2M TBP The CMPO concentration was varied from 0.02 to 0.2M	$[C_4min][NTf_2]$ $[hmim][NTf_2]$ $[omim][NTf_2]$ and n-DD	***1.***Remarkable enhancement in the distribution ratio is observed in the presence CMOP ***2.***The D_{Eu} value decrease from 1040 to 160 with increase in the concentration of nitric acid from1.0 to 5.0M ***3.***The D value is much higher in ionic liquid than n-DD because of facilitation the mass transfer of metal ions ***4.***The D_{Eu} value increases with increase in the concentration of CMPO ***5.*** By using ionic liquid diluents, , the undesirable third phase formation can be easily avoided. ***6.*** The D_{Eu} value decreases with increase in the chain length of alkyl group	The radioactivity of $^{(152+154)}$Eu(III) is measured by well-type NaI (TI) scintillation detector

						attached to the cation part of ionic liquid.	
8 Rout 2011(Rout et al. 2012)	Eu(III) in nitric acid	Eu(III)---5-300mg/mL (near saturation solubility) Nitric acid solution---0.01~5M Temperature:298 K-333K	TBP-CMOP	1.2 TBP-.2M CMPO	$[C_4min][NTf_2]$ n-DD	***1***.TheD_{Eu} value increases from 435 at 0.01M nitric acid, reaches a maximum value of ~1200 at 0.5M followed by decrease in D_{Eu} value. ***2***.Loading of europium in ionic liquid phase increases from 12~40 mg/mL with increase in Eu(III) concentration ***3***.Eu(III) loading increases with increase in the concentration of $[CMPO]_{ini}$ and $[Eu]_{ini.}$ The stoichimetry of Eu:CMPO varies depending upon loading of europium, from 1:3 at trace levels, to 1:1 at higher loadings in ionic liquid medium. ***4***.The boundary of third phase formation was	The radioactivity of $^{(152+154)}$Eu(III) is measured by well-type NaI (TI) scintillation detector

			determined as a function of concentrations of CMPO and TBP, as well as temperature. ***5***.Eu(III) decreases with increase in the concentrarion of TBP, and TBP is necessary to avoid “crud” formation ***6***.Eu(III) decreases with increase of temperature indicating the exothermic nature of extraction

2.3.4 Mass transfer

The mass transfer behaviour depends on the slug geometry and circulation pattern, which vary with the physical properties of liquids as well as with operating parameters such as flow rates, and mixing elements (Y/T-junction) geometry and the capillary dimensions (Zhao et al. 2006). For a given system (reactor/contactor and solute) involving mass transfer, its performance is usually evaluated in terms of mass transfer coefficient ($k_L\alpha s$) and extraction efficiency (E_{eff}). An important parameter that influence both terms, residence time, is defined as $\tau = V/Q_{tot,}$ where V is the volume of the microchannel and Q_{tot} is the volumetric flow rate of both phases. The residence time was considered to be identical for all molecules in continuous flow MSR, which is treated to be ideal plug flow reactor (Kashid et al. 2011). Due to insufficient description of Eu(III)-ionic chemical kinetics, the overall volumetric mass transfer coefficient will be calculated from experimental results. The driving force for mass transfer will vary along length of the microchannel and a log mean concentration difference (LMCD) can be defined as:

$$\Delta_{LMC} = \frac{(C_{aq,in} - KC_{org,in}) - (C_{aq,fin} - KC_{org,fin})}{\ln\left\{\frac{(C_{aq,in} - KC_{org,in})}{C_{aq,fin} - KC_{org,fin}}\right\}} \tag{2.3.2}$$

Now the mean value of mass transfer flux can be written as

$$\bar{N} = K_L \Delta_{LMC} \tag{2.3.3}$$

The mean value of the mass transfer flux is also equal to

$$\bar{N} = \frac{Q_{aq}(C_{aq,fin} - C_{aq,in})}{V\alpha} \tag{2.3.4}$$

The mean value of the mass transfer flux will be equal to

$$K_L\alpha = \frac{Q(KC_{org,fin} - KC_{org,in})}{V\,\Delta_{LMC}} \tag{2.3.5}$$

For our system, the initial concentration in organic phase is zero. Therefore, the mass transfer coefficient can be expressed as

$$\ln\left(\frac{C_{aq,fin} - C_{aq}^{e}}{C_{aq,in} - C_{aq}^{e}}\right) = -K_L\alpha\left(1 + \frac{1}{K}\frac{Q_{aq}}{Q_{org}}\right)\tau \tag{2.3.6}$$

$$K_L\alpha = \frac{1}{\left(1+\frac{1}{K}\frac{Qaq}{Q_{org}}\right)\tau} \ln\left(\frac{C_{aq,fin}-C^e_{aq}}{C_{aq,in}-C^e_{aq}}\right) \quad (2.3.7)$$

The extraction efficiency, which refers to the ratio of the amount of species transferred to the maximum amount transferable, is calculated from below equation:

$$E_{eff} = \frac{\text{Amount transferred}}{\text{Maximum transferable}} = \frac{C_{aq,in}-C_{aq,fin}}{C_{aq,in}-C^e_{aq}} \quad (2.3.8)$$

The extraction efficiency in microchannel not only depends on the mass transfer coefficient but also on the residence time of fluids. Berčič and Pintar (1997) estimated the mass transfer coefficient $k_L\alpha$ of gas-liquid in circular channel of 1.5 mm to 3.1 mm internal diameter (ID):

$$k_L\alpha = \frac{0.111\, u_{mix}^{1.19}}{((1-\varepsilon_G)L_{UC})^{0.57}} \quad (2.3.9)$$

In studies of gas-liquid Taylor flow, two separate contributions on the volumetric mass transfer coefficient was evaluated. One is from the dispersed gas bubble to the continuous liquid slug via the liquid film surround the bubble length (L_{film}), and the other one is from the two hemispherical caps to the liquid slugs based on the Hibgie penetration theory. The above two contributions lead to the following equation in circular channels:

$$k_L\alpha = k_{L,cap}\alpha_{cap} + k_{L,film}\alpha_{film} \quad (2.3.10)$$

The film contribution can be written according to the Fourier number, defined as a function of the exposure time and the diffusion time. It corresponds to short (Fo< 0.1) and long (Fo> 0.1) contact time of the liquid film with the rising gas bubble.

$$k_{L,film}\alpha_{film} = \frac{2}{\sqrt{\pi}}\sqrt{\frac{D_C u_G}{L_{film}}}\frac{4L_{film}}{d_{ch}L_{UC}}, \text{ Fo}< 0.1 \quad (2.3.11)$$

$$k_{L,film}\alpha_{film} = 3.41\frac{D_C}{\delta_{film}}\frac{4L_{film}}{d_{ch}L_{UC}}, \text{ Fo}> 0.1 \quad (2.3.12)$$

The Fo number is given as follows:

$$Fo_{film} = \frac{D_C}{t_{e,film}\delta^2_{film}} \quad (2.3.13)$$

$$\text{where, } t_{e,film} = \frac{L_{film}}{u_G} \quad (2.3.14)$$

Several authors (Harries et al. 2003, Sarrazin et al. 2007, Kashid et al. 2008) proposed a liquid-liquid mass transfer coefficient model depends on Fourier number defined as a function of the

exposure time and the diffusion time. The diffusion time is related to the diffusivity of the solute in the dispersed phase D_d and the characteristic length of diffusion in this phase, assumed to be equal to half the equivalent diameter of the droplet:

$$\frac{K_d d_d}{D_d} = 31.4\left(\frac{\rho_c U_d d_d}{\mu_c}\right)^{0.371}\left(\frac{\mu_c U_d}{\sigma}\right)^{0.371}\left(\frac{4D_d}{t_e d_d^2}\right)^{-0.338}\left(\frac{\mu_d}{\rho_d D_d}\right)^{-0.125} \quad (2.3.15)$$

$$t_e = \frac{(L_d - w_d) + \pi w_d/2}{U_d} \quad (2.3.16)$$

Di Miceli Raimondi et al. (2014) studied the liquid-liquid mass transfer coefficient K_d derived from the expression of mass flux through the interface per droplet surface unit, which is based on 2D direct numerical simulations. The correlation is as follows:

$$k_d d_d = \alpha\left(\frac{V_d}{V_{UC}}\right)^{0.17}(U_d w_c)^{0.69}\left(\frac{U_d}{\sigma}\right)^{-0.07}\left(\frac{w_c}{d_d}\right)^{0.75} \quad (2.3.17)$$

where d_d is the droplet equivalent diameter (diameter of a spherical droplet with the same volume), α is a constant that depends on the fluid properties and flow characteristic α=4.36e-04.

The Europium diffusion coefficient is important for the estimation of mass transfer estimation, especially numerical analysis of the transfer process. Ribeiro et al. (2011) measured the europium chloride distribution coefficient in bi-distilled water. The fitting coefficients of a polynomial equation [$D/(10^{-9}\ m^2 \cdot\ s^{-1}) = a_0 + a_1(c/mol \cdot dm^{-3}) + a_2(c/mol \cdot dm^{-3})^2$] to the mutual differential diffusion coefficients of europium chloride in aqueous solution at 298.15K was summarized in following equation, with a confidence interval of 99.7%.

$$D = 1.246 - 17.06c + 766.7c^2 \quad (2.3.18)$$

Where c is the Eu(III) concentration, mol/L. The Eu(III) diffusion coefficient in N-butyl-N-methylpyrrolidinium bis(trifluoromethylsulfonyl)imide ($BMPyNTf_2$) ionic liquid was studied by Jagadeeswara Rao et al. (2009) at various temperature. At 298℃ the diffusion coefficient of Eu(III) in $BMPyNTf_2$ was found to be $2.95\times 10^{-12}\ m^2\ s^{-1}$. Sengupta et al. (2013) determines the diffusion coefficient of Eu(III)/Eu(II) in 1-hexyl-3-methylimidazolium bromide (C_6mimBr) in an electrochemical way, and found the value to be $3.08\times 10^{-12}\ m^2\ s^{-1}$. Matsumiya et al. (2008) got the diffusion coefficients of Eu(III) and Sm(III) in NTf_2^- ionic liquids to be $10^{-12}\ m^2\ s^{-1}$. Yang et al. (2014) found the diffusion coefficients of Eu(III) in 1-butyl-3-methylimidazolium bromide (BmimBr) at 293K was $0.97\times 10^{-12}\ m^2\ s^{-1}$, and the value is $2.71\times 10^{-12}\ m^2\ s^{-1}$ at 308K.

The viscosity of BmimBr at 20 degree was 37.5mPa.s, and 22.5mPa.s at 25 degree (Tshibangu et al. 2011).

2.4 Laser Induced Fluorescence (LIF)

As a non-intrude measure method, Laser induced fluorescence (LIF) technique has been widely used to measure species concentration, flow field temperature and pH distributions etc. This is achieved by injecting a fluorescence dye into the detecting regime. With a molecular absorption of light energy at one wavelength, the dye can nearly instantaneous re-emission at another, usually longer, wavelength. The emission light will be captured on a digital camera, hence the fluid characteristic can be quantitative obtained based on calibration correlation with known concentrations.

Ghaini et al. (2011) visualized the wall film of liquid-liquid slug flow capillary using simplified light induced fluorescence method in hydrophobic PTFE capillaries of 1mm diameter, as shown in **Figure 2.14**. By processing the fluorescence intensity signal at the centre of the capillary at known slug velocities, the slug lengths and slug separations were accessible. The overall volumetric mass transfer coefficient increases with increase in the flow velocity for a given capillary, and the mass transport process is enhanced by decreasing the capillary diameter.

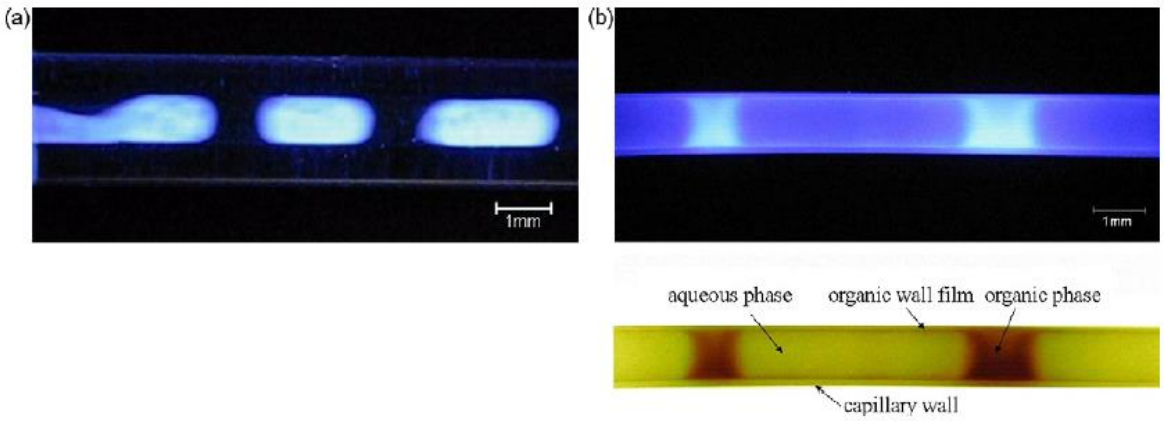

Figure 2.14: Slug formation and organic wall film formation in a PTFE-capillary (diphenylanthracene-petroleum-water, organic phase flowrate 0.3mL/h, ID=1mm) (Ghaini et al. 2010).

Shinohara et al. Shinohara et al. (2004) employed quinine as scalar to measure the pH field of chemically reacting flow in microfluidic devices by laser-induced fluorescence. Quinine is a

very good fluorescence indicator [4] under relatively low pH conditions that have a less quenching effect. The quantum efficiency of quinine is pH-dependent. The calibration of quinine in acetic acid and ammonia hydroxide under various pH values was shown in **Figure 2.15**. In order to reduce data noise, the spatial average over a 4*4 pixel region was taken, as follows,

$$I'(i,j) = \frac{\sum_{x=4\times(i-1)}^{x=4\times i}\sum_{x=4\times(j-1)}^{x=4\times j} I}{\sum_{x=4\times(i-1)}^{x=4\times i}\sum_{x=4\times(j-1)}^{x=4\times j} I_1} \qquad (1<i<256,\ 1<j<320) \qquad (2.4.1)$$

Where I_1 is the fluorescence intensity at pH 5.90.

Wang et al. (Wang et al. 2012) studied the miscible liquid-liquid mixing process in T-shaped micro-channels using μ-LIF (micro Laser induced fluorescence) technique. De-ionized water and ethanol were used for mixing experiment with rhodamine B as fluorescence tracer. By plotting the averaged fluorescence intensity (grayscale value) of prepared samples versus the tracer concentration, the calibration curve can be obtained as shown in **Figure 2.16**.

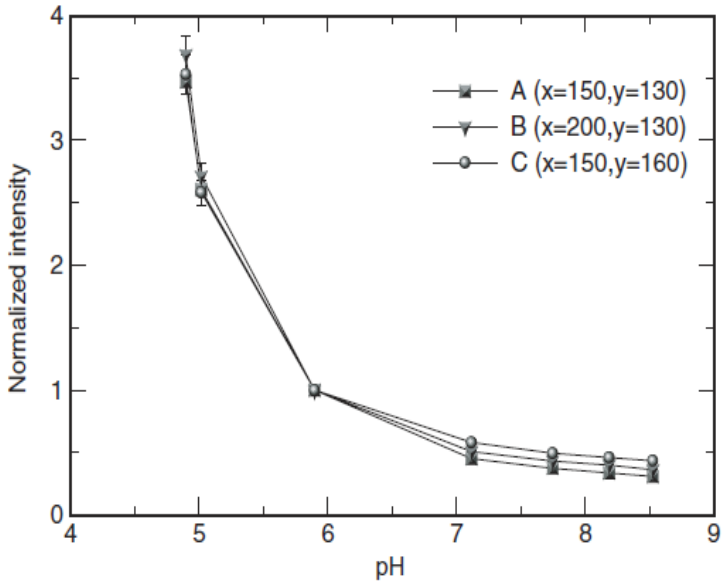

Figure 2.15: Sample calibration curves between fluorescence intensity (normalized by below equation) and pH at three locations(Shinohara et al. 2004).

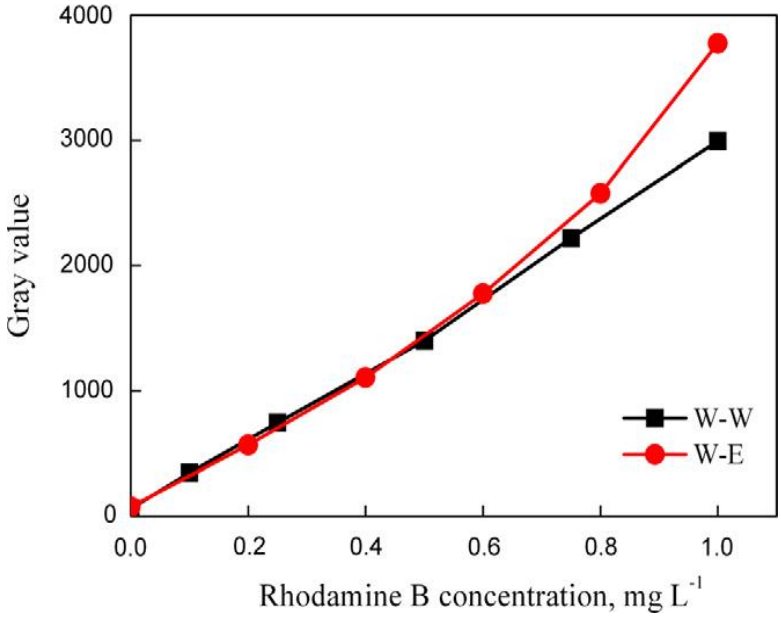

Figure 2.16: Relationship between the fluorescence intensity (grayscale value) and the concentration of rhodamine B. W-W and W-E represent the calibration for water-water mixing and water-ethanol mixing, respectively(Wang et al. 2012).

However, little attention has been paid to two immiscible phases flow with LIF measurement due to calibration difficulty. Although Liu et al. (2006) investigate the co-current flow of immiscible water-oil liquid flows in a vertical pipe using laser-induced fluorescence method, only flow structures and phase inversion can be obtained base on captured images (**Figure 2.17**). The hydrodynamic characteristic, like mass transfer, residence time etc, cannot be studied with LIF.

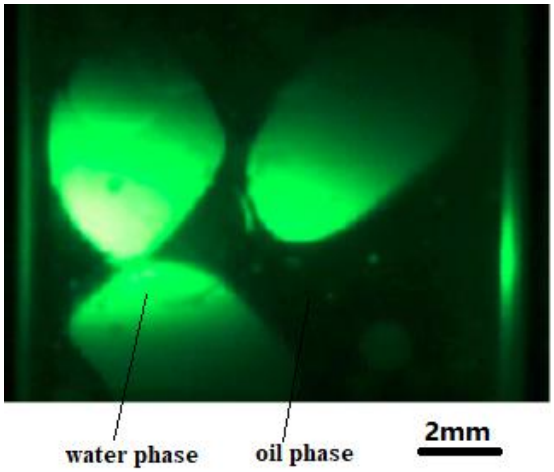

Figure 2.17: W/O dispersed flow at mixture velocity U_m=0.824 ms^{-1} and oil input volume fraction ε^{o}_{input}=77.4%(Liu et al. 2006).

Muhlfriedel and Baumann (2000) investigated mass transfer of a fluorescence dye (rhodamine B) across an interface between two partial immiscible liquids (1-butanol and water). The empirical correlation between the dye concentrations in two phases and measured averaged grey value as the direct measure of fluorescence intensity are studied. **Figure 2.18** shows two-dimensional concentration fields close to the interface during mass transfer at different moments, and the development analysis leads to several conclusions: 1) A jump of the concentration at the phase boundary could not be observed; 2) Within the area close to the phase boundary a concentration gradient is formed, which acts against the main mass transfer direction; 3) This gradient obviously develops due to the different solubility of the transferred material in the two phases; 4) A solution equilibrium is not reached during the experiment.

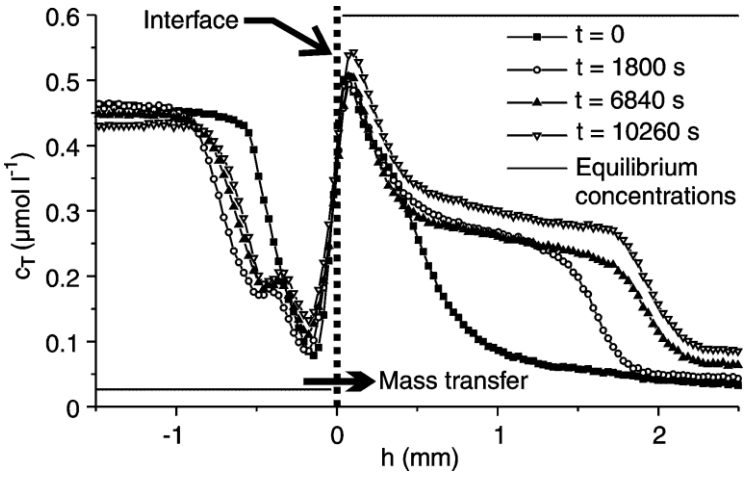

Figure 2.18: Concentration profiles close to the interface at different moments of exposure(Muhlfriedel and Baumann 2000).

Ghaini et al. (2011) employed an acid as a quenching agent to observe the internal circulation patterns within the liquid slugs, as the fluorescent dye was deactivated by the acid diffusing in from the dye-free phase. This also permits an approximate quantification of local concentration inside the slug by virtue of the resultant residual fluorescence intensities. Based on the observed quenching process, it was found the transport rate at the rearmost section of the cylindrical slug portion is very high. Due to the presence of a wall film, the shear transmitted to the slug surface is insufficient to induce an internal circulation over the whole slug. On the other hand, the greater shear forces on the continuous phase that is directly in contact with the wall induces the fully developed circulation vortex expected between the slugs of the dispersed phase.

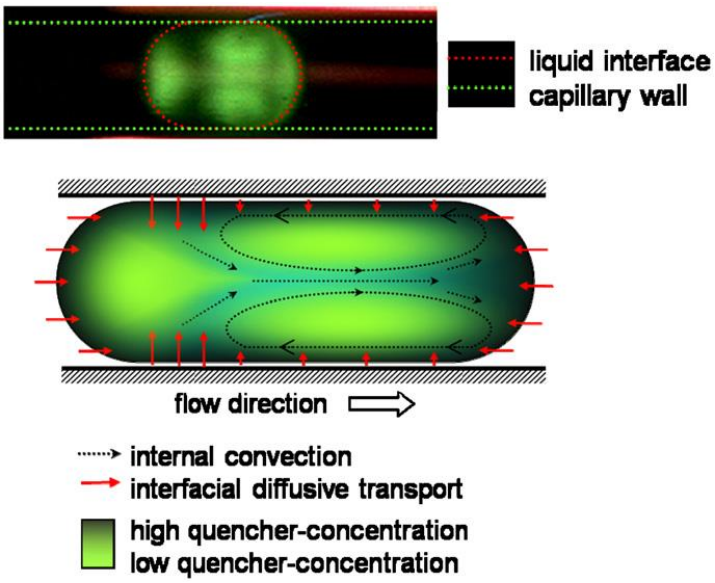

Figure 2.19: Quenching of fluorescence slugs and visualization of the microscale mixing process. Lower diagram: Schematic of the observed flow pattern(Ghaini et al. 2011).

2.4.1 Europium spectrum

Lanthanides are weakly fluorescing species, due to their low molar absorptivity and poor quantum yields. In the case of Eu(III), suitable change in solution environment will result in the change of absorption and fluorescence intensity of Eu(III). It is because the transitions involved, e.g. $^5D_0 \rightarrow {}^7F_2$ (612 nm), are forbidden by the Laporte selection rule they depend for their intensity largely on the degree of asymmetry in the environment. Hence an asymmetric environment surround Eu(III) would lead to a marked enhancement of the fluorescence. This point would be helpful for the optical device selection in Laser Induced Fluorescence experiment.

2.4.1.1 Eu(III) in aqueous phase

In nitric acid solution, Eu^{3+} has the formula $[Eu(NO_3)_m(H_2O)_n]^{(3-m)+}$ where the value of m is dependent upon the concentration of nitric acid. The difference is attributed to a near-linear increase in the fluorescence lifetime of $^5D_0$ state due to Eu^{3+}/NO_3^-complexation (Piriou and Svoronos 1985).

Coria-Garcia and Niemczyk (1991) found high nitric acid concentration causes an enhancement of the intensity in the fluorescence spectra of Eu(III). When solution is excited at

394nm, the most intense bands in the fluorescence spectrum of aqueous Eu^{3+} are 591, 616 and 694nm. **Figure 2.20** gives a comparison of the fluorescence spectra in water, 5M and 10M nitric acid. The 616 nm band shows a six-fold increment when the solvent changes from water to 10 M nitric acid solution, due to the inner sphere complexion of the nitrate ion with Eu^{3+}. The 591 and 594 nm, however, only shows a small increase (~ 5%) during the concentration changes.

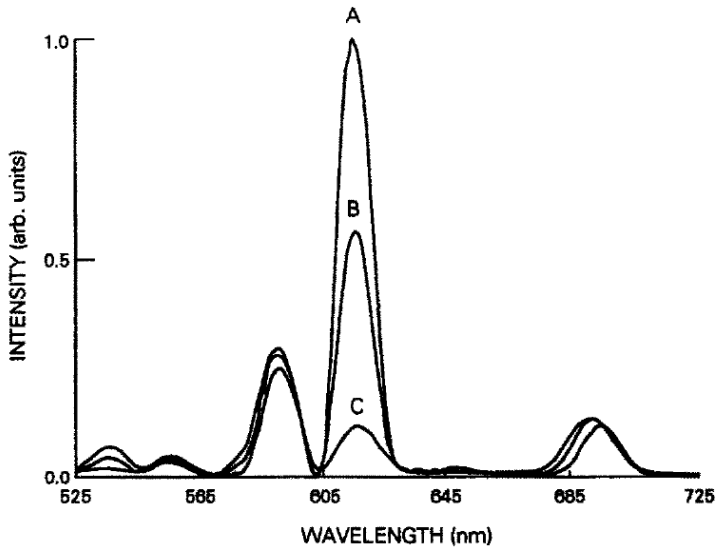

Figure 2.20: Fluorescence spectra of Eu^{3+} ions in solutions of varying nitric acid concentration. A: 10M HNO_3. B: 5.0M HNO_3. C: Triply distilled water(Coria-Garcia and Niemczyk 1991).

In order to quantify the fluorescence intensity over nitric acid concentration, the fluorescence intensity versus nitric acid concentration of the 588, 616 and 694 nm is plotted in **Figure 2.21**. The intensity of the 616 nm band increases linearly when nitric acid concentration increases from 2 to 10 M. The 588 and 594 nm band, however, are barely affected by the solution concentrations. This feature allows the application to measure nitric acid concentration based on fluorescence intensity.

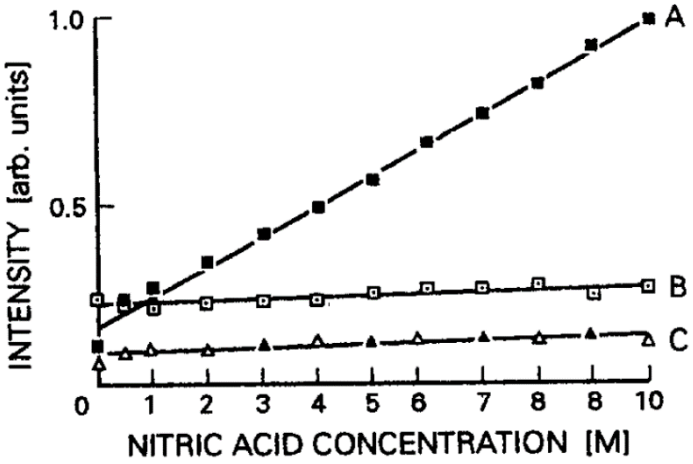

Figure 2.21: Intensity of the ion bands as a function of nitric acid concentration. A: 616nm. B: 588nm. C: 694nm(Bunzli and Yersin 1979).

2.4.1.2 Eu(III) in IL phase

For some hydrophilic ionic liquids, it is impossible to remove the residual water and its spectrum properties are significant affected by the water content. The effect of water was examined on laser excitation at 266 nm onto fluorescence characteristics of Eu^{3+} in the ionic liquid of C_4mimTf_2N. As given in **Figure 2.22**, the water was proven to be a 'protecting' agent by competitive complexion. Similar work was carried out by Devi et al (Shyamala Devi et al. 2011), where the water content in [C_4min][BA] and [C_4min][Tf_2N] was 1050 and 700 μg/mL, respectively. It was found the residence water doesn't predominately bind to Eu^{3+}, and the ionic liquid can lead to an enhancement of the fluorescence.

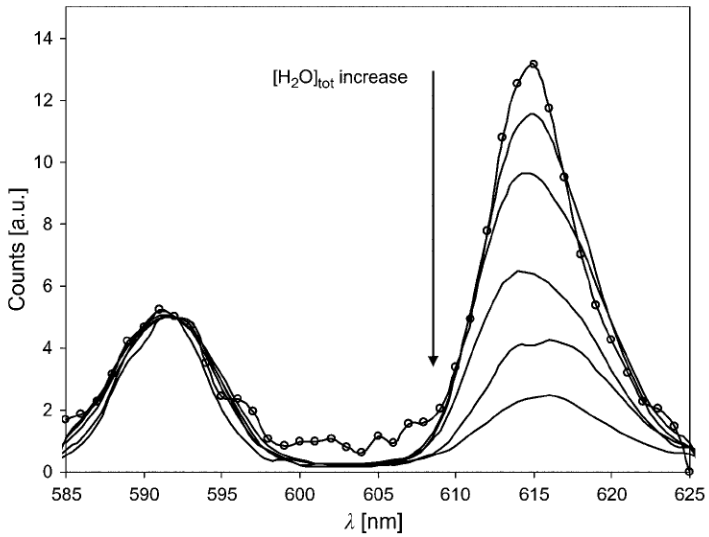

Figure 2.22: Emission spectra of Eu^{3+} in water environment, first irradiation sequence (solid lines). Emission spectra of the Eu^{3+} salt (dots). Normalization was performed at λ 592nm(Nagaishi et al. 2007).

Little work was carried out for the fluorescence characteristic of lanthanides in ionic liquid solution, while less was done combined with neutral extractant such as CMPO or Di(2-ethylhexyl)phosphoric acid (HDEHP). The Eu^{3+}-extractant complexes in 0.5M CMPO in tetrachloreethylene extracted from 1M $DClO_4$, as well as the species in 0.1M HDEHP in toluene from dilute HNO_3 was studied by Beitz and Sullivan(Beitz and Sullivan 1989). The emission spectra of Eu^{3+}organic phases after excited at 294 nm was shown in **Figure 2.23** and corresponding excitation spectra with the 579 nm peak band was given in **Figure 2.24**. The luminescence yield of the Eu/CMPO/$HClO_4$ solution was found to be significantly higher than that of the other two solutions.

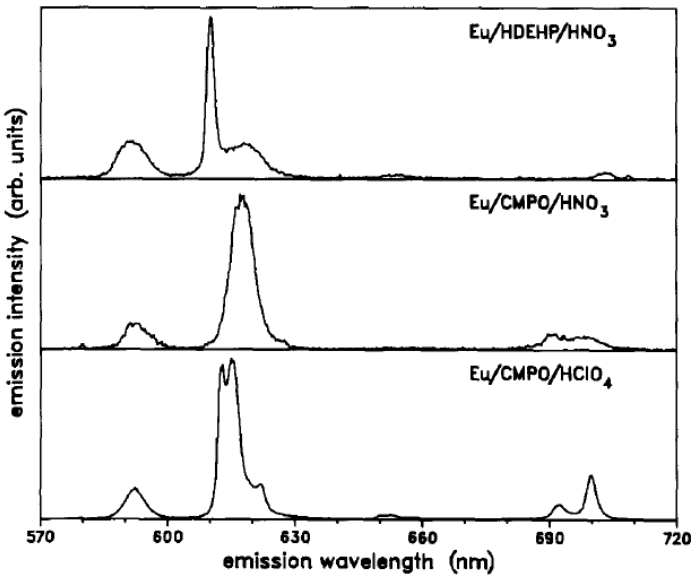

Figure 2. 23: Luminescence emission spectra of Eu^{3+}-extractant complexes in organic solvents following near-UV excitation. The luminescence bands are transition from $_5D^0$ state of Eu^{3+} to component of the lower-lying $_7F^0$ manifold (Beitz and Sullivan 1989).

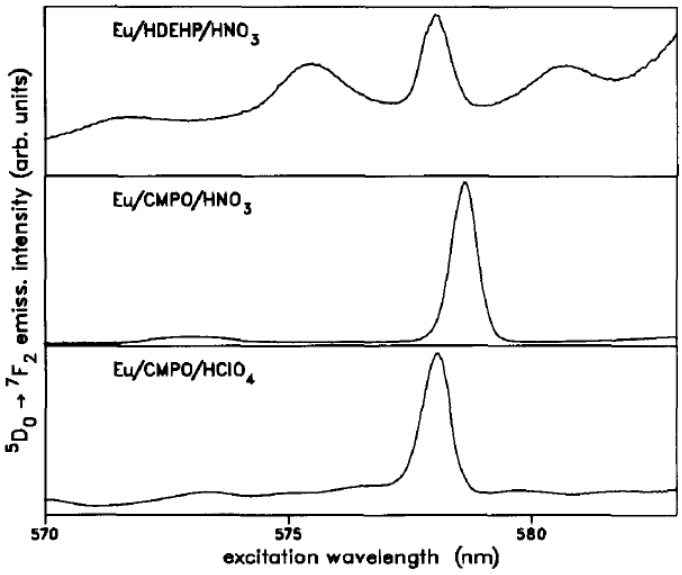

Figure 2. 24: Luminescence excitation spectra of Eu^{3+}-extractant complexes in organic solvents following tunable dye laser excitation. In each case, the sharp band near 579 nm is attributed to the $_7F^0 \rightarrow _5D^0$ transition of Eu^{3+} (Beitz and Sullivan 1989).

The fluorescence spectrum of $Eu(OTf)_3$ dissolved in $[C_4mim][Tf_2N]$ was carried out by Stumpf et al. (2007). The samples were excited at 394 nm, and the emission spectrum shows two peak maxima at 588 and 609 nm that can be ascribed to $^5D_0 \rightarrow {}^7F_1$ and $^5D_0 \rightarrow {}^7F_2$ transitions. The maximum band shoulder between 609 and 612 nm indicates that more than one Eu-species is formed.

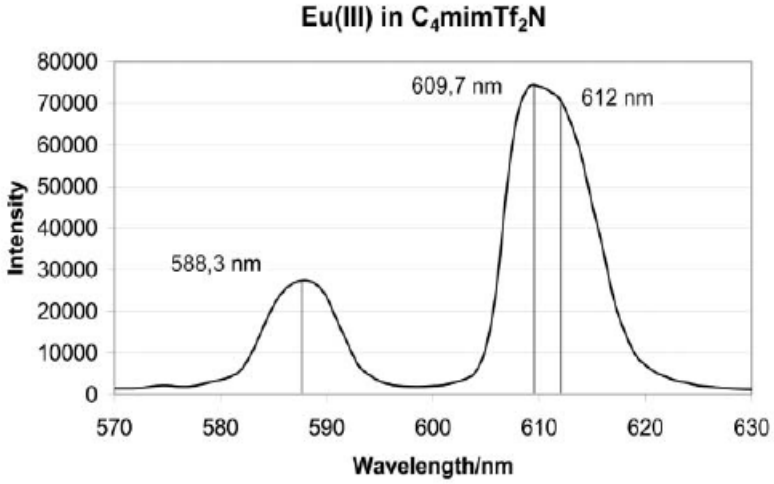

Figure 2.25: Fluorescence emission spectrum of $Eu(OTf)_3$ dissolved in $[C_4mim][Tf_2N]$ (Stumpf et al. 2007)

2.5 Overview

Although the gas-liquid flow in microreactors have been widely used and encountered in many applications, such as heat exchanger, thin film deposition and space applications, the liquid-liquid flow is still of great interest because the dispersed phase can contribute more to the mass and heat transfer compared to gas-liquid flow. Eu(III), as one of the common lanthanide elements present in nuclear spent fuel, was widely studied in equilibrium extraction but barely in continuous microfluidic extraction system. In addition, most Laser Induced Fluorescence measurement was carried out using addition dye like Rhodamine 6/6G as fluorescence tracer, while no observation of interphase mass transfer of plug flow based on the Eu(III) extraction process has been conducted to the best of the author's knowledge. The CFD simulation based on the unique extraction system was barely studied especially in a 3D computation domain including the plug formation process.

In what follows, the continuous extraction and mass transfer of Eu(III) using ionic liquid as continuous solution in liquid-liquid plug flow are investigated with bright field. Particle Image

Velocimetry, with which the hydrodynamic characteristic can be simultaneously studied. The mass transfer coefficient and interfacial area in the microchannel were compared to the previous correlations obtained from conventional extractors. Various hydrodynamic characteristics, including film thickness, plug velocity, plug length and plug volumes are studied under different operational conditions. The mass transfer process, especially in plug formation process, are investigated by tracking the Eu(III) movement. The experimental observations are also compared with CFD simulation based on a 3D computational domain. These features will help in optimizing the microfluidic plug flow for mixing, as well as mass and heat transfer enhancement.

Chapter 3. Experimental details

3.1 Introduction

As given in Chapter 2, the metal extraction can be enhanced using micro reactor in microchannels using ionic liquid mixtures. To simulate the spent nuclear fuel environment, the Europium nitrate pentahydrate ($Eu(NO_3)_3 \cdot 5H_2O$) is dissolved in various nitric acid solutions, and extracted using a TRUEX based system (CMPO/TBP/diluent). The ionic liquid $[C_4min][NTf_2]$ replaces the conventional diluent solutions. The solution physical and fluorescence properties, as well as the reaction mechanisms are discussed, and the experimental procedures and methodology for each setup are described. In the end, the computational domain and boundary conditions used in the CFD simulation are discussed in detail.

3.2 Solution preparation

The ionic liquid $[C_4min][NTf_2]$, with viscosity of 0.052 Pa·s and density of 1420 $kg \cdot m^{-3}$, was obtained from the QUILL Research Centre, Queen's University of Belfast. The tri-n-butylphosphate (TBP), which acts as a modifier to prevent the formation of 'crud-type' precipitate (Rout et al. 2011), was purchased from Sigma-Aldrich. CMPO was used as extractant and obtained from Carbosynth Limited. For the preparation of the ionic liquid phase, certain amount of CMPO was added into TBP and the mixture was mechanically shaken for 2 hours. Then the mixture was introduced into the ionic liquid $[C_4min][NTf_2]$ and stirred. The concentrations of CMPO and TBP in the ionic liquid were equal to 0.2M and 1.2 M, respectively. Various standard nitric acid solutions were obtained from Sigma-Aldrich and used as aqueous phase. The ionic liquid was pre-equilibrated with the desired concentration of nitric acid solution before extraction, because both H^+ and $NO3^-$ can dissolve in the IL phase. The solubility of H^+ and $NO3^-$ into the ionic liquid follows a physical absorption than a chemical extraction mechanism (Billard et al. 2011), and neither TBP nor CMPO influence it. The fluid properties of the ionic liquid (0.2M CMPO-1.2M TBP/$[C_4min][NTf_2]$) and aqueous solutions (1M nitric acid) are summarized in **Table 3.1** (measured at UCL laboratory). Each measurement was repeated 3 times to ensure reproducibility. The liquid viscosity and density were measured with a digital DV-III Ultra Rheometer (Brookfield, UK) and a DMA 5000 density meter (Anton Paar, UK), respectively. The interfacial tension was measured using a

DSA 100 drop analyzer (Kruss GmbH, Germany). The refractive index was measured with an Abbe 5 Refractometer (Bellingham and Stanley, UK). The diffusion coefficient of Eu(III) in the aqueous and ionic liquid phases was obtained from the literature(Matsumiya et al. 2008, Rao et al. 2009, Ribeiro et al. 2011, Sengupta et al. 2012, Yang et al. 2014).

Table 3.1: Properties of the test fluids

Property/parameter (25°C)	Fluid/value
Density (ρ)/[kg/m^3]	Ionic liquid phase: 1259 Aqueous phase: 1030
Dynamic viscosity (μ)/[cp]	Ionic liquid phase: 25.59 Aqueous phase: 0.75
Interfacial tension(γ)/[mN/m]	Ionic liquid phase /Aqueous phase =6.70
Eu(III) diffusion coefficient(D)/[m^2· s^{-1}]	Ionic liquid phase: 2.95×10^{-12} Aqueous phase: 7.86×10^{-8}
Refractive index(n)	Ionic liquid phase: 1.427 Aqueous phase: 1.339 FEP channel: 1.34 Deionized water: 1.335

3.2.1 Fluorescence spectrum of Eu(III)

The Eu(III) excitation and emission spectra are crucial for the choice of appropriate optical equipment, like laser wavelength and optical filter. To obtain these spectra, various concentrations of $Eu(NO_3)_3$ in 1M nitric acid solution are excited by a 450x Xenon arc lamp from FLS920 Fluorescence Spectrometer (Edinburgh Instruments, UK), as shown in **Figure 3.1**. These studies were carried out in the Department of Chemistry, University of Birmingham. Compared to the water-based spectra, nitric acid enhances the excitation spectrum intensity, with the most intense band centred in 395 nm. Eu(III) in the acid solution is in form of $[Eu(NO_3)_m(H_2O)_n]^{(3-m)+}$, where the value of m is dependent upon the concentration of nitric

acid (Piriou and Svoronos 1985). With increasing Eu(III) concentration, the excitation spectra intensity also enhanced.

As shown in **Figure 3.1**, there are several fluorescence bands in for aqueous Eu(III) when the solution is excited at 394nm, and the most intense bands are at 591, 616 and 694nm. The intensity of the 616 nm band is very sensitive to the coordination environment reflecting the hypersensitive character of $^5D_0 \rightarrow {}^7F_2$ electronic transition (Stumpf et al. 2007). With variation of the strength of the ligand field the intensity of the emission at 616 nm changes. The emission intensity of Eu(III) in nitric acid was enhanced compared to pure water, because the formation of a unique asymmetric environment surrounding the rare-earth ion which leads to a marked enhancement of fluorescence induced by the increased transition probability(Gallagher 1964). A plot of emission intensity versus Eu(III) concentration at the 616 nm band is shown in the inset, which shows linearly relationship with $R^2 = 0.9911$.

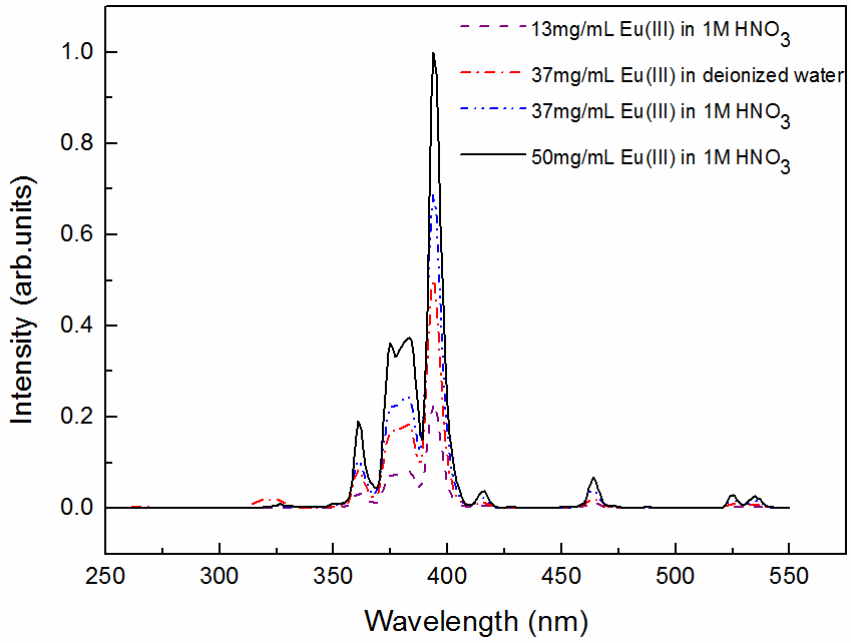

Figure 3.1: Excitation spectra of Eu(III) at various concentrations in 1M HNO_3 and deionized water solution. From bottom to top: 13 mg/mL in 1M HNO_3, 37 mg/mL in 1M deionized water, 37 mg/mL in 1M HNO_3, 50 mg/mL in 1M HNO_3

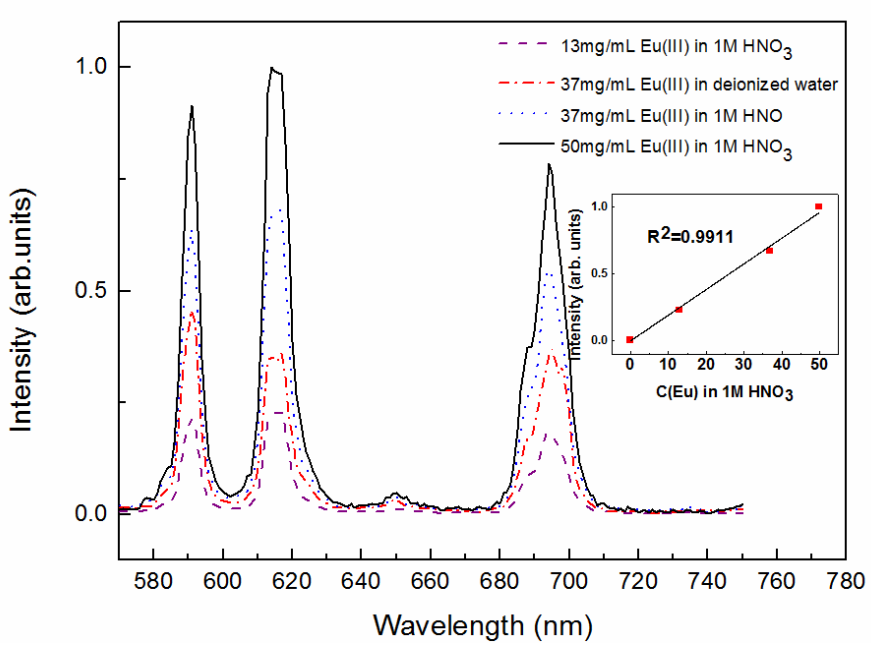

Figure 3.2: Fluorescence spectra of Eu(III) at various concentrations in 1M HNO_3 and deionized water solution. From bottom to top: 13 mg/mL in 1M HNO_3, 37 mg/mL in 1M deionized water, 37 mg/mL in 1M HNO_3, 50 mg/mL in 1M HNO_3. The inset shows the linear relationship between fluorescence intensity and Eu(III) concentration excited at 394nm.

3.2.2 Chemical mechanism

The chemical structure of $[C_4min][NTf_2]$ ionic liquid is shown in **Figure 3.3**. The stoichiometry of metal-solvate in the ionic liquid phase varies from 1:3 (Eu : CMPO) at trace levels to 1:1 at higher Eu(III) loadings. It is determined by the slope analysis of $\log D_{Eu}$ against $\log[CMPO]_{org}$ (Rout et al. 2011) , where species with overline exist in the ionic liquid phase only:

$$Eu^{3+} + \overline{xCMPO} + 3NO_3^- \leftrightarrow \overline{Eu(NO_3)_3 \cdot (CMPO)_x} \qquad (3.2.1)$$

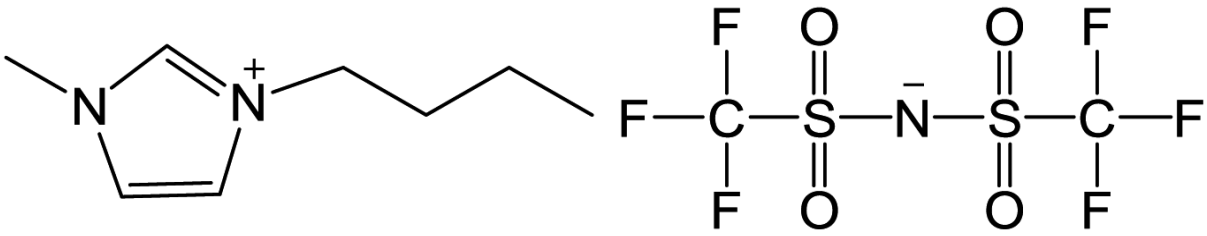

Figure 3.3: **Chemical structure of the ionic liquid 1-butyl-3-methylimidazolium bis[(trifluoromethyl)sulfonyl]amide ($[C_4min][NTf_2]$).**

However, the equilibrium often involves ion exchange between the aqueous and the ionic liquid phases. Billard et al. (2011) found that the cation part of the ionic liquid, C_4mim^+, was present into the aqueous phase after extraction. By dissolving C_4mimCl into the aqueous phase, it was shown that the presence of C_4mim^+ reduced the extraction efficiency (Nakashima et al. 2005). In some cases anion exchange was also observed, for example Tf_2N^- transferred to aqueous Htta solution when Eu(III) was extracted from ionic liquid (Okamura et al. 2012). However, there is no clear evidence of anion exchange when ionic liquid acts as diluent, because Tf_2N^- is a weakly coordinating anion (Binnemans 2007). According to the above, the mechanism can be written as:

$$Eu^{3+} + \overline{xCMPO} + 3NO_3^- + 3\overline{C_4mim^+} \leftrightarrow \overline{Eu(NO_3)_3 \cdot (CMPO)_x} + 3C_4mim^+ \qquad (3.2.2)$$

When ILs are used to recover Eu(III) in conjunction with neutral extractants, the reaction takes place in the ionic liquid phase and not in the aqueous phase as it happens with conventional solvents. The determination of Eu(III)-CMPO-ionic extraction kinetic is more complex than conventional reactions. Sarkar et al (Sukhamoy Sarkar et al. 1980) suggested for the extraction of certain rate earth metals with specific reagents that the reactions are so rapid that they may be classed as purely diffusion controlled processes, which means the formation of products from the activated complex is much faster than the diffusion of reactants. This, however, may not be entirely true due to the high viscosity of ionic liquids and complex reactant products. There has been very limited research on the Eu(III)-CMPO-ionic extraction kinetic. Pulse radiolysis of 1:1 complexes of Eu(III) aminopolycarboxykates was studied in aqueous perchlorate solution (Nagaishi et al. 2002). The decay curve of the reaction was found to be of pseudo first-order. Brigham (Brigham 2013) investigated lanthanide extraction by HDEHP in n-dodecane from DTPA, and proved the reaction follows a pseudo first and second-order complexion kinetics. In addition, the second order rate constant of Eu(III) extraction was around 10^4 $M^{-1}S^{-1}$ (Brigham 2013), which falls into the range of a fast reaction (1 to 10^{10} $M^{-1}S^{-1}$(Caldin 2001)). Based on the above discussion, the present extraction system was treated as fast reaction, although further research is still needed to describe the system more previously. A schematic presentation of the concentration profiles at the interface is shown in **Figure 3.4**.

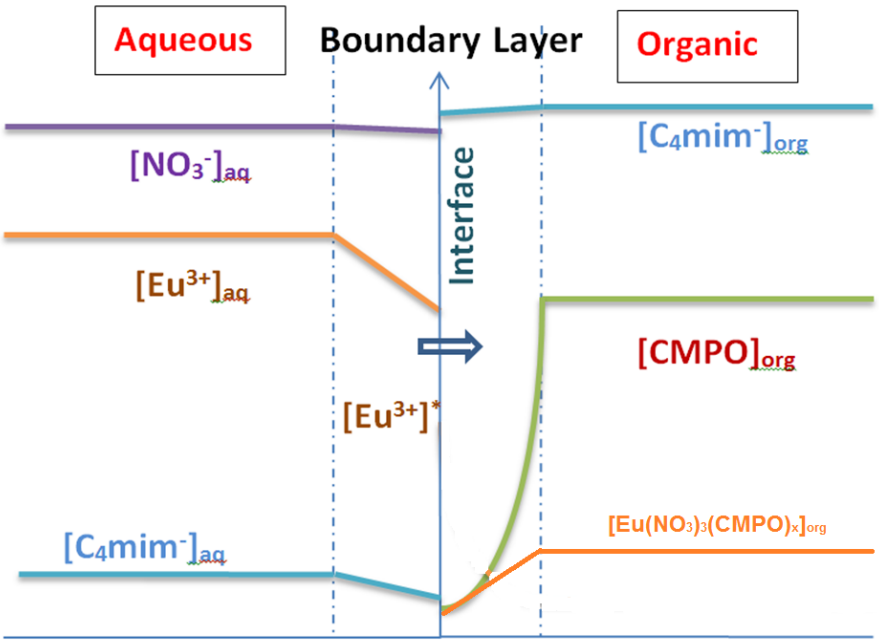

Figure 3.4: Schematic presentation of the concentration profiles at the interface

In the present work the component A (Eu(III)) of the aqueous phase diffuses into the ionic liquid phase comprising of reactant B (CMPO); A and B react in the ionic liquid. The criterion for a pseudo-first-order reaction can be presented by:

$$\left[1+\frac{D_A k_2 [B]}{k_L^2}\right]^{0.5} \ll 1+\frac{[B]D_B}{[A^*]D_A} \qquad (3.2.3)$$

where D_A and D_B is the molecular diffusivity of Eu (III) in the ionic liquid and the aqueous phases, [B] is the CMPO concentration in the ionic liquid (kmol/m^3), while [A*] is the Eu(III) solubility in the aqueous phase (kmol/m^3). The solubility of Eu(III) in nitric acid solutions was found to be 300mg/mL (Rout et al. 2011), which is far more than the concentration being used in present work (50 mg/mL). k_2 is the second order reaction rate constant (m^3/(kmol·s)), equal to be 1.4× 10^{-5} dm^3 mol^{-1} s^{-1} (A.Adin and A.G.Sykes 1966). k_L is the overall mass transfer coefficient (m/s), obtained from the present experiments by dividing the overall volumetric mass transfer coefficient with the specific interfacial area, which is around 6.2× 10^{-10} m/s. Using the above information, the criterion for a pseudo-first-order reaction is valid (left term is around 15, right term is nearly 3000). Therefore the Eu(III) recovery using 0.2M CMPO-1.2M TBP/[C_4mim][NTf_2] from nitric acid can be treated as pseudo-first-order reaction, which is one of the fast reaction type.

3.2.3 pH value before and after extraction

In the Laser Induced Fluorescence measurement, to ensure the fluorescence signal is only affected by the Europium concentration, the pH values of the aqueous phase (with 50mg/mL $Eu(NO_3)_3$) and the IL phase before and after extraction were measured with pH/Ion meter S220 (Seven Compact, UK) respectively. Each measurement was repeated 3 times and the average values are given in **Figure 3.5**. Under all nitric acid concentrations, the pH value in the aqueous phase barely changes after extraction, giving an average difference of 3.41%. The pH in the IL phase, however, reduces by 42.83% on average after reaction. For example, the pH value in 1M nitric acid solution changes from 0.11 to 0.1 during extraction, but from 0.57 to 0.18 in the IL phase. With such a large difference, both the europium concentration and the pH value will influence the fluorescence signal. Therefore, the Eu(III) concentration in the aqueous phase only will be studied with LIF.

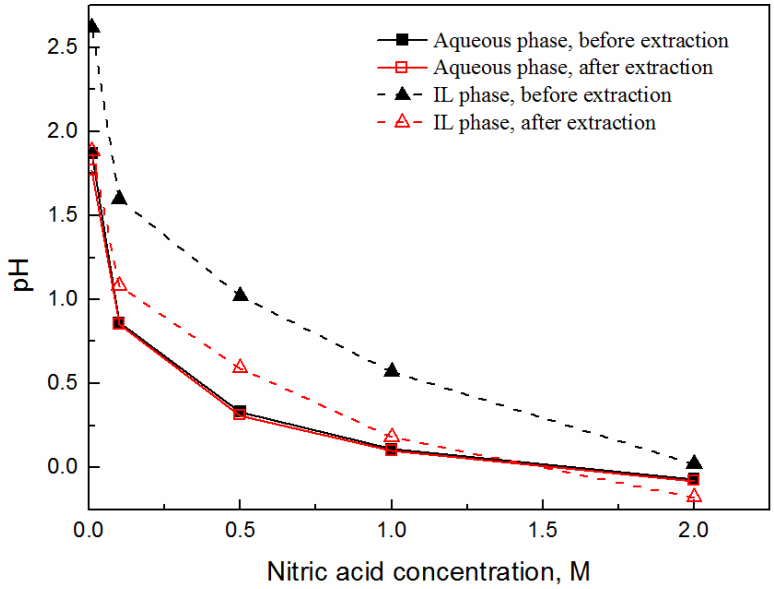

Figure 3.5: Variation of pH value in aqueous (50mg/mL $Eu(NO_3)_3$ in nitric acid solution) and IL phases before and after extraction.

3.3 Experimental setup and procedure

3.3.1 Experimental apparatus

A sketch of the experimental set up is shown in **Figure 3.6**. Two Kds Legato syringe pumps (KD Science Inc., USA) were used to feed the two liquid mixtures to a T-junction with an error

of 1%. The aqueous phase was injected perpendicular to the channel axis and the ionic liquid phase was introduced at the axis of the main channel. A schematic of the 0.2 mm ID microchip from the top view is shown in **Figure 3.7**. The main channel length (CL) for the 0.5 mm ID capillary varied from 5 to 25 cm. The different lengths were used to vary the residence time in the extractor without changing the mixture velocity which can affect the flow pattern. Both phases were introduced at the same volumetric flow rate which varied from $Q_{aq}=Q_{IL}=0.65$ to 21.21 ml/hr.

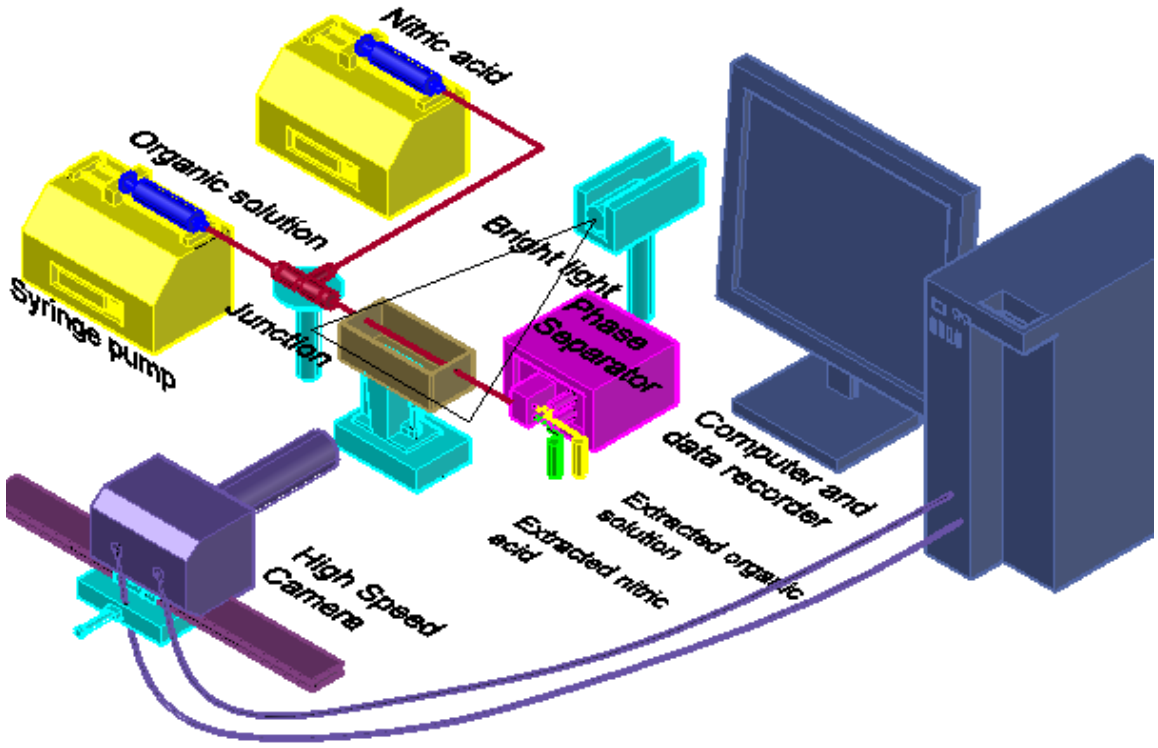

Figure 3.6: Sketch of the experimental set up including the high speed imaging system

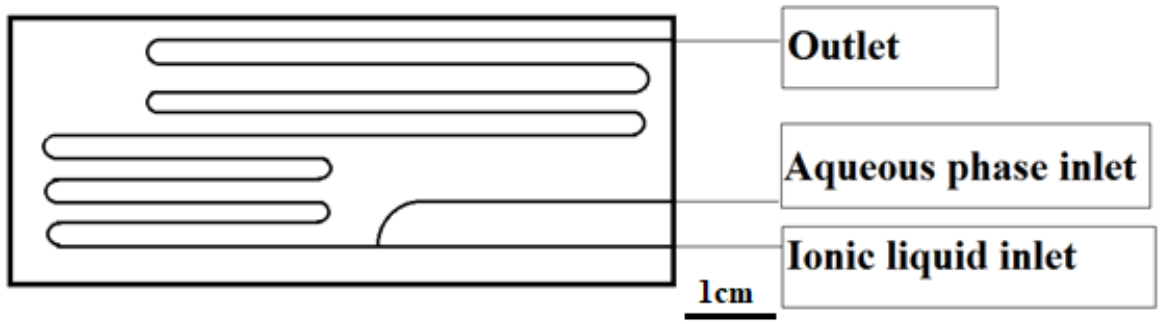

Figure 3.7: Top view sketch of the 0.2mm ID microchip.

Plug flow formed in all cases studied, with the aqueous solution forming always the dispersed plugs and the ionic liquid the continuous phase. A phase splitter should be applied to the separate two phases after residence time in the reactor immediately. At the channel exit, a flow splitter with a PTFE channel as the main branch and a stainless steel channel as the side branch was used to separate the two phases continuously (for details see (Scheiff et al. (2011), Tsaoulidis et al. (2013))). An Asia FLLEX module (Syrris Ltd, UK) was also used as a continuous phase separator operated by adjusting the pressure differential across a hydrophobic PTFE membrane. This separator could not be used at high flow rates, though, because of high pressure drops. A schematic of the separator and the aqueous and ionic liquid (IL) solution through it is given in **Figure 3.8**. The separated phases were analysed for Eu(III) concentration in a USB2000+ UV-Vis spectrometer (Ocean Optics, UK). After each set of experiments, the microchannel was cleaned with dichloromethane to remove any residual ionic liquid, then with acetone to remove any dichloromethane left. At last, compressed air was injected to the channel to ensure that all the chemicals have been moved. All experiments were conducted under ambient temperature (23.8-25.5°C).

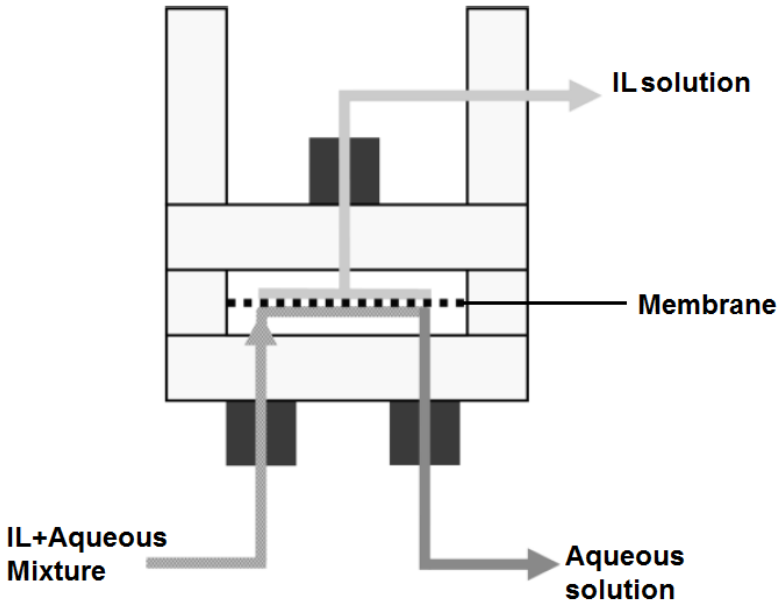

Figure 3.8: Schematic of the separator and aqueous and ionic liquid (IL) solution through the membrane.

3.3.2 Time resolved velocity field measurements from PIV

The velocity fields inside the aqueous plugs and the hydrodynamic characteristics of the pattern, such as film thickness and plug length, were investigated with bright field micro-Particle Image Velocimetry (μPIV). The test section was volumetric illuminated with a 60-Watt continuous arc lamp, with a diffuser plane added between the backlight and the test section to minimize reflections. The interface between the two immiscible fluids appears as a shadow under this background illumination, which was captured by a high speed camera (Photron Fastcam-Ultima APX; 1024 ×1024 pixels) at frequencies adjusted between 2000 to 8000 Hz depending on the flow rates. To increase magnification, the camera was coupled with an air-immersion, long focal distance microscope lens (LEICA MONOZOOM 7) and amplifier with magnification M= 18.9 (NA= 0.42).

For the velocity measurements, 3μm red dyed polystyrene microspheres (Thermo Scientific; Firefili Fluorescent Red) were added as tracers in the aqueous phase for 0.5mm ID channel measurement, and the shadow of these particles was captured on a white background in the raw pictures. With the current configuration the field of view diameter could reach 0.63 mm and the depth of field (Meinhart et al. 2000) can be described by:

$$\delta_z = \frac{3n\lambda}{NA^2} + \frac{2.16d_p}{\tan\theta} + d_p \quad (3.4.1)$$

where n is the refractive index of the immersion medium between the microfluidic device and the objective lens (air), λ is the light wavelength in a vacuum, NA is the numerical aperture of the objective lens, d_p is the diameter of the PIV tracer particles and θ is the small light collection angle. For the present experiment, Eq. (3.4.1) yields δ_z around 16 μm. A better criterion was proposed by Meinhart et al. (1999) where the distance along the optical axis is found where a particle becomes sufficiently unfocused. In this work, the distance can be precisely measured as the camera and the microchannel are mounted on a translation stage employing a micrometre, which fully controlled 3D movement of the microfluidic system. The out of plane resolution was estimated at 19.8 ± 0.5 μm.

Velocity field calculations between image pairs were processed with the Insight 4G Software (TSI). At first the grayscale values of the raw images were inversed as the software requires bright particle signals on a black background (Hagsäter et al. 2007, Chinaud et al. 2015). Then a median filter was applied to the images to eliminate any background noise. The images were further normalized with a minimum intensity mask to improve the velocity field computation, which yields high particle-to-background contrast signal. The displacement of tracer particles between two consecutive frames was calculated using a square domain discretization of 32 × 32 pixels with 50% overlap to satisfy the Nyquist sampling criterion (Dore et al. 2012), which gives velocity spatial resolution of 26.72 μm × 26.72 μm in the 0.5 mm channel. The FFT correlation was used for correlation calculation while the correlation peak position was detected with a Gaussian curve by fitting the highest pixel and its four nearest neighbours. The computed velocity vectors were evaluated based on three criteria: the median test as mentioned above, peak to noise ratio of 1.50, and the six-sigma validation (Meadows and Agrawal 2015). The rejected vectors were replaced with the median value of neighbouring velocity vectors. A post-processing routine was developed in MATLAB to calculate the ensemble average of about 30 images of the instantaneous velocity vectors. For the averaging the velocity profiles at different locations were repositioned using the plug tip location as a reference, which was detected by analysis the sudden change of standard deviation of centreline velocity profiles across the plug (Yamaguchi et al. 2009). The location of the plug tip was determined with an error of ± 20 pixels (± 52 μm).

To obtain the plug geometric parameters for each set of flow rates about 30 plugs were averaged, with deviation between 4.25 - 7.10 % for film thickness, and 5.33 - 9.52 % for plug length. The

continuous ionic film, as well as the plug length, was detected by distinguishing the clear black line between the immiscible two-phase interface and channel wall from the grayscale inversed images. Then the thickness can be obtained by subtracting the width of the aqueous plug from the channel internal diameter and divided by 2. The plug velocity was calculated by measuring the displacement of plug tip between two successive high speed images. Over 30 image pairs were used to calculate average plug velocities at different conditions with a deviation of 2.25 - 13.71 %. There were small variations in the plug velocity due to small changes in pressure in the channel during plug formation at the inlet and plug exit.

3.3.3 Laser induced fluorescence measurement

A 395nm CW laser (Laser 2000 Ltd., UK), which matches the peak excitation wavelength of Eu(III), was used to volumetric illuminate the microfluidic device from a 45^{o} angle. By using this laser, the resulting emission is maximised with a wavelength band centred on 616nm. It has been verified that images produced using this laser (E = 100mJ) have an integrated intensity approximately 2.5 times greater than those produced using a common Nd:YAG laser (λ_{max}=532nm, E = 400mJ). The fluorescence signal was detected by a 12-bit CCD intensifier camera (PCO Sensicam, Dicam Pro) with resolution 1280 ×1024 pixels to enable a higher frequency of acquisition. It was coupled with an optical microscope train (TSI instruments, UK) in combination with a long focal distance microscope lens with a magnification of 20 (Nikkon, Japan). An orange bandpass filter that only transmits 620 ± 10nm wavelength band was placed in front of the camera so that unwanted light can be blocked. The focal plane was located at channel centre, which has been calibrated by maximizing the channel diameter from the front wall. With this configuration the fluorescence images were recorded at a frequency of 14.5 Hz and spatial resolution of 0.63 μm/pixel.

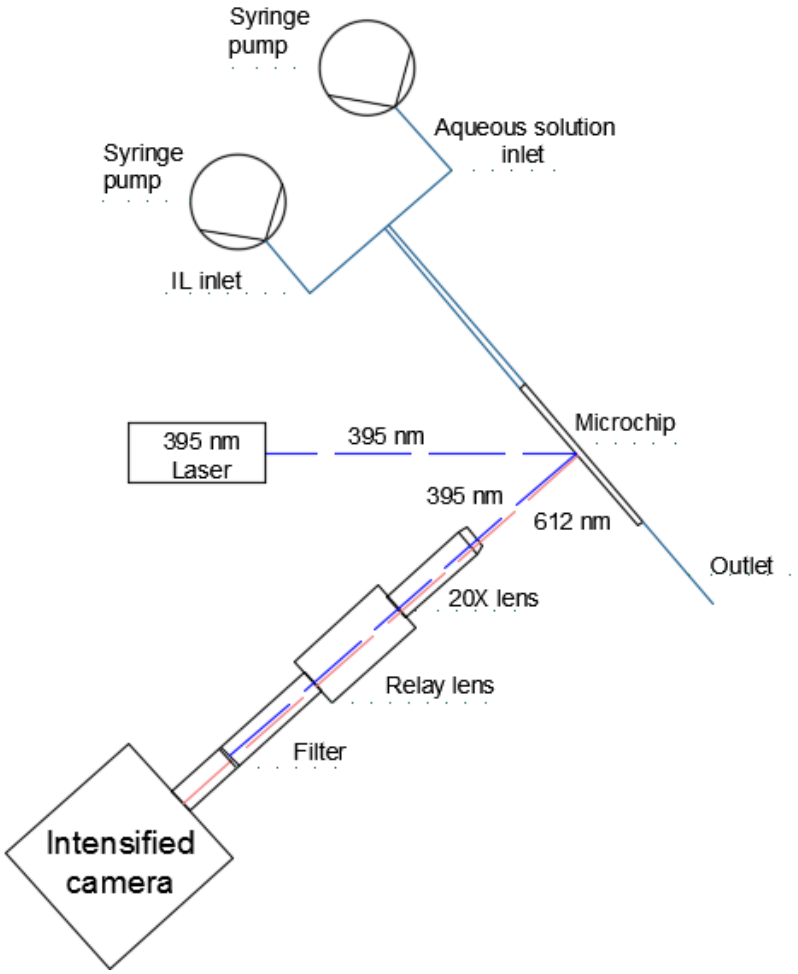

Figure 3.9: Schematic of the Laser Induced Fluorescence apparatus

The Insight 4G (TSI instrument) software was used to capture the images while data analysis was carried out with an in-house MATLAB^{TM} code. The images were firstly reduced to an identified region of homogeneous illumination from the excitation source. Then the light intensity value of each pixel was converted into concentration values using **Figure 6.1** by the linear calibration relationship pixel-by-pixel. An integration of Eu(III) in the plug is performed along the axial centreline to calculate the total interphase mass transfer. As the europium can be distributed in both phases, the fluorescence will blur the plug interface. Therefore, reference experiments using bright field Particle Image Velocimetry (PIV) were carried out to obtain the film thickness and plug length under the same operating conditions. The plug front is determined by detection of the location of the maximum gradient of Eu(III) along the channel axial centreline, then the plug length obtained from PIV measurement was added for the plug end detection.

3.4 CFD simulation

A fixed, three dimensional computational domain with the same geometry as the experimental test section was used for the numerical simulations, as shown in **Figure 3.10 (a).** The entrance lengths for continuous ionic liquid and dispersed aqueous phase are 0.7 mm and 1.5mm in 0.2 and 0.5mm ID channel respectively, to ensure fully developed laminar profile (Han 1960, Dombrowski et al. 1993). The total channel length of 44 channel diameters was chosen so that the plug flow could be fully developed (Lakehal et al. 2008). The specified aqueous velocity is imposed into the ionic liquid pre-occupied computation domain. The outlet is setup as a pressure outlet boundary instead of an outflow boundary to avoid difficulties with backflow. No slip boundary conditions are applied to all wall areas. For the simulations the commercial CFD software FLUENT 12.1 (ANSYS Inc.) was chosen, which employs the Volume of Fluid (VOF) method for tracking the liquid-liquid interface. The first order upwind and Green-Gauss node based gradient calculation scheme were used for time marching of the momentum/continuity equations and gradient calculation, respectively (Navaneetha Krishnan et al. 2010, Talimi et al. 2012). The time step is controlled by a specified maximum value for the Courant number, $Co=\Delta t/(\Delta x/V)$, where Δt, Δx and V is the time step, grid size and fluid velocity respectively. A high Co value leads to an unstable numerical approach while a low Co value means very small time step size and consequently a large simulation time. A maximum Co of 0.25 was adopted in this work, since the elements are very fine close to the interface and wall, the time steps are typically in order of 10^{-7} s. The convergence criteria for velocities and pressure were set to 0.01. The absolute values of residuals achieved were found to be sufficiently low, $O(10^{-6})$ for velocities and $O(10^{-10})$ for continuity.

The effect of wall adhesion forces need to be accurately treated to capture the plug growth and detachment behavior at the wall in the injector region (Fang et al. 2008, Liu and Zhang 2009), by specifying the liquid-liquid-solid contact angle. The unit interface normal in the cells near the wall is calculated by $\hat{n} = \hat{n}_w \cos\theta_w + \hat{t}_w \sin\theta_w$, where $\hat{n}_w$ and $\hat{t}_w$ are the unit vectors normal and tangential to the wall respectively. To obtain the contact angle inside the microchannel, the Young-Laplace equation was employed (Cherlo et al. 2010):

The surface tension was measured using a DSA 100 drop analyzer (Kruss GmbH, Germany) and the contact angle was obtained by detecting the air-liquid curvature inside the channel at steady state. Taking the surface tension of nitric-ionic system as $\sigma_{NI} = 0.0067$ N/m, for air-nitric system as $\sigma_{AN} = 0.04002$ M/m, for air-ionic system as $\sigma_{AI} = 0.02016$ N/m and the contact angle

for air-nitric as θ_{AN} = 61.5º, air-ionic system as θ_{AI} = 35º, the contact angle for the nitric-ionic system is obtained as 58.6º. This value, however, failed to predict the plug length with deviation between 19.92 - 155.20%, as encountered by Cherlo et al. (2010). Another method is direct detecting the contact angle on the microchip surface in nitric acid environment. With an equilibrium contact angle of 117.54º, accurate plug length can be obtained for U_{mix} = 0.005 to 0.02 m/s, giving average deviation of 7.17 %. For U_{mix} = 0.03 to 0.05 m/s, higher contact angle ranging from 122º to 131º was used for precise simulation (Li et al. 2014), with deviation ranging 9.55 to 13.08% compared to experimental results.

To be able to capture accurately the film thickness between the plugs and the channel wall as well as the plug breakage at the channel inlet, a very fine mesh needs to be chosen. The plug shape calculated from CFD at three different grid sizes is compared in **Figure 3.10 (b)** against the experimental results for U_{mix}= 0.03 m/s. As can be seen the film thickness from the 3µm grid size fits best the experimental results, although it slightly underpredicts the plug length by 2.03%. The symmetric grids were used to reduce calculation sources and also shown in **Figure 3.10 (b).** This size mesh will be used for further analysis and involves nearly 6 million hexahedron (82.84%) and tetrahedron (17.16%) type cells.

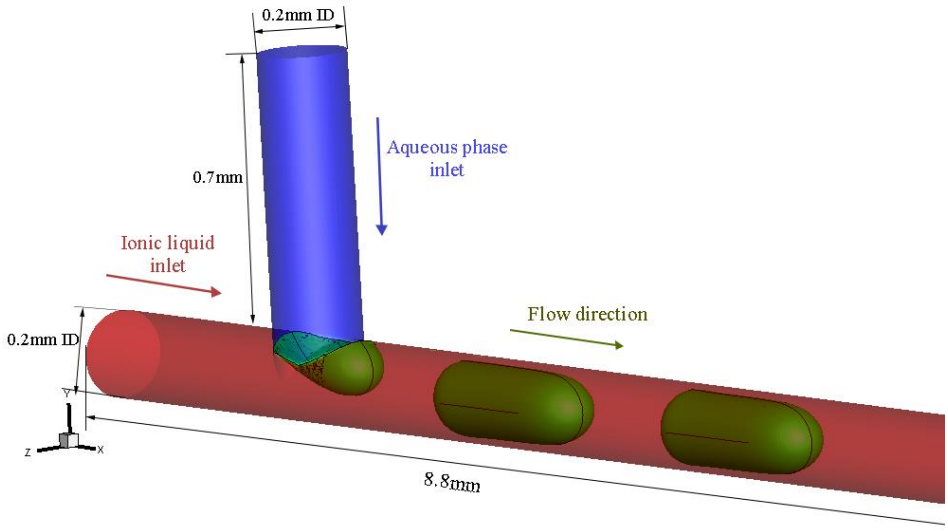

(a)

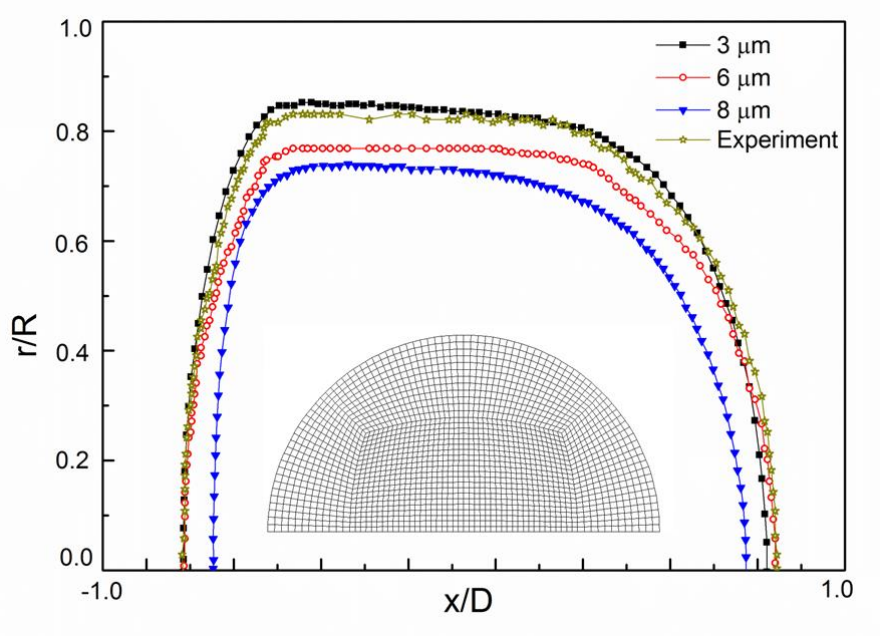

(b)

Figure 3.10: (a) Schematic of the T-shaped computational domain in the 0.2mm channel. The inlet channel lengths for the ionic liquid (continuous) and the aqueous (dispersed) phases are both 0.7 mm. The total length of the test section is 8.8mm. (b) Grid dependence of plug shape at $Q_{aq} = Q_{IL} = 3.39$ ml/h in the 0.2mm ID channel. Also shown is the computational mesh in half of the cross sectional plane.

3.5 Conclusions

The improved TRUEX system (CMPO/TBP/[C_4min][NTf_2]) was used to extract Eu(III) by dissolving the Europium nitrate pentahydrate in various concentrations of nitric acid solution. Knowledge of the solution fluorescence is crucial for the selection of optical equipment in Laser Induced Fluorescence measurements. It was found that Eu(III) under 395 nm excitation has the most intense band, and gives the highest emission at 616nm. The extraction can be viewed as a pseudo-first-order reaction with fast reaction rate. Since the temperature and pH values barely changed before and after extraction in the nitric acid phase, LIF measurements were carried out in dispersed aqueous plug. In the numerical simulations, the Volume of Fluid (VOF) method was found to successfully track the liquid-liquid interface, and CFD will be used to gain understanding of the extraction in the microfluidic system.

Chapter 4. Eu(III) extraction in microchannel

4.1 Introduction

The extraction of Eu(III) from nitric acid solutions was studied in intensified small scale separation units using an ionic liquid solution (0.2M n-octyl(phenyl)-N,N-diisobutylcarbamoylmethyphosphine oxide (CMPO) -1.2M Tributylphosphate) (TBP)/1-butyl-3-methylimidazolium bis[(trifluoromethyl)sulfonyl]amide; ([C_4min][NTf_2]) as the extraction phase. The investigations were carried out in channels with 0.2 mm and 0.5 mm diameter for phase flowrates that result in plug flow with the aqueous solution as the dispersed phase. The interfacial area in plug flow and the velocity profiles within the plugs were studied with high speed imaging and bright field micro Particle Image Velocimetry. Distribution and mass transfer coefficients were found to have maximum values at nitric acid concentration of 1M. Mass transfer coefficients were higher in the small channel, where recirculation within the plugs and interfacial area are large, compared to the large channel for the same mixture velocities and phase flow rates. Within the same channel, mass transfer coefficients decreased with increasing residence time indicating that significant mass transfer takes place at the channel inlet where the two phases come into contact. The experimental results were compared with previous correlations on mass transfer coefficients in plug flows.

4.2 Results and discussion

4.2.1 Distribution coefficients in equilibrium extraction

To characterize the mass transfer process a number of parameters will be used. The Eu(III) distribution coefficient, D_{Eu}, is defined as the ratio of concentration of europium in the ionic liquid phase to the concentration in the aqueous phase:

$$D_{Eu} = \frac{C_{aq,ini} - C_{aq}^{e}}{C_{aq}^{e}} \qquad (4.2.1)$$

The Eu(III) distribution coefficients for the aqueous-ionic liquid system were measured at different nitric acid concentrations (0.01, 0.1, 0.5, 1.0 and 2.0M). In the experiments, equal volumes of nitric acid solution containing europium nitrate and of ionic liquid solution (0.2M CMPO-1.2M TBP/[C_4min][NTf_2]) were mechanically shaken for 3 hours. The initial loading

of Eu(III) in the aqueous phase was 20, 30 and 50 mg/mL, respectively. After equilibrium, the Eu(III) concentration was measured in the aqueous phase in a UV-Vis spectrometer. **Figure 4.1** illustrates the Eu(III) distribution coefficient (D_{Eu}) as a function of initial nitric acid concentration ($C_{aq,ini}$). Each equilibrium experiment was repeated 5 times. The relative deviation was quite large for the low Eu(III) loading (20mg/mL), ranging between 3.69% and 28.76%, but decreased to 2.55 - 14.18% at 50 mg/mL loading, where the absorption signal in the UV-Vis is stronger and more stable than at lower loadings. The Eu(III) concentration in the ionic liquid phase was also measured with UV-Vis. The amount after extraction was between 89.65 to 101.54% of the initial Eu(III) loading. It would be difficult to have better agreement because the IL cations, the NO_3^- or the impurities in the imidazolium-based ionic liquids also have absorptison characteristics in the UV range that can mask the Eu(III) signal (Billard et al. 2011).

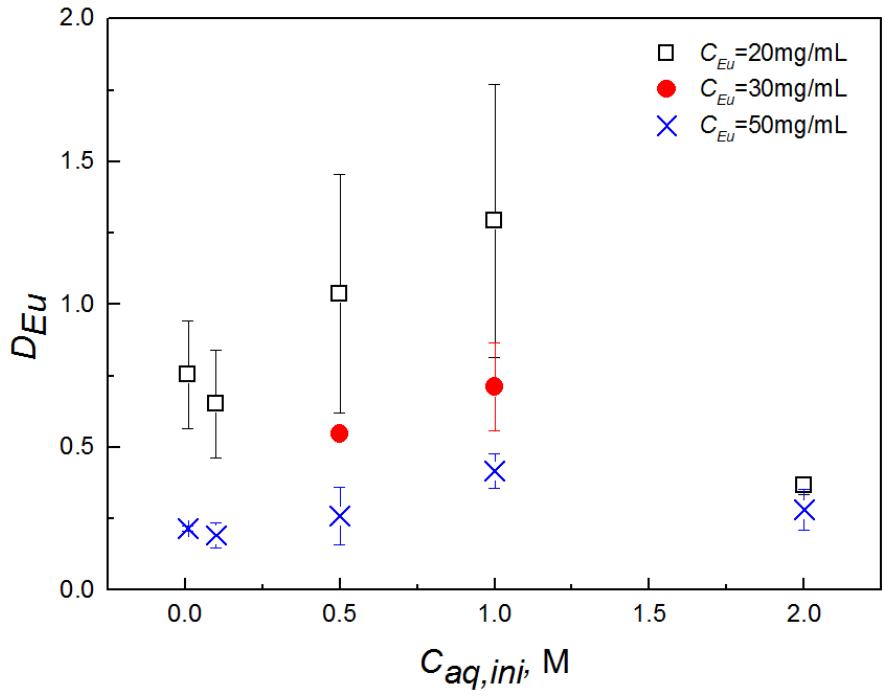

Figure 4.1: Eu(III) distribution coefficients against initial nitric acid concentration at different initial Eu(III) loading. Aqueous phase: 0.01-2M HNO_3; organic phase: 0.2M CMPO-1.2M TBP/[C_4mim][NTf_2].

As can be seen from **Figure 4.1**, the distribution coefficient reduces with increasing Eu(III) loading, which means that the Eu(III) in the aqueous phase is more difficult to be distributed into the ionic liquid phase. However, 50 mg/mL concentration was chosen for the microchannel

extraction experiments because of the low concentration measurement errors. Furthermore, the distribution coefficient has its highest value at 1.0M nitric acid concentration for all initial Eu(III) loadings, which is in agreement with the results by Rout et al. (2011). The distribution coefficients obtained when ionic liquid is used are by a factor of 10 higher to those achieved with the conventional TUREX solvent (0.2M CMPO-1.2M TBP/n-DD) (Rout et al. 2011).

4.2.2 Mass transfer in continuous extraction

The overall volumetric mass transfer coefficients of the Eu(III) extraction in the 0.5 mm ID microchannel, calculated from Eq. (2.3.10), are shown in **Figure 4.2 (a)** as a function of residence time. To obtain different residence times (τ), the channel length was varied from 5 cm, 15 cm to 25 cm, at the same volumetric flow rates of the two liquids $Q_{aq}= Q_{IL}$=3.534 ml/hr. The volumetric mass transfer coefficient was found to decrease non-linearly with increasing residence time. On average, the mass transfer coefficient of τ = 10s (CL = 5 cm) was 1.5 times higher than that of τ = 30 s (CL=15 cm) under all nitric acid solutions, while the change between τ=30 s and τ = 50 s (CL=25 cm) was small. This suggests that the mass transfer at the inlet of the channel contributes significantly to the overall mass transfer in the separation unit. The nitric acid concentration affects the mass transfer coefficient in a similar way that it affects the distribution coefficient (**Figure 4.2 (a)**). The highest mass transfer was found at 1.0M nitric acid concentration, followed by the 0.5 and 2.0 M concentrations. The lowest K_La were found for 0.1M nitric acid concentration.

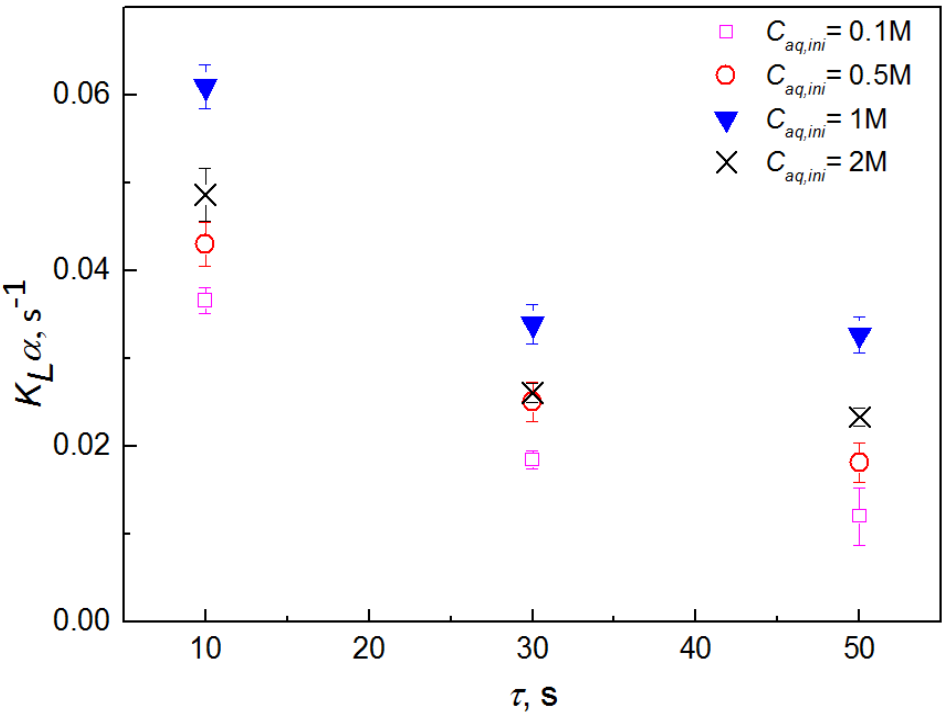

(a) Volumetric mass transfer coefficients

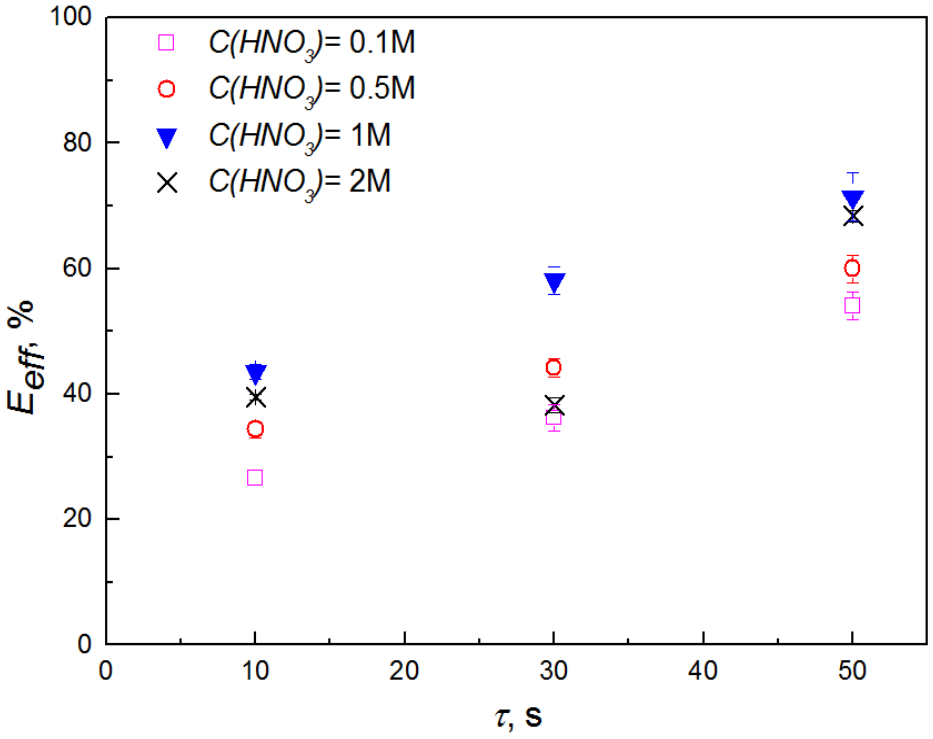

(b) Extraction efficiency

Figure 4.2: Variation of Eu(III) (a) extraction efficiency and (b) volumetric mass transfer coefficient with residence time for different initial nitric acid concentrations;

U_{mix}=0.5cm/s, CL=5, 15, 25cm.

The effect of residence time on extraction efficiency can be seen in **Figure 4.2 (b).** In all cases the extraction efficiency increases with residence time. In the shortest channel (CL=5 cm and τ=10 s) the extraction efficiency is relatively low (43.55%) despite the high mass transfer coefficients. The highest E_{eff} was found at 1M nitric acid concentration and at the longest residence time, where it reaches 71.50% of the equilibrium value.

4.2.2.1 Effect of mixture velocity on Eu(III) extraction

The effect of mixture velocity on overall volumetric mass transfer coefficient was investigated in the 0.5mm ID microchannel (CL=15 cm) at varying nitric acid concentrations, for equal volumetric flow rates of the two phases ranging from Q_{aq}=Q_{IL}=3.534 to 21.21 ml/hr. As can be seen in **Figure 4.3** for 1M nitric acid concentration the mass transfer coefficient increases with increasing mixture velocity, which means the extraction system is mass transfer dominated. The increase in the mass transfer coefficient is partly attributed to the small increase in interfacial area (see **Figure 4.3**). This contribution, however, is small; for example the area increases by 4.64% when the mass transfer coefficient rises by 54% for change in velocity from 0.5 to 3 cm/s. Mixture velocity, affects mass transfer in plug flow via two mechanisms: (a) convection due to internal circulation in the plugs and slugs; (b) molecular diffusion due to concentration gradients adjacent to the interface (Kashid et al. 2007, Dessimoz et al. 2008). The increase in mixture velocity increases the intensity of internal circulation and enhances convective mass transfer (Tsaoulidis and Angeli 2015). The circulation also helps interface renewal that increases the concentration gradients and therefore mass transfer close to the interface. The mass transfer performance, however, does not depend only on mixture velocity and as can be seen at nitric acid concentration different from 1M, the effect of mixture velocity on the mass transfer coefficient is less significant. The extraction of Eu(III) is a physical process combined with chemical reaction, and depends on both mass transfer and intrinsic reaction kinetics (Xu et al. 2013).

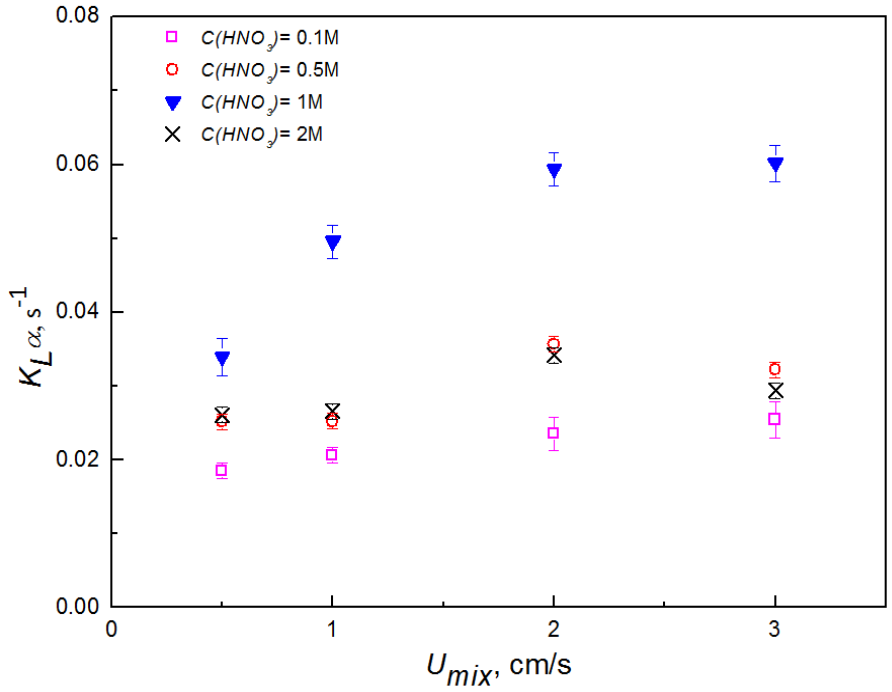

Figure 4.3: Variation of Eu(III) volumetric mass transfer coefficient with mixture velocity for different initial nitric acid concentrations; CL=15cm, 0.5mm ID.

To evaluate the role of film thickness on mass transfer, van Baten and Krishna (2004) proposed different correlations for mass transfer from the plug caps and the film in the plug flow regime:

$$K_{L,cap} = 2\frac{\sqrt{2}}{\pi}\sqrt{\frac{DU_P}{d_c}} \tag{4.2.2}$$

$$K_{L,film} = 2\sqrt{\frac{D}{\pi t_{film}}}\frac{\ln(1/\Delta)}{(1-\Delta)} \quad Fo< 0.1 \text{ (short contact)} \tag{4.2.3}$$

$$K_{L,film} = 3.41\frac{D}{\delta_{film}} \quad Fo> 0.1 \text{ (long contact)} \tag{4.2.4}$$

$$K_L\alpha = K_{L,cap}\alpha_{cap} + K_{L,film}\alpha_{film} \tag{4.2.5}$$

where the Fourier number (Fo) is defined as $Fo=D/t_{film}\ \delta_{film}^2$, and Δ is a dimensionless parameter based on Fo. The plug velocity, U_p, is obtained based on the plug displacement from the high speed imaging. The contact time of the liquid film, $t_{film} = L_{film}/(U_p + U_{film})$, is calculated under the assumption that the film velocity is nearly negligible in the microchannel. The mass transfer via the film can be evaluated depending on the value of the Fourier number (Fo), where

Fo< 0.1 and Fo> 0.1 for short and long contact time respectively. The aqueous plug in the present work shows long film contact times as Fo ranges between 0.486 and 1.235. The Eu(III) $K_{L,film}$ in the 0.2 mm ID channel was found to decrease from 4.702 to 3.353 × 10^{-7} m·s^{-1} when U_{mix} increased from 0.01 to 0.06 m/s, and $K_{L,cap}$ increased from 1.151 to 2.985 × 10^{-5} m·s^{-1} under the same operation conditions. These results show that 99% Eu(III) is extracted via the cap regions, and the film region has a minor effect on the overall mass transfer. It explains why high K_La occurs at larger U_{mix}, where plug formation frequency increases and shorter plugs form, which would result in increased cap regions that enhance mass transfer. At U_{mix}>0.04 m/s where Fo>0.8 and Δ≈0 (van Baten and Krishna (2004)), the ionic liquid film approaches saturation, and its contribution to the overall mass transfer becomes insignificant.

The Eu(III) extraction efficiency is shown in **Figure 4.4** for the 0.5 mm ID microchannel (*CL*=15 cm). The extraction efficiency increases with increasing residence time (decreasing mixture velocity). The highest extraction efficiencies are obtained for 1M nitric acid concentration similar to distribution coefficients (see **Figure 4.4**). Although the mass transfer coefficient at U_{mix}=3 cm/s has the highest values, the corresponding extraction efficiencies are only 36.24% to 58.13% of the equilibrium value due to the short residence times (τ=5s).

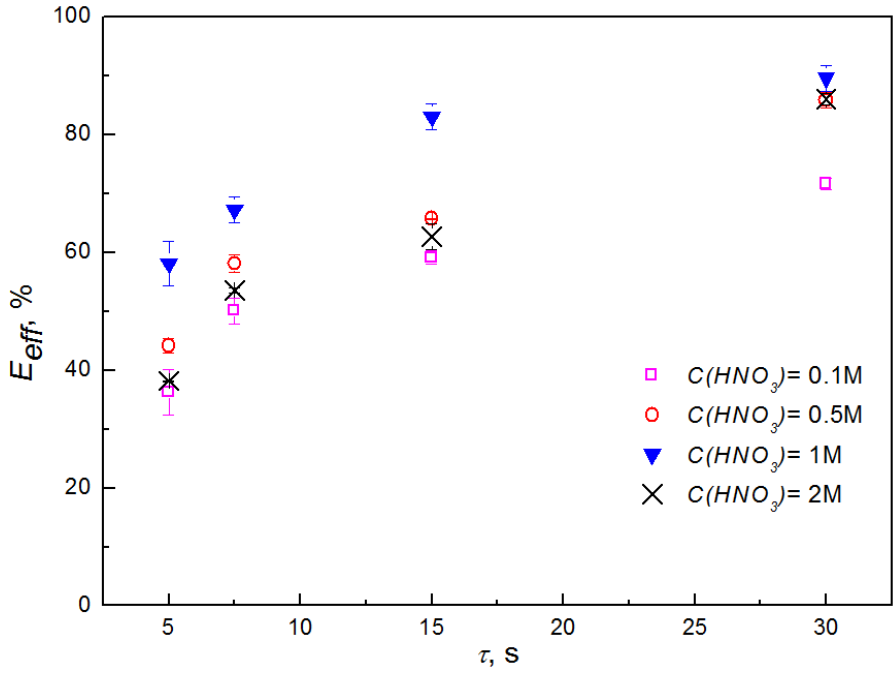

Figure 4.4: Variation of Eu(III) extraction efficiency with residence time for different initial nitric acid concentrations; CL=15cm, 0.5mm ID.

4.2.2.2 Effect of capillary size on Eu(III) extraction

The effect of channel size on overall volumetric mass transfer coefficient is shown in **Figure 4.5** for 0.2 and 0.5 mm ID capillaries as a function of mixture velocity at the same channel length (*CL*=25 cm). 1M nitric acid was used as aqueous phase, and equal flow rates of the both phases were used varying from 0.065 to 14.14ml/h. Generally, K_La are higher in the small channel because of the large interfacial area compared to the 0.5 mm channel. As depicted in **Figure 4.5** the average interfacial area increases from 3600 m^2/m^3 to 8250 m^2/m^3 when the capillary internal diameter reduces from 0.5mm to 0.2mm. The difference between the mass transfer coefficients increases with mixture velocity. For example, at U_{mix}=1 cm/s the difference is about 10.5% of the 0.5 mm channel K_La, but increases to 21.4% at U_{mix}=3 cm/s. The increased surface renewal rate and recirculation intensity caused by higher plug velocities in the small channel are considered to be responsible for the difference. In fact, the plug velocity is always higher than the mixture velocity in the liquid-liquid plug flow regime, due to the existence of a nearly stagnant ionic film surrounding the aqueous phase plug. The non-dimensional film thickness (δ_{film}/R) in the 0.2 mm ID channel was found to be 8.47-32.92% larger than in the 0.5 mm ID channel from the imaging experiments, depending on the mixture velocity. Therefore the enclosed plug moves slightly faster in the small channel. This is also confirmed by the imaging experiments, which showed that plugs in the 0.2 mm ID channel moved 5.94- 17.74% faster compared to the large channel.

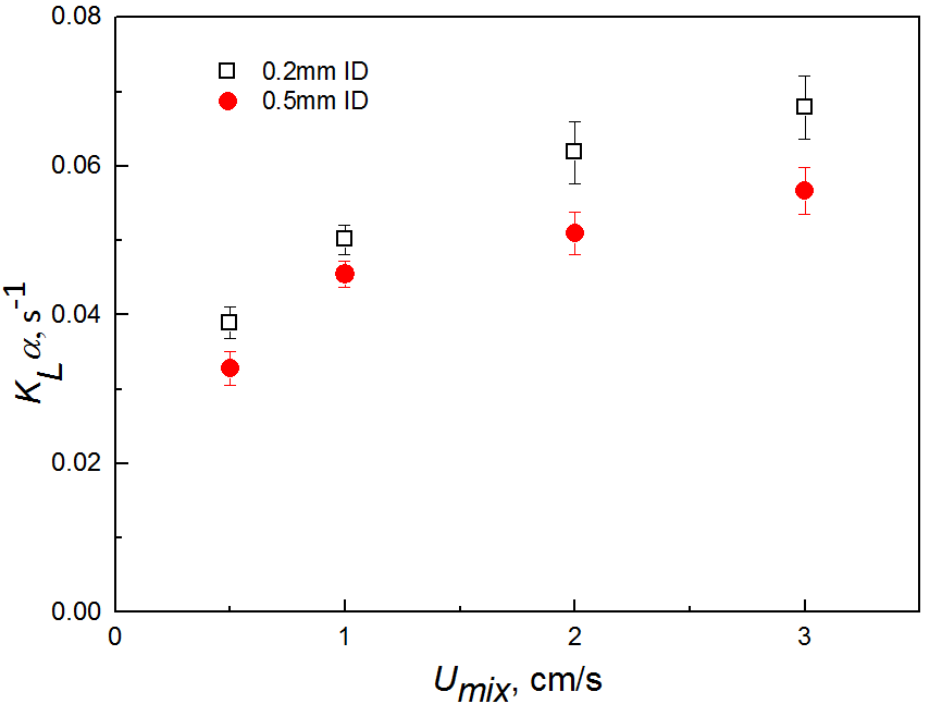

Figure 4.5: Variation of Eu(III) volumetric mass transfer coefficient with mixture velocity for different capillary sizes, 0.2mm and 0.5mm ID; CL=25cm.

4.2.2.3 Effect of recirculation intensity on Eu(III) extraction

The convective mass transfer inside the plugs is strongly affected by the recirculation patterns, which are caused by the shear between the continuous phase and the plug axis. To obtain the recirculation patterns, for each set of conditions the instantaneous velocity profiles of 30 plugs were averaged, with a deviation of 4.35-9.99%. The average plug velocity was then calculated by integrating the laminar velocity profiles of the averaged velocity field along the plug length. The recirculation pattern was finally obtained by subtracting the average velocity from the local velocities in the plug. An example of the averaged recirculation pattern inside a plug is shown in **Figure 4.6 (a)** for $Q_{aq}=Q_{IL}=3.534$ ml/hr. It consists of two counter rotating vortices with closed streamlines and symmetrical about the channel axis. The recirculation intensity within the plug is characterized by the recirculation time which is the time needed to displace material from one to the other end of the plug (Thulasidas et al. 1997, Kececi et al. 2009, Dore et al. 2012). A two-dimensional recirculation time was calculated as follows (Dore et al. 2012):

$$\tau(x) = \frac{L_p y_0}{\int_0^{y_0} u(x,y)dy} \cong \frac{L_P y_0}{\Delta \sum_{i=1}^{i=N} u_i|x} \qquad (4.2.6)$$

where y_o is the location of the stagnation point projected onto the observation mid-plane. As can be seen from **Figure 4.6 (b)** the recirculation time is almost constant in the middle of the channel but increase towards the front and back ends of the plug where the streamlines are not well defined. The recirculation time is usually treated as constant inside the liquid plug(Thulasidas et al. 1997, Kashid et al. 2005, Tsoligkas et al. 2007). However, Dore et al. (2012)experimentally found that the circulation pattern may not be fully symmetric, especially at shorter plugs.

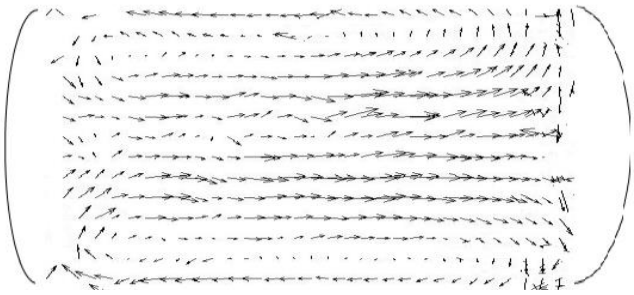

(a) Averaged recirculation pattern

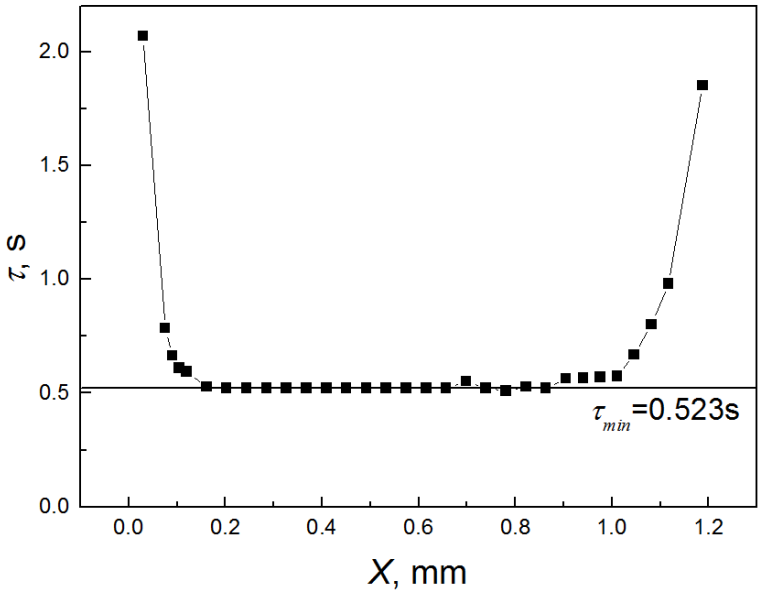

(b) Averaged recirculation time

Figure 4.6: (a) Averaged recirculation pattern and (b) averaged recirculation time profile along an aqueous plug; 0.5mm ID channel, $Q_{aq}=Q_{IL}$=3.53 ml/h.

The recirculation times averaged for the middle part of the plug are plotted in **Figure 4.7** against

the plug travel time, in the 0.5mm ID channel for $Q_{aq}=Q_{IL}=3.534$ to 21.21 ml/hr. The plug travel time is defined as the time needed by the liquid plug to travel a distance of its own length, given by $T_p=L_p/U_{mix}$, where L_p is the plug length. The corresponding mass transfer coefficients are also plotted. As discussed above, high mixture velocities (U_{mix}) result in shorter plug lengths, thus leading to a shorter plug travel time (T_p). In shorter plugs, decreased recirculation times are observed, which means the fluid in the plug will experience a larger number of revolutions and better mixing. This is supported by the increase in the mass transfer coefficient at low T_p, where the circulation time is also short. A similar trend was also observed by Kashid et al. (2005) who argued that high mixture velocities increase recirculation intensity because of increased shear between the wall surface and the plug. Meanwhile, higher mixture velocity increases the thickness of the film surrounding the plug and decreases the plug diameter, which results in a shorter path length for the Eu(III) diffusion in the radial direction that also helps mass transfer.

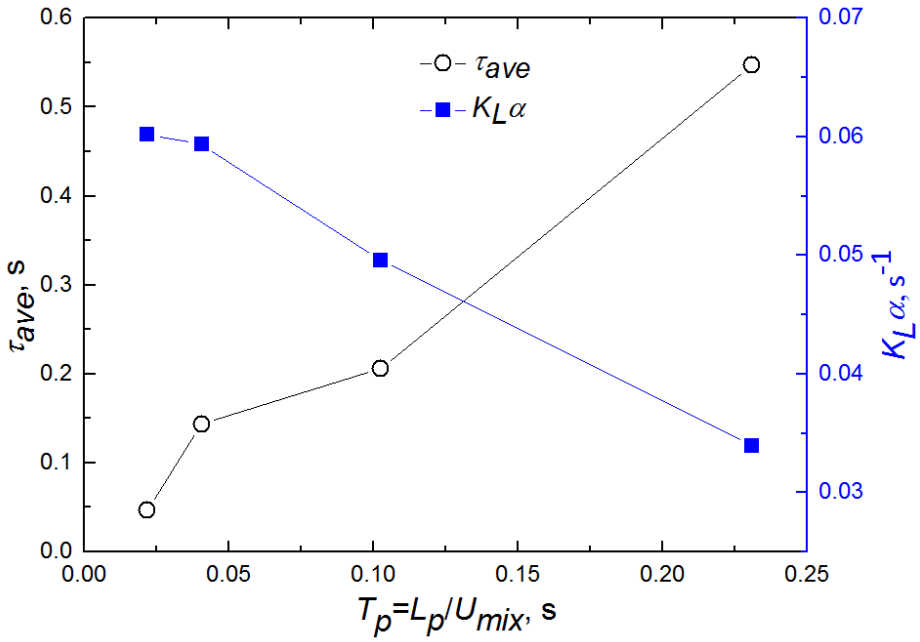

Figure 4.7: Recirculation time and mass transfer coefficient as a function of plug travel time. Aqueous phase: 1M nitric acid; organic phase: 0.2M CMPO-1.2M TBP/[C4mim][NTf2]; CL=15cm; 0.5mm ID; $Q_{aq}=Q_{IL}$.

4.2.3 Comparison of k_La with correlations

Mass transfer in multiphase small scale units is a complex process, which depends not only on

the hydrodynamic characteristics but also on the kinetics of the species transfer. Several models have been proposed to estimate mass transfer coefficients in gas-liquid and liquid-liquid plug flow either empirical or developed from the film and penetration theories. Bercic and Pintar (1997) suggested a correlation, Eq. (4.2.7), for gas-liquid flow which considers only the contribution of the plug caps since, as the authors argued, the film becomes quickly saturated. This model was able to predict accurately $k_L\alpha$for long bubbles and liquid slugs. Vandu et al. (2005) suggested a model for the mass transfer coefficient where the dominant contribution was from the film (Eq. (4.2.8)). A constant was introduced whose value was estimated from the best fitting of experimental data from different unit cell lengths L_{UC}, gas hold up ε_G and rise velocity U_p. Yue et al. (2009) proposed an empirical correlation (Eq. (4.2.9)) suitable for short films and non-uniform concentration in the plugs, which differs from the well mixed assumption of the previous models. Similarly, Kashid et al. (2010) developed an empirical correlation (Eq. (4.2.10)) specifically for liquid-liquid plug flow as a function of Reynolds number, Capillary number, diameter and length of the capillary. The correlation was able to predict the experimental data within 95% even when the density, viscosity and interfacial tension of the aqueous phase was changed with the addition of surfactants.

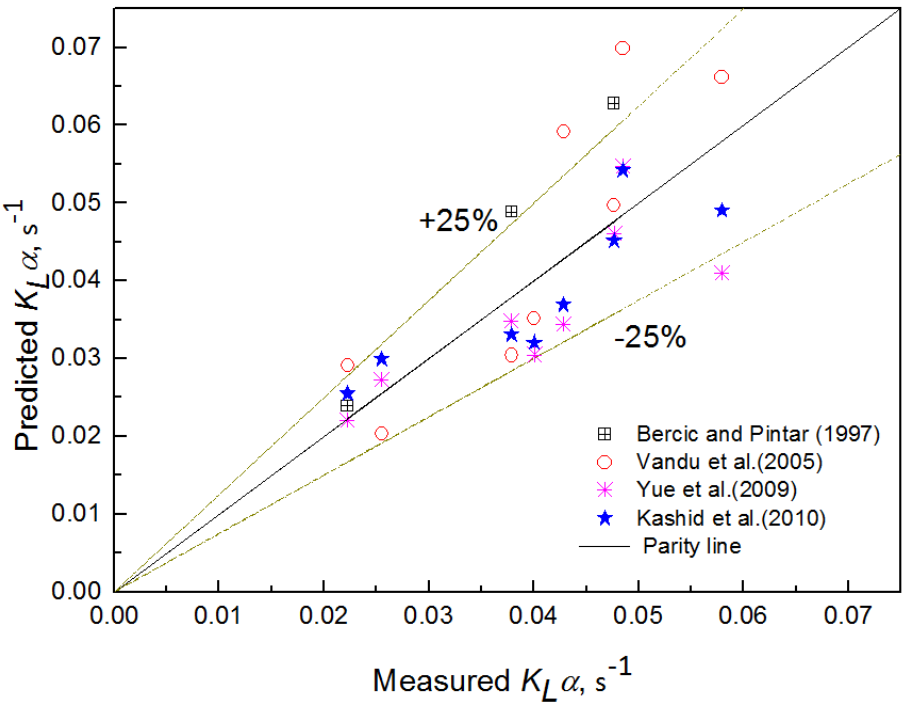

Figure 4.8: Comparison of experimental K_La values against predicted ones. (System: 1M nitric acid-0.2M CMPO-1.2M TBP/[C_4mim][NTf_2]; $Q_{aq}=Q_{IL}$; ID=0.2 and 0.5 mm capillary).

The mass transfer coefficients measured in 0.2 and 0.5mm ID channels are compared with these correlations in **Figure 4.8**. The fitting parameters in the correlations byVandu et al. (2005) (Eq. (4.2.8)), Yue et al. (2009) (Eq. (4.2.9)) and Kashid et al. (2010) (Eq. (4.2.10)) were determined from least square regression analysis of the data in both channels:

$$k_L\alpha = 0.111\frac{(U_p+U_s)^{1.19}}{((1-\varepsilon_G)L_{UC})^{0.57}} \tag{4.2.7}$$

$$k_L\alpha = 3.65\sqrt{\frac{DU_p}{L_{UC}}}\frac{1}{ID} \tag{4.2.8}$$

$$k_L\alpha = \frac{1.67}{ID}\left(\frac{U_p}{ID}\right)^{0.5}\left(\frac{L_p}{ID}\right)^{0.15}\left(\frac{L_p+L_S}{ID}\right)^{0.05} \tag{4.2.9}$$

$$k_L\alpha\frac{L_p}{u_{mix}} = 0.0257Ca^{-0.6}Re^{0.05}\left(\frac{ID}{L_p}\right)^{-0.1} \tag{4.2.10}$$

The model suggested by Bercic and Pintar (1997) shows deviations as high as 55.41% compared to the experiment results. This correlation does not include the effect of channel size, and it was developed for velocities higher than those used in this work. Besides, the liquid slug length (3-13.5 cm) and unit cell length (1.7-22 cm) considered for the model development were about 100 times larger than in the current work. The model by Vandu et al. (2005) gives better predictions particularly for the large channel with standard deviation varying from 11.53 to 42.12%. The correlation was in fact developed for gas-liquid flow in 1-3 mm ID capillaries, for bubbles and liquid slugs longer (L_{UC}=5 – 60 mm) than in the present work (L_{UC}=0.314-1.153 mm). The predictions of the two empirical correlations (Eqs. (4.2.9) and (4.2.10)) are better, with deviations less than 20%. The model by Yue et al. (2009) (standard deviation 5.35-16.72%) was developed based on the physical absorption of oxygen from rising air bubbles into water in square microchannels with ID=0.4 mm. The differences from the current data may be attributed to the low mass transfer resistance in the gas phase bubbles compared to liquid plugs. The model by Kashid et al. (2010) which was developed from liquid-liquid systems agrees best with the experiment results (standard deviations 5.16 -11.88%). Empirical correlations may agree better with the experimental data because the effects of chemical reaction kinetics and inlet junction configuration can be included in the constants, while such effects are not taken into account in the models based on film and penetration theory on a fully formed plug (Eqs. (4.2.7) and (4.2.8)).

Preliminary Eu(III) extraction experiments were carried out with cyclohexane as organic phase diluent for comparison in the 0.5 mm ID channel. The Eu(III) was extracted with 50% TBP in cyclohexane from 2 M nitric acid, and the distribution coefficient was found to be between 0.024 and 0.041. Under the same flow rate of both phases, the K_La of the cyclohexane system (0.0262-0.0643s^{-1}) was similar to that of the ionic liquid system (0.0339-0.0602s^{-1}). However, the Eu(III) initial loading when cyclohexane was used was only 0.31 mg/mL (2×10^{-3} M), because of the low limiting organic concentration (LOC). In conventional systems like n-DD or cyclohexane as organic diluent, the LOC of europium is 9 mg/mL; beyond this concentration the organic phase will split into two phases a heavier (rich in metal-solvate) and a lighter phase (rich in diluent) called third phase formation. This is not observed when the ionic liquid is used, even when the loading of Eu(III) in the ionic liquid phase increased from 12 to 40 mg/mL (Rout et al. 2011). Therefore the high process capacity is an additional benefit of the present system.

The mass transfer coefficients and interfacial areas found in this work are compared against those from other microfluidic units and conventional extract ion units in **Table 4.1**. For the comparisons of K_La values in microfluidic system, previous studies using different liquid-liquid extraction systems are listed as well. As can be seen, the interfacial areas are comparable to those obtained in other microfluidic systems but significantly higher than those in conventional extraction units. The mass transfer coefficients are again higher than the ones achieved in conventional extractors but not as high as those in different microfluidic applications. This may be due to the low distribution coefficients found for the Eu(III) extraction.

Table 4.1: Comparison of K_La values in liquid-liquid microfluidic systems using T/Y-junctions.

Liquid-liquid contactor	System	K_La (s^{-1})	a (m^2 m^{-3})	Reference
T-junction capillaries, ID=0.2 and 0.5mm	0.2M CMPO-1.2M TBP/[C_4mim][NTf_2]---1M nitric acid	0.005-0.05	3750-8250	Present work
T-junction capillaries, ID= 0.5mm	50% TBP in cyclohexane---1M nitric acid	0.0262-0.0643	3613-3979	Present work

Soda-lime glass 0.38mm depth chip	Kerosene/acetic acid/ water+NaOH	Order of magnitude of 0.5	N/A	Burns and Ramshaw (2001)
PTFE capillary with Y-junction, 0.5, 0.75 and 1mm	Kerosene/n-butanol/water	0.02-0.31	590-4800	Kashid et al.(2007)
Rectangular glass microchannel 0.4mm	Hexane trichloroacetic acid/ water+NaOH	0.2-0.5	10700-11200	Dessimoz et al. (2008)
Capillary microreactor, ID=0.5mm	n-butyl formate-aqueous NaOH solution	0.90-1.67	1600-3200	Ghaini et al. (2010)
Square (glass, 0.4mm), T-square (glass, 0.4mm), T-trapezoidal, 0.269mm), Y-rectangular (0.15mm ID), Concentric (glass, 0.15mm)	Nonreacting water-acetone – toluene	0.01-0.74	N/A	Kashid et al. (2011)
Opposed T-junction, ID=0.6, 0.8 and 1.0mm	Sodium hydroxide---n-butyl acetate	0.006-0.37	1300-4100	Xu et al. (2013)
T-junction Teflon channel, ID=0.5mm	30%TBP in $[C_4mim][NTf_2]$---3M nitric acid	0.049-0.312	N/A	Tsaoulidis et al. (2013)
T-junction, PTFE capillary with 2mm ID, 0.0016 to 0.45m/s	$CuSO_4/H_2SO_4$/AD-100/260#	0.03-0.26	N/A	Yang et al. (2013)
T-junction serpentine microchannel , ID=0.278 and 0.319 mm	30% TBP in dodecane (nitric acid)--- water	0.001-4	N/A	Sen et al. (2014)
Square Glass T-junction	Water/acetone/toluene	1.61-8.44	6090-13400	Raimondi et al. (2014)

microchannel , 210 μm				
Packed extraction columns	n-butyl formate-aqueous NaOH solution	0.0034-0.005	80-450	Verma and Sharma (1975)
RTL extractors (Graesser raining bucket)	n-butyl formate-aqueous NaOH solution	$(0.6\text{-}1.3)\times10^{-6}$	90-140	Alper (1988)

4.3 Conclusions

The intensified extraction of Eu from nitric acid solutions into an ionic liquid phase 0.2M CMPO-1.2M TBP/[C_4mim][NTf_2] was studied experimentally in small channels with diameters 0.2 and 0.5 mm. Experiments were carried out in the plug flow regime, where the aqueous solution formed the dispersed plugs and the ionic liquid solution was the continuous phase. Phase equilibrium studies showed that the distribution coefficients had the highest value at nitric acid concentration equal to 1M. The geometric characteristics of the flow pattern (plug length, film thickness and interfacial area) were investigated with high speed imaging while velocity fields within the aqueous phase plugs were obtained using high speed bright field micro PIV.

The results revealed that the interfacial areas and the mass transfer coefficients were significantly higher than in conventional contactors. In addition, K_La were found to be higher in the small channel compared to the large one for the same mixture velocities, as a result of large interfacial areas and reduced circulation times. Within the same channel, the mass transfer coefficients increased and then decreased with increasing nitric acid concentration in accordance with the partition coefficients. The mass transfer coefficients were also found to decrease with residence time suggesting that significant mass transfer occurs at the channel inlet. The mixture velocity affected the mass transfer coefficient particularly in the case of 1M nitric acid concentration. The circulation times within the plugs, calculated from the detailed velocity profiles, were found to decrease with decreasing plug size and increasing mixture velocity; small circulation times result in better mixing and mass transfer. The empirical

correlation suggested by Kashid et al. (2010) was able to predict the current results (with deviations 5.16-11.88%) better than other literature correlations.

Chapter 5. Plug characterization using PIV

5.1 Introduction

Understanding the hydrodynamic characteristic of the liquid-liquid Taylor flow is crucial in the emerging field of plug-based microfluidics and other lab-on-a-chip system. In this study, we use bright field Micro-Particle Image/high speed photography to realize simultaneous interface detection and velocity measurement in the fast moving plugs of 1M HNO_3 dispersed in a continuous ionic liquid solution (0.2M CMPO -1.2M TBP/[C_4min][NTf_2]), in 0.2 and 0.5 mm internal diameter (ID) microchannels. Correlations regarding film thickness, plug velocity and plug length are developed based on a group of dimensionless parameters. It is observed the liquid film surrounding the plug is largely affected by the changes in the front cap in the current operation condition (0.0224< Ca <0.299), and the droplet volume is highly dependent on channel diameter as well as mixture velocity. The volume-of-fluid (VOF) method is then used to model the velocities and pressure distribution of the droplet and shows good agreement with experimental results and previous models. These features will help in optimizing the microfluidic plug flow for mixing, as well as mass and heat mass transfer enhancement.

5.2 Results and discussion

5.2.1 Wettability Characteristic

Flow patterns in the glass microchannel were found to be very sensitive to the phase that initially filled the channel. Initially the ionic liquid phase was injected from the main channel, to ensure that it filled the whole channel. Then the aqueous solution was injected from the side channel under the same flow rate (U_{org}=U_{aq}=0.03m/s). As shown in **Figure 5.1**, periodic aqueous plug (dispersed phase) flow was generated while the ionic liquid was the continuous phase. The same procedure was repeated with the aqueous solution initially filling the main channel. In this case, however, different patterns were observed. Since the ionic liquid phase preferentially wets the glass, it eventually comes in contact with the wall. In this case both phases are in contact with the wall and the patterns are very unpredictable, as shown in **Figure 5.2**. Eventually the ionic liquid solution would become the continuous phase, with the aqueous

being the dispersed phase. In general, no matter which phase initially wets the glass channel, ionic liquid phase will become the continuous one.

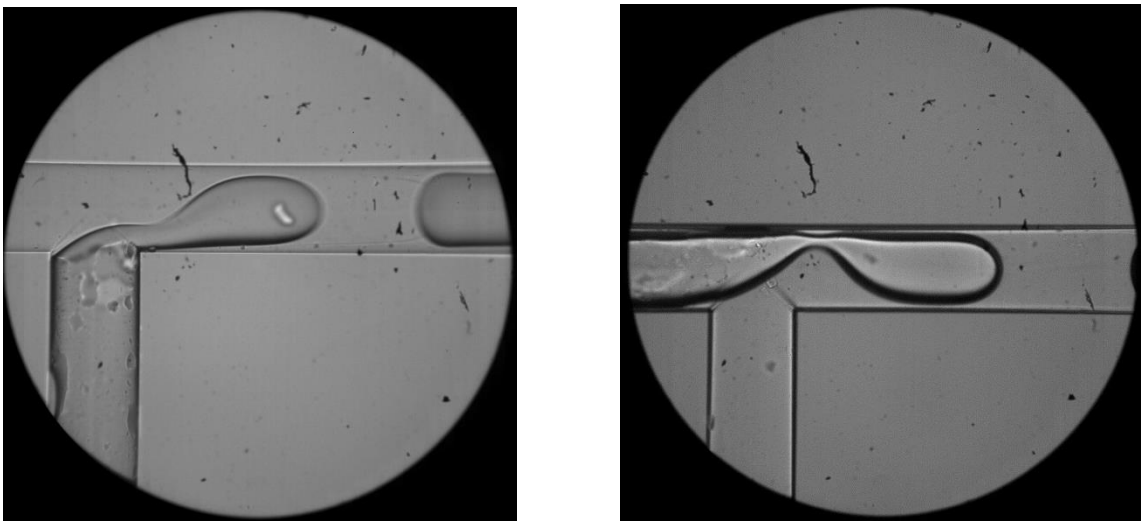

(a) (b)

Figure 5.1: Photograph of droplet formation in the T-junction with (a) ionic phase phase initially filled from mainchannel; (b) aqueous phase initially filled from mainchannel (Vorg=Vaq=0.03m/s, Qorg/Qaq=1).

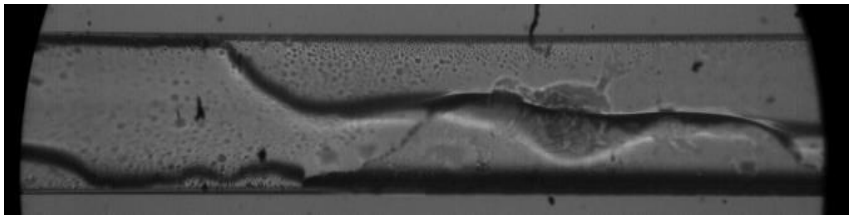

Figure 5.2: Photograph of microchannel wall with water the phase initially filling the channel.

Numerical work was conducted to validate the experimental findings with aqueous phase initially filled with the main channel. 8μm grid size was used to calculate the plug formation prosses in the T-junction, with the aqueous phase initially injected along the main channel. A similar flow pattern as experiment was observed as shown in **Figure 5.3**: the ionic liquid phase from the side channel gradually replaced the aqueous phase as continuous phase downstream, the inlet and became the continuous one. Based on the velocity vector on the channel middle transverse plane in **Figure 5.3**, although the injection velocity of each phase is the same (U_{IL}=Uaq=0.03m/s), the velocity of the dispersed phase is much higher than that of the

continuous phase after the junction; this is to be expected as the disperse phase is located in the middle part of the channel and away from the walls. Moreover, a high velocity zone was found close to the inlet where the aqueous plug is forming, and reaches the highest velocity when the aqoues phase is about to detach and form the dispersed plug. The liquid-liquid detachment in the T-junction is controlled by the viscous forces and interfacial tension.

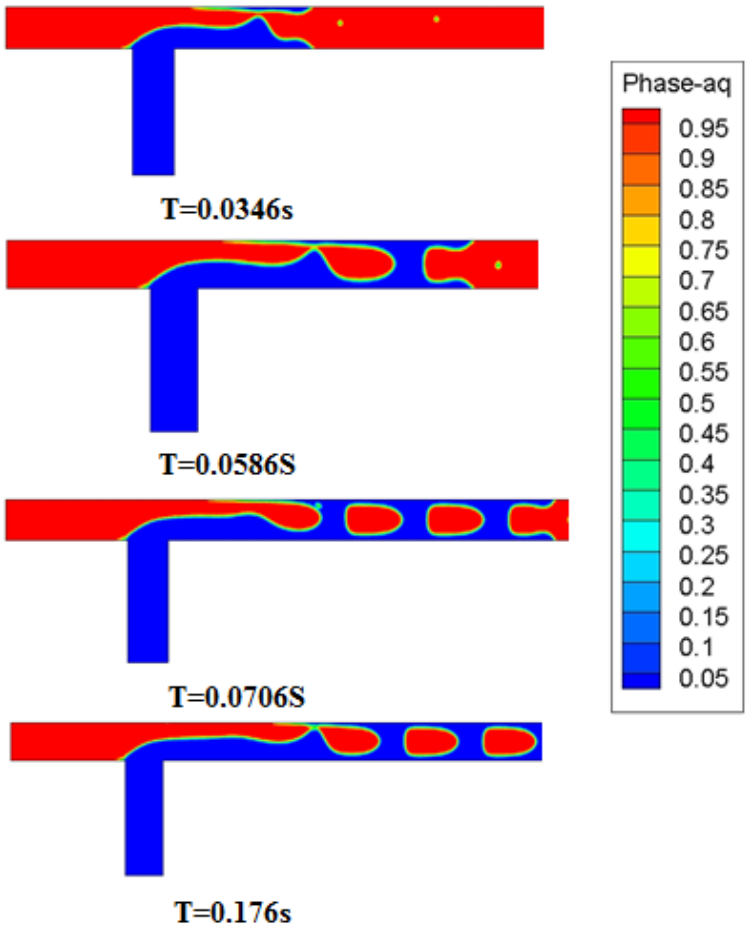

Figure 5.3: Plug formation process on the middle plane(V_{org}=V_{aq}=0.03m/s, Q_{org}/Q_{aq}=1). The color band represents the phase volume rate of aqueous phase.

5.2.2 Flow pattern map

The flow pattern after the formation was studied with ionic liquid phase as initial filling liquid from the main channel. The flow rate of the two liquid solutions varied from 0.0653 ml/h^{-1} to 15.684ml/h^{-1}, and the flow ratio (Q_{IL}/Q_{aq}) varied from 0.005 to 12. In all cases, the ionic liquid phase flow rate was kept constant and that of the aqueous phase varied. In **Figure 5.4**, the flow pattern map is presented based on the Reynolds and Capillary dimensionless numbers.

Five flow patterns were observed: droplet, plug, slug, annular and anuular+slug flow. Based on the work done by Foroughi and Kawaji (2011), the aqueous plug and slugs can be distinguished according to their lengths. If the average length of the aqueous segments was equal to or less than 5 channel diameters, the flow was classified as a plug flow; but if the length was more than 5 channel diameters, the flow was classified as a slug flow. In all cases, the Bo number (ratio of gravitational forces over surface tension) is around 0.016 so the effect of gravity can be neglected.

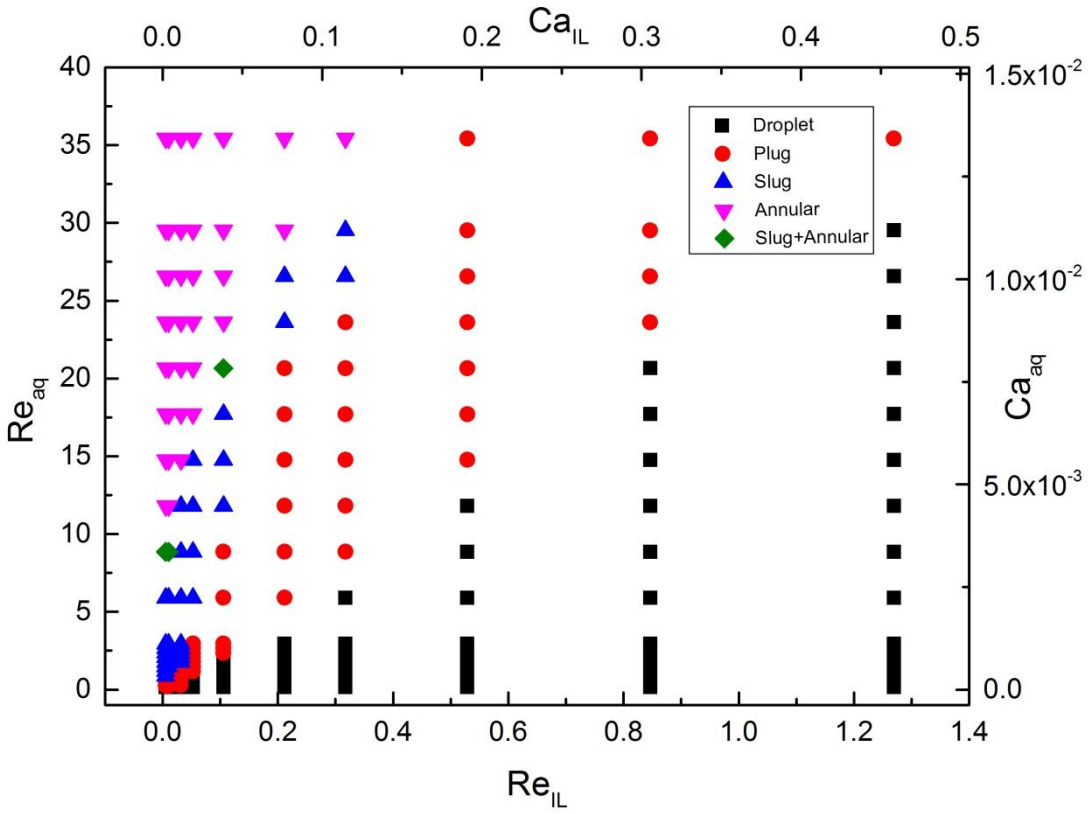

Figure 5.4: Flow pattern map for 0.2M CMPO-1.2M TBP/[C4min][NTf2] and 1M nitric acid flow in 0.2 mm ID microchanel initially filled with the ionic liquid solution.

At low aqueous phase flow rates the main pattern is droplet flow (**Figure 5.5 (a)**), which usually refers to a pattern where the drops are smaller than the channel diameter. This flow pattern can also be observed at higher ionic liquid flow rates, where the aqueous phase occupies relatively small volume in the mixture. With an increase in the aqueous phase flow rate, a transition occurs from droplet to plug (**Figure 5.5 (b)**) and then to slug flow (**Figure 5.5 (c)**). The plugs have a bullet shaped nose and flat rear interface, while the slug is very symmetric and surrounded by the ionic liquid film. In these patterns the interfacial tension is dominant, so the core flow is discontinuous and dispersed. At higher aqueous phase flow rates a continuous core

is formed; at certain conditions this alternates with slugs, indicating that interfacial tension and inertial forces are still comparable. With a further increase in the aqueous phase flow rate, the flow pattern changes to annular flow with continuous sausage-shaped interface deformations (**Figures 5.5 (d)** and **(e)**); in this case inertia starts becoming the dominant force. Irregular interface undulations are observed (**Figure 5.5 (d)**) at the lower aqueous phase flow rates but the interface becomes smoother with increasing flow rates. Inertial forces tend to make the ionic liquid-aqueous interface wavy due to shear instability, while viscous effects and surface tension tend to keep the interface smooth [18].

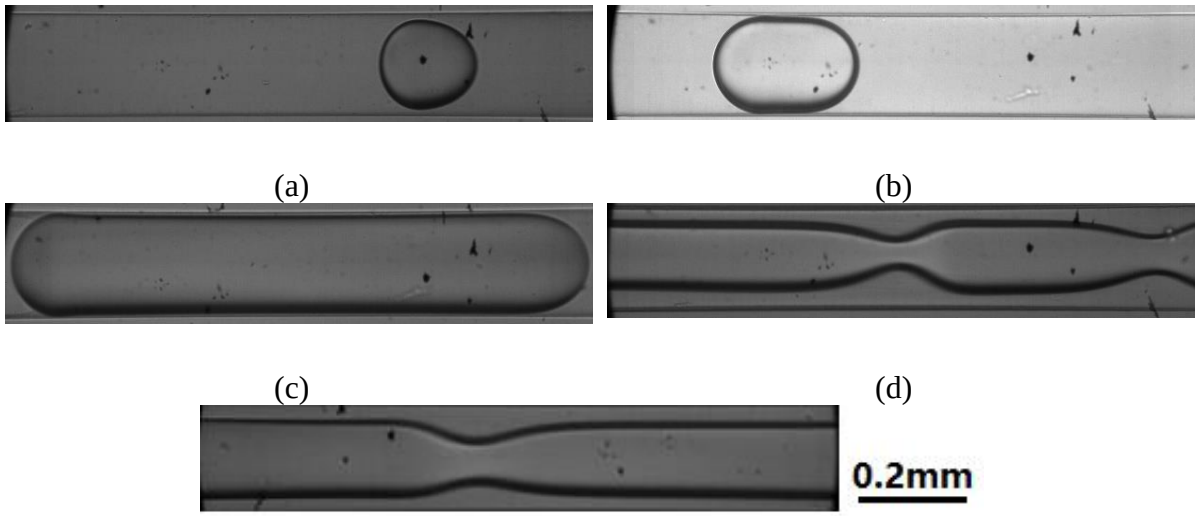

(e)

Figure 5.5: Flow patterns observed in ionic liquid-aqueous two-phase flow in a glass microchannel initially filled with ionic liquid phase. The flow direction is from left to right.

5.2.3 Film thickness

Depending on the plug length the film thickness may not be uniform along the plug (see **Figure 5.6**). The dimensionless plug length (L_p/D) varied between 1.14 and 2.31 in both 0.2 and 0.5 mm ID channels. It was found that for L_p/D between 1.82 and 2.31, a region of uniform film thickness was always present between the hemispherical caps of the plug and the film thickness was measured in this area. However, for $1.14 < L_p/D < 1.82$, the film thickness varied along the plug length. In these cases the film thickness was obtained by averaging the thickness at 5 points along the film.

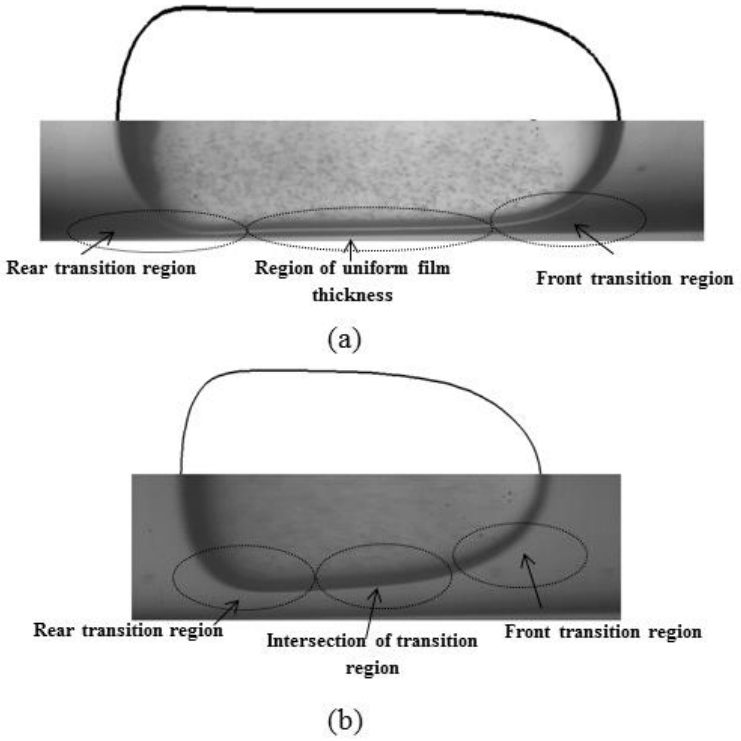

Figure 5.6: Image of aqueous plug flow at different dimensionless length (a) L_p/D =2.28 and (b) L_p/D =1.61in 0.5mm ID channel.

Because the refractive indices of the channel wall (n=1.544), the ionic liquid phase (n=1.427) and the aqueous phase (n=1.334) do not match there is an error in the calculation of the film thickness, shadow area is apparent at the highly curved interface (droplet edge and inner channel wall) but clear distinguish of the liquid-liquid interface can be obtained with the strong LED illumination, which revealed the interface appears as a bright line in the dark wall region. The optical correction method proposed by Han and Shikazono (2009) and Mac Giolla Eain et al. (2013) was employed to calculate the actual film thickness. By considering the wall curvature and the refractive index difference, it was found that the error in the film thickness is between for 8.36– 14.48 % for all conditions studied. The effect of gravity can be neglected in the present work as the *Bo* number (ratio of gravitational over surface tension forces) is significantly less than 1 (0.016 and 0.052 in 0.2 mm and 0.5 mm channel, respectively).

In small channels the liquid film thickness is dominated by the balance between viscous and surface tension forces, represented by the Capillary number, Ca (Angeli and Gavriilidis 2008, Han and Shikazono 2009). The normalized ionic liquid film thickness δ/D against the Capillary number is shown in **Figure 5.7** for equal phase flow rate $Q_{aq} = Q_{IL}$ = 0.653 - 42.41 ml/hr. The

Ca was calculated based on plug velocity ($Ca = \mu_{IL} U_p / \sigma$) and varied between 0.0224 and 0.299. The plug velocity was obtained by measuring the plug tip displacement between consecutive images. The Ca values are about 9.82 – 25.14 % larger than those based on mixture velocity (U_{mix}).

As can be seen in **Figure 5.7**, the dimensionless film thickness increased non-linearly with increasing Capillary number. The dimensionless film thickness is slightly lower in the 0.2 mm ID channel compared to the 0.5 mm ID one for the same Ca. Also shown in the figures are plots of literature correlations as given in Table 2.1. The Bretherton (1961) model fails to predict the film thickness for both channels tested, as the current Ca numbers exceeded the prediction range of their model (Ca < 0.003). The fitting parameters in the correlations proposed by Irandoust and Andersson (1989) and Aussillous and Quéré (2000), which are based on gas-liquid flows, have been modified from least square regression analysis of the current experimental data. These models show that the film thickness is solely related to the Capillary number, and ignore the effects of inertial forces at relatively high velocities. They therefore, predict better the experimental data at low Ca. Poor agreement was found between the experimental data and the Dore et al. (2012) model, which was developed for liquid-liquid plug flow, with a deviation between 6.63 – 73.76 %. Han and Shikazono (2009) proposed a correlation for gas-liquid flows which accounts for the effects of surface, viscous and inertial forces by incorporating the Reynolds and Weber numbers in addition to Ca. Their model, however, overpredicts the film thickness by 11.24 – 88.19 %. The viscosity difference between the phases is considered to be responsible for the poor agreement. In gas – liquid flows, the shear forces between the phases can be ignored as the gas viscosity is negligible. In liquid-liquid flows, however, the reduced viscosity difference means a significant increase in interfacial shear forces, which results in a non-negligible flow in the continuous film surrounding the dispersed plug, hence the film thickness and plug velocity is different from the gas-liquid flows (Mac Giolla Eain et al. 2013). Therefore most correlations developed for gas-liquid flow shows poor agreement with the experimental data when applied to liquid-liquid systems. Langewisch and Buongiorno (2015) suggested a film thickness correlation based on extensive numerical studies of gas-liquid slug flows (Table 2.1), which agrees well with the Han and Shikazono (2009) model (deviation < 3.9 %), but is over a broader range of Ca and Re numbers (0.005 < Ca < 2; 0 < Re < 900). Mac Giolla Eain et al. (2013) suggested a correlation from experimental data on liquid-liquid flows for 0.002 < Ca < 0.119, where the We number was included to account for inertial forces at high velocities. The correlation agrees

well with the experimental data with a deviation of 0.64 – 16.8%. An expression including *Ca* and *Re* numbers was suggested by Tsaoulidis and Angeli (2016), for 0.03 < Ca < 0.18, which however overpredicts the current experimental data by 1.574 – 34.61 %. The effect of channel size could be nearly negligible in gas-liquid flows, where the average difference in film thickness between 0.2 and 0.5 mm ID channels is only 0.722 % (based on Han and Shikazono (2009) model, from **Figure 5.7**) at 0.0224 < Ca < 0.299. In the liquid-liquid systems, however, the average difference could be 13.66 % under the same conditions. Based on the current results an improved correlation based on the Mac Giolla Eain et al. (2013) model is suggested (Eq. (5.2.1)) that is valid for an extended range of Ca between 0.0224 and 0.299, with deviations 0.27 % - 11.26 % from the experimental data.

$$\frac{\delta}{R} = 0.385\mathrm{Ca}^{0.265}\mathrm{We}^{0.098} \qquad (5.2.1)$$

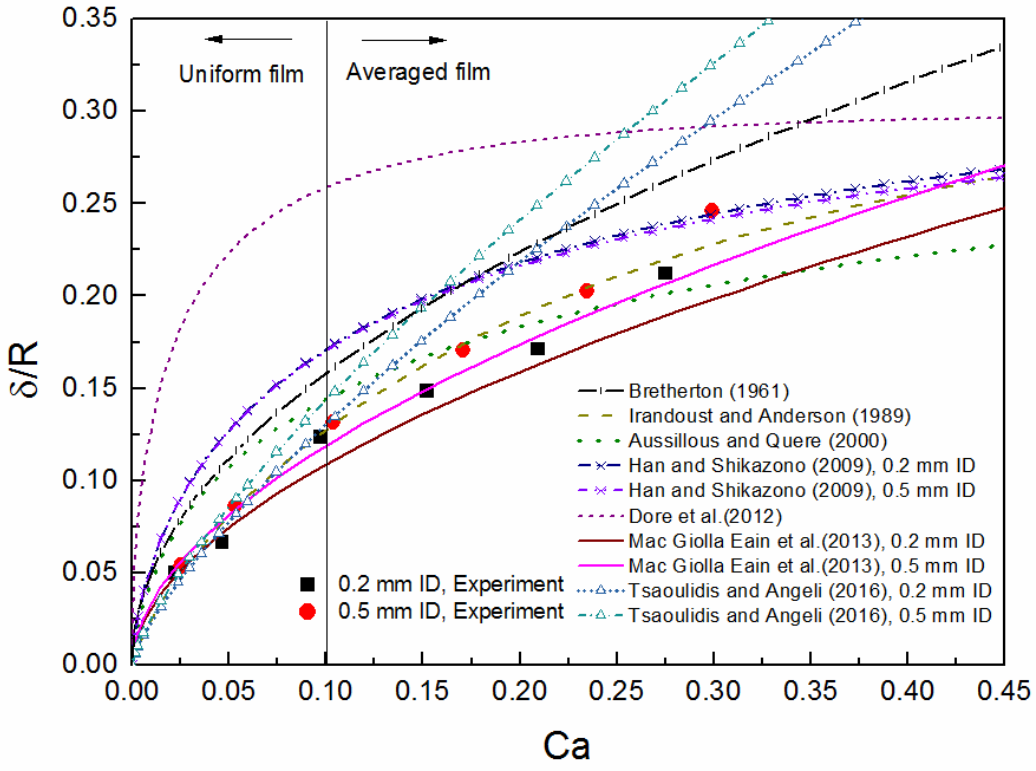

Figure 5.7: Non-dimensional film thickness against Capillary number for experimental data and literature correlations.

5.2.4 Plug velocity

The plug velocity is shown in **Figure 5.8** for both the 0.2 mm and 0.5 mm ID channels for equal phase flow rate $Q_{aq} = Q_{IL} = 0.653$ - 42.41 ml/hr. The plug velocity is always higher than the mixture velocity, because of the film which surrounds the plugs. With increasing mixture velocity, the normalized film thickness (δ/R) in both channels increases, leading to a larger deviation between U_{mix} and U_p. It can also be seen that the plug velocity in the 0.5mm ID channel is higher than in the 0.2mm channel by 5.42 – 14.48 % for the same mixture velocity ($0.005 < U_{mix} < 0.03$ m/s), which is expected since the film thickness is also larger in the 0.5 mm channel. The experimental results are compared with literature correlations from gas-liquid and liquid-liquid systems, as summarized in Table 2.2. Since the plug velocity is related to film thickness, the correlations in their majority include the Capillary number or the film thickness.

Correlations from Table 2.2 were used to compare the experimental results. The correlation by Bretherton (1961) overpredicted the experimental results with average deviation of 36.91% due to the inappropriate applicability of the model ($Ca < 0.003$). Liu et al. (2005) model showed good agreement with present work, with average deviations of 6.91% and 12.76% for 0.2 and 0.5 mm channel. However, their correlation only includes the effect of Capillary number but not the channel size. The correlation by Kashid et al. (2005) developed from experimental data on liquid-liquid plug flow, includes the film thickness rather than the Ca and agrees very well with the current data with an average deviation of 5.85 %. A similar expression was proposed by Langewisch and Buongiorno (2015) for gas-liquid Taylor flow, which however overpredicts the experimental data by 9.94 – 68.21 %. The difference can be attributed to their inaccurate prediction in film thickness for gas-liquid flow.

The velocity profiles inside the aqueous phase plugs were obtained with PIV as discussed in Section 2. An example of average profiles, obtained from 30 instantaneous velocity fields, is shown in **Figure 5.9 (a)** for $Q_{aq} = Q_{IL} = 7.068$ ml/h ($L_p = 1.155$ mm) in the 0.5mm ID channel. Since the refractive index of the two phases is not matched there are reflections close to the interface particularly at the plug front and rear where the interface curvature is higher and velocity fields cannot be obtained in these areas. Compared to the fluorescence PIV flow field, the bright field velocity distribution obtained is not fully symmetric(Silva et al. 2008, Dore et al. 2012), mainly due to the relatively high measurement uncertainty as outlined in Section 2.

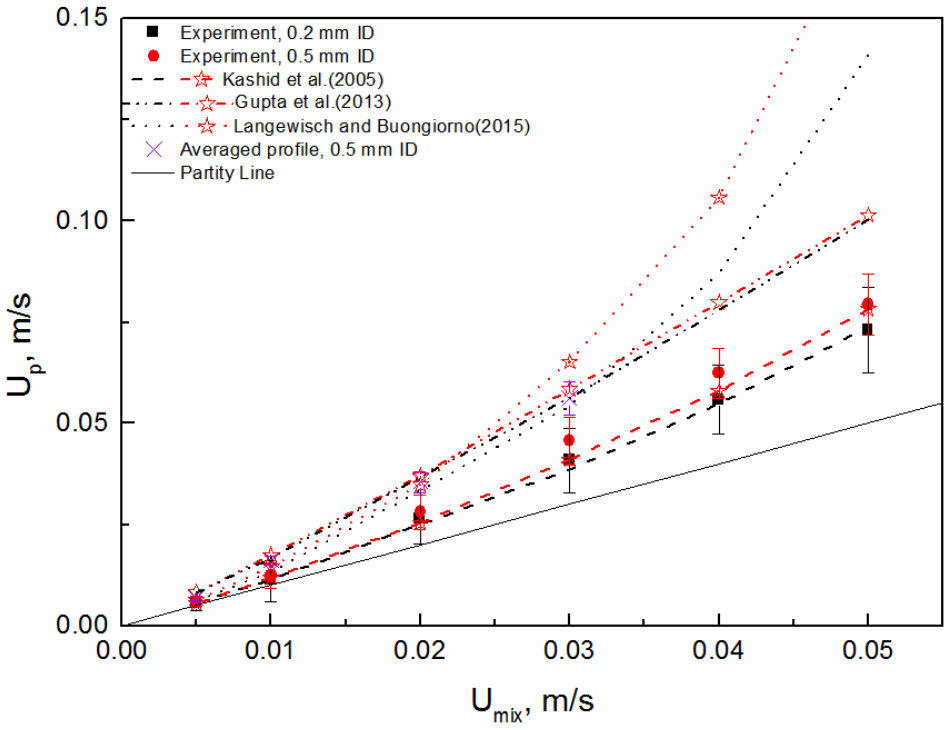

Figure 5.8: Variation of plug velocities with mixture velocities for different capillary diameters. Black and red symbol represents 0.2 and 0.5 mm ID channel respectively.

The profiles of the horizontal velocity component, non-dimensionalised with the maximum velocity, are shown in **Figure 5.9 (b)** for of 13 vertical planes along the plug. The spacing between the profiles is approximately 121.25 μm. All profiles have a parabolic shape with the peak located near the centreline of the channel (r / R = -0.041). The maximum velocity is found at the plug vertical centre (X/Lp = 0.522). Moving towards the liquid/liquid interfaces at the plug front and back, the velocity reduces and the profiles become more flat. The average plug velocity can also be calculated by spatial averaging these time-ensemble profiles (Meinhart et al. 2000, Chinaud et al. 2015), as depicted in **Figure 5.9**. As can be seen they are higher than those calculated from plug displacement by 4.47 – 10.99 %, which is expected because the profiles close to the front and rear of the plug where velocities are low, where not measured. The plug velocity based on the tip displacement method will be used subsequently.

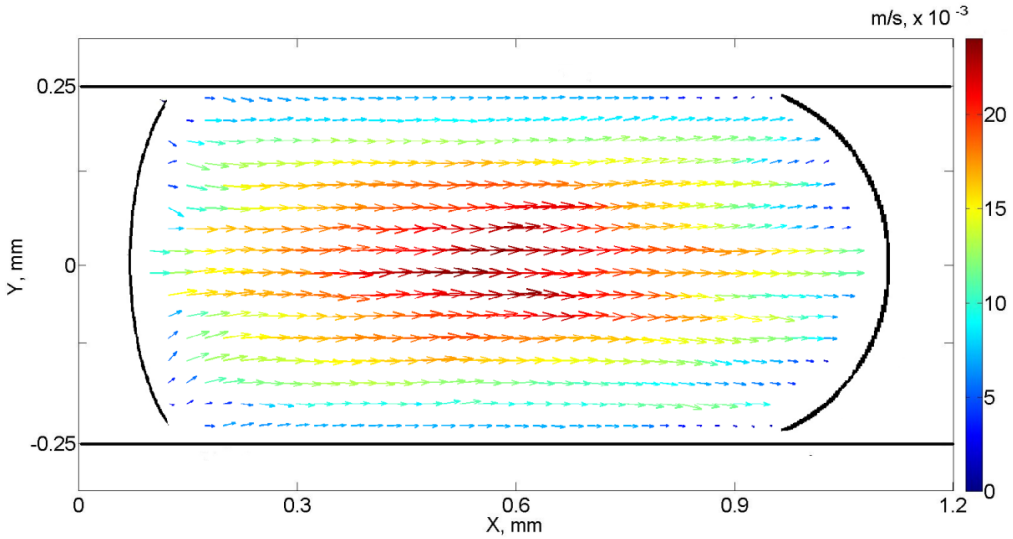

(a)

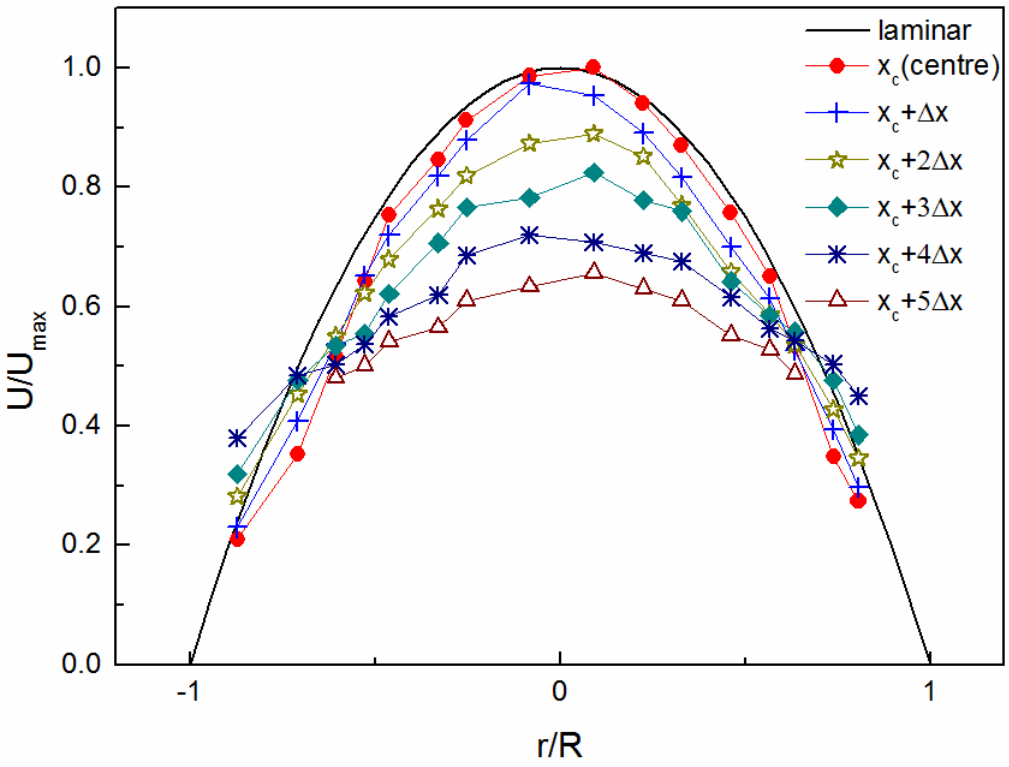

(b)

Figure 5.9: (a) Ensemble average velocity field inside the plug at Qaq = QIL = 7.068 ml/h in the 0.5mm ID channel. The magnitude of the velocity is shown in colour (Lp=1.155 mm); (b) Non-dimensional horizontal component of total velocity at different locations along a plug, for $Q_{aq} = Q_{IL}$ = 7.068 ml/h in the 0.5mm ID channel. The spacing between each profile is approximately 104.25 µm.

5.2.5 Plug length

The dimensionless plug lengths in both channels where found to be $1.14 < L_p/D < 2.48$ and fall into the transition regime ($1 < L_p/D < 2.5$ for circular T-junction microchannels) where the shear stresses, the surface tension and the pressure difference are all affecting the forming plug (Christopher et al. 2008, Xu et al. 2008, Fu et al. 2010, Fu et al. 2012). In this regime, both the Capillary number and the phase flow rate ratio should be considered. The dimensionless plug length is plotted in **Figure 5.10** against both Ca (based on plug velocity) and Q_{aq}/Q_{IL} for the 0.2mm and 0.5mm ID channels, as well as against the mixture velocity in the inset graph. As can be seen, L_p/D decreases with increasing U_{mix} at equal phase flow rates, while it is larger in the 0.2mm channel compared to the 0.5 mm ID one by 6.40 – 23.68 % under the same U_{mix}. The dimensionless length in both channels can be scaled with Ca as $L_p/D \sim Ca^{-0.273}$, and with the flowrate ratio as $L_p/D \sim (Q_{aq}/Q_{IL})^{0.512}$. Since both Ca and flow rate ratio affect the plug length in the transition regime a correlation is proposed (Eq. (5.2.2)) based on the correlation developed by Xu et al. (2008), which agrees well with the experimental data, with an average deviation of 13.13 %:

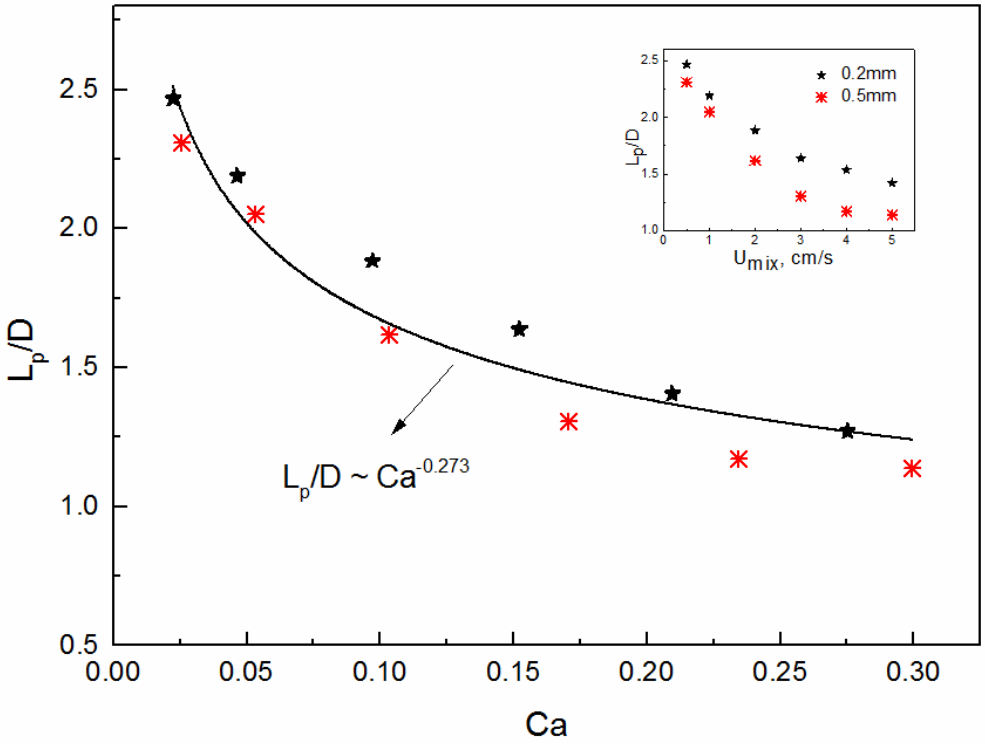

(a)

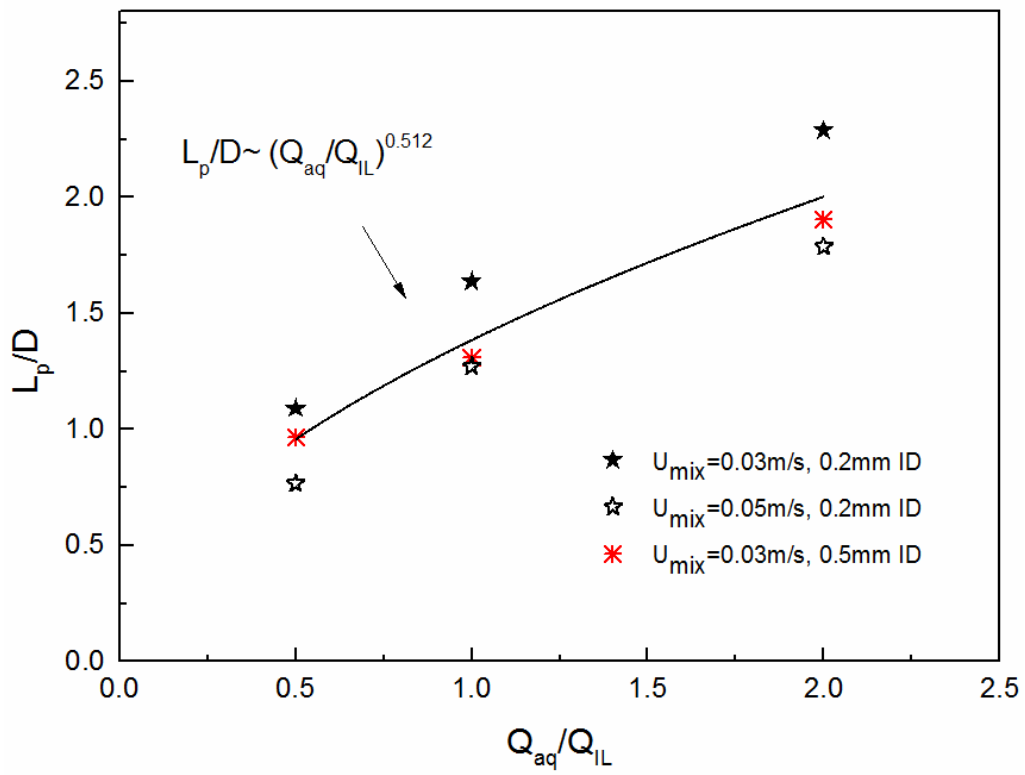

(b)

Figure 5.10: Dimensionless plug length Lp/D against (a) Capillary number Ca for equal phase flow rates, and (b) flow rate ratio Q_{aq}/Q_{IL}, in the 0.2mm and 0.5mm ID channels. Inset in (a) shows the dependence of L_p/D on U_{mix} for equal phase flow rates.

$$\frac{L_p}{D} = 0.757\left(Q_{aq}/Q_{IL}\right)^{0.512} Ca^{-0.273} \quad (5.2.2)$$

The calculated results from Eq. (5.2.2) provide slightly better fit for 0.5 mm (deviation of 6.03%) than 0.2 mm channel (deviation of 8.81%), as the small channel is more sensitive to pressure changes during plug formation caused by discontinuous pump pushing or plug exiting. Several correlations have been developed to estimate the plug length in two-phase plug flow, either empirically or from physical models on the plug formation mechanism. Representative correlations are summarized in Table 2.3 and compared with the experimental results in **Figure 5.11**. Laborie et al. (1999) developed an empirical correlation from gas-liquid flow studies in 1-4 mm vertical circular channels at relatively high velocities (0.1-1 m/s). The gas bubble length was found to increase with increasing superficial velocities, contrary to the current observations. Qian and Lawal (2006) from numerical simulations of gas-liquid flow in a T-

junction microchannel, proposed a correlation for different inlet geometries, superficial velocities and fluid properties, and found that the dimensionless length depends mainly on Re, Ca and gas hold up ε_G. Similar models were also proposed by Sobieszuk et al. (2010) and Tsaoulidis and Angeli (2016), which however over predict the results by 94.04 – 157.16% and 22.45 – 81.26% respectively.

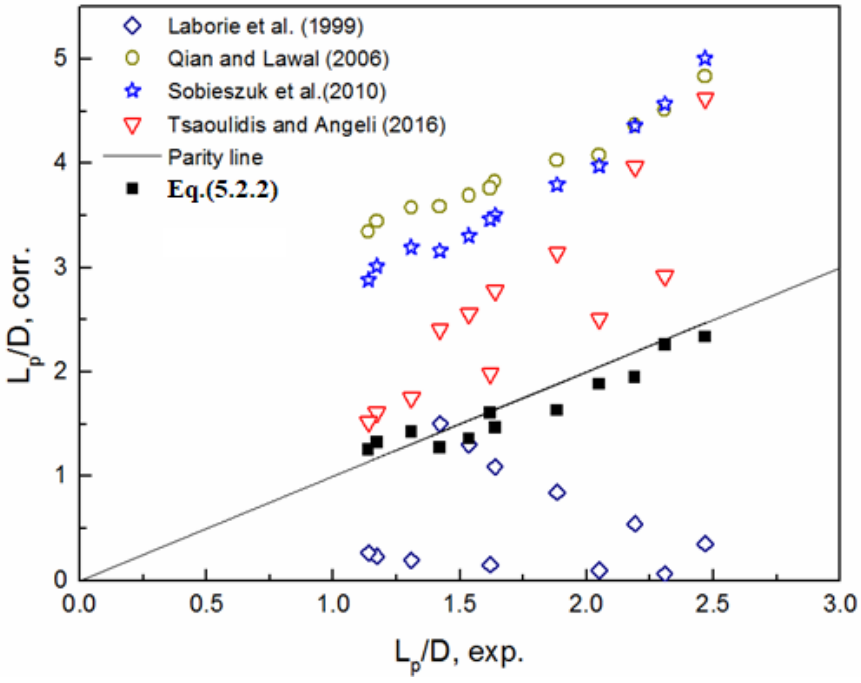

Figure 5. 11: Comparison of the experimental results of plug length and from empirical correlation listed in Table 2.3 in 0.2mm and 0.5mm ID microchannel.

5.2.6 Plug shape

5.2.6.1. Plug volume

The versatility of microfluidic system lies essentially in the ability to reliable transport and precisely control of the fluid volumes of each individual droplet. In this work, the volume of individual axisymmetric plug can be accurately calculated by 3D rotating the detected interface along the channel centerline. As shown in **Figure 5.12**, the droplet volume was varied by changing the flow rate of the two phases by the homogeneous volume fraction in 0.2mm and 0.5mm ID circular channel. At high mixture velocities, the relative long camera exposure time (although 8000Hz image recording frequency is used) slightly blurs the fast-moving aqueous

plug, which brings difficulty in precious locating the interface, leading to the maximum relative error in calculating the volume up to 10.49%.

The channel dimension has large influence on droplet volume under the same mixture velocity. With nearly doubled channel diameter (from 0.2mm to 0.5mm), the volume of individual droplet could increase by 13-17 times. For a certain channel, the isolated plug volume decreases with the growth of mixture velocity, due to the reductive plug length. The non-dimensional equivalent diameter d*, defined as the ratio of diameter of a spherical droplet having same volume as that of a Taylor droplet to channel diameter, shows a decreasing trend with increasing U_{mix}, but barely affected by the channel dimension. At very low Capillary numbers ($0.004 < Ca < 0.009$), the bubble/droplet reaches volume-independent shapes when $d^*>1.1$(Lac and Sherwood 2009, Gupta et al. 2013), where only the droplet length changes but the leading and trailing menisci is unaffected by the droplet volume. However, at high Capillary numbers like the current study ($0.0211 < Ca < 0.261$), both the front and tail meniscuses change in both channels.

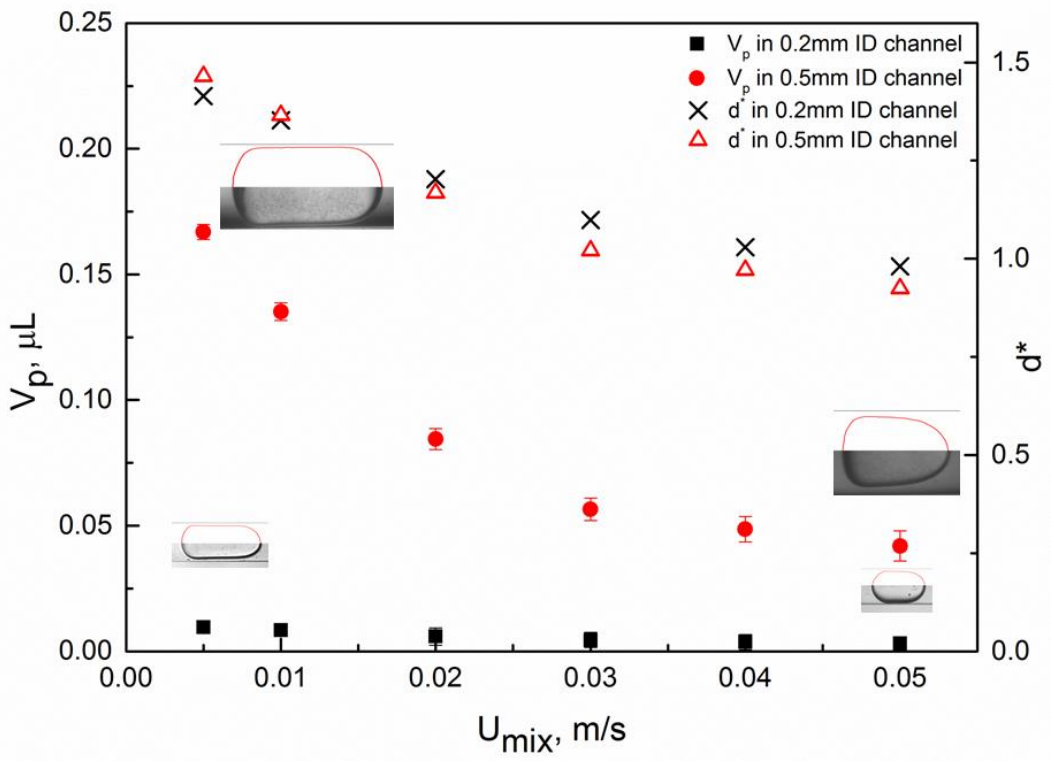

Figure 5.12: Variation of plug volume with mixture velocities for different capillary diameters.

5.2.6.2 Specific interfacial area

The rate of mass transfer between two phases depends on the interfacial area available. For the calculation of the interfacial area in plug flow it is assumed that the dispersed plugs have a cylindrical body and hemispherical caps at the front and back. When a continuous film is a present at the channel wall the interfacial area can be calculated as follows with an error of less than 10%(Raimondi et al. 2014):

$$\alpha_p = \frac{4W_p(L_P - w_p) + \pi W_p^2}{L_{UC} ID^2} \tag{5.2.3}$$

where L_{uc} is the unit cell length (one slug and one plug), and W_p and L_p represent the plug width and length, respectively. The plug geometric parameters for each set of flow rates were obtained by averaging results from 30 plugs, with deviations between 4.25-7.10% for film thickness, and 5.33-9.52 % for plug and unit cell length.

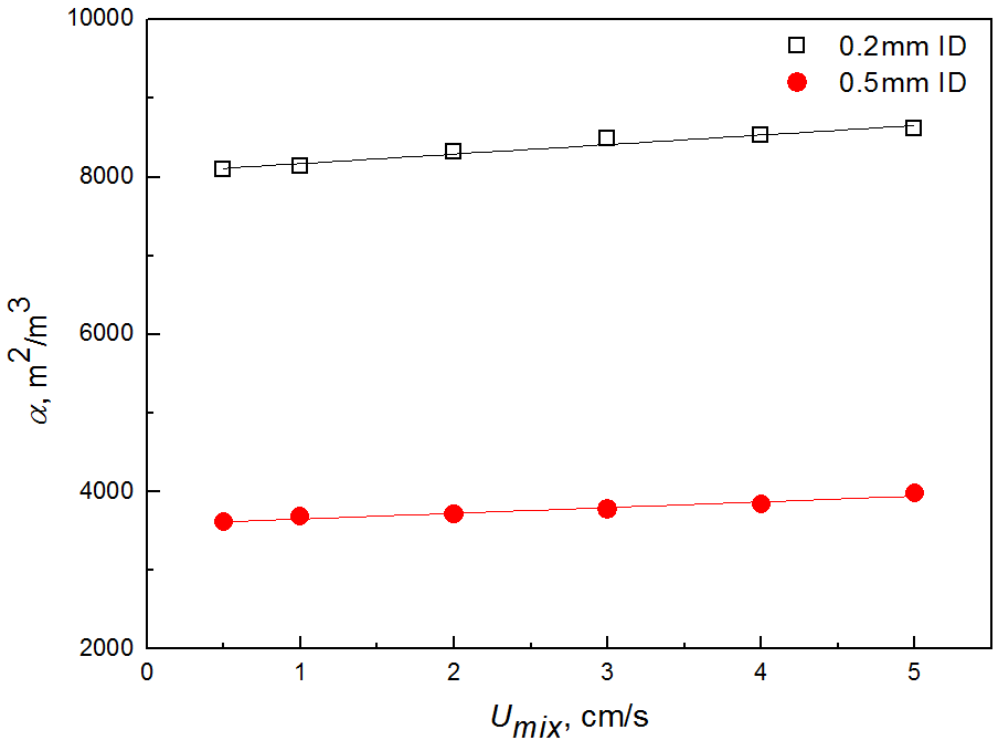

Figure 5.13: Specific interfacial area against mixture velocity for different capillary diameters. Aqueous phase: 1M nitric acid; organic phase: 0.2M CMPO-1.2M TBP/[C4mim][NTf2].

The effect of mixture velocity on interfacial area can be seen in **Figure 5.13** for equal flow rates of the two phases from $Q_{aq}=Q_{IL}=3.534$ to 21.21 ml/h. The interfacial area was found to increase slightly with increasing U_{mix}. As the mixture velocity increases the plug formation frequency increases while shorter plugs form, which results in larger interfacial area values. However, the capillary diameter has a more profound effect; the interfacial area in the large channel is almost 3 times smaller than in the small one for the same mixture velocity. It has been suggested that the organic film can be ignored during mass transfer at low mixture velocities (Ghaini et al. 2010). However, when ionic liquid is the continuous phase the film (δ_{film}/R = 0.1585-0.3022, where δ_{film} and R are film thickness and channel radius, respectively) is thicker than with conventional organic solvents (δ_{film}/R = 0.0928-0.1295) and may affect mass transfer.

5.2.6.3 Dimensionless radius

The shape of the plugs was also investigated and the radius of the front and tail plug ends is presented in **Figure 5.14.** At the lowest Ca (U_{mix} = 0.005 m/s), both plug ends resemble a hemisphere with dimensionless radius close to unity: $r_{tail}^{*}=r_{tail}/r^{*}\approx1$, with a smaller front menisci curvature $r_{front}^{*}=r_{front}/r^{*}=0.76$. As the Capillary number increases the curvature of the front plug cap increases (radius decreases) while the rear cap becomes more flat and its curvature decreases (radius increases). The channel size does not affect the plug shape significantly and there is only a difference of 1.87- 6.11% between the two channels. It affects, however, more the front cap shape with a difference of 10.57-37.38% between the two channels for the same mixture velocities. Therefore the variations in the thickness of the liquid film surrounding the plug are mainly affected by changes in the front cap.

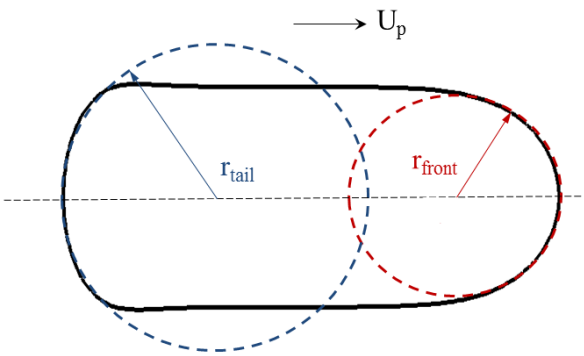

(a)

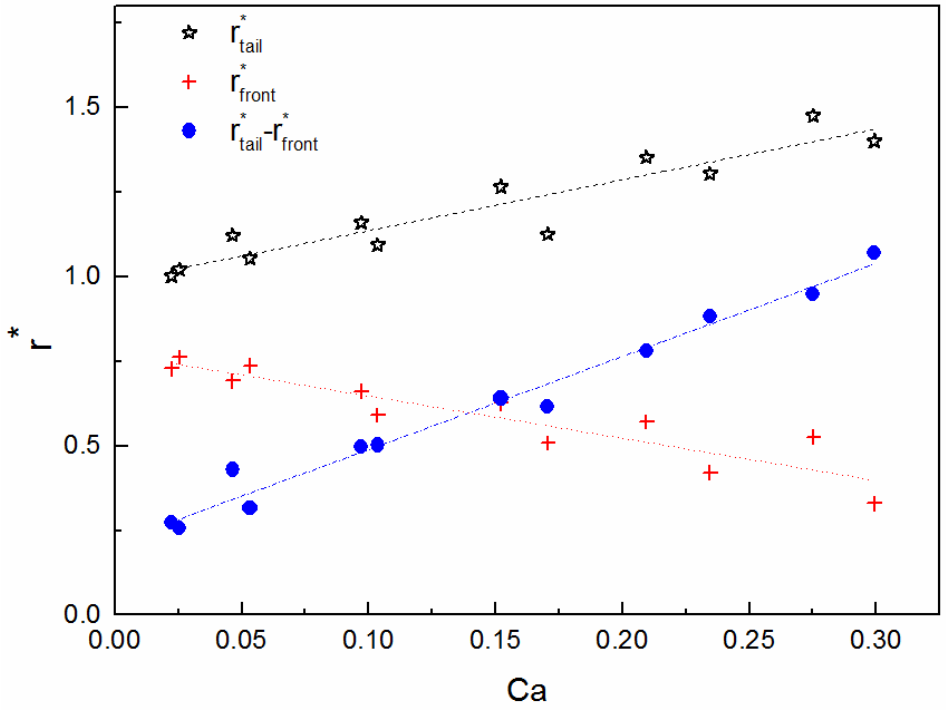

(b)

Figure 5.14: (a) Schematic of an isolated aqueous droplet at $Q_{aq} = Q_{IL}$ = 7.068 ml/h in 0.5mm ID channel; (b) Dimensionless radius of the fitted sphere to the leading and trailing menisci of the droplet against Capillary number in 0.2mm and 0.5mm ID channel.

5.2.7 Velocity profiles

The velocity profiles in the plug obtained from the CFD simulations and the PIV measurements are shown in **Figure 5.15 (a)** and compared with the laminar profile for U_{mix} = 0.01 m/s in the 0.5mm ID channel (Q_{aq} = Q_{IL}=14.14ml/h ,Lp/D = 2.28).The profiles have been non-dimensionalised using the averaged maximum velocity (at the centre of the plug). The numerical U_{max} inside the aqueous plug was obtained by looping and comparing the velocity in the dispersed domain using UDF (User-Defined Function). The measurements were taken at 1.14D from the plug front, which is almost free from the droplet rear and front influence. The results are also compared against the profile given by in Eqs. (5.2.4-5.2.6) (Lac and Sherwood 2009, Jovanović et al. 2011, Gupta et al. 2013)

Plug: $0 < r < R_p$

$$U_{x,p} = 2U_{mix}\frac{\left[\left(1-\frac{R_p^2}{R^2}\right)+\frac{1}{\lambda}\left(\frac{R_p^2}{R^2}-\frac{r^2}{R^2}\right)\right]}{\left(1+\frac{R_p^4}{R^4}\right)\left(\frac{1}{\lambda}-1\right)} \quad (5.2.4)$$

Film: $R_p < r < R$

$$U_f = 2U_{mix}\frac{\left(1-\frac{R_p^2}{R^2}\right)}{\left(1+\frac{R_p^4}{R^4}\right)\left(\frac{1}{\lambda}-1\right)} \quad (5.2.5)$$

$$U_{x,f} = 2U_f\frac{1-\frac{r^2}{R^2}}{1-\frac{R_p^2}{R^2}} \quad (5.2.6)$$

where $U_{x,p}$ and $U_{x,f}$ is the velocity distribution in the aqueous plug and ionic film respectively, U_f is the average film velocity, λ is the ratio of the plug viscosity to that of the continuous phase, and $R_p = R - \delta$ is the plug radius in the middle. To develop the above model it was assumed that a uniform film thickness exists around the plug and the flow in the plug region resembles annular flow with equal pressure drop in both phases. A similar model for the film velocity profile was proposed by Fouilland et al. (2010), from time resolved PIV investigations in gas-liquid flows:

$$U_{x,f} = U_{mix}\frac{1-\frac{R_p^2}{R^2}}{1+\frac{R_p^4}{R^4}\left(\frac{1}{\lambda}-1\right)} \quad (5.2.7)$$

As can be seen from **Figure 5.15 (b)** there is good agreement between the CFD simulations and the experimental average velocity profiles in the plug (average deviation 20.94 %), particularly in the center of the channel. Close to the channel wall there is larger uncertainty in the velocity measurements due to the reflections. The differences from the single phase laminar profile ($U = U_{max}(1 - r^2/R^2)$) are attributed to the insufficient developed laminar profile inside the short plug in the channel center. The velocity profile in the film is shown in **Figure 5.16**, where the CFD predictions are compared against Eqs. (5.2.6) and (5.2.7). The results indicate a Couette local velocity profile. The maximum velocity within the liquid film occurs at the plug surface, while the maximum film velocity ($U_{f,\,max}$) is much smaller than the U_{max} within the plug. The profile predicted by Eq. (5.2.7) (Fouilland et al. 2010) agrees better with the CFD results with a difference up to 19.78%. The CFD model slightly underpredicts the film thickness by 3.37% compared to experimental value.

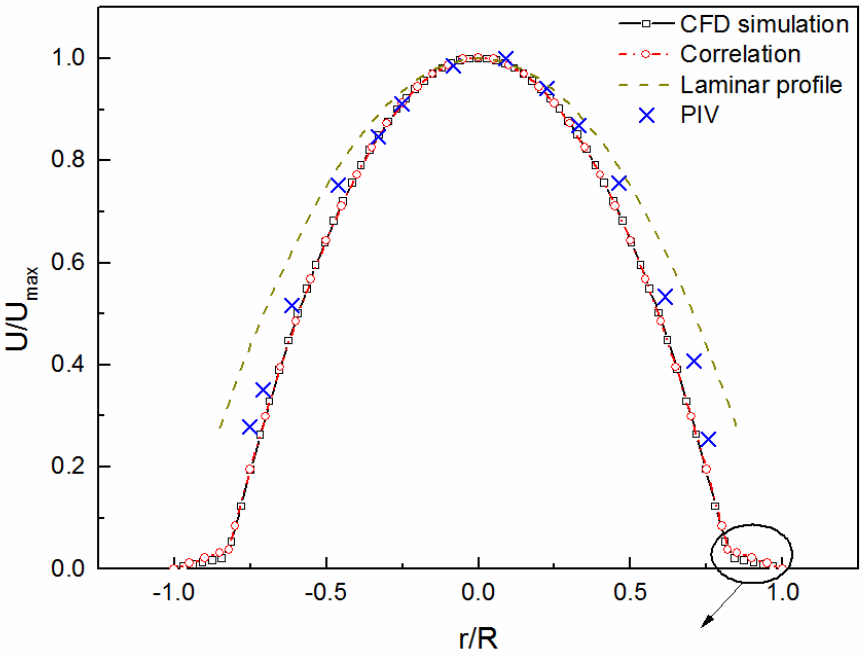

(a)

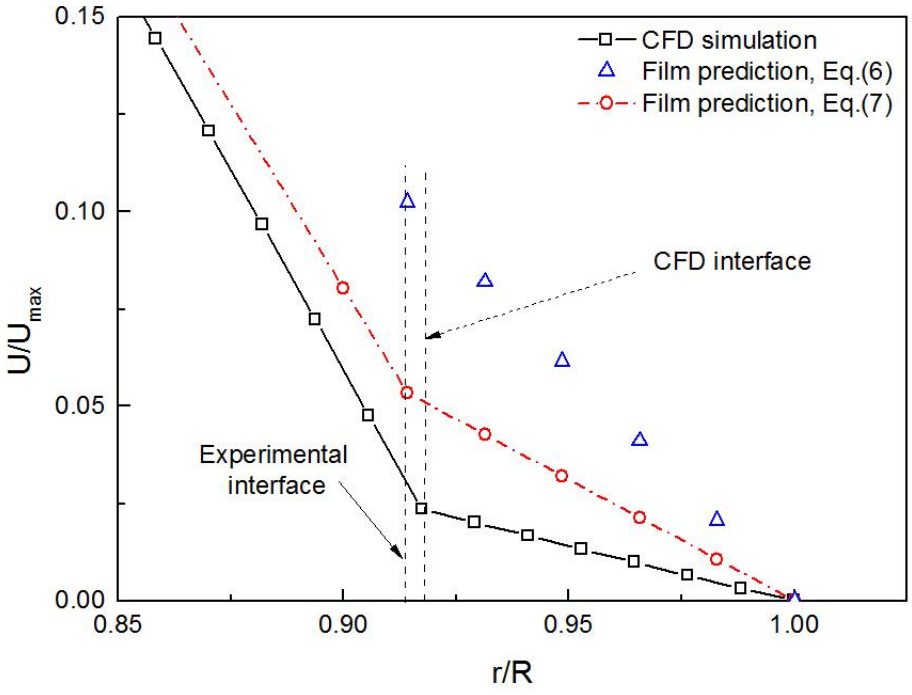

(b)

Figure 5.15: (a) Comparison of the velocity profiles from the CFD simulations and the PIV measurements for $Q_{aq} = Q_{IL} = 7.068$ ml/hr in the 0.5mm ID channel at a distance of 2.05 R from the plug front tip. Also shown are the laminar profile and the one predicted by Eq. (5.2.4). (b) Velocity profiles predicted from Eqs. (5.2.6) and (5.2.7) and the CFD simulations.

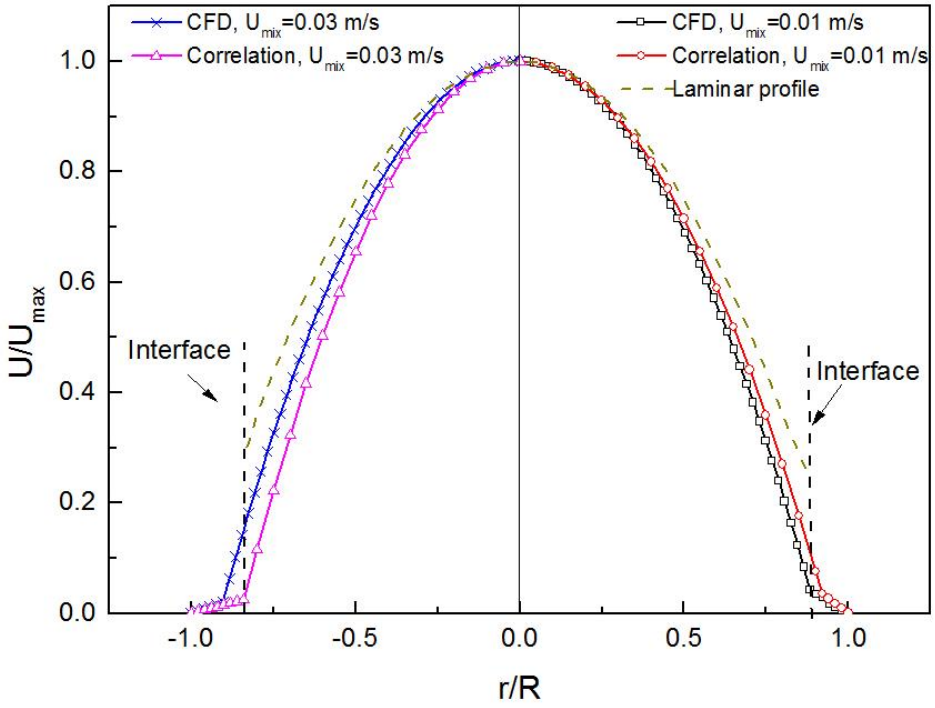

Figure 5.16: Comparison of the velocity profiles in the centre of the plug obtained from the CFD simulations with those predicted by Eq. (5.2.7) for $Q_{aq} = Q_{IL} = 7.068$ ml/hr (right) and $Q_{aq} = Q_{IL} = 21.21$ ml/hr (left) in the 0.2mm ID channel. The laminar flow profile is also shown.

The velocity profiles in both the plug and the film at the middle of the plug location for two different mixture velocities, 0.01 m/s and 0.03 m/s in the 0.2mm ID channel are shown in Figure 5.17. The higher U_{mix} results in reduced plug width and increased deviation from the laminar profile, as well as increased film velocity due to less developed profile inside the short plug. For $U_{mix} = 0.01$ m/s, the ratio of maximum velocity in the plug and the film ($U_{max} / U_{f,max}$) is 73.74, but decreases to 13.05 for $U_{mix} = 0.03$ m/s. Overall, using the velocity profile correlations by Gupta et al. (2013), Eq. (5.2.4), for the central region of the plug and by Fouilland et al. (2010), Eq. (5.2.7), for the film, the flow field can be accurately described for axial locations at the middle of the plugs.

The circulation patterns in the plugs can be found by subtracting the plug velocity from the average velocity profiles. The patterns from both the PIV measurements and the CFD simulations are shown in **Figure 5.18** for $U_{mix} = 0.01$ m/s in 0.5 mm channel ($Q_{aq} = Q_{IL} = 14.14$

ml/h). The results are in good agreement and show two main vortices on the upper and the lower part of the channel. The vortex centers are located in both cases at around $r^0/R=0.747$ (r^0 is the distance of the stagnation point from channel centre) , which agrees with the value of 0.765 given by Thulasidas et al. (1997). Two smaller counter-clockwise vortices, at the front and rear cap of the plug, are predicted by the simulation but cannot be detected in the PIV measurements as the velocity field is not well resolved in these areas. The existence of these vortices is believed to be caused by the change of tangential shear force (Kurup and Basu 2011). The very small vortices at the front of the primary ones near the channel axis, are considered to be spurious results generated numerically (Abadie et al. 2015).

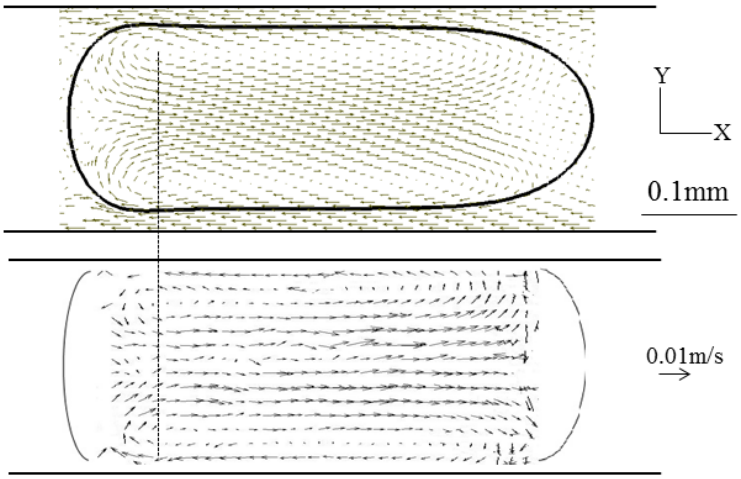

(a)

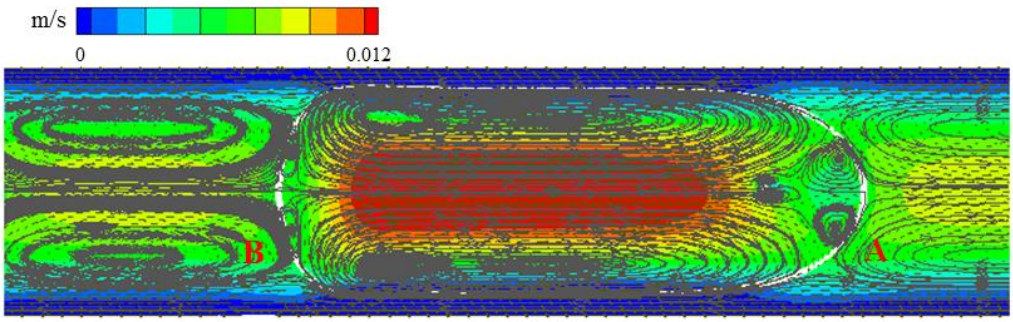

(b)

Figure 5.17: (a) Comparison of velocity distribution and internal recirculation in a plug at Umix = 0.01 m/s in the 0.5 mm ID channel for $Q_{aq} = Q_{IL}$ = 7.068 ml/hr from CFD simulations (top) and PIV measurements (bottom). (b) Numerical recirculation patterns in both phases for the same operation conditions. The velocity magnitude is superimposed in colour.

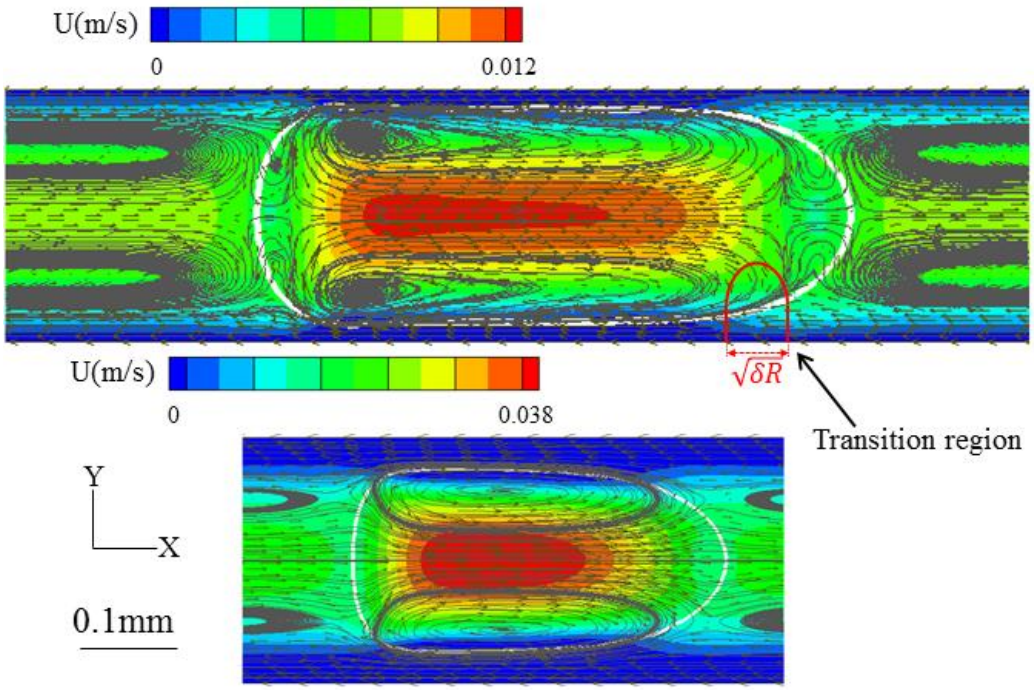

Figure 5.18: CFD velocity distribution and internal recirculation at Umix = 0.01 m/s (top) and Umix = 0.03 m/s (below) in 0.2 mm channel. The velocity magnitude is superimposed in colorful scale.

The circulation patterns are influenced not only by the flow velocity, but also the channel size. A comparison between the two channels is given in **Figure 5.19** for U_{mix} = 0.01 m/s an U_{mix} = 0.03 m/s in the 0.2 mm channel. With increasing U_{mix}, the cores of the main vortices move towards the centre of the plug, suppressing the secondary vortices at the front until they completely disappear. For all the studied cases, a rapid curvature change transition region (shown in Fig. 16) exists as the plug can be treated as a low viscosity drop for segmented flow with $\lambda \ll 1$ and $\lambda \ll (\delta/R)^{-1/2}$ ($\lambda = \mu_{aq}/\mu_{IL}$) (Bretherton 1961, Hodges et al. 2004). Within this region, the surface tension induces a pressure gradient that drives continuous ionic liquid flow from slug to thin film region, and a single 'Bretherton' stagnation point lies on the drop interface. The lengthscale of the transition region, $\sqrt{\delta R}$, is relatively small compared to the channel radius, and becomes larger at high U_{mix}, from 0.052 mm at U_{mix} = 0.01 m/s to 0.092 mm at U_{mix} = 0.05 m/s.

A comparison of the velocity distribution on difference channel cross sections along the plug is given in **Figure 5.19** for U_{mix} = 0.03 m/s in the 0.2mm channel. The total velocity magnitude is significantly larger in the plug center (plane b) compared to the ends (planes a/c). Therefore within the primary recirculation section, the horizontal component of velocity is dominant as the fluid in the aqueous plug mainly moves along the channel axis. At the plug two ends, the radial velocity component (U_r) is increased. This increased radial velocity can significantly enhance mass transfer between the two phase via the interface at the plug ends and explains why 99% of mass transfer has been found to happen in the cap regions of the plug compared to the film region (Li and Angeli 2016).

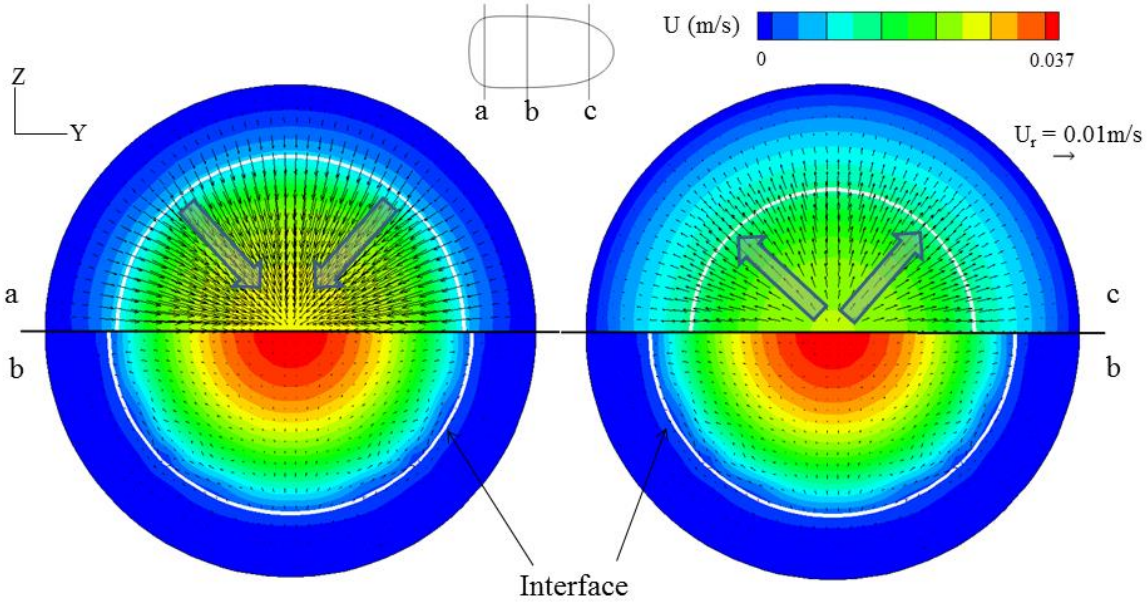

Figure 5.19: Velocity distribution on different cross sections along the dispersed plug; Plane b is the recirculation center; plane a and c is where the recirculation starts and ends, respectively. The velocity magnitude is superimposed in colorful scale. The radius velocity is represented by vectors.

5.2.8 Pressure variation

The pressure in the channel was also calculated in the CFD simulations and an example of the profile along the 0.2mm ID channel is shown in **Figure 5.20** for U_{mix} = 0.03 m/s. The capillary contains a succession of dispersed plugs and slugs of the continuous fluid, separated by transition regions around the interface. The pressure gradient in the fully-developed continuous

slug can be described by the Hagen-Poiseuille law, while each plug has an additional component due to Laplace pressure at the interfaces.

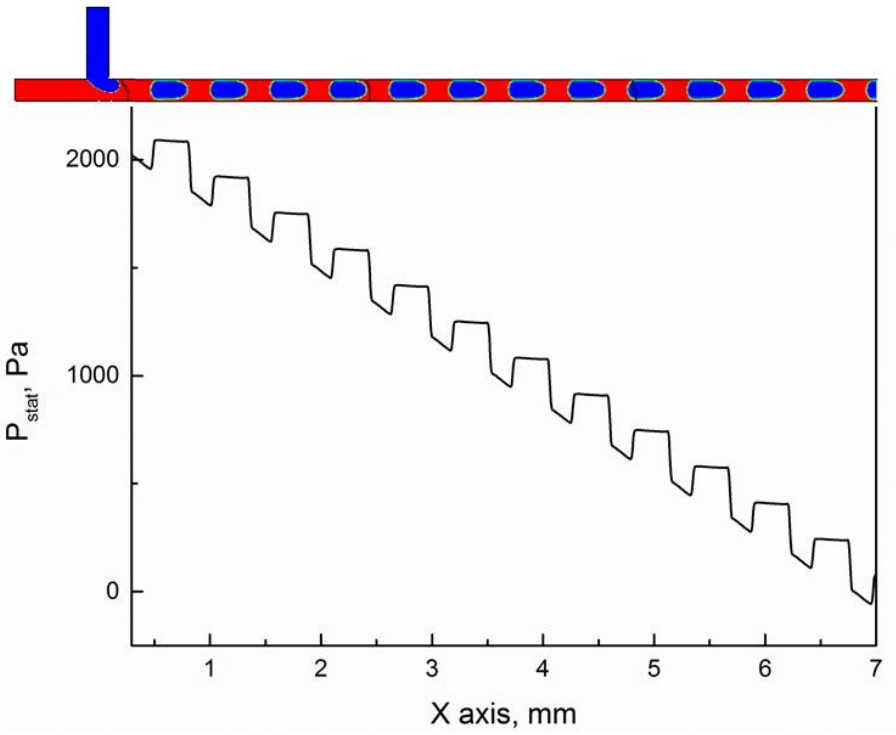

Figure 5.20: CFD simulation of behaviour static pressure along the length of the channel a fully developed Taylor flow system, U_{mix} = 0.03 m/s, ID = 0.2 mm.

The detailed wall pressure distribution along a plug calculated from CFD is shown in **Figure 5.21** for three different cases. The tails of the plugs have been brought to the same axial location, while the minimum pressure of all cases has been shifted to 0 to facilitate the comparisons. The dotted line represents the projected pressure based on a linear regression of the pressure variation before and after the plug in the continuous phase slug. A typical wall pressure variation for a sufficiently long plug is given by the U_{mix} = 0.01 m/s in the 0.5 mm ID channel case. Within the continuous phase slug, the pressure decreases linearly because of friction. When the interface at the plug rear is reached, the pressure first decreases, due to the presence of an inundation on the liquid-liquid interface, and then increases sharply because of the Laplace pressure. In the film region the pressure decreases smoothly (as the liquid in the film is nearly stagnant) until the front of the plug is reached, where it reduces significantly. In the continuous slug phase the pressure continues to reduce due to friction. Compared to the profiles in the 0.2 mm ID channel, the Laplace pressure (increase in pressure at the plug rear) is much

smaller at the same U_{mix}. In the small channel, however, no uniform pressure decrease is observed as the film does not have a uniform thickness around the plug especially at U_{mix}=0.03 m/s where the plug is short.

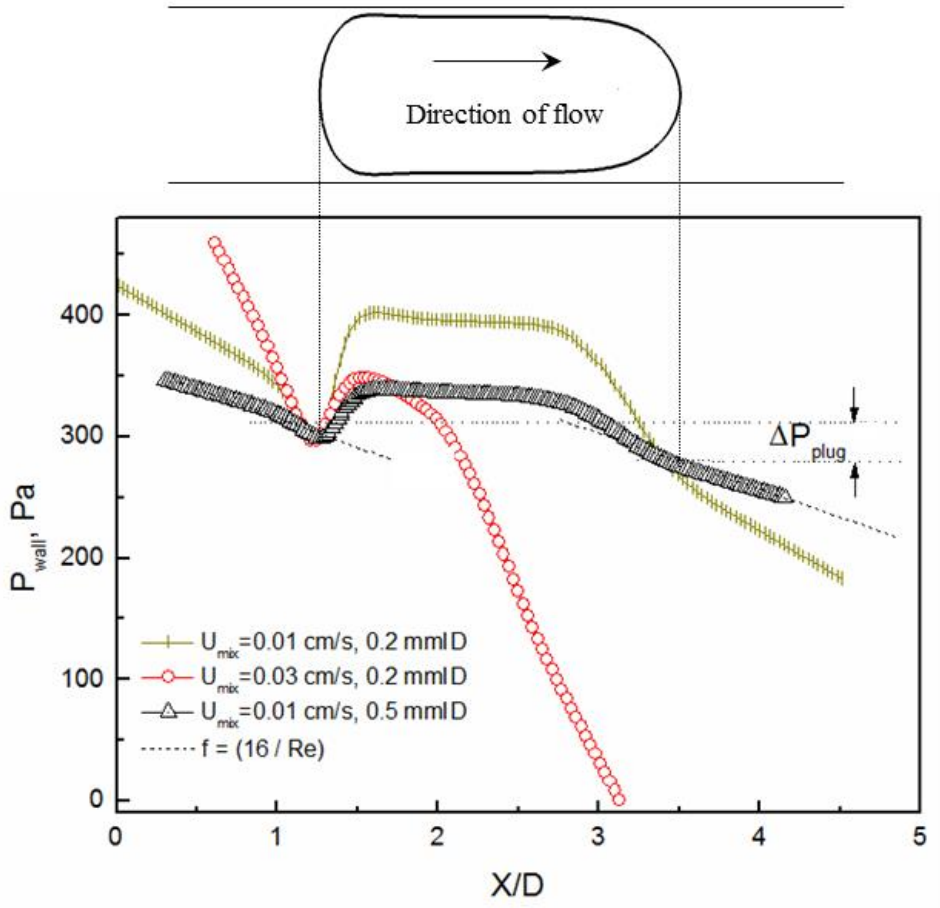

Figure 5.21: Wall pressure distribution along downstream direction of Taylor flow in 0.2 mm and 0.5 mm ID channel. The dotted line represents the projected pressure based on a linear regression ahead and behind the segmented plug.

The total pressure drop can be calculated as the sum of the single phase pressure drop and the additional Laplace pressure drop. By combining the Hagen-Poiseuille law, the friction factor for total pressure drop can be written as follows (Kreutzer et al. 2005, Walsh et al. 2009):

$$fRe = \underbrace{16}_{\text{Poiseuille flow}} + \underbrace{\frac{\alpha}{L^*}\left(\frac{Re}{Ca}\right)^{\beta}}_{\text{Interfacial}} \tag{5.2.8}$$

$$\frac{\Delta P}{L} = \varepsilon\left[f\left(\frac{1}{2}\rho U_{mix}^2\right)\frac{4}{D} + \rho g\right] \tag{5.2.9}$$

where f, is the Fanning friction factor, L^*=L/D is the dimensionless length and ε is the dispersed phase fraction. The friction factor calculated from numerical predictions of the pressure drop in both channels is plotted against $L^*(Ca/Re)^{0.33}$ in **Figure 5.22**. The inset in the figure illustrates the two limits of single phase pressure drop and of interfacial pressure as well as their sum over a wide range of conditions. Both asymptotes contribute significantly to the total pressure drop. The contribution of interfacial pressure drop to the total pressure drop can only be neglected for sufficient long plugs. The best fit to fRe data follows an order of -1 for $L^*(Ca/Re)^{0.33}$, with a deviation of ± 12.77%.

$$fRe = 16 + \frac{0.225}{L^*}\left(\frac{Re}{Ca}\right)^{0.33} \quad (5.2.10)$$

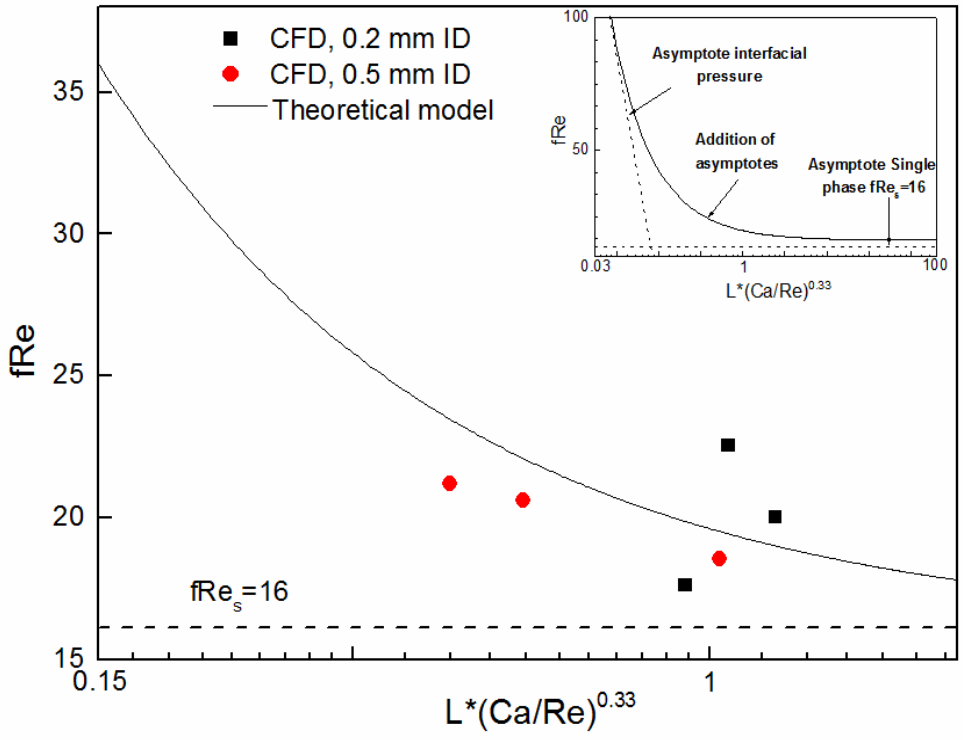

Figure 5.22: Non-dimensional friction factor in the 0.2 mm and 0.5 mm ID channels for $Q_{aq} = Q_{IL}$= 1.13-35.34 ml/hr. The inset shows the asymptotes for single phase and for interfacial pressure.

The pressure drop per unit length over a plug and slug unit from the CFD simulations is compared against Eq. (5.2.10) in both channels in **Figure 5.23**. The magnitude of the total pressure drop decreases significantly as the capillary size increases and the difference becomes more significant at the higher mixture velocities. With increasing mixture velocity, the

differences between the model and the simulations also increase with maximum deviation of about 13.68%. The differences mainly arise for two reasons: 1) The formation of Eq.(5.2.10) was developed at high Re condition (150 < Re < 1400 for gas-liquid flow (Kreutzer et al., 2005)), but Re in present work falls between 0.049 and 1.229; 2) The plug length used in the additive model, has larger deviation compared to CFD results for short droplets as outlined in Section 2.2, resulting in the relatively larger errors at high mixture velocities.

An alternative model in calculating the overall pressure drop for Taylor flow is to consider three factors (Jovanović et al. 2011, Gupta et al. 2013, Tsaoulidis and Angeli 2016): 1) Pressure drop in continuous ionic liquid that can be described by the Hagen-Poiseuille law; 2) Pressure drop in the cylindrical (or uniform film thickness) region of dispersed droplet. In the previous section we assumed uniform film thickness and equal pressure gradients in the core and film region for annular velocity prediction, therefore the moving film pressure drop model proposed by Fouilland et al. (2010) can still be used; 3) The interfacial pressure drop at the front and rear ends of the droplets, which are highly depends on the interface curvatures, can be calculated by Bretherton (1961) model for low viscosity droplets (given in Section 3.5). The overall pressure drop per unit length can therefore be given by Eq. (11):

$$\frac{\Delta P}{L} = \frac{8\mu_c U_{mix}}{R^2}\frac{L_s}{L} + \frac{8\mu_c U_p}{R^2\left(1+\frac{R_p{}^4}{R^4}\right)\left(\frac{1}{\lambda}-1\right)}\frac{L_{film}}{L} + \frac{C}{L}\frac{\gamma}{R}(3Ca)^{2/3} \qquad (5.2.11)$$

Where the constant C is employed to accurately describe the interface curvature(Jovanović et al. 2011) and Marangoni effects(Kreutzer et al. 2005). The plug velocity derived from the displacement method is used in the moving film model. As shown in **Figure 5.22**, it was found C = 1.03 gives smallest average deviation of 20.71% over the range of Ca numbers studied (0.0224 < Ca < 0.299), with higher accuracy in 0.5 mm channel. The nonuniform film thickness surrounding the short plugs and rapid curvature change at two ends are responsible for the deviations.

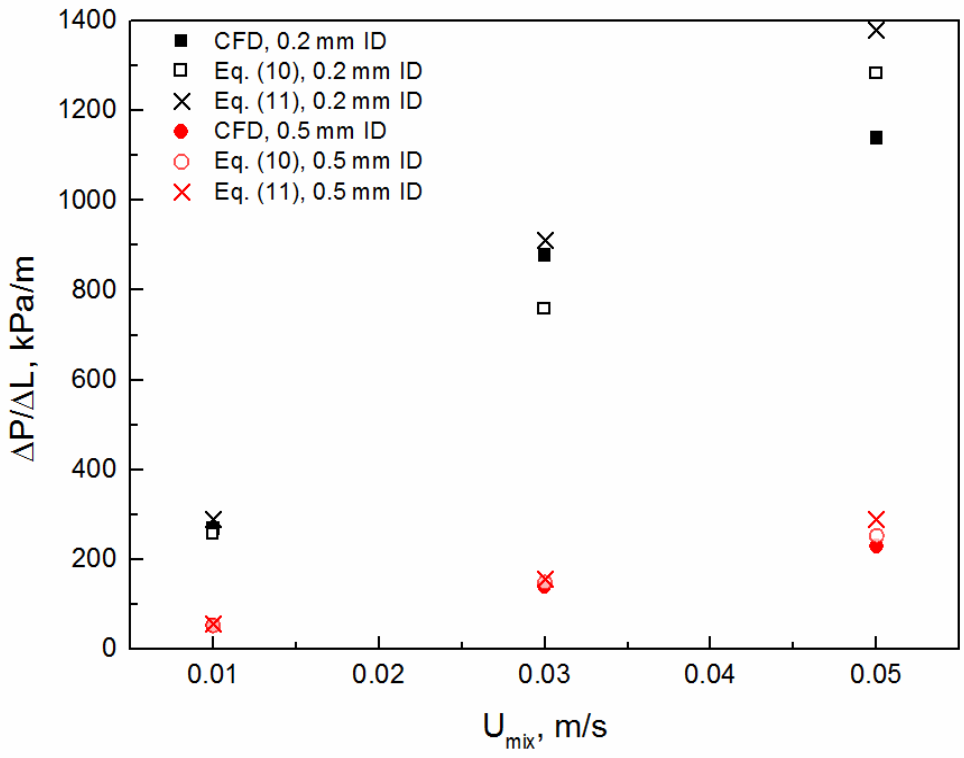

Figure 5.23: Pressure gradient over a unit cell of a plug and a slug from CFD simulations (filled symbols) and the models given by Eqs. (5.2.10) and (5.2.11) (open symbols) in the 0.2 mm and 0.5 mm ID channels for $Q_{aq} = Q_{IL}$ = 1.131 – 35.34 ml/hr.

5.3 Conclusions

A systematic study of the hydrodynamics of liquid-liquid Taylor flow in 0.2 and 0.5 mm ID channel has been carried out using bright field micro-PIV and CFD techniques, with 1M HNO_3 and a mixture of ionic liquid (0.2 M CMPO-1.2 M TBP/[C_4min][NTf_2]) as dispersed and continuous phase respectively for enhanced Europium (III) recovery. The dimensionless film thickness is slightly smaller in 0.2 mm channel under the same Ca, and an improved correlation on the Mac Giolla Eain et al. (2013) model is proposed for film thickness within the current operation range (0.0224< Ca <0.299). The plug velocities in both channels, calculated from displacement or velocity profile intersection method, are always higher than mixture velocity, due to the existence of the nearly stagnant film surrounding the plug. The plug length is influenced by a combination effect of Capillary number and flow rate ratio, which represents the balance of cross flow shear force and Laplace pressure at the plug formation stage.

Quantitative analysis in two-phase interface shows plug volume is highly dependent on channel size and mixture velocity.

Experimental data from bright field micro-PIV and numerical CFD results evidence a parabolic form of the horizontal velocity profiles inside the dispersed plug, and Couette-shape velocity profile in the continuous film. The recirculating flow pattern is influenced by several parameters such as flow velocity, channel size and viscosity ratio between the dispersed and carrier fluid. This work also confirms the scaling group in a correlation for the pressure drop prediction in liquid-liquid Taylor flow as a function of L^* and Ca/Re, which includes both single-Poeseuille and interfacial pressure drop.

Chapter 6. Mass transfer behaviour using LIF

6.1 Introduction

Experimental studies of mass transfer in the nitric acid/ ionic liquid microfluidic system were carried out using Laser Induced Fluorescence technique. The extractant species Eu(III) acted as the indicator as well because of its fluorescence properties. As a non-intrusive measurement method, Laser induced fluorescence (LIF) technique has been widely used to measure species concentration, flow field temperature and pH distributions. The fluorescence dye absorbs light energy at a particular wavelength, and emits at another, usually larger, wavelength. The fluorescence energy emitted per unit volume is defined as(Guilbault 1990):

$$I = I_0 C \emptyset \varepsilon \quad (6.1.1)$$

where I_0 is the incident light flux ($W \cdot m^{-2}$), C is the concentration of fluorescent species ($kg\ m^{-3}$), $\emptyset$ is the absorption coefficient, and ε is the quantum efficiency. Guilbault (1990) proposed that the absorption coefficient is influenced by temperature and pH value. In this work the room temperature variations can be neglected (24.8 - 25.2 °C), and the pH value barely changes before and after the Europium extraction in the nitric acid solution. The Eu(III) concentration changes in the aqueous phase were observed and measured under various operating conditions. Experimental results indicate that 30-50% of the mass transfer happens close to the inlet during plug formation.

6.2. Results and discusion

6.2.1 Calibration of micro-LIF measurement in droplet flow systems

The Eu(III) concentration values at the channel inlet and at two locations along the channel length are measured using LIF technique. At each measurement location 1000 images are acquired with the camera. At each measurement position, calibrations are required to convert the intensity grayscale values into the Eu(III) concentration. $Eu(NO_3)_3$ was dissolved in 1M nitric acid by mechanically shaking for 3 hours to ensure the initial loading of Eu(III) was 0, 10, 20, 30, 50 mg/mL, respectively. These concentrations are low and do not change the properties of the nitric acid solution. The relationship between the fluorescence intensity (in

terms of grayscale value) and the Eu(III) concentration in the nitric acid solution as shown in **Figure 6.1**, is linear with R^2 equal to 0.9813. In the ionic liquid phase the europium is in the form $Eu(NO_3)_3 \cdot (CMPO)_x$ which could not be prepared separately; therefore only the concentration in the nitric acid solution was measured. It is important to carry out the measurements at the same locations where the calibration took place and the laser, camera and microchannel were fixed.

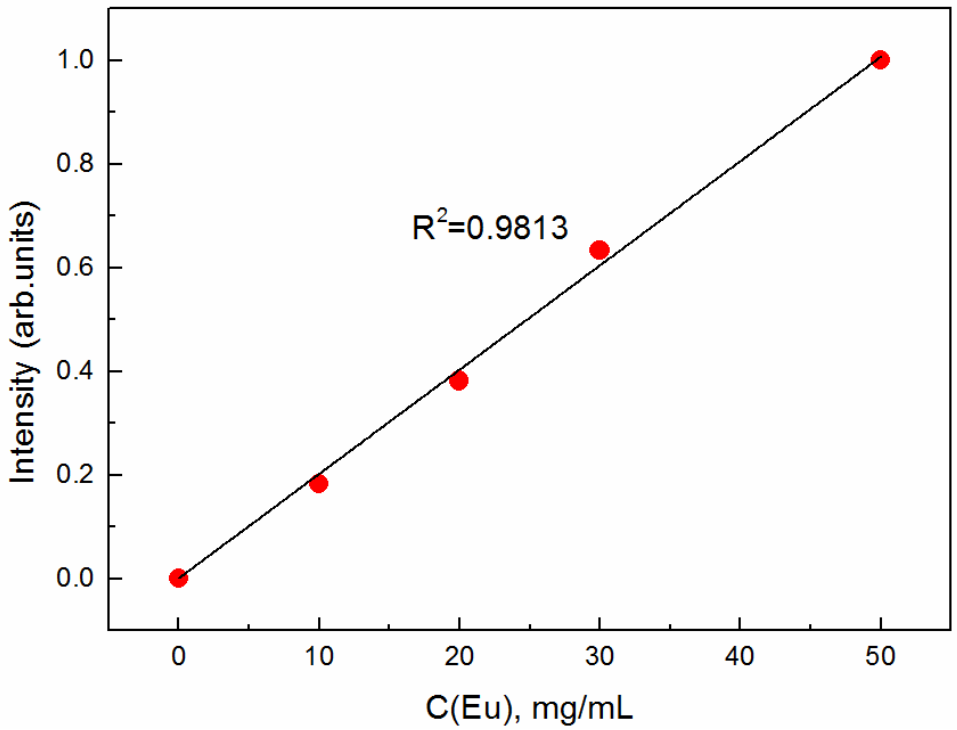

Figure 6.1: Relationship between the fluorescence intensity (grayscale value) and the concentration Eu(III) in nitric acid solution.

6.2.2 Qualitative behaviour of interphase mass transfer

Figure 6.2 gives an example snapshot of the mass transfer process in the aqueous plug at different channel axial locations and times at Q_{aq} = Q_{IL}= 0.113 ml/hr. The ionic liquid [C_4min][NTf_2] itself can be easily excited by laser at a wide range of wavelengths from 250 to 550 nm (shown in Appendix B; this is because the cation and ligand structures have strong fluorescing properties (Melby et al. 1964)). To ensure the emission signal from Eu(III) is strong enough to be detected, the 50 mg/mL concentration as initial loading in nitric acid was used in the following experiments, which is also consistent with the extraction study.

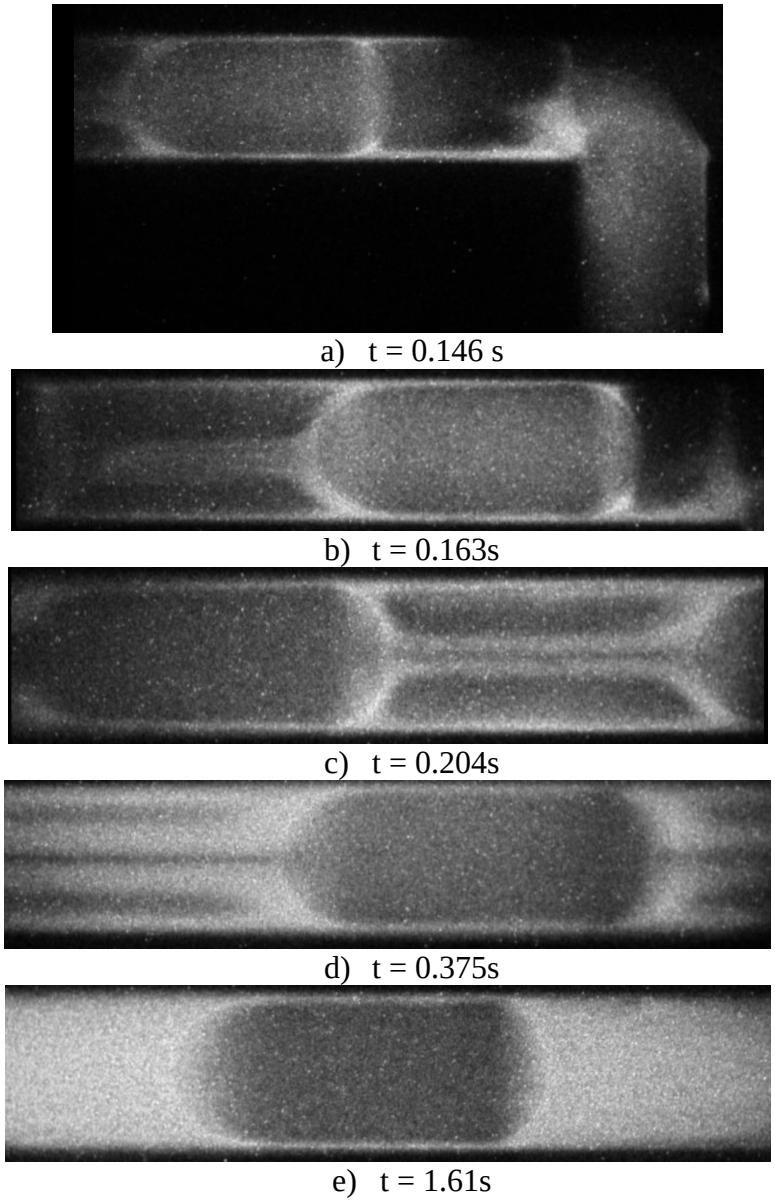

Figure 6.2: Snapshot of mass transfer process at different travelling time at $Q_{aq} = Q_{IL}$= 0.113 ml/hr. The direction of flow is from right to left.

The Eu(III) starts to spread into the ionic liquid phase when the two solutions contact after the inlet, indicating that the mass transfer process has begun. In fact during the plug formation stage, there is significant interphase mass transfer. Using the numerical model developed in Chapter 3, the plug formation process was modelled and the velocity profiles and circulation patterns are shown in **Figure 6.3** for $Q_{aq} = Q_{IL}$= 0.565 ml/hr. As can be seen a vortex forms at the plug tip.

As discussed in (Glawdel et al. 2012), the generation process can be divided into three stages, lag stage, filling stage and necking stage. To quantify the plug formation time of each stage, the formation time is defined as $\Omega = t/T$, where t is capturing time of sample pictures in **Figure 6.3** and T is the total generation time of a droplet. Due to the shear effects from the continuous ionic liquid phase, internal recirculation patterns form. At the lag stage, two small counter-rotating vortices near the interface are developed, which increase the Eu(III) transfer from the nitric acid to the ionic liquid phase even before the generation of a plug. This process takes nearly half of the droplet generation time ($0 < \Omega < 0.48$), meaning a significant amount Eu(III) has already transferred. In the filling stage, the plug expands until its tip almost blocks the whole cross-section area of the main channel. In this case, the pressure in the upstream area increases, and the ionic liquid moves at a relative high speed in the gas region between the plug and the wall. Counter-rotating vortices form not only in the nitric acid solution, but also in the continuous ionic liquid phase downstream the plug. The filling stage takes nearly ¼ of the plug generation circle, and it greatly enhances the mass transfer process due to the increased interfacial area and strong circulation patterns. At the last stage (necking stage), the plug elongates at the downstream direction, and the effective mass transfer area is further increased. The vortices in the continuous phase are fully developed, and two additional small vortices are observed at the plug front tip. The duration of this stage is shorter than that of the previous two stages. Then the neck of the plug is squeezed further until it breaks and the plug detaches.

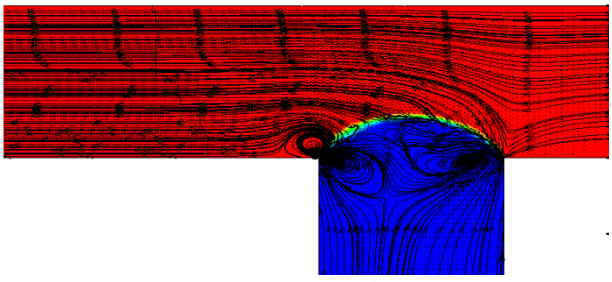

a) $\Omega = 0.48$

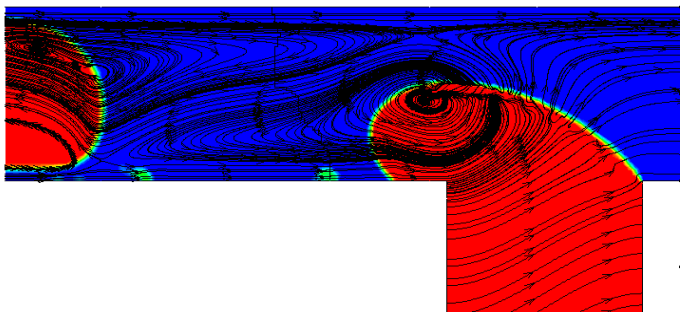

b) $\Omega = 0.61$

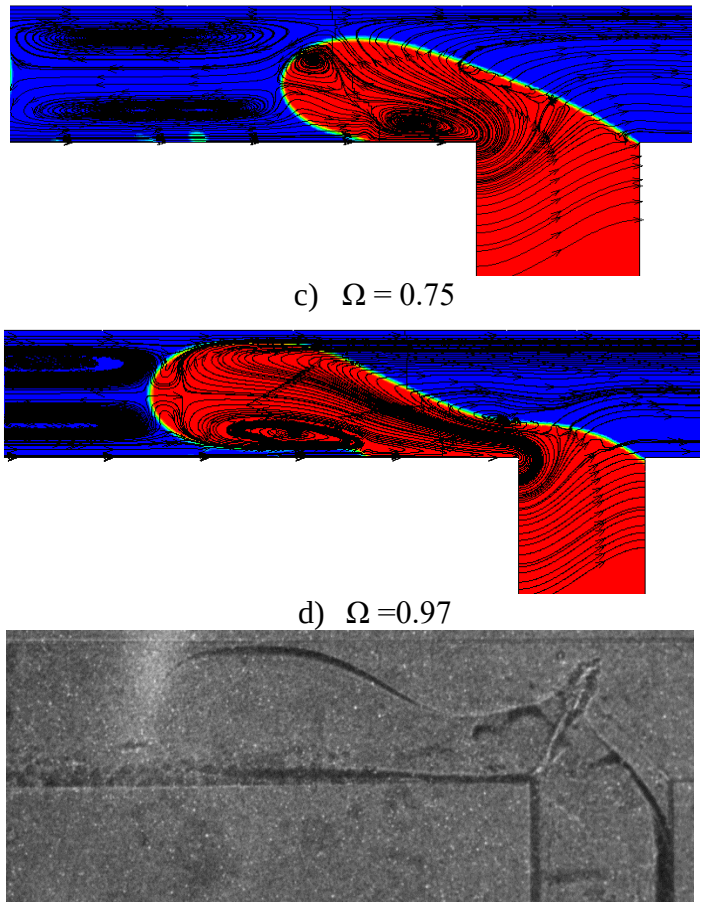

c) Ω = 0.75

d) Ω =0.97

e)

Figure 6.3: Comparison of CFD (a-d)and experimental observation(e) in the plug generation process at $Q_{aq} = Q_{IL} = 0.565$ ml/hr. a) lag stage, b)and c) filling stage, d)necking stage. The necking stage from CFD d) and experiment e) show good agreement. Ω represents the generation extent of each stage.

A pair of recirculation patterns exists downstream the plug but no fluorescence signal is observed upstream in the LIF images shown in **Figure 6.2 a** and **b**. This means the Eu(III) transfers from the nitric acid to the ionic liquid solution through the top interface and dispersed internally due to recirculation at the front of the plug, which is consistent with the circulation patterns shown in **Figure 6.3**. The right and upper corners of the T-junction have lower mass transfer. After the plug is detached, the fluorescence intensity in the aqueous plug continues to decrease but it increases in the ionic liquid solution. In **Figure 6.2 c**, Eu(III) is spreading along the streamlines because concentration gradients exist along the fluid trajectories in the slug. The accelerating spreading process along the trajectory is driven by the general motion of the ionic liquid, and the estimated time for the process is $t^* = (L^2/D)Pe^{-2/3}$, where Peclect

number is defined as $Pe=U_{mix}L/D$, where U is the mixture velocity, L is the size of slug and D the diffusion constant, giving values of 0.387 to 1.756 for the present operational conditions.

The Eu(III) starts to diffuse normally to the streamlines after it has homogeneous distributed along the streamlines, driven by molecular diffusion. As given in **Figure 6.2 d**, the fluorescence ring in the slug boundary is much thicker than that in **Figure 6.2 c**. By applying Fick's law of diffusion, the diffusion time is $t_D = W^2/D$ in the slug, where W is the width of the droplet. In terms of chemical reaction, the Eu(III) chemical complex shows high fluorescence characteristic and the ionic liquid further enhance it. Therefore the signal from slug is stronger than in the dispersed droplet. In **Figure 6.2 d**, a steady state is reached for the concentration field in both phases. At equilibrium condition although nearly 65% Eu(III) still exists in the dispersed aqueous phase (based on extraction results in Chapter 4), the fluorescence signal from the ionic liquid is very strong and masks the signal from plug ends when extraction equilibrium condition achieved.

The normalised concentration profiles of Europium in the aqueous plugs are shown in **Figure 6.4** at the time when the plug has just detached from the inlet for 3 different mixture velocities. Concentration is normalized by the initial loading concentration (50mg/mL). Under all conditions Eu(III) is unevenly distributed inside the droplet: the Eu(III) concentration in the right and lower parts is higher than in the rest of the plug. A concentration gradient near the outer interface is observed, especially at larger mixture velocity. This means that a significant amount of Eu(III) has been transferred from the plug to the ionic liquid. Riaud et al. (2014)showed that the freshest layer exists on plug periphery and the oldest ones accumulate in the centre. For shorter plugs at high mixture velocities, the fast surface renewal and strong recirculation patterns further enhance the mass transfer at the plug formation stage.

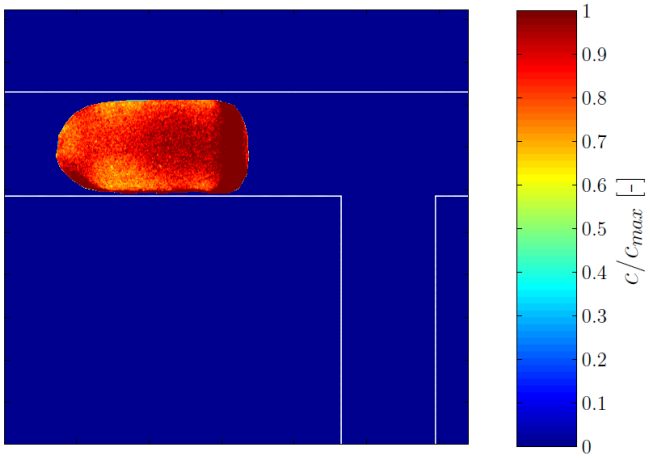

a) U_{mix} = 0.001 m/s

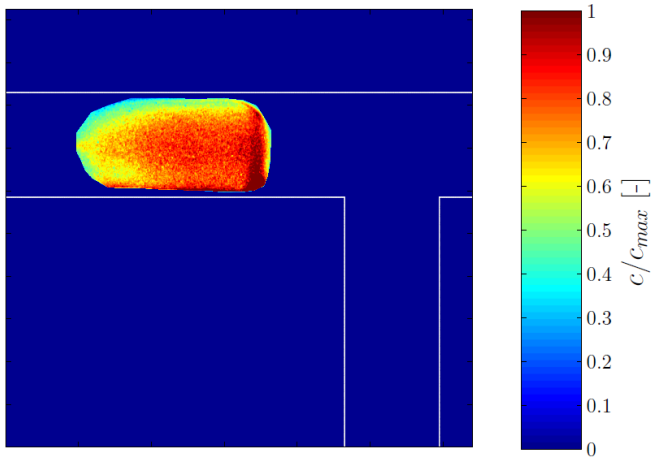

b) U_{mix} = 0.005 m/s

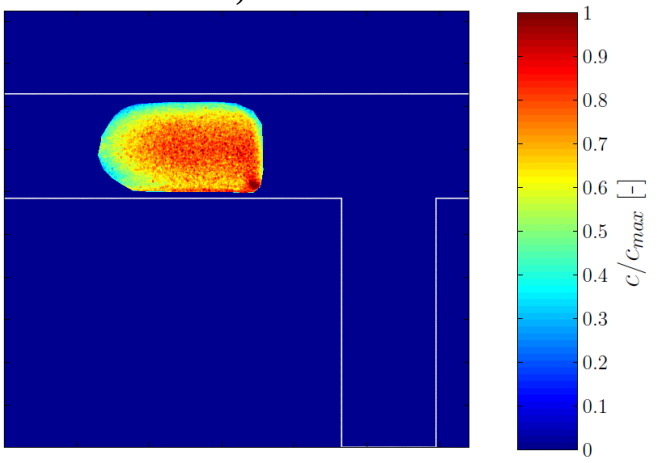

c) U_{mix} = 0.01 m/s

Figure 6.4: Concentration profiles of Europium in the aqueous plug during plug formation process at t=0 s, for $Q_{aq} = Q_{IL}$= 0.113 ml/hr, 0.565 ml/hr and 1.13 ml/hr.

6.2.3 Quantitative behaviour of interphase mass transfer

To quantify the mass transfer process, the average Europium concentration values are determined in the plug over time, from the concentration values at each pixel in the image. Considering the strong light at the interface areas caused by light reflection, the concentration values in these areas were not considered. The average Eu(III) concentration of the plug near the channel exit (**Figure 6.2e**) was calculated and compared against the extraction results described in Chapter 4. The LIF results, however, is up to 76.4 % higher than the extraction results, which is attributed to the neglect of the signals at the plug boundary areas. As a result, the mass transfer near the channel exit will not be analysed.

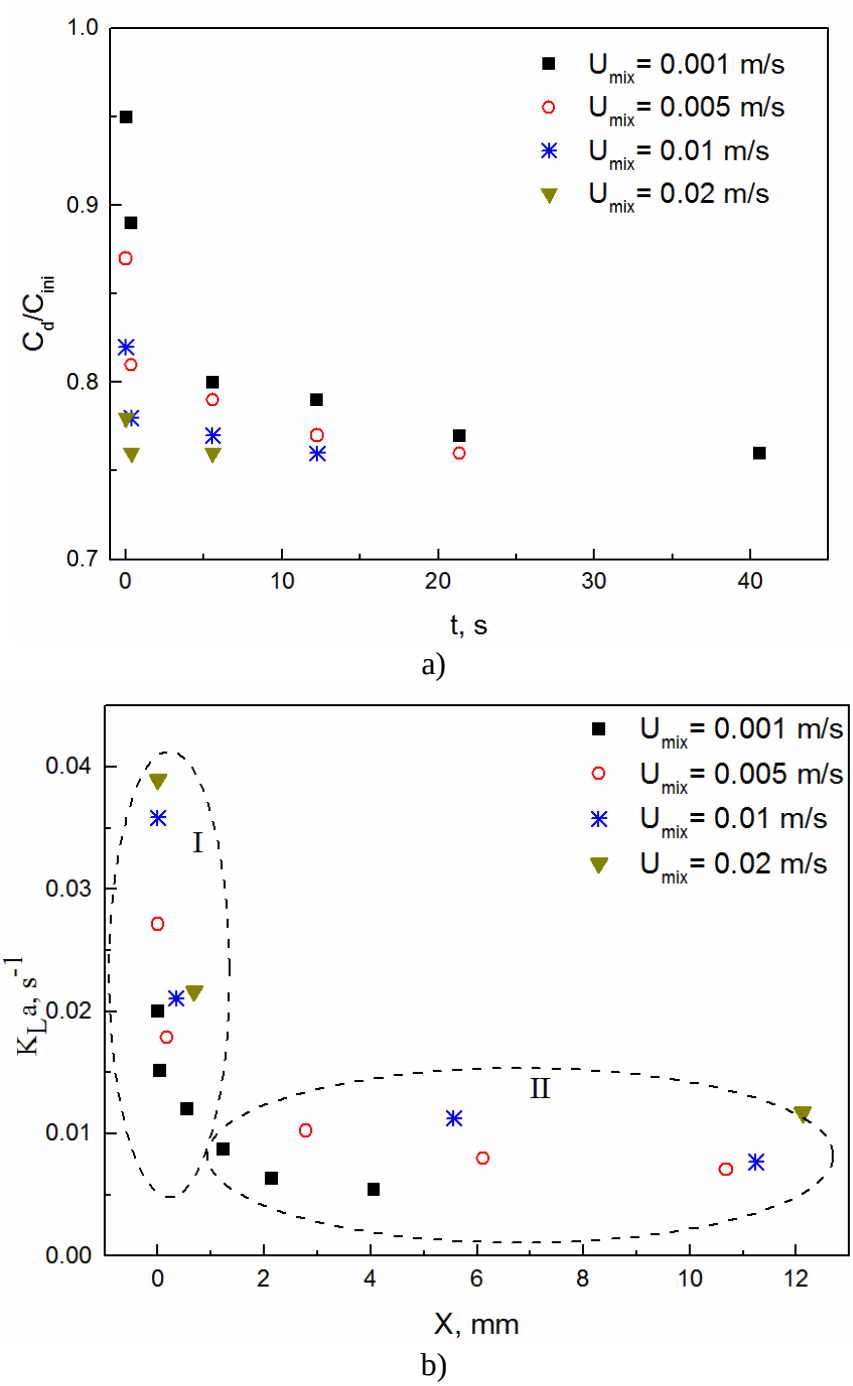

Figure 6.5: a) Normalized Eu(III) concentration in aqueous plug versus travelling time and b) mass transfer coefficient versus independent distance near the T-junction under various mixture velocities, for $Q_{aq} = Q_{IL}$= 0.113 ml/hr, 0.565 ml/hr, 1.13 ml/hr and 2.26 ml/hr. Zone I and II refers to the plug generation and plug moving stage respectively.

The concentration field and mass transfer coefficient versus plug travelling time and distance (respectively) under various mixture velocities are shown in **Figure 6.5**. The travelling time is calculated by dividing the distance between the plug tail and initial detachment point, X (m)

with the mixture velocity. As expected, plugs at low U_{mix} have higher concentrations for the same travelling time, because less Eu(III) is transferred into the ionic liquid,. From the concentration values at the plug front end and top layer region, it is found that up to 70% of the Eu(III) transfers through these areas. High mixture velocities favour Eu(III) transfer at the plug formation process, thus leading to low initial concentrations at t = 0 s compared to the low velocities.. Thus higher mass transfer coefficients are found in this case as shown in **Figure 6.5b**. In this figure, the mass transfer process can be divided into two stages: the plug generation stage (I) and the plug moving stage (II). It is found that 27.02 – 50.57% of the overall mass transfer occurs at the plug formation stage, while the values increase with mixture velocity; this agrees with previous observations that around 40% of the mass transfer happen at this stage (Riaud et al. 2014).

6.3 Conclusions

In this chapter, a qualitative and quantitative study of the mass transfer during plug formation and flow in the T-junction microchannels was conducted using Laser Induced Fluorescence. The extractant species Eu(III) is fluorescent and its concentration profiles can be monitored with LIF. Circulaiton patterns appear in the aqueous plugs even before the plugs form. This process takes nearly half of the droplet generation time, which means that a significant amount of Eu(III) has been transferred. After experiencing convection and normal diffusion extraction equilibrium achieved. The fluorescence signal from the ionic liquid when Eu(III) transfers into it is very strong. The results show that the mass transfer process can be divided into two stages: the plug generation stage and the plug moving stage. Up to 70% Eu(III) transfers through the plug front end and top layer region. The experimental results indicate that 30-50% of the mass transfer happens in the plug formation stage.

Chapter 7. Conclusions and suggestions for future work

The continuous development of small scale and miniaturised equipment are driven by the technical and environmental reasons within the frame of process intensification. As a strong photoluminescence and magnetic element, the enhanced mass transfer behaviour of Eu (III) in microchannels combined with ionic liquid are systematic studied with the background of nuclear fuel recovery. The thesis contributes to the development of aqueous-ionic liquid microreactor operating at Taylor flow by optimizing the microfluidic performance. This chapter summarizes the main conclusions from the thesis and gives recommendations for the future work.

7.1 Overview of thesis

As given in the first Chapter, there were three main objectives. Initially, the intensified extraction of Eu(III) from nitric acid solutions into an ionic liquid phase 0.2M CMPO-1.2M TBP/[C_4mim][NTf_2] was studied experimentally in small channels with diameters 0.2 and 0.5 mm. Comparing the equilibrium results under various nitric acid concentrations, it was found that the highest distribution coefficients occurred at 1M nitric acid concentration. 50 mg/mL Eu(III) concentration was chosen for the microchannel extraction experiments to reduce the measurement errors in concentration. Experiments were carried out in the plug flow regime, where the aqueous solution formed the dispersed plugs and the ionic liquid solution was the continuous phase.The interfacial area during plug flow in the microchannels was investigated with high speed imaging while velocity fields within the aqueous phase plugs were obtained using high speed bright field micro PIV. It was found that the interfacial area in the large channel was almost 3 times smaller than in the small one for the same mixture velocity; also larger interfacial area was found in higher mixture velocities compared to low ones, because at high velocities the plugs had high frequency and short lengths. k_La were found to be higher in the small channel compared to the large one for the same mixture velocities, as a result of large interfacial areas and reduced circulation times. Within the same channel, the mass transfer coefficients increased and then decreased with increasing nitric acid concentration in agreement with the partition coefficients. The mass transfer coefficients were also found to decrease with residence time suggesting that significant mass transfer occurs at the channel

inlet. The mixture velocity affected the mass transfer coefficient particularly in the case of 1M nitric acid solution. The circulation times within the plugs, calculated from the detailed velocity profiles, were found to decrease with decreasing plug size and increasing mixture velocity; small circulation times result in better mixing and mass transfer. The empirical correlation on mass transfer coefficient suggested by Kashid et al. (2010) was able to predict the current results (with deviations 5.16-11.88%) better than other literature correlations. The results showed that the interfacial area and the mass transfer coefficients were significantly higher than in conventional contactors, with values of 100 and 6.2 times higher respectively.

In Chapter 5, the hydrodynamic characteristics of liquid-liquid Taylor flow in 0.2 and 0.5 mm ID channel were studied experimentally using bright field micro-PIV and with CFD simulations. The parameters influencing the Taylor flow, such as wettability characteristic, film thickness, plug velocity, plug length, plug shape, velocity profiles and pressure variation were discussed. The dimensionless film thickness is slightly smaller in the 0.2 mm channel under the same Ca, and an improved correlation based on the one suggested by Mac Giolla Eain et al. (2013) is proposed for film thickness within the current operation range ($0.0224 < Ca < 0.299$). The plug velocities in both channels, calculated from the plug front displacement or from the velocity profiles within the plug, are always higher than the mixture velocity, because of the nearly stagnant film surrounding the plug. The plug length is influenced by both the Capillary number and the flow rate ratio (Q_{aq}/Q_{IL}), which represents the balance of cross flow shear force and Laplace pressure at the plug formation stage. The results also show that the plug volume is highly dependent on the channel size and the mixture velocity. Experimental data from bright field micro-PIV and numerical CFD results reveal a parabolic form of the horizontal velocity profiles inside the plug, and Couette-shape velocity profile in the continuous film. The recirculating flow pattern within the plugs is influenced by several parameters such as flow velocity, channel size and viscosity ratio between the dispersed and carrier fluid. This work also confirms the dependence of pressure drop in liquid-liquid Taylor flow from L^* and Ca/Re, which includes both single phase Poeseuille and interfacial pressure drop.

In Chapter 6, the mass transfer process of Eu(III) in the aqueous-ionic liquid microfluidic system was visualized using Laser Induced Fluorescence technique. The Eu(III) excitation spectrum was enhanced in the nitric acid solution, with the most intense band centred at 395 nm. The intensity in the 616 nm emission band shows a linear relationship with the Eu(III) concentration. A significant amount of Eu(III) is transferring into the ionic liquid phase during

the plug formation stage at the inlet . After experiencing convection and normal diffusion extraction equilibrium achieved, while the fluorescence signal from ionic liquid is reversely stronger than the residence Eu(III) in droplet. The quantitative results show that the mass transfer process can be divided into two stage: the plug formation stage and the plug propagation stage. Up to 70% of the Eu(III) is transferred through the plug front end and the top region. Experimental results indicate that 30-50% of the mass transfer happens in the plug formation process, where new interfaces are generated and there are a number of small vortices that help mixing, especially at higher $U_{mix.}$

7.2 Future work

Nuclear spent nuclear fuel reprocessing is a broad subject while this thesis only focused on the 1-n-butyl-3-methylimidazolium based ionic liquid recovery in small scale channels. Rather than a nitric acid environment, the spent nuclear waste has various components and high temperature. Metal like Uranium (95% of the waste mass), Plutonium (1%), minor actinides and other Lanthnides are presented in the radioactive waste even though several post-processing procedures have been taken. Various task specific ionic liquids should be developed to selectively recover aim elements. The immobilize-based ionic liquid, however, have difficulty in recovery of the extracted metal ions from the IL phase because the hydrophobic ionic species extracted becomes part of the IL and cannot be isolated by evaporation after forward extraction. The continuous extraction performance based on the Htta and DGA recovery system as stated in Chapter 2 should be studied. Moreover, the ion-exchange from the ionic liquid to aqueous solution is another serious disadvantage that should be considered.

The mass transfer study based on common ionic liquid is still limited by the lack of knowledge of the chemical reaction mechanism, especially the metal behaviour in the interphase area. All experiments in the present work were carried out in room temperature. The real spent nuclear waste is normally above 50º in spent fuel pools(Johnson 1977), which would affect the ionic liquid viscosity and may potentially influence the IL recovery behaviour. Therefore the heat transfer of the microfluidic system should also be studied. On the other hand, although ionic liquid has higher partition coefficients than conventional solutions due to high solubility, it does not improve the continuous mass transfer process as high as in the equilibrium process. It also complicates the Laser Induced Fluorescence measurement as most ionic liquid can be excited over a large range wavelength laser. Therefore novel ionic liquids that can resist high temperatures without affecting the extraction performance should be developed.

There are many multiphase systems that can enhance mass transfer other than microchannels. The Plate Fin Heat Sinks (PFHSs), for example, have been widely used to increase mass transfer due to the easy machining, simple structure and low cost. Another alternative is the membrane techniques, which improve mass transfer due to their large interfacial area. These techniques, together with microchannels, have large pumping requirements because of the high pressure drop over the equipment. Therefore working with low viscosity liquids should be taken into consideration.

The aqueous and ionic liquid phase in the present work have similar wetting properties, and this leads to a totally different plug formation pattern if the T-junction is not thoroughly cleaned. With the addition of surfactant in either phase, the interfacial tension can be modified and so does with the plug length and shape (Xiong et al. 2007). The refractive index of the phases could be matched and improve the performance of optical techniques, such as LIF, as there would not be light reflection at the interface. However, the effect of surfactant on the chemical reaction should be clarified, and the separation after extraction needs to be studied as well.

Although mass transfer under Taylor flow benefit from the recirculation patterns and large surface-to-volume ratio, its performance in other flow regimes should also be considered, such as annular flow or impinging flow. In terms of Taylor flow, gas-liquid-liquid can be employed to further enhance extraction compared to liquid-liquid flow, due to the increased droplet length/interfacial area separated by the inert gas. Non-Newtonian polymer fluids can be used to create ‘elastic turbulence’ in serpentine channels, which can increase transfer up to 300% compared to Newtonian fluids under the same operation condition(Whalley et al. 2015). An old problem for microfluidic industrial application is the scale-up or number-up of microchannels, with the design of inlet manifold as the main concern. A well-designed system, such as multi-layer microreactor, that can guarantee the simultaneous contact of two phases should be studied.

In terms of numerical studies, the interphase mass transfer simulation in the T-junction was limited by the high computation cost caused by high resolution grid. A more economic model, such as a front tracking method, where a separate front marks the interface but a fixed coarse gird that is only modified near the front to follow the interface, should be investigated. The lattice-Boltzmann method (LBM) in simulating multiphase flow, especially in modelling dilute species, can be used for future microfluidic hydrodynamic and mass transfer predictions.

Refereed journal papers

Qi Li, Panagiota Angeli, 2017, *Experimental and numerical hydrodynamic studies of ionic liquid-aqueous plug flow in small channels*. Chemical Engineering Journal, 328, 717-736.

Qi Li, Panagiota Angeli, 2016. *Intensified Eu(III) extraction using ionic liquids in small channels*. Chemical Engineering Science 143, 276-286.

Qi Li, Jianfei Song, Chuan Li, Yaodong Wei, Jianyi Chen, 2013. *Numerical and experimental study of particle deposition on inner wall of 180° bends*. Powder Technology 237, 241-254.

Chuan Li, Qi Li, Zhu Jiang, Hui Cao, Yongliang Li, Yulong Ding, 2017, *Thermal performance of carbonate-based salt composite phase change materials for thermal energy storage*. Energy Storage Science and Technology 6(4): 655-661.

Qi Li, Weheliye Weheliye Hashi, Panagiota Angeli. *Study of mass transfer in ionic liquid-aqueous microdroplet systems*. (In preparation).

Conference and Symposia

Qi Li, Dimitrios Tsaoulidis, Eduardo Garciadiego Ortega, Panagiota Angeli. *Experimental and CFD studies on Eu(III) extraction using ionic liquids in microchannels.* Sustainable Nuclear Energy Conference. Nottingham UK. 12-14 April 2016.

Marti Cortada Garcia, Luca Mazzei, Valentina Dore, Qi Li, Wehliye Wehliye Hashi, Panagiota Angeli. *Experimental and computational fluid dynamic studies of mixing for complex oral health products*. University College London, London, UK. 22-23 March 2016.

Qi Li, Dimitrios Tsaoulidis, Panagiota Angeli. *Experimental and numerical investigations of ionic liquid-aqueous flow in microchannel.* 68th Annual Meeting of the APS Division of Fluid Dynamics, Boston, Massachusetts. November 22-24, 2015.

Dimitrios Tsaoulidis, Qi Li, Panagiota Angeli. *Two-phase liquid-liquid flows generated by impinging liquid jets.* 68th Annual Meeting of the APS Division of Fluid Dynamics, Boston, Massachusetts. November 22-24, 2015.

Qi Li, Panagiota Angeli. *Enhanced lanthanide element recovery in small channels using ionic liquids*. UCL Nuclear Meeting, University College London, London UK. 24 April 2015.

Qi Li, Dimitrios Tsaoulidis, Panagiota Angeli. *Experimental and numerical investigations of ionic liquid-aqueous flows in small channels for Europium recovery.* 4th European Conference on Microfluidics. Limerick, Ireland. 10-12 December 2014.

Qi Li, Panagiota Angeli, Crystal Porter, Valentina Dore, Robert Sochon, Luca Mazzei. *Numerical studies of non-Newtonian fluids mixing using two co-axial impellers.* IChemE: Mixing in Health and Personal Care Industries. London, University College London, 5th Nov 2014.

Qi Li, Dimitrios Tsaoulidis, Panagiota Angeli. *Hydrodynamic characteristics of ionic-aqueous flow in small scale channels relevant to nuclear fuel reprocessing.* The 20th Joint Annual Conference CSCST-SCI. London Imperial College London. 14th Sep 2013.

Qi Li, Dimitrios Tsaoulidis, Panagiota Angeli. *Experimental and CFD investigations of hydrodynamics of ionic liquid-aqueous flows in small channels*. 13th International Conference on Microreaction Technology. Budapest, Hungary. June 23-25, 2013.

Dimitrios Tsaoulidis, Qi Li, Panagiota Angeli. *Hydrodynamics and mixing characterstics in small channels using ionic liquids for spent nuclear fuel reprocessing applications*. 8th International Conference on Multiphase Flow. Jeju Korea, May 26-31, 2013.

Dimitrios Tsaoulidis, Qi Li, Panagiota Angeli. *Flow characteristics of liquid-liquid flow pattern in small channels.* 10th International Symposium on Particle Image Velocimetry-PIV13. Delft, The Netherlands, 1-3 July 2013.

Qi Li, Dimitrios Tsaoulidis, Panagiota Angeli. *Hydrodynamic and mass transfer in small channels relevant to nuclear fuel reprocessing*. ChemEngDayUK, Imperial College London, London UK. 07 April 2013.

References

A.Adin and A.G.Sykes (1966). "The kinetics of the oxidation of europium with vanadium and chroium in aqueous perchloric acid solutions." Journal of Chemistry Society **A**: 1230-1236.

Abadie, T., et al. (2015). "On the combined effects of surface tension force calculation and interface advection on spurious currents within Volume of Fluid and Level Set frameworks." Journal of Computational Physics **297**: 611-636.

Afkhami, S., et al. (2011). "Numerical investigation of elongated drops in a microfluidic T-junction." Physics of Fluids (1994-present) **23**(2): 022002.

Angeli, P. and A. Gavriilidis (2008). "Hydrodynamics of Taylor flow in small channels: a review." Proceedings of the Institution of Mechanical Engineers, Part C: Journal of Mechanical Engineering Science **222**(5): 737-751.

Assmann, N., et al. (2013). "Continuous Micro Liquid-Liquid Extraction." Chemical Engineering & Technology **36**(6): 921-936.

Aussillous, P. and D. Quéré (2000). "Quick deposition of a fluid on the wall of a tube." Physics of Fluids **12**(10): 2367-2371.

Aussillous, P. and D. Quéré (2000). "Quick deposition of a fluid on the wall of a tube." Physics of Fluids **12**(10): 2367.

Beitz, J. V. and J. C. Sullivan (1989). "Laser-induced fluorescence studies of europium-extractant complexes in organic phases." Journal of the Less-Common Metals **148**: 159-166.

Bercic, G. and A. Pintar (1997). "The role of gas bubbles and liquid slug lengths on mass transport in the Taylor flow through capillaries." Chemical Engineering Science **52**(21-22): 3709-3719.

Berčič, G. and A. Pintar (1997). "The role of gas bubbles and liquid slug lengths on mass transport in the Taylor flow through capillaries." Chemical Engineering Science **52**(21–22): 3709-3719.

Billard, I., et al. (2011). "Liquid–liquid extraction of actinides, lanthanides, and fission products by use of ionic liquids: from discovery to understanding." Anal Bioanal Chem **400**(6): 1555-1566.

Billard, I., et al. (2011). "Understanding the Extraction Mechanism in Ionic Liquids: UO22+/HNO3/TBP/C4-mimTf2N as a Case Study." Solvent Extraction and Ion Exchange **29**(4): 577-601.

Binnemans, K. (2007). "Lanthanides and actinides in ionic liquids." Chemical reviews **107**(6): 2592-2614.

Breisig, H., et al. (2017). "Droplet-based liquid–liquid extraction inside a porous capillary." Chemical Engineering Journal **307**: 143-149.

Bretherton, F. P. (1961). "The motion of long bubbles in tubes." Journal of Fluid Mechanics **10**(2): 166-188.

Brigham, D. M. (2013). "Lanthanide-polyamiopolycarboxylate complexation kinetics in high lactate media: investigating the aqueous phase of talspeak(PhD thesis)." Washington State University.

Bunzli, J. G. and J. Yersin (1979). "Fluorescence spectra and lifetime measurements of aqueous solutions of europium nitrate and perchlorate." Inorg. Chem. **18**: 605-607.

Burns, J. R. and C. Ramshaw (2001). "The intensification of rapid reactions in multiphase systems using slug flow in capillaries." Lab Chip **1**(1): 10-15.

Caldin, E. F. (2001). "The mechanisms of fast reaction in solution." IOS Press: Oxford: 8.

Chen, I. Y., et al. (2002). "An empirical correlation for two-phase frictional performance in small diameter tubes." International Journal of Heat and Mass Transfer **45**: 3667-3671.

Cherlo, S. K. R., et al. (2009). "Experimental and Numerical Investigations of Two-Phase (Liquid−Liquid) Flow Behavior in Rectangular Microchannels." Industrial & Engineering Chemistry Research **49**(2): 893-899.

Cherlo, S. K. R., et al. (2010). "Experimental and Numerical Investigations of Two-Phase (Liquid−Liquid) Flow Behavior in Rectangular Microchannels." Industrial & Engineering Chemistry Research **49**(2): 893-899.

Chinaud, M., et al. (2015). "Studies of plug formation in microchannel liquid–liquid flows using advanced particle image velocimetry techniques." Experimental Thermal and Fluid Science **69**: 99-110.

Christopher, G. F., et al. (2008). "Experimental observations of the squeezing-to-dripping transition in T-shaped microfluidic junctions." Physical Review E **78**(3): 036317.

Chun, S., et al. (2001). "Influence of Structural Variation in Room-Temperature Ionic Liquids on the Selectivity and Efficiency of Competitive Alkali Metal Salt Extraction by a Crown Ether." Anal Chem **73**(15): 3737-3741.

Coria-Garcia, J. C. and T. M. Niemczyk (1991). "Determination of nitric acid concentration by using europium ion fluorescence." Talanta **38**: 767-772.

De Morais, C. (2000). Recovery of europium and yttrium from color TV tubes. 55 Congresso Anual Associacao Brasileria de Metalurgia e Materiais, Rio de Janeiro, Brazil.

Dessimoz, A.-L., et al. (2008). "Liquid–liquid two-phase flow patterns and mass transfer characteristics in rectangular glass microreactors." Chemical Engineering Science **63**(16): 4035-4044.

Di Miceli Raimondi, N., et al. (2014). "Experiments of mass transfer with liquid–liquid slug flow in square microchannels." Chemical Engineering Science **105**: 169-178.

Dombrowski, N., et al. (1993). "The influence of reynolds number on the entry length and pressure drop for laminar pipe flow." The Canadian Journal of Chemical Engineering **71**(3): 472-476.

Dore, V., et al. (2012). "Mixing patterns in water plugs during water/ionic liquid segmented flow in microchannels." Chemical Engineering Science **80**: 334-341.

Fang, C., et al. (2008). "3-D numerical simulation of contact angle hysteresis for microscale two phase flow." International Journal of Multiphase Flow **34**(7): 690-705.

Foroughi, H. and M. Kawaji (2011). "Viscous oil–water flows in a microchannel initially saturated with oil: Flow patterns and pressure drop characteristics." International Journal of Multiphase Flow **37**(9): 1147-1155.

Fouilland, T. S., et al. (2010). "Film and slug behaviour in intermittent slug–annular microchannel flows." Chemical Engineering Science **65**(19): 5344-5355.

Fu, T., et al. (2010). "Squeezing-to-dripping transition for bubble formation in a microfluidic T-junction." Chemical Engineering Science **65**(12): 3739-3748.

Fu, T., et al. (2012). "Droplet formation and breakup dynamics in microfluidic flow-focusing devices: From dripping to jetting." Chemical Engineering Science **84**: 207-217.

Gallagher, P. (1964). "Absorption and fluorescence of europium (III) in aqueous solutions." The Journal of Chemical Physics **41**(10): 3061-3069.

Garstecki, P., et al. (2006). "Formation of droplets and bubbles in a microfluidic T-junction-scaling and mechanism of break-up." Lab Chip **6**(3): 437-446.

Ghaini, A., et al. (2010). "Effective interfacial area for mass transfer in the liquid–liquid slug flow capillary microreactors." Chemical Engineering and Processing: Process Intensification **49**(4): 358-366.

Ghaini, A., et al. (2011). "Hydrodynamic studies of liquid–liquid slug flows in circular microchannels." Chemical Engineering Science **66**(6): 1168-1178.

Glatzel, T., et al. (2008). "Computational fluid dynamics (CFD) software tools for microfluidic applications – A case study." Computers & Fluids **37**(3): 218-235.

Glawdel, T., et al. (2012). "Droplet formation in microfluidic T-junction generators operating in the transitional regime. I. Experimental observations." Physical Review E **85**(1): 016322.

Goel, D. and V. V. Buwa (2008). "Numerical Simulations of Bubble Formation and Rise in Microchannels." Industrial & Engineering Chemistry Research **48**(17): 8109-8120.

Goonan, T. G. (2011). Rare Earth Elements--end Use and Recyclability, US Department of the Interior, US Geological Survey.

Grimes, R., et al. (2007). "Film thickness for two phase flow in a microchannel." Advances and Applications in Fluid Mechanics **2**(1): 59-70.

Guilbault, G. G. (1990). Practical fluorescence, CRC Press.

Gupta, R., et al. (2009). "On the CFD modelling of Taylor flow in microchannels." Chemical Engineering Science **64**(12): 2941-2950.

Gupta, R., et al. (2013). "Hydrodynamics of liquid–liquid Taylor flow in microchannels." Chemical Engineering Science **92**: 180-189.

Hagsäter, S. M., et al. (2007). "Investigations on LED illumination for micro-PIV including a novel front-lit configuration." Experiments in fluids **44**(2): 211-219.

Han, L. S. (1960). "Hydrodynamic Entrance Lengths for Incompressible Laminar Flow in Rectangular Ducts." Journal of Applied Mechanics **27**(3): 403-409.

Han, Y. and N. Shikazono (2009). "Measurement of the liquid film thickness in micro tube slug flow." International Journal of Heat and Fluid Flow **30**(5): 842-853.

Harries, N., et al. (2003). "A numerical model for segmented flow in a microreactor." International Journal of Heat and Mass Transfer **46**(17): 3313-3322.

Hirt, C. W. and B. D. Nicholes (1981). "Volume of fluid (VOF) method for the dynamics of free boundaries." Journal of Computational Physiscs **39**: 201-225.

Hodges, S., et al. (2004). "The motion of a viscous drop through a cylindrical tube." Journal of Fluid Mechanics **501**: 279-301.

Horwitz, E. P., et al. (1982). "Selected Alkyl(phenyl)-N,N-dialkylcarbamoylmethylphosphine Oxides as Extractants for Am(III) from Nitric Acid Media." Separation Science and Technology **17**(10): 1261-1279.

Huddleston, J. G., et al. (1998). "Room temperature ionic liquids as novel media for 'clean' liquid-liquid extraction." Chem. Commun: 1765-1766.

Irandoust, S. and B. Andersson (1989). "Liquid film in Taylor flow through a capillary." Industrial & Engineering Chemistry Research **28**(11): 1684-1688.

J.F.Brennecke and E.J.Maginn (2001). "Ionic liquids: innovative fluids for chemical processing." AIChE Journal **47**: 2384-2389.

Jagadeeswara Rao, C., et al. (2009). "Electrochemical behavior of europium (III) in N-butyl-N-methylpyrrolidinium bis(trifluoromethylsulfonyl)imide." Electrochimica Acta **54**(20): 4718-4725.

Jensen, M. P., et al. (2003). "Mechanisms of Metal Ion Transfer into Room-Temperature Ionic Liquids: The Role of Anion Exchange." J. AM. Chem. Soc(125): 15466-15473.

Joanicot, M. and A. Ajdari (2005). "Droplet Control for Microfluidics." Science **309**(5736): 887-888.

Johnson, A. B. J. (1977). Behavior of spent nuclear fuel in water pool storage, ; Battelle Pacific Northwest Labs., Richland, Wash. (USA)**:** Medium: ED; Size: Pages: 104.

Jovanović, J., et al. (2012). "Liquid–Liquid Flow in a Capillary Microreactor: Hydrodynamic Flow Patterns and Extraction Performance." Industrial & Engineering Chemistry Research **51**(2): 1015-1026.

Jovanović, J., et al. (2011). "Liquid–liquid slug flow: hydrodynamics and pressure drop." Chemical Engineering Science **66**(1): 42-54.

Jovanović, J., et al. (2011). "Liquid–liquid slug flow: Hydrodynamics and pressure drop." Chemical Engineering Science **66**(1): 42-54.

Kashid, M. and L. Kiwi-Minsker (2011). "Quantitative prediction of flow patterns in liquid–liquid flow in micro-capillaries." Chemical Engineering and Processing: Process Intensification **50**(10): 972-978.

Kashid, M. N. and D. W. Agar (2007). "Hydrodynamics of liquid–liquid slug flow capillary microreactor: Flow regimes, slug size and pressure drop." Chemical Engineering Journal **131**(1-3): 1-13.

Kashid, M. N., et al. (2005). "Internal Circulation within the Liquid Slugs of a Liquid−Liquid Slug-Flow Capillary Microreactor." Industrial & Engineering Chemistry Research **44**(14): 5003-5010.

Kashid, M. N., et al. (2010). "Numbering-up and mass transfer studies of liquid–liquid two-phase microstructured reactors." Chemical Engineering Journal **158**(2): 233-240.

Kashid, M. N., et al. (2005). "Internal circulation within the liquid slugs of a liquid–liquid slug-flow capillary microreactor." Industrial&Engineering Chemistry Research **2005**(44): 5003-5010.

Kashid, M. N., et al. (2012). "Analytical method to predict two-phase flow pattern in horizontal micro-capillaries." Chemical Engineering Science **74**: 219-232.

Kashid, M. N., et al. (2007). "Computational modelling of slug flow in a capillary microreactor." Journal of Computational and Applied Mathematics **203**(2): 487-497.

Kashid, M. N., et al. (2007). "Computational modelling of slug flow in a capillary microreactor." Journal of Computational and Applied Mathematics **203**(2): 487-497.

Kashid, M. N., et al. (2010). "CFD modelling of liquid–liquid multiphase microstructured reactor: Slug flow generation." Chemical Engineering Research and Design **88**(3): 362-368.

Kashid, M. N., et al. (2011). "Gas–liquid and liquid–liquid mass transfer in microstructured reactors." Chemical Engineering Science **66**(17): 3876-3897.

Kashid, M. N., et al. (2008). "On the hydrodynamics of liquid-liquid slug flow capillary microreactors." Asia-Pacific Journal of Chemical Engineering **3**(2): 151-160.

Kashid, M. N., et al. (2008). "On the hydrodynamics of liquid–liquid slug flow capillary microreactors." Asia-Pacific Journal of Chemical Engineering **3**(2): 151-160.

Kawahara, A., et al. (2005). "Effects of Channel Diameter and Liquid Properties on Void Fraction in Adiabatic Two-Phase Flow Through Microchannels." Heat Transfer Engineering **26**(3): 13-19.

Kececi, S., et al. (2009). "Recirculation time and liquid slug mass transfer in co-current upward and downward Taylor flow." Catalysis Today **147**: S125-S131.

Khodaparast, S., et al. (2014). "Application of micro particle shadow velocimetry μPSV to two-phase flows in microchannels." International Journal of Multiphase Flow **62**: 123-133.

Kiwi-Minsker, L. and A. Renken (2005). "Microstructured reactors for catalytic reactions." Catalysis Today **110**(1-2): 2-14.

Kralj, J. G., et al. (2007). "Integrated continuous microfluidic liquid–liquid extraction." Lab Chip **7**(2): 256-263.

Kreutzer, M. T., et al. (2005). "Inertial and interfacial effects on pressure drop of Taylor flow in capillaries." AIChE Journal **51**(9): 2428-2440.

Kučera, J., et al. (2007). "Pollution of agricultural crops with lanthanides, thorium and uranium studied by instrumental and radiochemical neutron activation analysis." Journal of Radioanalytical and Nuclear Chemistry **271**(3): 581-587.

Kurup, G. and A. S. Basu (2011). Shape dependent Laplace vortices in deformed liquid-liquid slug flow. 2011 Annual International Conference of the IEEE Engineering in Medicine and Biology Society, IEEE.

Laborie, S., et al. (1999). "Characterisation of gas–liquid two-phase flow inside capillaries." Chemical Engineering Science **54**(23): 5723-5735.

Lac, E. and J. Sherwood (2009). "Motion of a drop along the centreline of a capillary in a pressure-driven flow." Journal of Fluid Mechanics **640**: 27-54.

Lakehal, D., et al. (2007). "Computational heat transfer and two-phase flow topology in miniature tubes." Microfluidics and Nanofluidics **4**(4): 261-271.

Lakehal, D., et al. (2008). "Computational heat transfer and two-phase flow topology in miniature tubes." Microfluidics and Nanofluidics **4**(4): 261-271.

Lan, W., et al. (2017). "Study on “interface – shrinkage – driven” breakup of droplets in co-flowing microfluidic devices." Chemical Engineering Science **158**: 58-63.

Langewisch, D. R. and J. Buongiorno (2015). "Prediction of film thickness, bubble velocity, and pressure drop for capillary slug flow using a CFD-generated database." International Journal of Heat and Fluid Flow **54**: 250-257.

Lee, C.-J. and B.-R. Yang (1995). "Extraction of trivalent europium via a supported liquid membrane containing PC-88A as a mobile carrier." The Chemical Engineering Journal and the Biochemical Engineering Journal **57**(3): 253-260.

Lew, K. (2010). "The 15 Lanthanides and the 15 Actinides." The Rosen Publishing Group: 30.

Li, Q. and P. Angeli (2016). "Intensified Eu (III) extraction using ionic liquids in small channels." Chemical Engineering Science.

Li, X.-B., et al. (2012). "Study on the mechanism of droplet formation in T-junction microchannel." Chemical Engineering Science **69**(1): 340-351.

Li, Y., et al. (2014). "Computational investigations of the mixing performance inside liquid slugs generated by a microfluidic T-junction." Biomicrofluidics **8**(5): 054125.

Liu, H., et al. (2005). "Hydrodynamics of Taylor Flow in Vertical Capillaries: Flow Regimes, Bubble Rise Velocity, Liquid Slug Length, and Pressure Drop." Industrial & Engineering Chemistry Research **44**(14): 4884-4897.

Liu, H. and Y. Zhang (2009). "Droplet formation in a T-shaped microfluidic junction." Journal of applied physics **106**(3): 034906.

Liu, L., et al. (2006). "Laser-induced fluorescence (LIF) studies of liquid–liquid flows. Part I: Flow structures and phase inversion." Chemical Engineering Science **61**(12): 4007-4021.

Lowe, H. and W.Ehrfeld (1999). "State-of-the art in microreaction technology: concepts, manufacturing and applications." Electrochimica Acta **44**: 3679-3689.

M.N.Kashid, et al. (2005). "Internal Circulation within the Liquid Slugs of a Liquid−Liquid Slug-Flow Capillary Microreactor." Ind.Eng.Chem.Res. **44**: 5003-5010.

Mac Giolla Eain, M., et al. (2013). "Film thickness measurements in liquid–liquid slug flow regimes." International Journal of Heat and Fluid Flow **44**: 515-523.

Magnusson, D., et al. (2009). "Demonstration of a TODGA based Extraction Process for the Partitioning of Minor Actinides from a PUREX Raffinate." Solvent Extraction and Ion Exchange **27**(1): 26-35.

Matsumiya, M., et al. (2008). "Electrochemical behaviors of multivalent complexes in room temperature ionic liquids based on quaternary phosphonium cations." Journal of Electroanalytical Chemistry **622**(2): 129-135.

Meadows, J. and A. K. Agrawal (2015). "Time-resolved PIV of lean premixed combustion without and with porous inert media for acoustic control." Combustion and Flame **162**(4): 1063-1077.

Mehdizadeh, A., et al. (2011). "Numerical simulation of thermofluid characteristics of two-phase slug flow in microchannels." International Journal of Heat and Mass Transfer **54**(15-16): 3457-3465.

Meinhart, C., et al. (2000). "Volume illumination for two-dimensional particle image velocimetry." Measurement Science and Technology **11**(6): 809.

Meinhart, C. D., et al. (1999). "PIV measurements of a microchannel flow." Experiments in fluids **27**(5): 414-419.

Meinhart, C. D., et al. (2000). "A PIV Algorithm for Estimating Time-Averaged Velocity Fields." Journal of Fluids Engineering **122**(2): 285-289.

Melby, L. R., et al. (1964). "Synthesis and Fluorescence of Some Trivalent Lanthanide Complexes." Journal of the American Chemical Society **86**(23): 5117-5125.

Modolo, G., et al. (2007). "Development of a TODGA based Process for Partitioning of Actinides from a PUREX Raffinate Part I: Batch Extraction Optimization Studies and Stability Tests." Solvent Extraction and Ion Exchange **25**(6): 703-721.

Modolo, G., et al. (2007). "Demonstration of a TODGA-Based Continuous Counter-Current Extraction Process for the Partitioning of Actinides from a Simulated PUREX Raffinate, Part II: Centrifugal Contactor Runs." Solvent Extraction and Ion Exchange **26**(1): 62-76.

Muhlfriedel and Baumann (2000). "Concentration measurements during mass transfer across liquid-phase boundaries using planar laser induced fluorescence." Experiments in fluids **28**: 279-281.

Nagaishi, R., et al. (2007). "Spectroscopic and electrochemical properties of europium(III) ion in hydrophobic ionic liquids under controlled condition of water content." Journal of Alloys and Compounds **431**(1-2): 221-225.

Nagaishi, R., et al. (2002). "Pulse radiolysis study on reactions of a hydroate electron with Europium-Aminopolycarboxylate complexes in aqueous perchlorate media." Journal of Physical and Chemstry **106**: 9036-9041.

Nakashima, K., et al. (2003). "Ionic liquids as novel solvent for lanthanide extraction." Analytical Sciences **19**: 1097-1098.

Nakashima, K., et al. (2003). "Ionic liquids as a novel solvent for lanthanide extraction." Analytical Sciences **19**(8): 1097-1098.

Nakashima, K., et al. (2005). "Feasibility of ionic liquids as alternative separation media for industrial solvent extraction processes." Industrial & Engineering Chemistry Research **44**(12): 4368-4372.

Navaneetha Krishnan, R., et al. (2010). "Performance of numerical schemes in the simulation of two-phase free flows and wall bounded mini channel flows." Chemical Engineering Science **65**(18): 5117-5136.

Okamura, H., et al. (2012). "Laser-induced fluorescence and infrared spectroscopic studies on the specific solvation of tris(1-(2-thienyl)-4,4,4-trifluoro-1,3-butanedionato)europium(III) in an ionic liquid." Polyhedron **31**(1): 748-753.

Okubo, Y., et al. (2008). "Liquid–liquid extraction for efficient synthesis and separation by utilizing micro spaces." Chemical Engineering Science **63**(16): 4070-4077.

Panja, S., et al. (2013). "Liquid – Liquid Extraction and Pertraction of Eu(III) from Nitric Acid Medium Using Several Substituted Diglycolamide Extractants." Separation Science and Technology **48**(14): 2179-2187.

Piriou and Svoronos (1985). "Spectroscopic study of the Eu3+ ion in nitric acid aqueous solutions." Journal of the Less-Common Metals **112**: 275-285.

Piriou, B. and D. R. Svoronos (1985). "Spectroscopic study of the Eu3+ ion in nitric acid aqueous solutions." Journal of the Less Common Metals **112**(1): 275-285.

Prileszky, T. A., et al. (2016). "Statistics of droplet sizes generated by a microfluidic device." AIChE Journal: n/a-n/a.

Qian, D. and A. Lawal (2006). "Numerical study on gas and liquid slugs for Taylor flow in a T-junction microchannel." Chemical Engineering Science **61**(23): 7609-7625.

Rabah, M. A. (2008). "Recyclables recovery of europium and yttrium metals and some salts from spent fluorescent lamps." Waste management **28**(2): 318-325.

Raimondi, N. D. M., et al. (2014). "Experiments of mass transfer with liquid–liquid slug flow in square microchannels." Chemical Engineering Science **105**: 169-178.

Rao, C. J., et al. (2009). "Electrochemical behavior of europium (III) in N-butyl-N-methylpyrrolidinium bis (trifluoromethylsulfonyl) imide." Electrochimica Acta **54**(20): 4718-4725.

Renardy, M., et al. (2001). "Numerical Simulation of Moving Contact Line Problems Using a Volume-of-Fluid Method." Journal of Computational Physics **171**(1): 243-263.

Resende, L. V. and C. A. Morais (2010). "Study of the recovery of rare earth elements from computer monitor scraps – Leaching experiments." Minerals Engineering **23**(3): 277-280.

Riaud, A., et al. (2014). "Lattice-Boltzmann method for the simulation of multiphase mass transfer and reaction of dilute species." Physical Review E **89**(5): 053308.

Ribeiro, A., et al. (2011). "Diffusion behaviour of trivalent metal ions in aqueous solutions." Chemistry and Chemical Technology **5**(2).

Rout, A., et al. (2011). "Extraction and third phase formation behavior of Eu(III) IN CMPO–TBP extractants present in room temperature ionic liquid." Separation and Purification Technology **76**(3): 238-243.

Rout, A., et al. (2011). "Room temperature ionic liquid diluent for the extraction of Eu(III) using TRUEX extractants." Journal of Radioanalytical and Nuclear Chemistry **290**(1): 215-219.

Rout, A., et al. (2012). "Extraction behavior of actinides and fission products in amide functionalized ionic liquid." Separation and Purification Technology **97**: 164-171.

Rout, A., et al. (2012). "Ionic liquid extractants in molecular diluents: Extraction behavior of europium (III) in quarternary ammonium-based ionic liquids." Separation and Purification Technology **95**: 26-31.

Rout, A., et al. (2012). "Liquid-liquid extraction of Pu(IV), U(VI) and Am(III) using malonamide in room temperature ionic liquid as diluent." J Hazard Mater **221-222**: 62-67.

S.Chun, et al. (2001). "Influence of structural variation in room-temperature ionic liquids on the selectivity and efficiency of competitive alkali metal salt extraction by crown ether." Anal. Chem. **73**: 3737-3741.

S.Dai, et al. (1999). "Solvent extraction of strontium nitrate by a crown ether using room temperature ionic liquids." J. Chem. Soc., Dalon Trans: 1201-1202.

S.Irandoust and B.Andersson (1989). "Liquid film in Taylor flow through a capillary." Ind.Eng.Chem.Res. **28**: 1684-1688.

Sarrazin, F., et al. (2007). "Hydrodynamic structures of droplets engineered in rectangular micro-channels." Microfluidics and Nanofluidics **5**(1): 131-137.

Schaeffer, N., et al. (2017). "Recovery of an yttrium europium oxide phosphor from waste fluorescent tubes using a Brønsted acidic ionic liquid, 1-methylimidazolium hydrogen sulfate." Journal of Chemical Technology & Biotechnology **92**(10): 2731-2738.

Scheiff, F., et al. (2011). "The separation of immiscible liquid slugs within plastic microchannels using a metallic hydrophilic sidestream." Lab Chip **11**(6): 1022-1029.

Schulz, W. and E. Horwitz (1986). "Recent progress in the extraction chemistry of actinide ions." Journal of the Less Common Metals **122**: 125-138.

Sengupta, A., et al. (2012). "Extraction of Am(iii) using novel solvent systems containing a tripodal diglycolamide ligand in room temperature ionic liquids: a 'green' approach for radioactive waste processing." RSC Advances **2**(19): 7492.

Sengupta, A., et al. (2013). "A comparative study of the complexation of Am(III) and Eu(III) with TODGA in room temperature ionic liquid." Journal of Radioanalytical and Nuclear Chemistry **298**(1): 405-412.

Shao, N., et al. (2009). "Flow regimes for adiabatic gas–liquid flow in microchannels." Chemical Engineering Science **64**(11): 2749-2761.

Shinohara, K., et al. (2004). "Measurement of pH field of chemically reacting flow in microfluidic devices by laser-induced fluorescence." Measurement Science and Technology **15**(5): 955-960.

Shyamala Devi, V., et al. (2011). "Novel room temperature ionic liquid for fluorescence enhancement of Eu3+ and Tb3+." Journal of Luminescence **131**(4): 739-748.

Silva, G., et al. (2008). "Micro-PIV and CFD characterization of flows in a microchannel: velocity profiles, surface roughness and Poiseuille numbers." International Journal of Heat and Fluid Flow **29**(4): 1211-1220.

Sobieszuk, P., et al. (2010). "Bubble lengths in the gas–liquid Taylor flow in microchannels." Chemical Engineering Research and Design **88**(3): 263-269.

Spelt, P. D. M. (2005). "A level-set approach for simulations of flows with multiple moving contact lines with hysteresis." Journal of Computational Physics **207**(2): 389-404.

Stumpf, S., et al. (2007). "Differences of Eu(iii) and Cm(iii) chemistry in ionic liquids: investigations by TRLFS." Dalton Transactions(2): 240-248.

Stumpf, S., et al. (2007). "Differences of Eu(III) and Cm(III) chemistry in ionic liquids: investigations by TRLFS." Dalton Trans(2): 240-248.

Sukhamoy Sarkar, et al. (1980). "Liquid-liquid extraction with an interphase chemical reaction in agitated columns.1. Mathmatical models." Industrial& Engineering Chemistry Process Design and Development **19**: 665-671.

T.Welton (1999). "Room-temperature ionic liquids. Solvents for synthesis and catalysis." Chem.Rev. **99**: 2071-2083.

Talimi, V., et al. (2012). "A review on numerical studies of slug flow hydrodynamics and heat transfer in microtubes and microchannels." International Journal of Multiphase Flow **39**: 88-104.

Taylor.G (1960). "Deposition of a viscous fluid on the wall of a tube." Journal of Fluid Mechanics **10**: 161-165.

Thulasidas, T., et al. (1997). "Flow patterns in liquid slugs during bubble-train flow inside capillaries." Chemical Engineering Science **52**(17): 2947-2962.

Thulasidas, T. C., et al. (1997). "Flow patterns in liquid slugs during bubble-train flow inside capillaries." Chemical Engineering Science **52**(17): 2947-2962.

Tsaoulidis, D. and P. Angeli (2015). "Effect of channel size on liquid-liquid plug flow in small channels." AIChE Journal: n/a-n/a.

Tsaoulidis, D. and P. Angeli (2016). "Effect of channel size on liquid-liquid plug flow in small channels." AIChE Journal **62**(1): 315-324.

Tsaoulidis, D., et al. (2013). "Flow patterns and pressure drop of ionic liquid–water two-phase flows in microchannels." International Journal of Multiphase Flow **54**: 1-10.

Tshibangu, P. N., et al. (2011). "Density viscosity and conductivity study of 1-Butyl-3-Methylimidazolium Bromide." International Journal of Electrochemistry Science **6**: 2201-2213.

Tsoligkas, A. N., et al. (2007). "Influence of orientation upon the hydrodynamics of gas–liquid flow for square channels in monolith supports." Chemical Engineering Science **62**(16): 4365-4378.

van Baten, J. M. and R. Krishna (2004). "CFD simulations of mass transfer from Taylor bubbles rising in circular capillaries." Chemical Engineering Science **59**(12): 2535-2545.

Van der Graaf, S., et al. (2006). "Lattice Boltzmann Simulations of Droplet Formation in a T-Shaped Microchannel." Langmuir **22**(9): 4144-4152.

Vandu, C. O., et al. (2005). "Mass transfer from Taylor bubbles rising in single capillaries." Chemical Engineering Science **60**(22): 6430-6437.

Vasudeva Rao, P. R. and Z. Kolarik (1996). "A REVIEW OF THIRD PHASE FORMATION IN EXTRACTION OF ACTINIDES BY NEUTRAL ORGANOPHOSPHORUS EXTRACTANTS." Solvent Extraction and Ion Exchange **14**(6): 955-993.

Walker, E. D. (2016). Numerical Studies of Liquid-Liquid Segmented Flows in Square Microchannels Using a Front-Tracking Algorithm, PhD thesis. Louisiana State University.

Walsh, E., et al. (2009). "Pressure drop in two phase slug/bubble flows in mini scale capillaries." International Journal of Multiphase Flow **35**(10): 879-884.

Wang, G., et al. (2011). "Lanthanide-doped nanocrystals: synthesis, optical-magnetic properties, and applications." Accounts of chemical research **44**(5): 322-332.

Wang, W., et al. (2012). "Visualization of micro-scale mixing in miscible liquids using μ-LIF technique and drug nano-particle preparation in T-shaped micro-channels." Chemical Engineering Journal **192**: 252-261.

Whalley, R., et al. (2015). "Enhancing heat transfer at the micro-scale using elastic turbulence." Theoretical and Applied Mechanics Letters **5**(3): 103-106.

Xiong, R., et al. (2007). "Formation of bubbles in a simple co-flowing micro-channel." Journal of Micromechanics and Microengineering **17**(5): 1002.

Xu, B., et al. (2013). "Mass transfer behavior of liquid–liquid slug flow in circular cross-section microchannel." Chemical Engineering Research and Design **91**(7): 1203-1211.

Xu, J. H., et al. (2008). "Correlations of droplet formation in T-junction microfluidic devices: from squeezing to dripping." Microfluidics and Nanofluidics **5**(6): 711-717.

Yamaguchi, E., et al. (2009). "μ-PIV measurements of the ensemble flow fields surrounding a migrating semi-infinite bubble." Experiments in fluids **47**(2): 309-320.

Yan, Y., et al. (2012). "Numerical simulation of junction point pressure during droplet formation in a microfluidic T-junction." Chemical Engineering Science **84**: 591-601.

Yang, L., et al. (2013). "An Experimental Study of Copper Extraction Characteristics in a T-Junction Microchannel." Chemical Engineering & Technology **36**(6): 985-992.

Yang, X., et al. (2014). "Electrochemical and Thermodynamic Properties of Ln(III) (Ln = Eu, Sm, Dy, Nd) in 1-Butyl-3-Methylimidazolium Bromide Ionic Liquid." PLoS ONE **9**(4): e95832.

Yang, X., et al. (2014). "Elextrochemical and thermodynamic properties of Ln(III) in 1-Butyl-3-Methylimidazolium Bromide Ionic liquid." PLoS ONE 9(4): e95832: doi:10.1371/journal.pone.0095832.

Yue, J., et al. (2009). "An experimental study of air–water Taylor flow and mass transfer inside square microchannels." Chemical Engineering Science **64**(16): 3697-3708.

Zhao, Y., et al. (2006). "Liquid-liquid two-phase flow patterns in a rectangular microchannel." AIChE Journal **52**(12): 4052-4060.

Appendixes

Appendix A. Sensitivity analysis of grid independence

The CFD software FLUENT was used to simulate the two-phase mixing hydrodynamics with a T-junction inlet. A high quality mesh is required to predict the thin film near the wall. Therefore the mesh in the mixing zone and near wall areas should be carefully dealt with. Theoretically hexahedron types more preferred for high stability and continuity, while tetrahedron as the second choice. Three meshing methods were developed and illustrated below. The grids were evaluated in terms of skewness: better grid quality shows lower skewness value.

1) The channel cross-section is separated by constructing a square in the middle, and four half fan-shaped areas around the square. The connection part was meshed with tetrahedron. Based on grid checking results, most grid (skewness<0.5) show good quality.

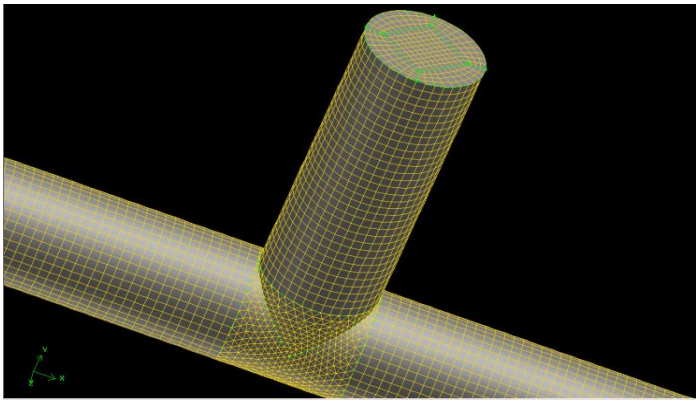

From value	To value	Count in range	% of total count (90424)
0	0.1	53920	59.63
0.1	0.2	15158	16.76
0.2	0.3	7579	8.38
0.3	0.4	6952	7.69
0.4	0.5	4335	4.79
0.5	0.6	1515	1.68
0.6	0.7	816	0.90
0.7	0.8	141	0.16
0.8	0.9	8	0.01
0.9	1	0	0.00
0	1	90424	100.00

Measured minimum value: 1.0835e-009
Measured maximum value: 0.821425

Figure A.1: Reprehensive of the meshed T-junction configuration with the first method (above) and grid checking results (below)

2) The channel cross-section is separated with four circular arcs, and four half fan-shaped areas around the arc. The connection was also meshed with tetrahedron. The grid shows better quality compared with the first method.

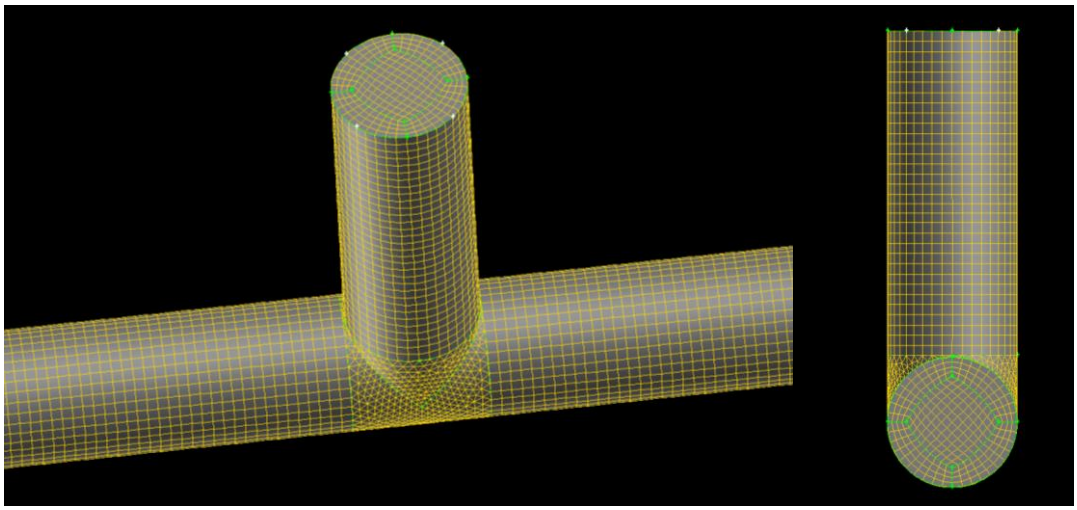

From value	To value	Count in range	% of total count (91379)
0	0.1	51511	56.37
0.1	0.2	18410	20.15
0.2	0.3	8021	8.78
0.3	0.4	8460	9.26
0.4	0.5	2709	2.96
0.5	0.6	1426	1.56
0.6	0.7	741	0.81
0.7	0.8	93	0.10
0.8	0.9	8	0.01
0.9	1	0	0.00
0	1	91379	100.00

Measured minimum value: 4.38261e-005
Measured maximum value: 0.810171

Figure A.2: Reprehensive of the meshed T-junction configuration with the second method (above) and grid checking results (below)

3) Small channel was spitted from the main tube, and meshed separately bordered by main channel symmetry plane. The upper small channel was meshed with four circular arcs in the middle part, while the bottom part was meshed with tetrahedron. The main channel was meshed with hexahedron. The grid quality was not as good as the former two meshing methods, due to the high distortion of the main channel grid.

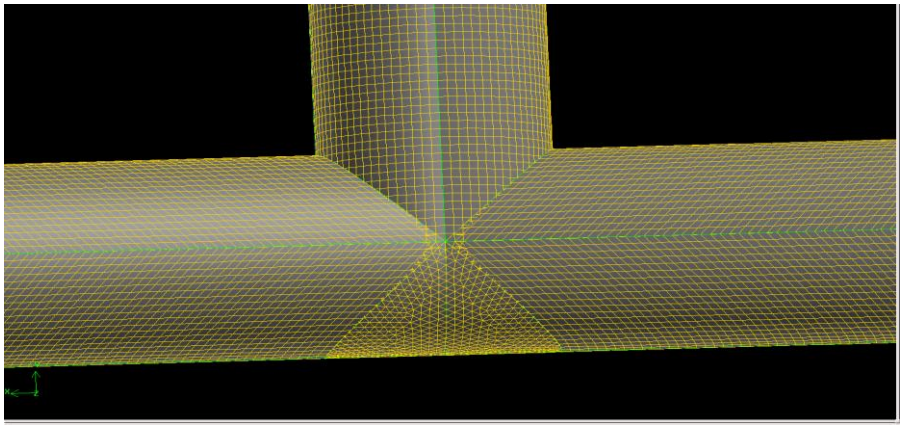

From value	To value	Count in range	% of total count (391616)
0	0.1	52264	13.35
0.1	0.2	94824	24.21
0.2	0.3	104020	26.56
0.3	0.4	77504	19.79
0.4	0.5	35216	8.99
0.5	0.6	14888	3.80
0.6	0.7	7396	1.89
0.7	0.8	3652	0.93
0.8	0.9	1516	0.39
0.9	1	336	0.09
0	1	391616	100.00

Measured minimum value: 0.000116214
Measured maximum value: 0.963768

Figure A.3: Reprehensive of the meshed T-junction configuration with the third method (above) and grid checking results (below)

As a result, meshes with the second method will be employed to calculate the simulation. In addition, axisymmetric grid was used to reduce calculation expense as shown in Figure A.4. The T-junction has an inner diameter of 0.5 mm with branches of the same size. The grid dependence was tested with mesh size of 6μm × 8μm, 8μm × 8μm and 8μm × 10μm. The tube diameter and length was set as 0.5mm and 10mm respectively. At first the mesh size of 8um*10um grid size was tested and evaluated. 1,353,365 grids are generated with this size, as depicted in **Error! Reference source not found.**.

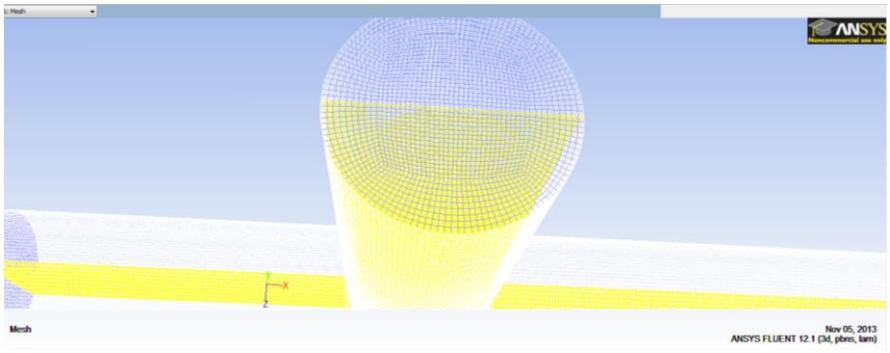

Figure A.4: A snapshot of microchannel mesh (Yellow part is the symmetry plane of the geometry)

Plugs in circular microchannel were also compared with 2D and 3D geometries. As shown in Figure A.5, the plug characteristic is totally different, and the formation pattern with 2D grid has never been reported by previous researchers to the best of author's knowledge, neither in the experimental observation. Therefore 3D domain should be employed to simulate the flow pattern in circular capillary.

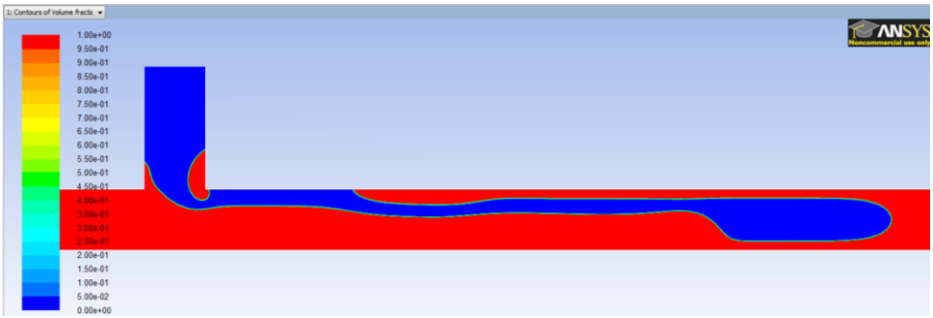

2D results

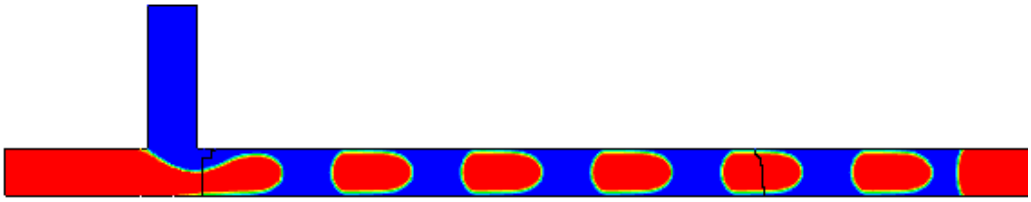

3D results

Figure A.5: Comparison of 2D and 3D results under same boundary condition (V_{aq}=V_{org}=0.06m/s)

Appendix B. Excitation and emission Spectrum of Eu(III)

For the selection of optical equipment in Laser Induced Fluorescence measurement, the fluorescence spectrum of each chemicals involved in the reaction should be studied, to ensure only the Eu(III) fluorescence signal can be captured. Various concentrations Eu(III) in aqueous and ionic liquid solution are tested, as well as in concentration diluent solution (50% TBP-cyclohexane).

Table B.1: Samples used in spectrum measurement

Sample 1	13mg/mL Eu(III) in 0.1M HNO_3 saturated ionic phase
Sample 2	13mg/mL Eu(III) in 1M HNO_3 saturated ionic phase
Sample 3	50mg/mL Eu(III) in 1M HNO_3
Sample 4	37mg/mL Eu(III) deionized water
Sample 5	37mg/mL Eu(III) in 1M HNO_3
Sample 6	0.7mg/mL Eu(III) in conventional organic liquid (50%TBP-cyclohexane)
Sample 7	Pure ionic liquid
Sample 8	Ionic liquid saturated with 1M HNO_3
Sample 9	Diluent 1: 10 of sample6

(a) Sample1. 13mg/mL Eu(III) in 0.1M HNO_3 saturated ionic phase

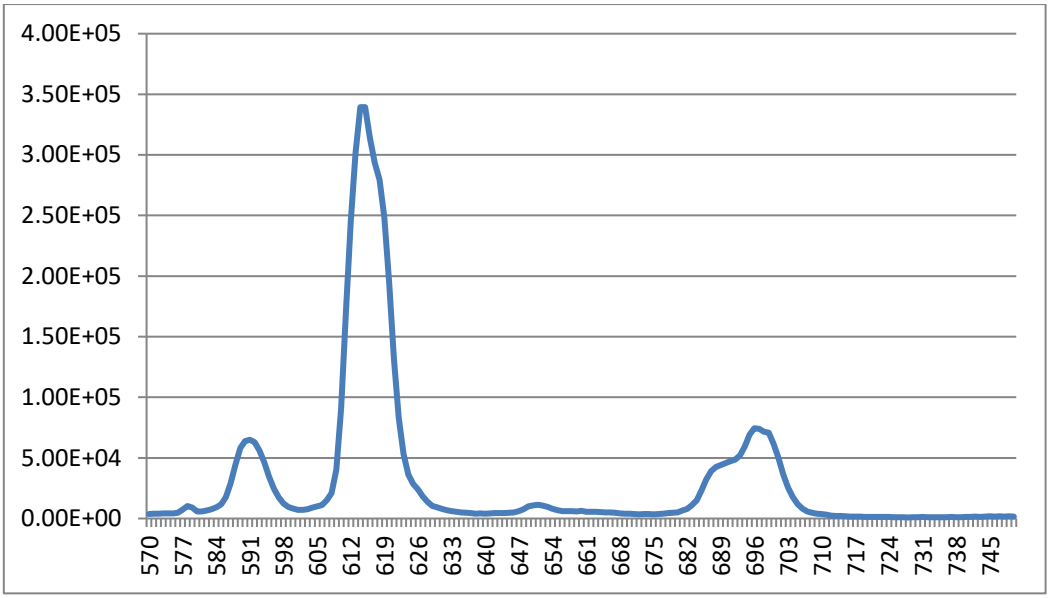

Figure B.1: Emission spectrum of sample 1. Excited at 395nm; wavelength range: 570nm-750nm; E_{xbw}=5.00 nm, E_{mbw}=2.00 nm; integrated intensity: $5.4*10^6$; Lamp Intensity: 462,000cps;

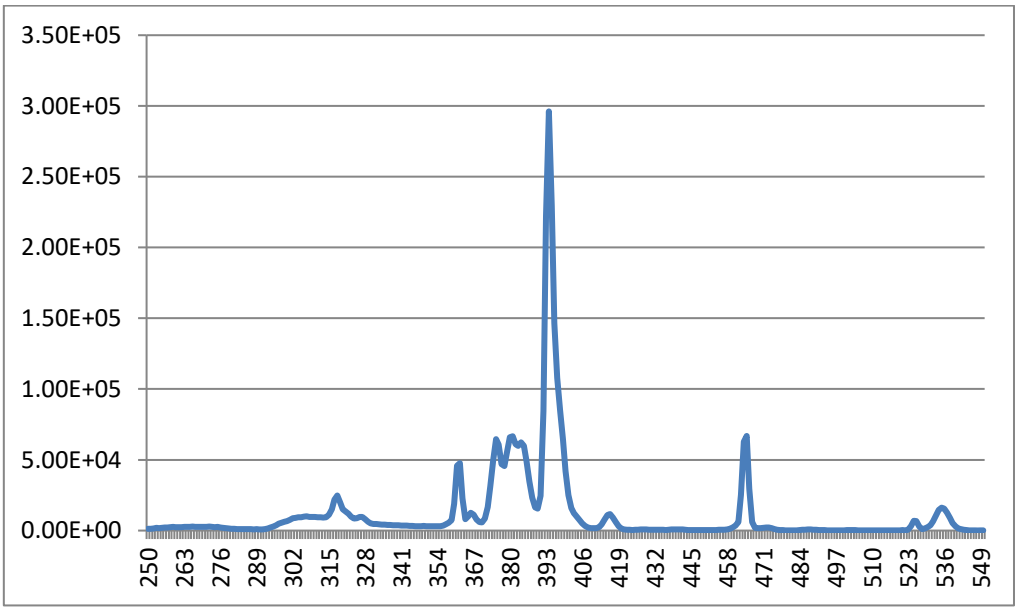

Figure B.2: Excitation spectrum of sample 1. Wavelength range 250-550nm; Emission peak: 614nm; E_{xbw}=2.00 nm, E_{mbw}=1.00.

(b) Sample2. 13mg/mL Eu(III) in 0.1M HNO_3 saturated ionic phase

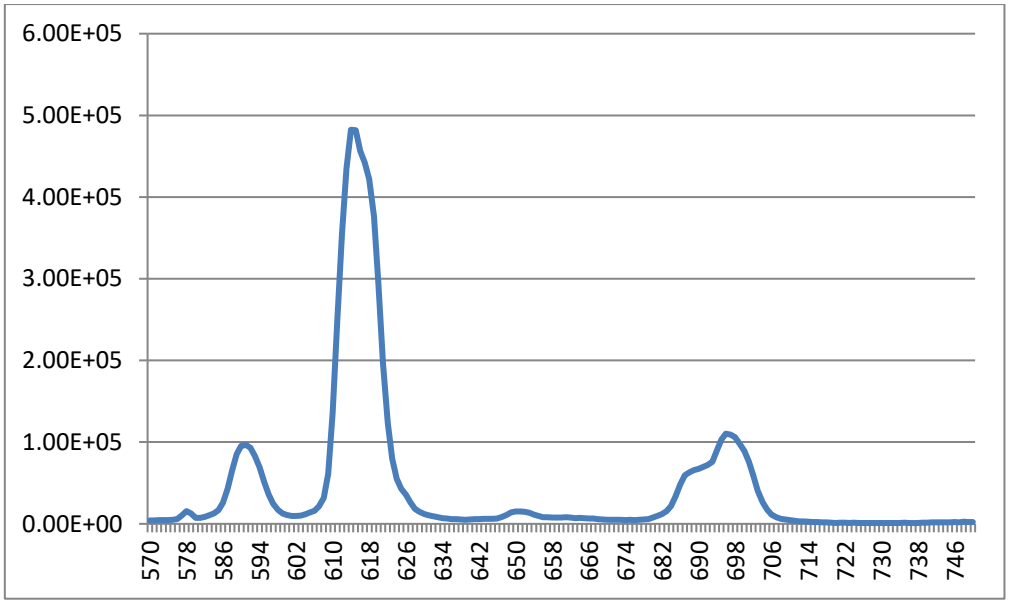

Figure B.3: Emission spectrum of sample 2. Excited at 395 nm; wavelength range: 570nm-750nm; E_{xbw}=5.00 nm, E_{mbw}=2.00 nm; integrated intensity: 7.876*10^6; Lamp Intensity: 462,000cps.

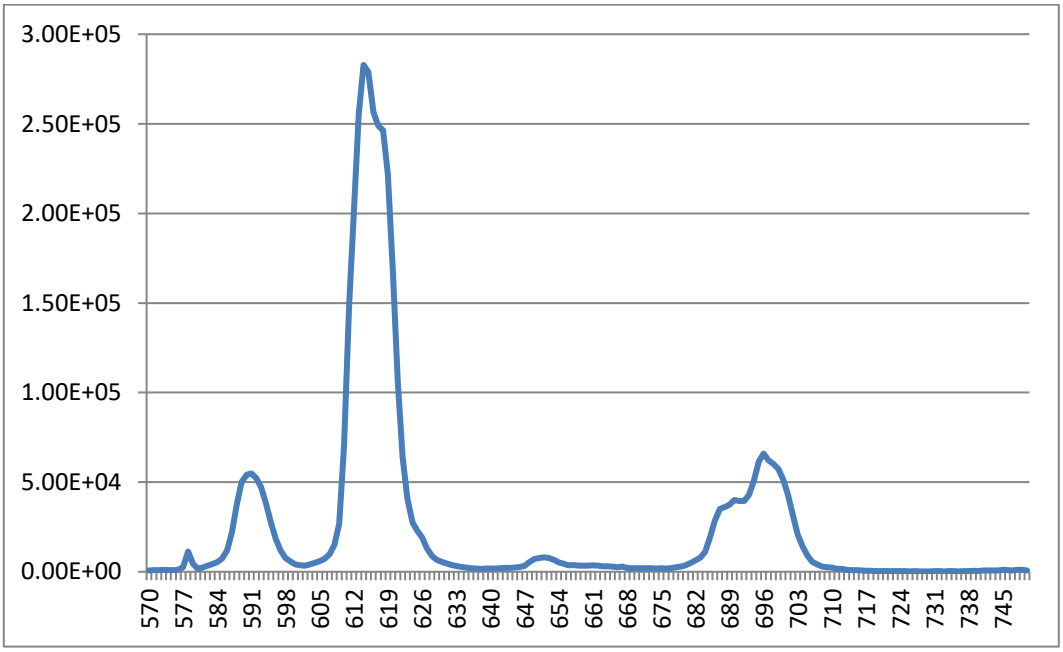

Figure B.4: Excitation spectrum of sample 2. Wavelength range 250-550nm; Emission peak: 614nm; E_{xbw}=2.00 nm, E_{mbw}=1.00, Integrated intensity: 4.34*10^6, Lamp Intensity: 327,000 cps

(c) Sample3. 50mg/mL Eu(III) in 1M HNO_3

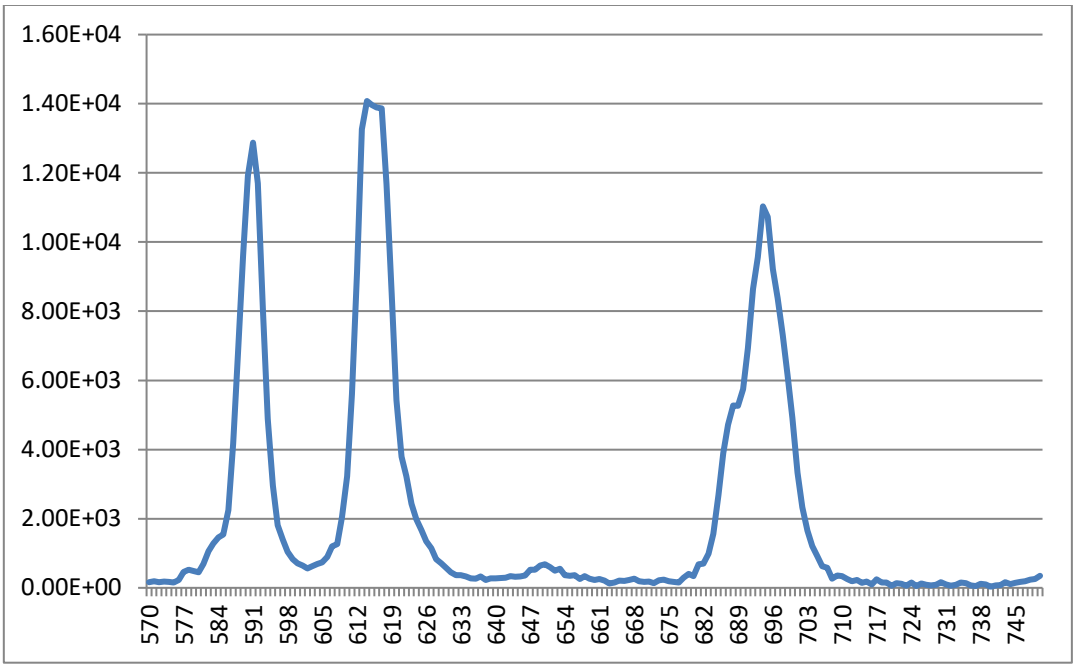

Figure B.5: Emission spectrum of sample 3. Excited at 395 nm; wavelength range: 570nm-750nm; E_{xbw}=5.00 nm, E_{mbw}=2.00 nm, integrated intensity: $3.759*10^6$.

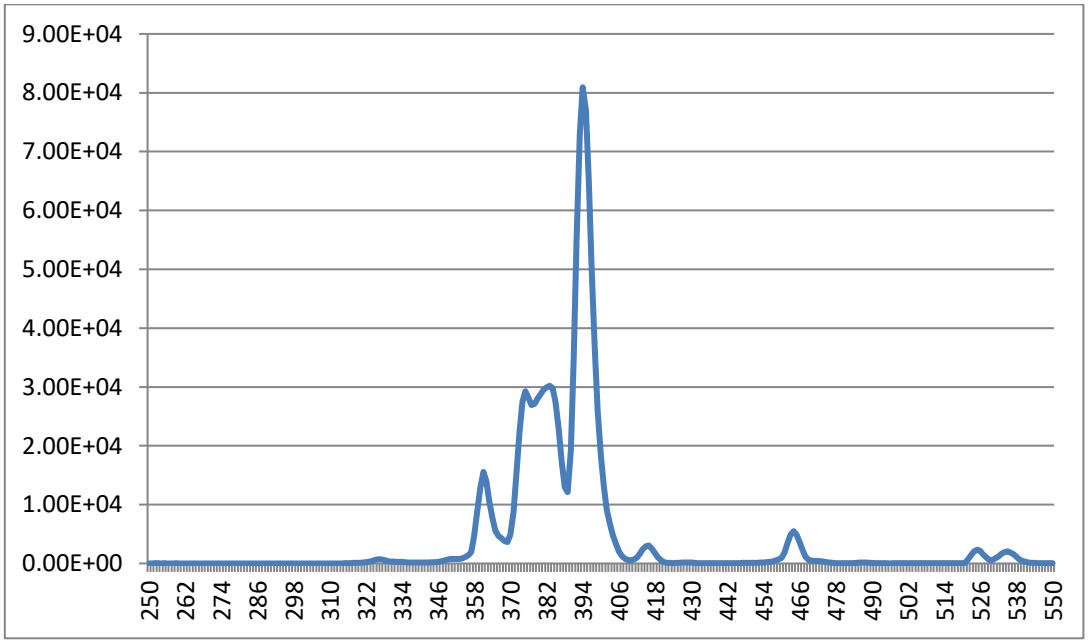

Figure B.6: Excitation spectrum of sample 3. Wavelength range 250-550nm; Emission peak: 614nm; E_{xbw}=2.00 nm, E_{mbw}=1.00, Integrated intensity: $5.55*10^5$.

(d) Sample4. 37mg/mL Eu(III) in deionized water

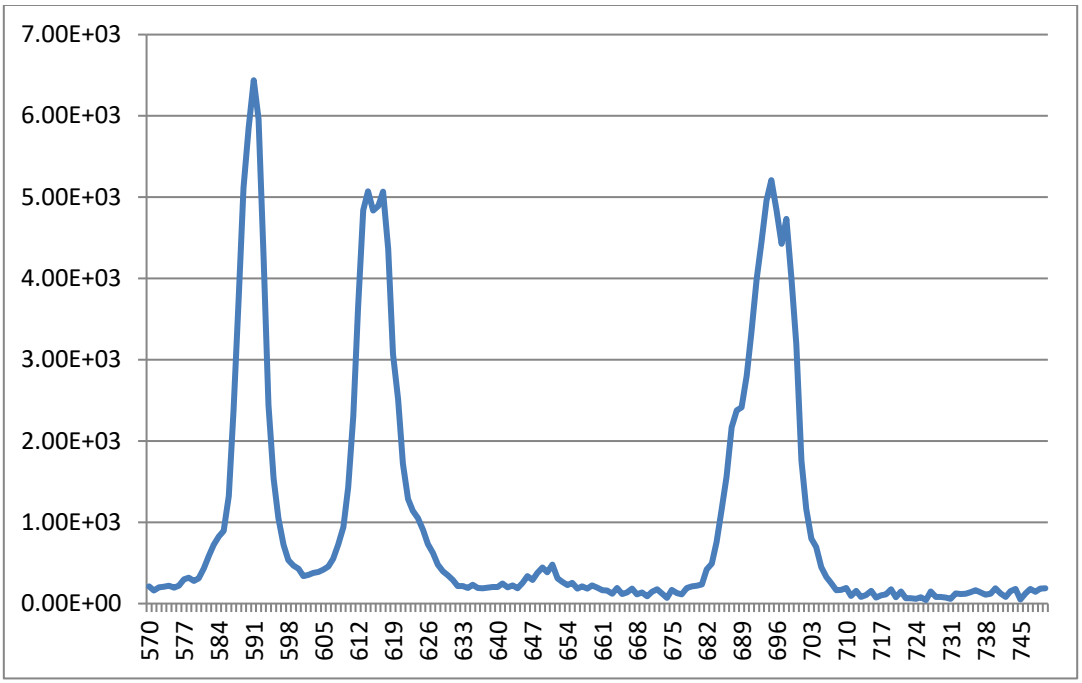

Figure B.7: Emission spectrum of sample 4. Excited at 395 nm; wavelength range: 570nm-750nm; E_{xbw}=5.00 nm, E_{mbw}=2.00 nm, integrated intensity: $1.821*10^5$.

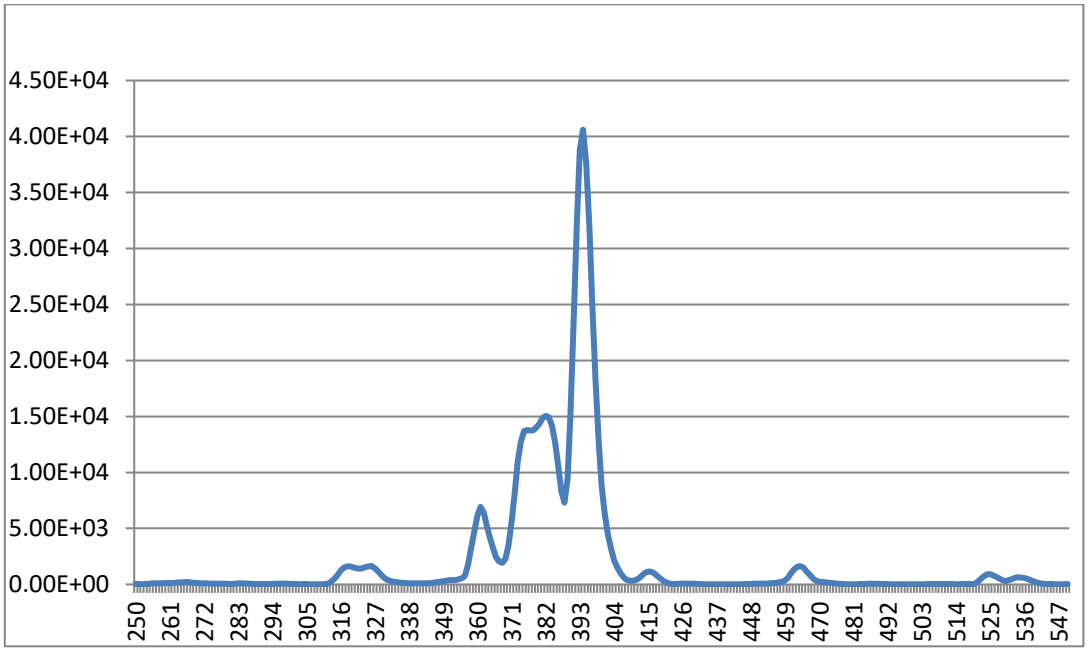

Figure B.8: Excitation spectrum of sample 4. Wavelength range 250-550nm; Emission peak: 614nm; E_{xbw}=2.00 nm, E_{mbw}=1.00, Lamp Intensity: 666,000cps.

(e) Sample5. 37mg/mL Eu(III) in HNO_3

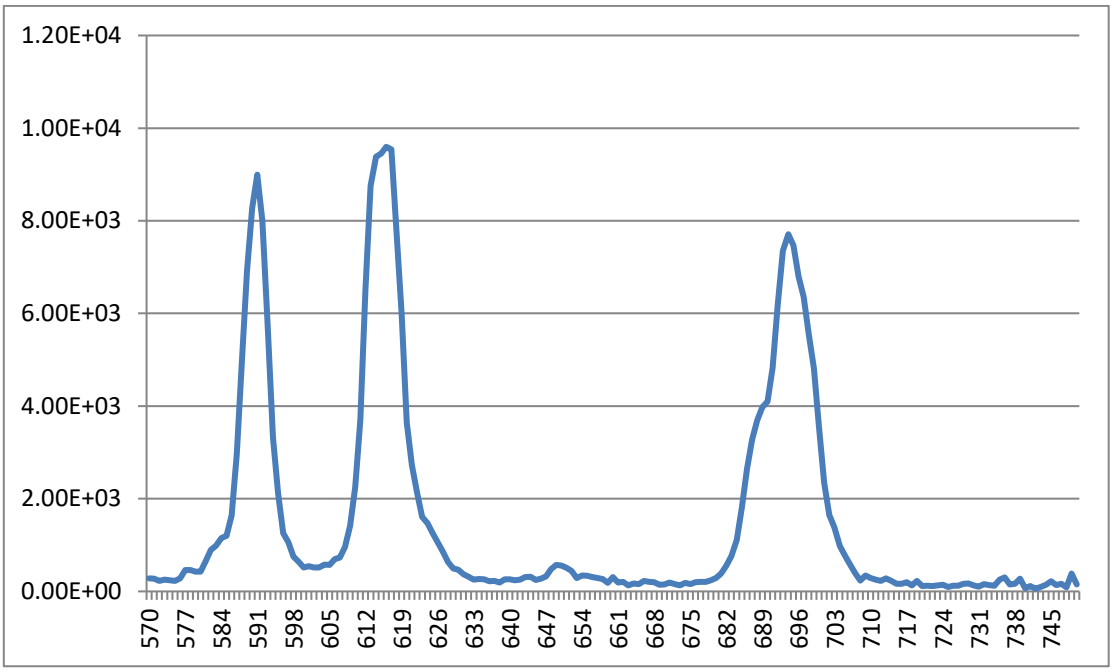

Figure B.9: Emission spectrum of sample 5. Excited at 395 nm; wavelength range: 570nm-750nm; E_{xbw}=1.00 nm, E_{mbw}=1.00 nm, integrated intensity: $2.73*10^5$, Lamp Intensity: 484,000cps.

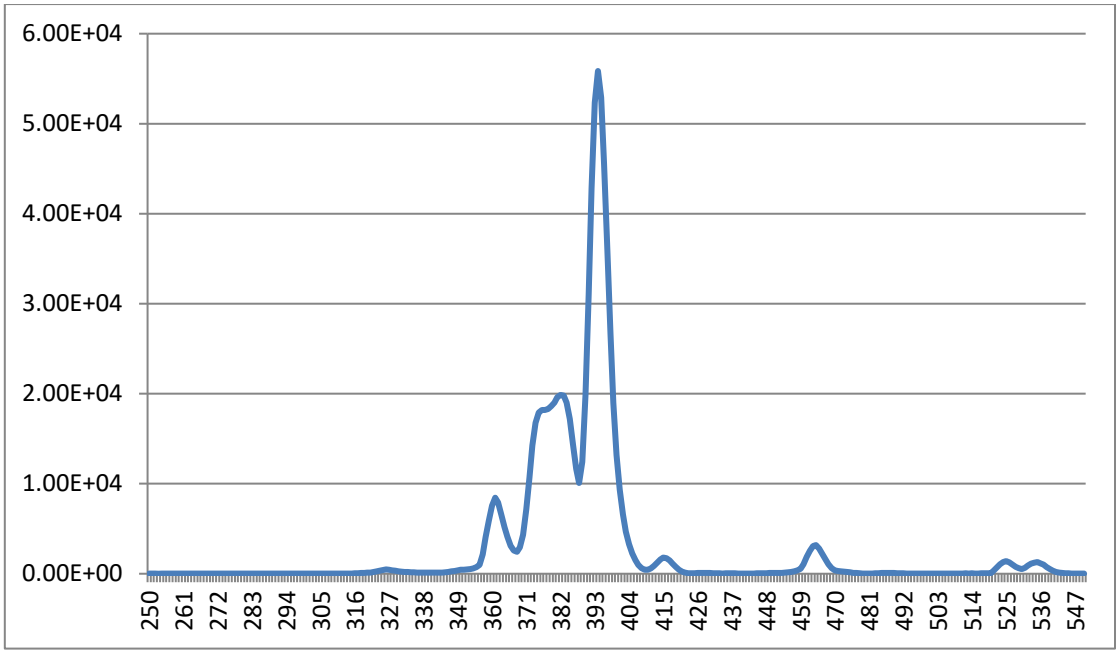

Figure B.10: Excitation spectrum of sample 5. Wavelength range 250-550nm; Emission peak: 614nm; E_{xbw}=2.00 nm, E_{mbw}=1.00, Lamp Intensity: 632,000cps.

(f) Sample6. 0.7mg/mL Eu(III) in conventional organic solution (50% TBP- cyclohexane)

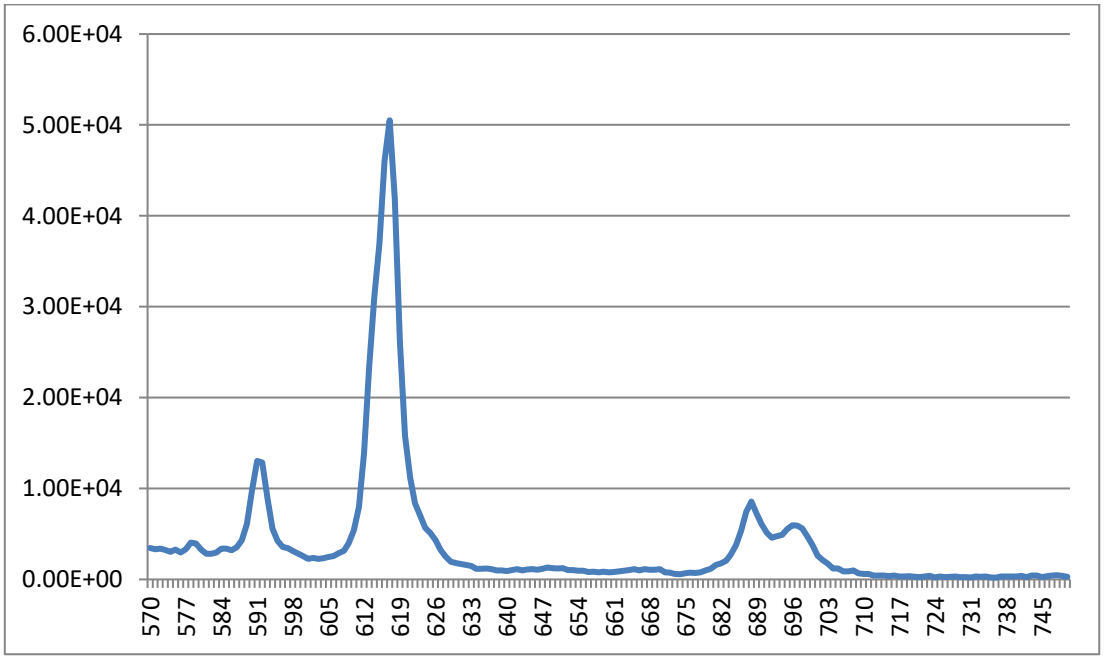

Figure B.11: Emission spectrum of sample 6. Excited at 395 nm; wavelength range: 570nm-750nm; E_{xbw}=1.00 nm, E_{mbw}=1.00 nm, integrated intensity: $6.88*10^5$, Lamp Intensity: 480,000cps.

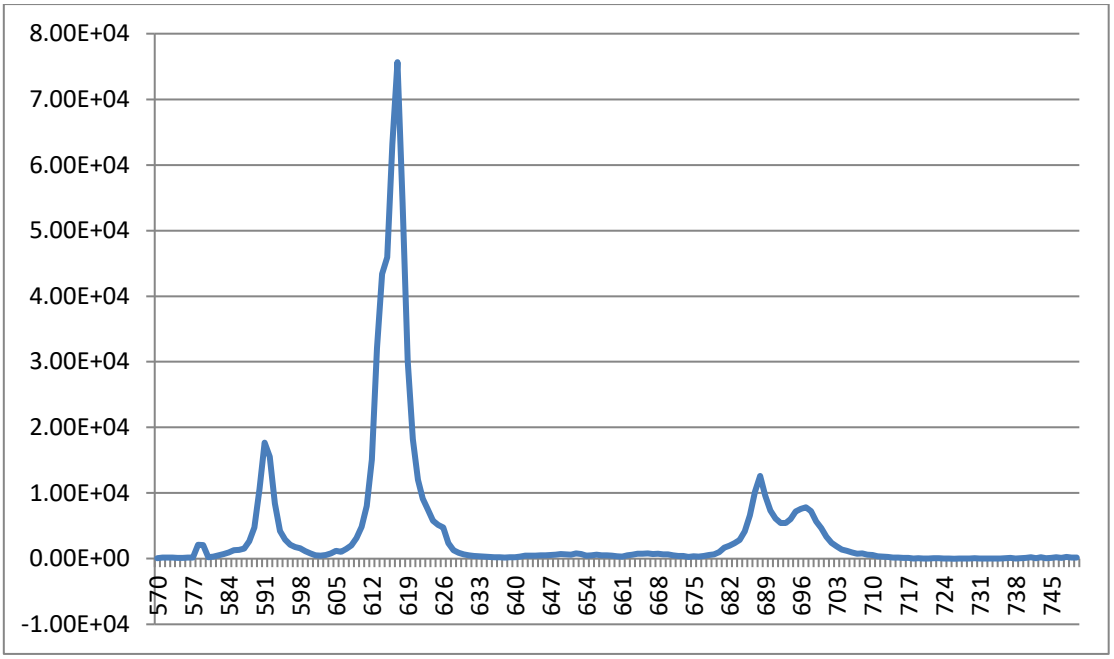

Figure B.12: Excitation spectrum of sample 6. Wavelength range 250-550nm; Emission peak: 614nm; E_{xbw}=2.00 nm, E_{mbw}=1.00, integrated intensity: 7.039*10^5, lamp Intensity: 666,000cps.

(g) Sample 7. Pure ionic liquid

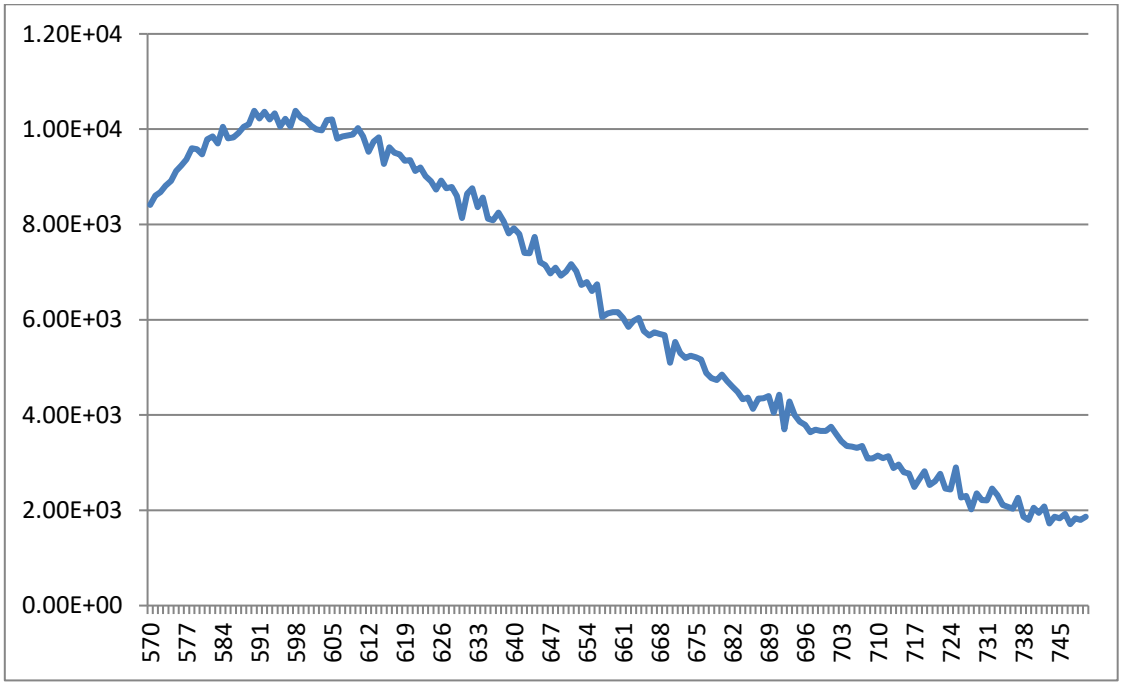

Figure B.13: Emission spectrum of sample 7. Excited at 395 nm; wavelength range: 570nm-750nm; E_{xbw}=5.00 nm, E_{mbw}=2.00 nm, integrated intensity: 1.12*10^6, Lamp Intensity: 480,000cps.

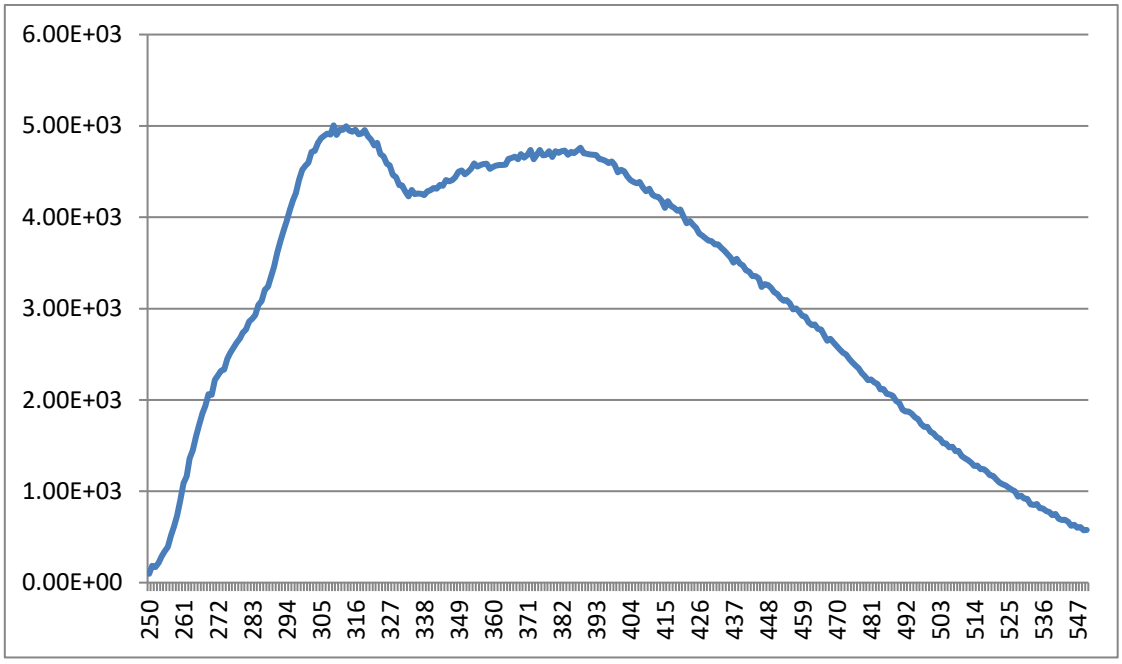

Figure B.14: Excitation spectrum of sample 7. Wavelength range 250-550nm; Emission peak: 614nm; E_{xbw}=2.00 nm, E_{mbw}=1.00.

(h) Sample 8. Ionic liquid saturated with 1M HNO_3

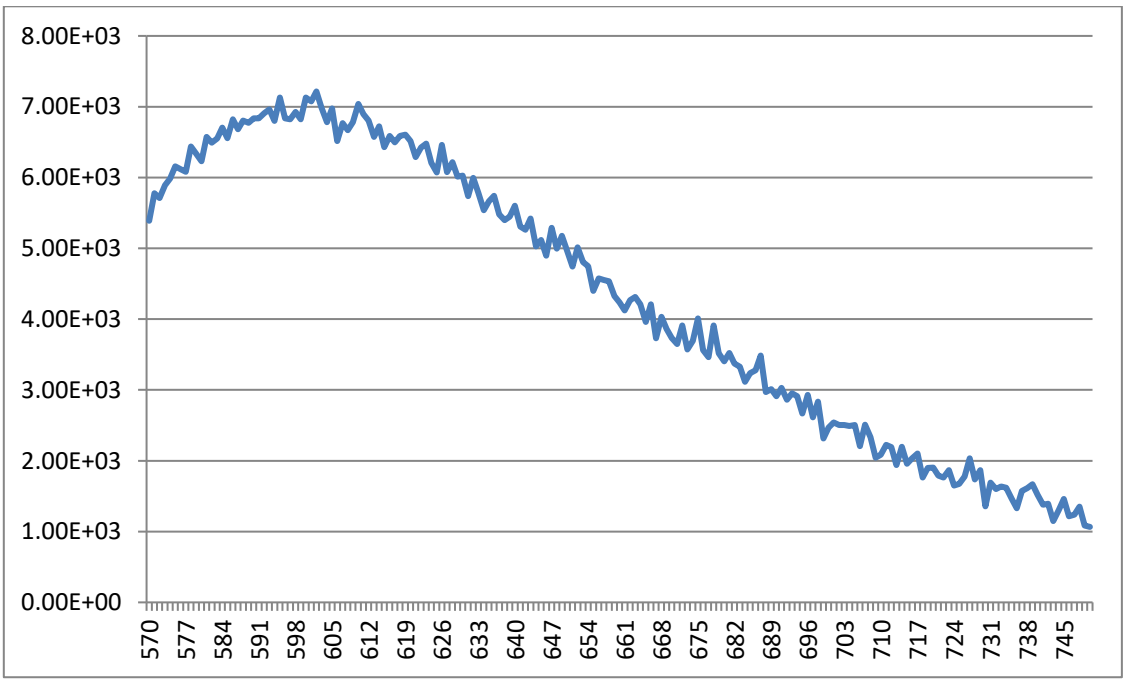

Figure B.15: Emission spectrum of sample 8. Excited at 395 nm; wavelength range: 570nm-750nm; E_{xbw}=5.00 nm, E_{mbw}=2.00 nm, integrated intensity: $7.78*10^5$, Lamp Intensity: 450,000cps.

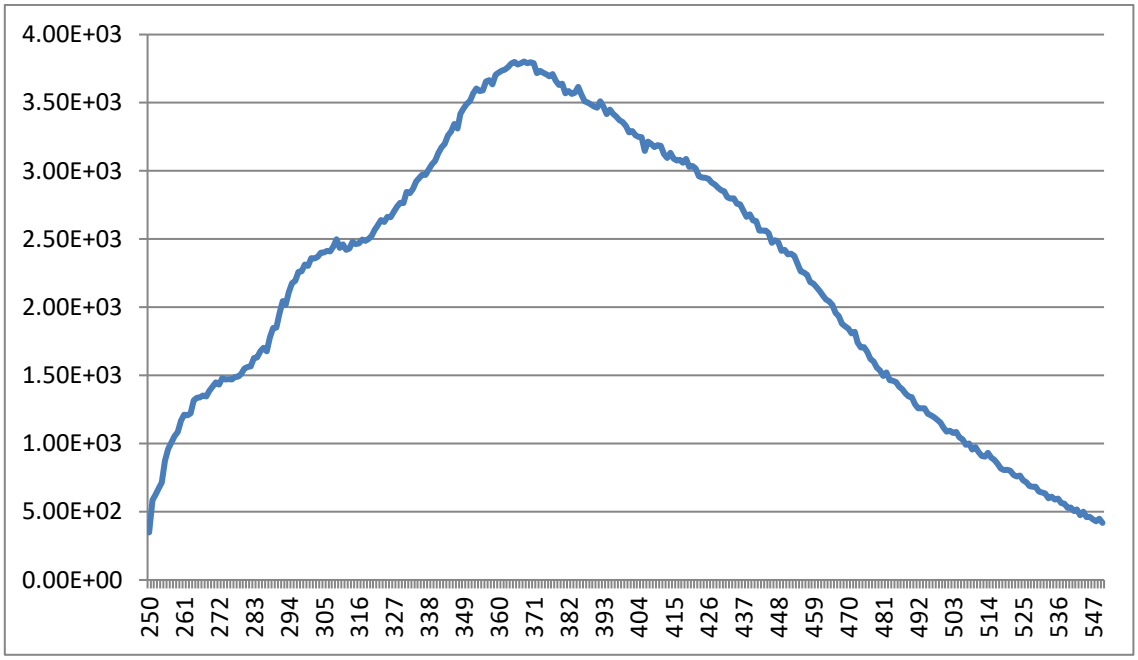

Figure B.16: Excitation spectrum of sample 8. Wavelength range 250-550nm; Emission peak: 614nm; E_{xbw}=2.00 nm, E_{mbw}=1.00.

(i) Sample 9. Diluent of sample 6

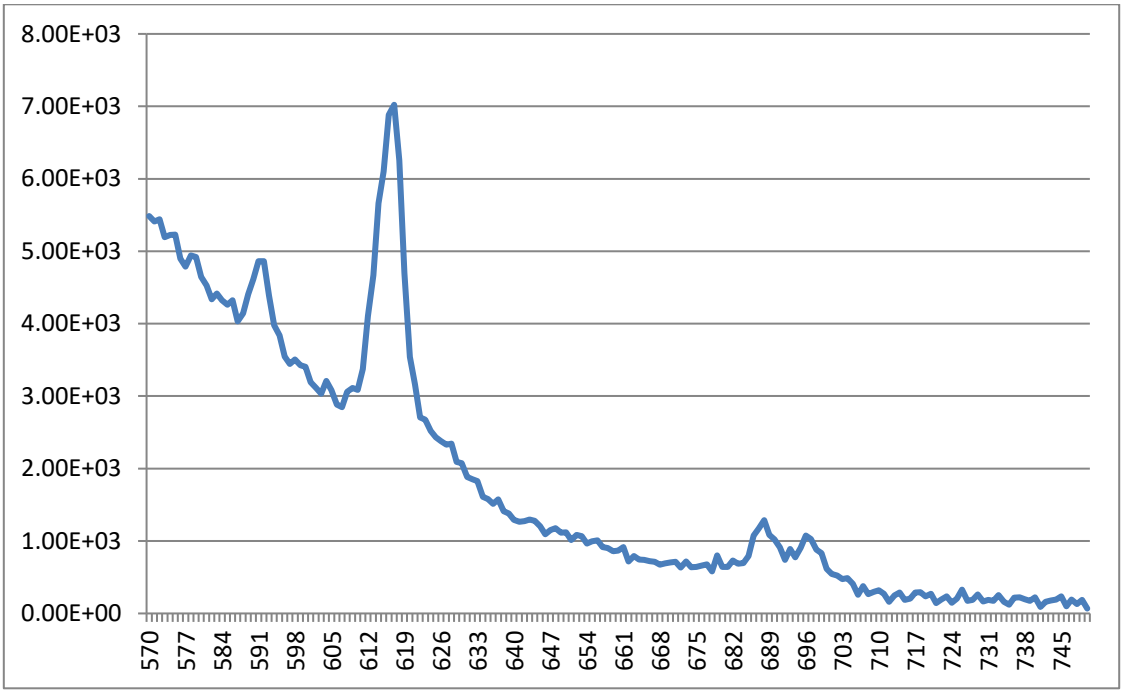

Figure B.17: Emission spectrum of sample 9. Excited at 395 nm; wavelength range: 570nm-750nm; E_{xbw}=5.00 nm, E_{mbw}=2.00 nm, integrated intensity: $3*10^5$, Lamp

Intensity: 480,000cps.